NANOSTRUCTURED SEMICONDUCTING POLYMER INORGANIC COMPOSITES FOR OPTO-ELECTRONIC APPLICATIONS

THESIS SUBMITTED TO

COCHIN UNIVERSITY OF SCIENCE AND TECHNOLOGY

FOR THE DEGREE OF

DOCTOR OF PHILOSOPHY

IN

POLYMER SCIENCE AND TECHNOLOGY

Under the Faculty of Technology

By

R. Ramakrishnan
(Reg. No. 4426)

Under the Supervision of

Dr. J. D. Sudha
&
Dr. Manoj Raama Varma

Chemical Sciences and Technology Division
CSIR-National Institute for Interdisciplinary Science and Technology (CSIR-NIIST), Trivandrum 695 019, Kerala

July 2016

Declaration

I hereby declare that the Ph.D thesis entitled "**Nanostructured Semiconducting Polymer Inorganic Composites for Opto-Electronic Applications**" is the result of investigations carried out by me at the Chemical Sciences and Technology Division of the CSIR-National Institute for Interdisciplinary Science and Technology (CSIR-NIIST), Trivandrum, under the Joint supervision of Dr. Manoj Raama Varma and Dr. J. D. Sudha and the same has not been submitted elsewhere for a degree.

In keeping with the general practice of reporting scientific observations, due acknowledgement has been made wherever the work described is based on the findings of other investigators.

(R. Ramakrishnan)

NATIONAL INSTITUTE FOR INTERDISCIPLINARY SCIENCE AND TECHNOLOGY (NIIST)

(Formerly Regional Research Laboratory)
Council of Scientific & Industrial Research (CSIR)
Industrial Estate P.O., Trivandrum–695 019,
Kerala, INDIA

July 25, 2016

CERTIFICATE

This is to certify that the Ph.D thesis entitled "Nanostructured Semiconducting Polymer Inorganic Composites for Opto-Electronic Applications" has been carried out by **Mr. R. Ramakrishnan** under our supervision at the Chemical Sciences and Technology Division of the CSIR-National Institute for Interdisciplinary Science and Technology (CSIR-NIIST), Trivandrum and the same has not been submitted elsewhere for a degree. All the relevant corrections, modifications and recommendations suggested by the audience and the doctoral committee members during the pre-synopsis seminar of **Mr. R. Ramakrishnan** have been incorporated in the thesis.

Dr. Manoj Raama Varma
Professor (AcSIR)
Thesis Supervisor

Dr. J. D. Sudha
Associate Professor (AcSIR)
Thesis Supervisor

.....to my dear amma, appa and anna

Acknowledgement

I have great pleasure to express my deep sense of gratitude to Dr. J. D. Sudha, my research supervisor, for her adroit guidance, constant encouragement, intellectual support, constructive criticism and above all the freedom she gave me during the course of my doctoral studies. I am greatly indebted to her for all the efforts she has put in for the successful completion of this thesis.

I have great pleasure to express my deep sense of gratitude to Dr. Manoj Raama Varma, my research supervisor for his guidance and continuous support, during the course of my doctoral studies.

I wish to thank Dr. A. Ajayaghosh, Present Director and Dr. Suresh Das, former Director of the CSIR-NIIST, Trivandrum for providing me the necessary facilities for carrying out the work.

I sincerely thank Professor Dr. Manfred Stamm and lab members of Leibniz Institute of Polymer Research, for the help rendered during my research stay in Dresden, Germany.

I thank all my doctoral committee members Prof. Sunil K Narayanan Kutty, Dr. Narayanan Unni and Dr. Saju Pillai for their help and support.

I sincerely thank Dr. K. R. Gopidas, Dr. D. Ramaiah, Dr. Prabhakar Rao, Dr. M. L. P. Reddy, Dr. E. Bhoje Gowd, Dr. K. B. Jinesh, Dr. Senoy Thomas, Dr. S. Ananthakumar, Dr. A. R. R. Menon and all the scientist in NIIST for their help and support extended to me.

I thank Dr. Luxmi Varma APC Chairperson and Dr. T. P. D. Rajan convenor CSIR-NIIST Trivandrum for their help and support. And also i thank Dr. N. Somananthan CSIR-CLRI for his support.

I extended my thankfulness to Mr. M. R. Chandran, Ms. Lucy Paul, Ms. Sowmya, Mr. Kiran Mohan, Mr. Robert Philip, Mr. Aswin Mr. Kiran J S, Mr. Guruswamy, Ms. Viji, Ms. Soumini, Mr. Veluswamy, Mr. Peer Mohammed A, Mr. S. Silambarasan, Ms. Jyothi B Nair, Mr. Vishnu and Mr. Ajesh P for their characterization studies.

I would also like to extend warm thanks to Dr. Reena V. L and Ms. Sivakala during my intial stage of research. My dear colleagues Ms. Rohini K. N, Ms. Neethu K. S, Mr. Renjith. S, Mr. A. Aashish, Ms. Molji. C, Ms. Reshma L. R, and Ms. Najiya K. P. P. for their constant help,advice, support and cooperation during my doctoral studies.

I would also like to thank my dear friends Mr. Eliyas Mohamed, Dr. Panneer selvan,Mr. Shanmugasundram, Mr. Jay, Mr. Vedhanarayanan, Mr. Thirumalai Kumaran, Dr. M. Suresh, Mr. Dharani, Mr. Suresh Kanan, Mr. Vaisaksh S, Mr. Maniganda, Mr. Shameel, Mr. B. Nagendra, Mr. Shaiju, my dear sister Ms. Anju, Ms. Deepa, Ms. Resmi, Ms. Lakshmi, Ms. Annu, Mr. Robbinson, Dr. Jinish Antony, Mr. Jaggaiah, Mr. Vipin, Mr. Dipu, Dr. Balamurugan, Dr. Selvakumar, Ms. Sijla, Ms. Deepthi, Ms. Jerin, Ms. Asha and all other friends for their love, help and support.

Words are insufficient to express my heartfelt thanks to my dear Amma, Appa and Anna for their love, guidance, motivation, constant source of support and encouragement.

Financial assistance from CSIR, Government of India is gratefully acknowledged.

Last but not least, I praise God, the almighty for providing me this opportunity and granting me the capability to proceed successfully.

R. Ramakrishnan

CONTENTS

List of Schemes

List of Tables

List of Figures

List of Abbreviations

SCPICs	Semiconducting Polymer-Inorganic Nanocomposites
PA	Polyacetylene
PVK	Poly (N-vinylcarbazole)
PANI	Polyaniline
PT	Polythiophene
PEDOT	Poly(3,4-ethylenedioxythiophene)
PPy	Polypyrrole
CV	Cyclic voltammetry
PS-*b*-PMMA	Polystyrene-*b*-polymethyl methacrylate
CS-AFM	Current-sensing atomic force microscopy
HOMO	Highest occupied molecular orbital
VB	Valence band
LUMO	Lowest unoccupied molecular orbital
CB	Conduction band
μ	Carrier mobility
n	Charge carrier concentration
ZnO	Zinc oxide
TiO_2	Titanium dioxide
0D	Zero dimensional
1D	One dimensional
2D	Two dimensional
3D	Three dimensional
I-V	Current-voltage
WORM	Write once read many times
DRAM	Dynamic random access memory
TE	Thermoelectric materials
DMSO	Dimethylsulphoxide
EG	Ethylene glycol
Bi_2Te_3	Bismuth telluride
PbTe	Lead telluride
OFET	Organic field effect transistor
SWNT	Single walled nanotube
OLED	Organic light emitting diodes
PPTC	Nanostructured polyaniline-polytitanate-clay nanocomposite
PHT	Polytitanate
PHTC	Polytitanate intercalated clay
B. E. T	Brunauer–Emmett–Teller
MO	Methyl orange

MB	Methylene blue
DRS	Diffuse reflectance spectroscopy
DLS	Dynamic light scattering
FT-IR	Fourier transform infrared spectroscopy
XRD	X-ray diffraction
WAXS	Wide angle X-ray scattering
EDS	Energy dispersive X-ray spectra
SEM	Scanning electron microscope
HR-TEM	High Resolution Transition electron microscope
DSSC	Dye sensitized solar cells
PCE	Power conversion efficiencies
V_{oc}	Open circuit voltage
J_{sc}	Short circuit current
FF	Fill factor
PDPPA	Pentadecylphenylphosphoricacid
fwhm	Full width in radians at half-maximum
$h\nu$	Photon energy
h	Plank's constant
ν	Wavenumber
t	Optical path length
TO	Transverse-optical
LO	Longitudinal-optical
AFM	Atomic force microscope
SAED	Selected area diffraction
FFT	Fast fourier transform
PVZ	Polyvinylcarbazole- ZnO nanocomposite
PVK	Polyvinylcarbazole
$FeCl_3$	Ferric chloride
Bu_4NPF_6	Tetrabutylammonium hexafluorophosphate
ITO	Indium tin oxide
PVK-TiO_2	Polyvinylcarbazole-titanium dioxide
PVP-ZnO	polyvinylpyrrolidone-zinc oxide
PL	Photoluminescence
NDR	Negative differential resistance
T	Temperature
PL	Poole–Frenkel emission model
SCLC	Space charge limit current
PZT	Poly (3, 4-ethylenedioxythiophene)–TiO_2/ZnO
ZTO	TiO_2/ZnO
EDOT	3, 4-ethylenedioxythiophene

L	Localization length
σ_0	High temperature limit of conductivity
ZT	figure of merit
α	Seebeck coefficient
σ	Electrical conductivity
κ	Thermal conductivity
VRH	Mott's variable range hopping model
T_0	Mott temperature
R_{hop}	Hopping distance
E_{hop}	Activation energy
R_H	Hall coefficient
e	Electronic charge
K	Boltzmann constant
ε	Dynamic permittivity
Φ	Energy barrier height
d	Thickness
ε_o	Dynamic permittivity of free space
PPMS	Physical Property Measurement System
Ag	Silver
Cu	Copper
$TiCl_4$	Titanium tetrachloride
MMT	Montmorillonite
Na-cloisite	Sodium cloisite
APS	Ammonium persulfate
C	Absorbance of dye solution
Co	Absorbance of original dye were measured every 5 minutes
S	Siemens

Preface

Recent developments on nanostructured conducting polymer-inorganic composites systems have receieved considerable research interest owing to their unique synergestic properties compared with their individual bulk counter parts which make them promising candidates for a broad spectrum of high technological applications such as in energy conversion, electronic devices, storage, sensors, actuators, memory devices, and biomedical devices. Nanostructured conducting polymers possess unique features such as high specific surface area, high charge carrier concentration, high electrical conductivity, high mechanical flexibility, light weight, solution processability and printability over a large area which make them favourable for their high tech applications. Among the conducting polymers, polyanilline, poly(3,4-ethylenedioxythiophene), poly(N-vinylcarbzole) are receiving much importance due to their low cost, environmental stability and unique doping mechanism. Conversely, semiconducting inorganic metal oxide such as zinc oxide and titania nanomaterials have emerged as an area of intense research interest motivated by their potential applications in electronics, non-linear optics, and magnetic devices due to their low band gap, small crystalline size and unique opto-electronic properties. In this perspective, studies on the development and applications of semiconducting polymer-inorganic metal oxide nanocomposite are interesting since it is expected to exhibit synergistic properties arising from the molecular level mixing of conducting polymer and inorganic counter parts.

In this program, we have done an overview of the recent research and developments in the area of semiconducting polymer-inorganic metal oxide nanocomposites, properties, mechanism and various functional applications.

Eventually we have developed and characterized various conducting polymer-titania/zinc oxide nanocomposites. Finally demonstrated their applications as photocatalyst, and also as an active material for the fabrication of devices such as DSSC, memory devices, thermoelectric device.

The present thesis has been divided into five chapters. The first chapter illustrates an overview of the recent developments in semiconducting hybrid nanocomposites including conduction mechanism, preparation strategies, properties, and their various applications.

The second chapter describes the preparation and properties of nanostructured polyaniline-polytitanate-clay (PPTC) nanocomposite and demonstration of its application as an efficient photocatalyst for the photodegradation methylene blue and methyl orange at room temperature. Studies revealed that the prepared nanocomposite can be used as a prospective candidate for the disposal of organic pollutants present in the environment.

The third chapter of this thesis depicts the bio-anchoring strategy for controlling the crystal growth and preparation of hierarchical multiscale ZnO structures. Further, demonstrated its application as an effcient photoanode in dye sensitized solar cells for improving the power conversion efficiency.

The design, synthesis and fabrication of poly(N-vinylcarbazole)-ZnO (PVZ) based non-volatile memory device are described in the fourth chapter of the thesis.

The fifth chapter portrays the preparation and properties of poly(3, 4-ethylenedioxythiophene)-TiO_2/ZnO(PZT) nanocomposite. Its application as an efficient active material for the fabrication of thermoelectric device.

Finally summarized the salient findings observed during this program.

Chapter 1

Nanostructured Semiconducting Polymer Inorganic Composites for Opto-Electronic Applications

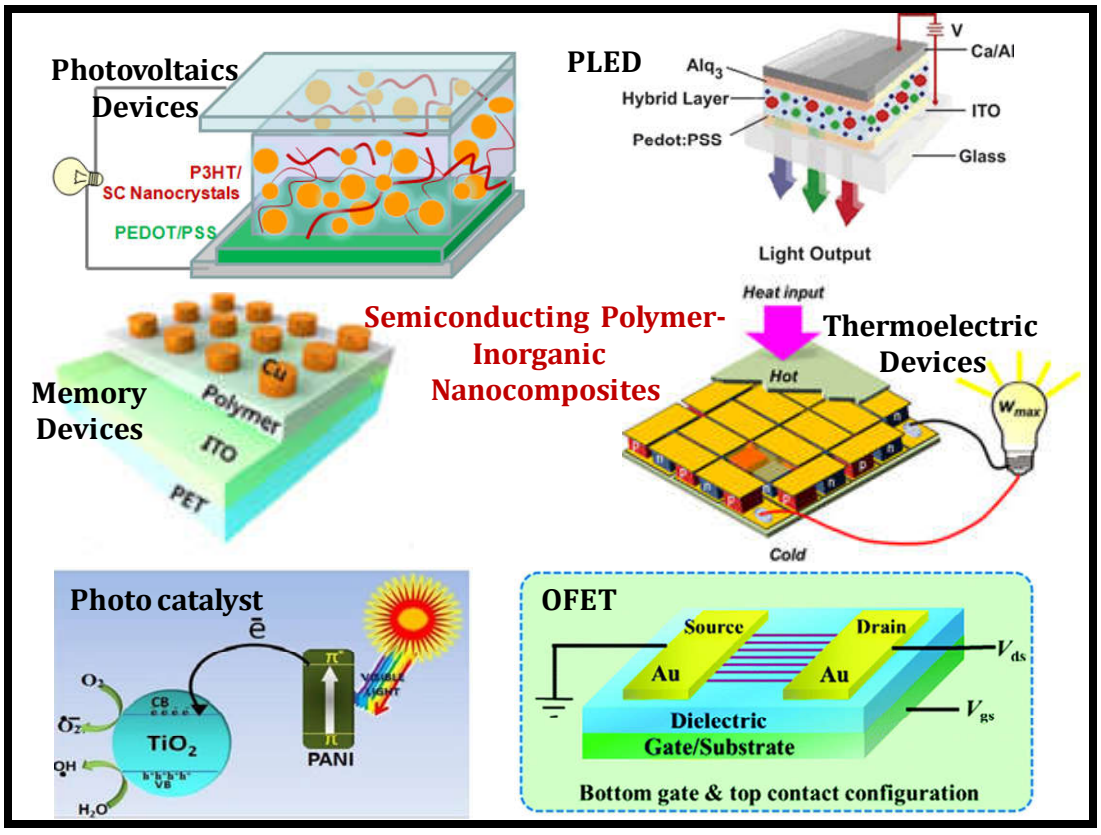

1.1. Abstract

Nanocomposites comprising of semiconducting polymers and inorganic materials offer favourable perspective for the development of high efficient opto-electronic devices through its tunable band gap, charge carrier mobility, increased charge carrier concentration in combination with an easy processability in large area, flexibility, light weight and low cost. The synergistic properties arising from the designed structures expected to exhibit properties and functions which is superior to its individual components. The incentive to co-assemble organic and inorganic semiconducting materials in the molecular level by tuning the interfacial interactions on the nanoscale can control the band gap and morphology for the formation of a highly efficient novel class of active materials for various electronic devices. The presence of conjugated polymer is expected to enhance the solution processability, light weight, flexibility, low cost whereas the inorganic counter parts are endowed with unique opto-electronic, chemical and mechanical properties. The present chapter illustrates an overview of nanostructured semiconducting polymer-inorganic composites, its fundamental aspects on the properties and applications such as photocatalysts, opto-electronic devices such as memory, thermoelectric, organic field effect transistors, organic light emitting diodes, solar cell and so forth.

1.2. Introduction

Development of Semiconducting Polymer-Inorganic Nanocomposites (SCPICs) having unique opto-electronic properties are receiving lots of attraction in recent years due to its intriguing properties and potential applications.[1]These

SCPICs are endowed with combined advantages of inorganic particles (e.g. metal oxides, metal nanoparticles and layered materials) and organic counterparts (e.g. conjugated oligomers and polymers). Recently researchers have taken greater efforts towards enhancing the properties of hybrid nanocomposites by accomplishing excellent percolation of inorganic nanoparticles within the polymer matrix.[2-4] Apart from achieving excellent percolation, enhancement in charge carrier mobility and charge carrier concentration is also a great challenge for the development of efficient opto-electronic devices. During the processing of hybrid nanocomposites, an intimate contact between polymer-inorganic nanoparticles is to be established which may help to increase the interfacial area between the junction and controlled distribution of the nanoparticles within the polymeric matrix. The advantages of nanocomposite materials is to facilitate the transfer of charge carriers across the interfaces which results in an increases in the charge carrier mobility and also enhance the electrical conductivity.[4] In addition, self organization, ordered structure, crystallinity, well defined morphologies and interaction between the semiconducting polymer-nanoparticle in the nano level also play pivotal role in the properties of hybrid nanocomposites.[5] SCPICs play a crucial role in the development of advanced functional nanomaterials which are expected to revolutionize the emerging opto-electronic technology such as flexible display panels, solar cells, volatile and non-volatile memory device, organic field effect transistors, thermoelectric devices and photocatalysts applications as shown in Figure 1.1.

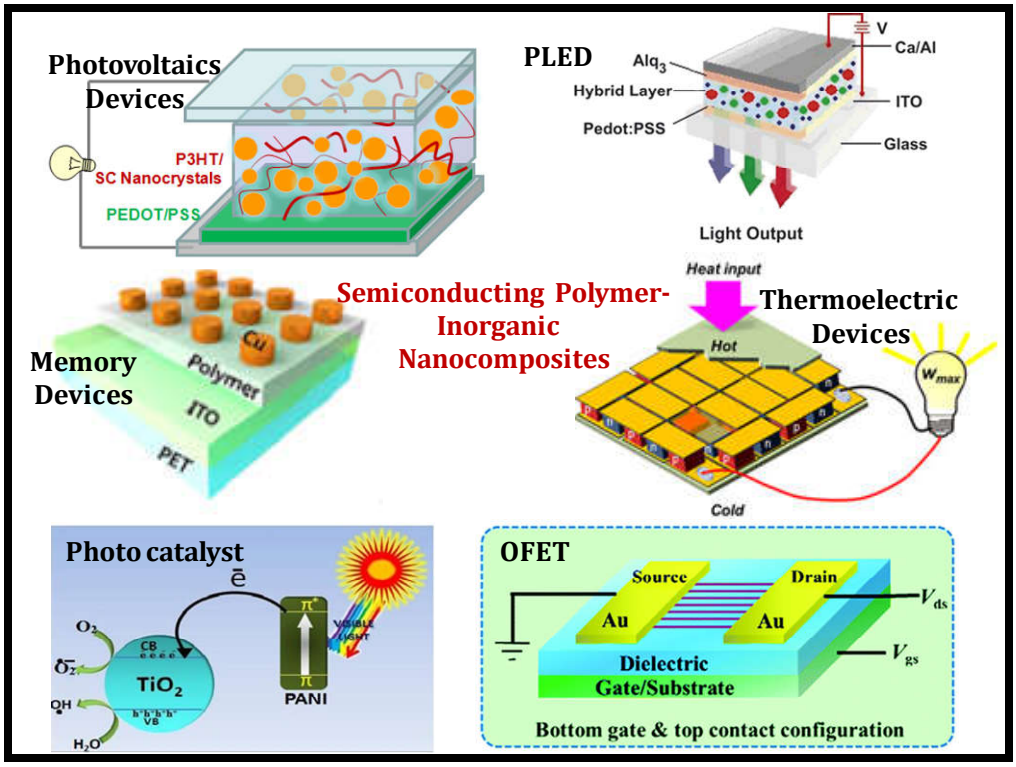

Figure 1.1. Applications of nanostructured semiconducting polymer-inorganic nanocomposites

1.3. Conducting Polymers

Conducting polymers are conjugated organic compounds with an extended π-orbital system through which electrons can move from one end of the polymer to the other. With the invention of conductive polyacetylene in the 1970s, conducting polymers have received significant attention from both science and engineering communities. The Nobel Prize in chemistry in the year of 2000 was awarded to Alan J. Heeger, Alan G MacDiarmid and Hideki Shirakawa for the discovery of conducting polymers.[6] For a polymer to be conducting, it should possess conjugated double bonds and the basic repeating units must be planar and should possess non-even number of electrons. When an electric field is applied, the π electrons move rapidly along the polymer backbone and making it conducting. Since the discovery of

intrinsically conducting polymers have explored their unusual opto-electronic properties for a wide range of applications because of its good processability, light weight, flexible, thermal stability, tunable conductivity and low production costs. Figure 1.2 represents the molecular structures of extensively studied conducting polymers such as polyacetylene (PA), poly (N-vinylcarbazole)(PVK), polyaniline (PANI), polythiophene (PT), poly(3,4-ethylenedioxythiophene) (PEDOT) and polypyrrole (PPy).

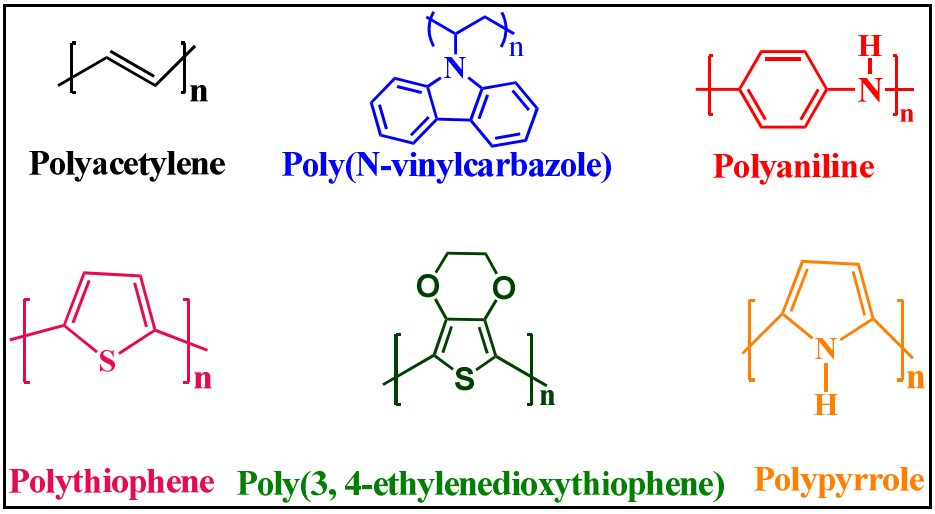

Figure 1.2. Molecular structures of extensively studied conducting polymers

1.3.1. Strategy for Preparation of Conducting Polymers

Conducting polymers are usually synthesized via oxidative coupling of monomers by chemical or electrochemical polymerization method. Chemical synthesis of PANI is carried out by the direct oxidation of aniline using an appropriate chemical oxidative radical initiator such as hydrogen peroxide, ammonium persulfate, in acidic medium.[7] Figure 1.3 represents the mechanism of formation of polyaniline during the oxidative radical polymerization of aniline. In the first step, aniline oxidized to form aniline radical cations and which is followed

by their combination of another aniline monomer to form a dimer. The subsequent propagation step is assumed to be similar to the electrophilic substitution process where the oxidized terminal amino group of oligomer (polymer) attacks para-position in monomer resulting to form PANI.

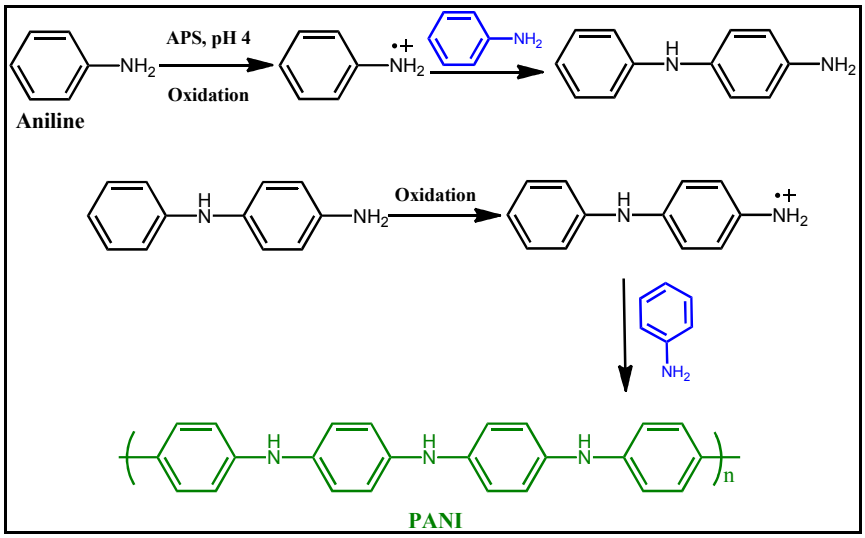

Figure 1.3. Chemical polymerization of PANI

In electrochemical synthesis of PANI, anodic oxidation of aniline is carried out using inert metallic electrode by two main modes: potentiostatic or galvanostatic. In general, electrochemical polymerization is employed using a three-electrode system (working, counter, and reference electrodes) in a solution comprising a monomer, an electrolyte, and appropriate additives. A number of crucial factors must be considered, including the electrolyte, deposition time/method (continuous versus pulsed) and applied potential. Each of these parameters has an effect on film morphology, conductivity, and mechanical properties, which directly impact the utility of the material for many applications. Figure 1.4 represents the mechanism of formation of PANI during the electrochemical polymerization of aniline. The cyclic voltammetry curve shows two

sets of distinct redox activity as indicated by the two pairs of anodic and cathodic current peaks. The first set of a redox couple which appears between 0 and 0.25 V is associated with the conversion of the fully reduced leucoemeraldine base to the partially oxidized emeraldine, and the second set of redox current peaks occurring between 0.6 and 0.8 V pertains to the conversion of emeraldine to the fully oxidized pernigraniline form.[8] As the reaction intermediates such as p-benzoquinone, p-aminophenol and some dimers during the polymerization are known to be trapped in the polymer the anodic hump at 0.5 V is generally attributed to redox reaction of p-benzoquinone.

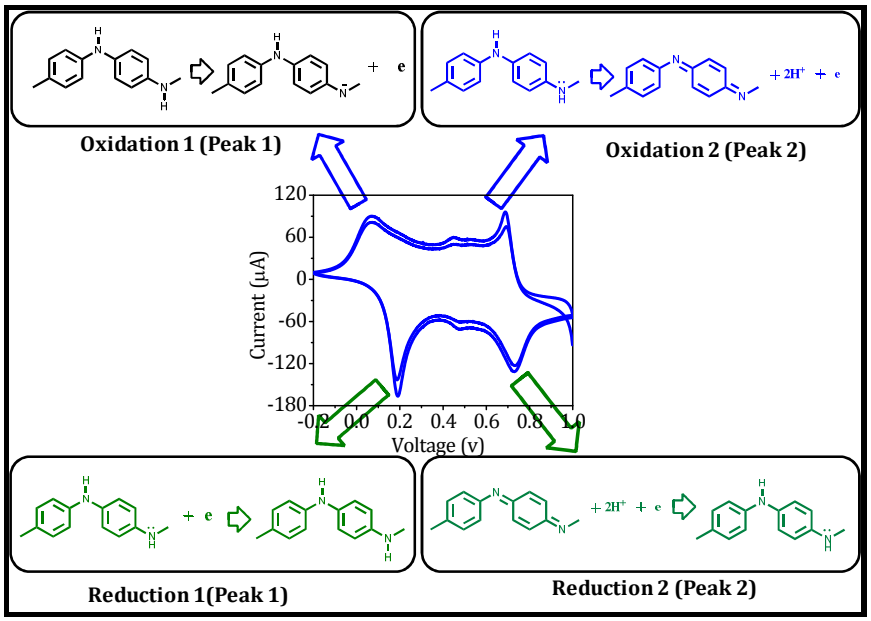

Figure 1.4. Electrochemical polymerization of PANI

1.3.2. Nanostructured Conducting Polymers

In the past two decades, tremendous efforts have been made towards the development of nanostructured conducting polymers since the realization of these materials can display a greater impact on the properties at the nanoscale.

Nanostructured conductive polymers with tunable size, shape, composition and spatial arrangement exhibit improved mechanical properties for strain accommodation, large surface areas, shortened pathways for charge/mass/ion transport and also new exciting features including flexibility, light weight and processability for the prepared nanostructures.[9-11] A wide variety of conductive polymer nanostructures have been developed and applied for a range of applications, such as energy conversion, storage, electronic devices, sensors, field-effect transistors, electrochromic display devices, supercapacitors, actuators and so forth. These novel materials are a fascinating playground for scientists and engineers to explore the effects of low dimensionality on a material's intriguing properties and their multifunctional applications.

Nanostructured conducting polymer can be synthesized by template based methods. The templates can be either hard template or soft template. The most commonly employed templates are anodic aluminium oxide, block co-polymers, porous silicate and mesoporous zeolites. The conventional hard template method is pioneered by Martin's group and has become a powerful tool for controllable synthesis of nanostructured conductive polymer.[12] Variety of nanostructured conducting polymer such as PANI, PPy, PHT and PEDOT have been chemically or electrochemically synthesized with tunable shape and size by conducting polymerization inside the pores of these templates. The main disadvantage of this method is removal of the template caused damage to the nanostructured conducting polymer during the post processing step. *Kim et al*. reported electrochemically generated dense array of vertically aligned PPy nanorods ($\sim 10^{11}/cm^2$) in a porous polystyrene-*b*-polymethyl methacrylate membrane

template (pore diameter of ~ 25 nm) as shown in Figure 1.5.[13] The height of the nanorods was controlled by the time used for the electro-polymerization under a constant voltage. It was also observed that, the self-supporting PPy nanorods were oriented normally to the substrate after removal of the template by washing with toluene. They exhibited a higher conductivity than a homogeneous PPy thin-film, as characterized by a technique of current-sensing atomic force microscopy. This study demonstrates a useful hard-template method to construct the ultrahigh density arrays of conducting polymer nanorods with good electric conductivity and current-voltage characteristics.

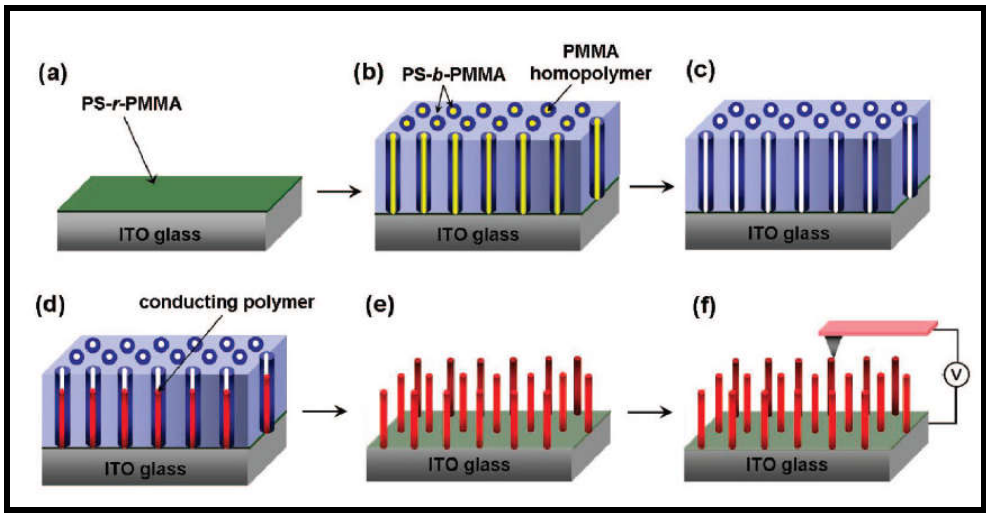

Figure 1.5. Schematic representation of the hard template approach for the synthesis of ultrahigh density arrays of PPy nanorods using nanoporous block copolymer membrane as hard template [Adapted from the reference 13]

Nanostructured conductive polymer can also be prepared using the soft template approach. The soft templates are usually made from mesophase structures such as surfactant micelles, liquid crystals, amphiphilic dopants and block copolymers etc.[14-17] The morphology of resulting products is controlled by the

nature and chain length of the surfactants as well as the concentrations of both monomers and surfactants. The dimension and shape of the formed nanostructured polymer can be controlled by tuning the size and shape of the micelle. Amphiphilic dopants such as dodecyl benzene sulphonic acid, camphor sulphonic acid form liquid crystalline phases which can act as dual role of dopant cum template. One advantage of this strategy is that dopant template will be a part of the nanostructured polymer and post processing step can be avoided.

The template-free method developed by Wan et al. is a simple self-assembly method without an external template.[18] The self-assembly method is induced by non-covalent forces between polymer chains, such as π-π stacking, dipole–dipole, hydrophobic, van der Waals forces, hydrogen bonding, electrostatic and ion–dipole interactions of the building blocks to spontaneously form anisotropic aggregates or oriented structures under suitable conditions.[19, 20]

1.4. Conduction Mechanism of Conducing Polymers

1.4.1. Doping

Conducting polymers are intrinsically conducting and the conductivity can be improved by the process of doping. The process of doping involves either removal of electrons or addition of electrons from the π -orbitals so as to produce charge carriers. Doping is achieved by the formation of charge carriers by electron donors such as sodium or potassium (n-doping, reduction) or by electron acceptors such as I_2, AsF_5, or $FeCl_3$ (p-doping, oxidation).[21] As a result of this process, the doped polymer backbone becomes negatively or positively charged with the dopant forming oppositely charged ions (Na^+, K^+, I_3^-, I_5^-, AsF_6, $FeCl_4^-$).[22] Application of an electric potential results in motion of counter ions in and out which enables to

switch the polymer between the doped conductive state and the undoped insulating state. The charge transport mechanism in the conducting polymers is mainly due to the formation of polarons and bipolarons in conducting molecules. This concept is also used for the explanation of the drastic colour changes produced during the doping process. The electronic energy diagrams and doping process in PPy is illustrated in Figure 1.6. Figure 1.6a represents the energy diagram of PPy in neutral form. Upon oxidation (removal of π- electrons from the valence band) of neutral PPy, there occurs the local relaxation of the benzoid structure toward a quinoid-like, which creates radical cations (polarons). Formation of polarons induces two new energy levels (Figure 1.6b) that are symmetrically positioned within the bandgap. Thus, two new electronic transitions at longer wavelengths emerge.

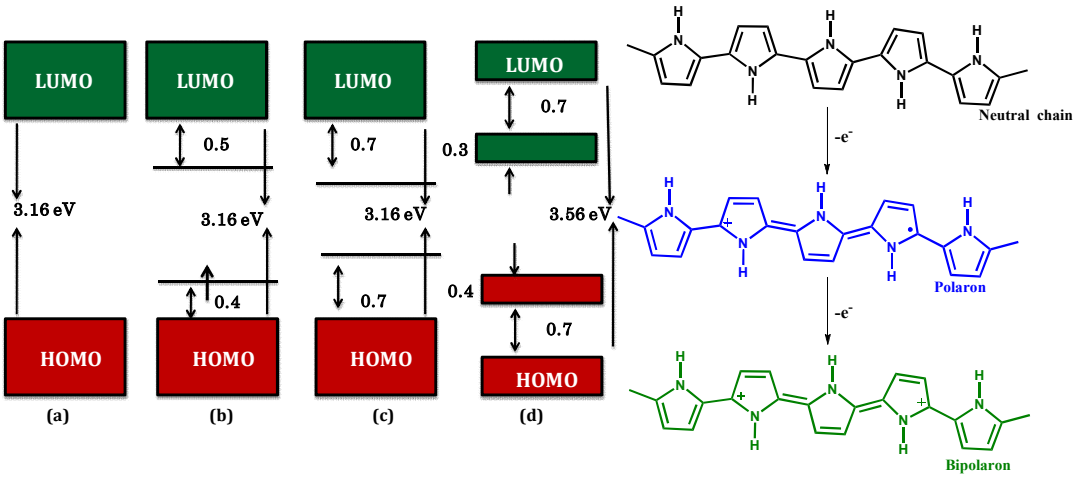

Figure 1.6. Electronic energy diagrams and structures for (a) neutral polypyrrole (b) polaron (c) bipolaron and (d) fully doped pyrrole [Adapted from the reference 23]

Further oxidation results in the formation of bipolarons which are the charge carriers of the coupled cations (dication). Since its having lower energy state empty, bipolarons are signified by the broad, low energy absorptions due to the transitions

from the top of the valence band (Figure 1.6c). As the polymer is oxidized further, the bipolaronic energy state overlaps and forms intermediate band structures which is given in Figure 1.6d. Doping level determines number of polaron and bipolarons, low doping levels gives rise to polarons, whereas higher doping levels produce bipolarons.[23]

1.4.2. Band Theory

According to molecular orbital theory, atomic orbital from one atom overlap with atomic orbital of another atom resulting in the formation of two molecular orbitals that are delocalized over both atoms. One of the molecular orbital is bonding (π) which has energy lower than both the combining atomic orbitals while the other is anti bonding (π*) with high energy. The band formed from the highest occupied molecular orbital (HOMO) will be completely filled and is called valence band (VB) while the band formed from the lowest unoccupied molecular orbital (LUMO) will be entirely empty and is called conduction band (CB). The forbidden energy gap value determines the electrical conductivity of the molecules. In case of insulators and semiconductors, this energy gap separating the two bands is high (>1.5 eV for semiconductor and >9 eV for insulator) whereas in the case of conductors, two bands overlap to facilitate maximum conduction.

Conductivity is attributed to the flow of mobile charge carriers. Since metal have a large number of mobile electrons they are good conductors and the conductivity is in the order 10^6 S/cm. The conductivity (σ) is directly proportional to the product of carrier mobility (μ), its charge (Q) and number of carrier or the concentration (n) as shown in equation (1.1),

$$\sigma = \mu . Q . n \qquad (1.1)$$

The electrical conductivity of organic material includes ionic conduction, hopping conduction, excitonic conduction, quantum mechanical conduction and tunneling between metallic domains. Figure 1.7 illustrates an overview of a broad conductivity range of insulators, semiconductors and metallic conductors.

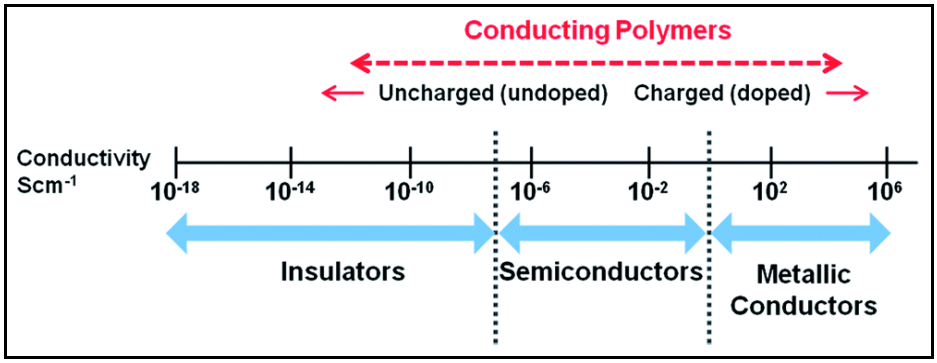

Figure 1.7. Conductivity chart of insulators, semiconductor and metallic conductors

1.5. Nanostructured Semiconducting Metal Oxides

Research and development on nanostructured semiconducting metal oxide has been growing largely around worldwide in the past few decades.[24,25] This is considered as a class of materials that can be distinguished on the basis of tailoring their properties from bulk to nano size. Nanostructures are defined as the materials with at least one dimension between 1 and 100 nm. The physical and chemical properties of a material can also be tuned significantly when the size of the particles is reduced to the nanometer scale because of quantum confinement effect.[26] Owing to the unique and beneficial properties of these nanomaterials exhibit excellent chemical, thermal stability, non-toxicity, low cost and they find applications in the area of energy saving and harvesting devices such as solar cells, transistors/FETs, light emitting devices and lithium ion batteries[27-30] and also as photocatalysts used for the degradation and adsorption of organic/inorganic pollutants present in

water.[31] Apart from these they have also tremendous applications in biological and medical sciences such as drug delivery, cancer treatments, fluorescent imaging, bio-labeling and bio tagging etc.[32-36]

Generally, in metal oxides, the S-shells of positive metallic ions are always fully filled by electrons and the d-shells are left with vacancy. This characteristic feature endows them with various unique properties, which involve electronic transitions, high dielectric constants, tunable band gaps, good electrical characteristics and so on. Therefore nanostructured metal oxides are considered to be one of the most fascinating functional materials. They can be prepared in a choice of morphologies such as nanoparticles, hexagonal discs, nanorods, nanowires, tapes, belts and flowers using various physical and chemical routes.[37-40]

1.5.1. Zinc oxide and Titanium dioxide

Among the various metal oxides, titania (TiO_2) and zinc oxide (ZnO) nanoparticles based n-type semiconductors have attracted significant attention over the last two decades due to their attractive opto-electrical properties, nontoxicity, long-term stability, catalytic property and low cost. They can be prepared using various methods such as sonochemical, hydrothermal, sol-gel reactions from their precursors. They have been extensively used in diverse applications such as solar cells, photocatalysts, sensors, photochromic devices, as white pigment in paints, as small additive in food and cosmetics, anti-inflammatory agents and also as a UV-absorbing material in sunscreen applications.

ZnO is transparent in its pure form with a band gap of 3.37eV, high ionization potential ~8eV, electron affinity ~4.7eV, electron effective mass 0.26, carrier mobility 130-200 $cm^2V^{-1}S^{-1}$, electron diffusion coefficient $1.7x10^{-4}$ and large

exciton binding energy ~60meV at room temperature.[41] This enables it exhibiting efficient near band edge excitonic emission. The large exciton binding energy leads to a close distance between the electron and hole pairs. As a result, even ZnO quantum dots are fluorescent. Depending on the crystallizing condition, ZnO has three crystal structures: wurtzite, zinc blende and rock salt as schematically shown in Figure 1.8.

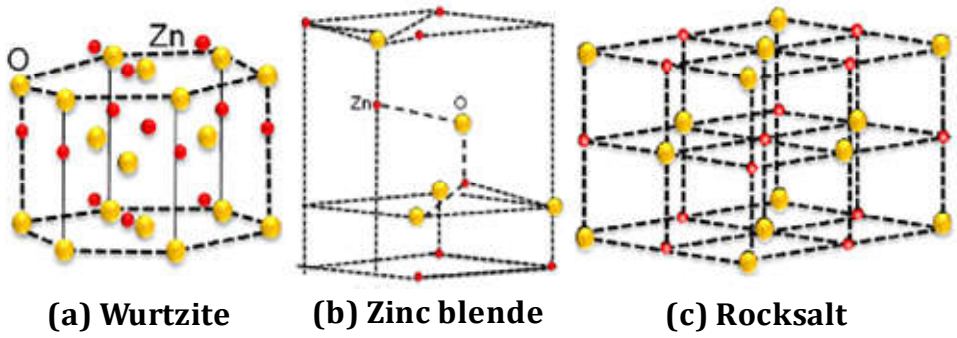

Figure 1.8. Crystal structures of zinc oxide **(a)** Wurtzite **(b)** Zinc blende and **(c)** Rocksalt.

The wurtzite structure is a thermodynamically stable crystal structure for ZnO under ambient conditions. If ZnO is grown on the surface of a cubic crystal, a zinc blende structure is expected; while the rock salt structure can be only achieved under high pressure (~10GPa).The ZnO wurtzite crystal structure has a hexagonal unit cell with lattice parameters equal to a= 0.324nm and c= 0.521nm. The ZnO structure consists of a number of zinc (Zn) and oxygen (O) surfaces stacked alternatively along the c-axis. Each Zn cation is surrounded by four O anions coordinated at the edges of a tetrahedron and the mechanical deformation of the tetrahedral structure leads to a polarization, i.e. the formation of electric dipole at the microscopic scale, which in turn results in the piezoelectric property of ZnO.

Titanium dioxide is a wide band gap semiconductor 3.22eV, electron effective mass 9, carrier mobility 0.1-4 $cm^2V^{-1}S^{-1}$ and electron diffusion coefficient $4.3x10^{-4}$ with similar physical properties as those of ZnO. Titania exhibited three different polymorphs i.e. anatase (tetragonal), rutile (tetragonal), brookite (orthorhombic) as shown in Figure 1.9.[42] Tetragonal structure of anatase and rutile are more ordered than the orthorhombic brookite structure. Rutile titania has a tetragonal crystal structure and contains six atoms per unit cell. Rutile is the most thermodynamically stable polymorph of titania at all temperatures, exhibiting the lower total free energy than metastable phases of anatase and brookite. Anatase titania has a crystalline structure that corresponds to the tetragonal system but the distortion of the TiO_6 octahedron is slightly larger for the anatase phase. The anatase structure is preferred over other polymorphs for solar cell applications because of its potentially higher conduction band edge energy and lower recombination rate of electron hole pairs.

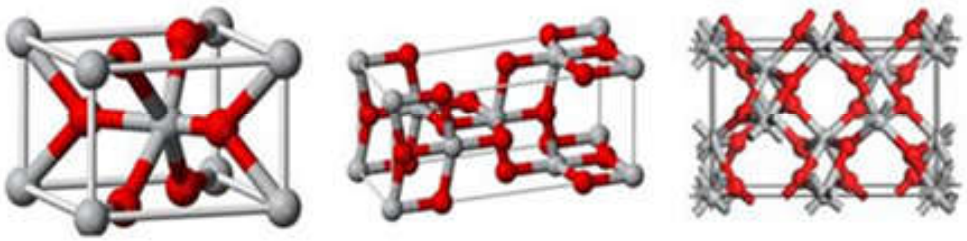

(a) Rutile **(b) Anatase** **(c) Brookite**

Figure 1.9. Crystal structures of titanium dioxide **(a)** Rutile **(b)** Anatase and **(c)** Brookite

1.5.2. Defects in Metal Oxide Nanoparticles

A defect is defined as an imperfection in the regular pattern of the atomic arrangement of a material due to the dislocation of an atom or more from their original positions. Such dislocation can be triggered by foreign atom (impurity) associated during the growth. This is referred to as an *extrinsic defect.* A defect might involve a host atom, in that case one speaks about an intrinsic defect.[43,44] Intrinsic defects can be classified into four categories depending on their geometrical structure:

- Zero dimensional (0D) defects or Point defects consist of an isolated atom in localized regions in the host crystal (e.g. vacancies).
- One dimensional (1D) defects or line defects consist of a row of atoms (e.g. a straight dislocation).
- Two dimensional (2D) defects or area defects consist of an area of atoms (e.g. twins).
- Three dimensional (3D) defects or volume defects consist of a volume of atoms (e.g. voids).

The 0D-defects (point defects) are the natural intrinsic defects created inside the metal oxides during the growth mechanism regardless the growth techniques. Such defects can be vacancies, interstitials, anti-sites and substitution defects. In the case of ZnO, the vacancy defects created when oxygen or zinc atoms are missing in one of the lattice site. Oxygen vacancy (V_o) acts as deep donor and located at ~2 eV below the conduction band while zinc vacancy (V_{Zn}) is a shallow acceptor located at ~0.31 eV above the valence band as shown in Figure 10. If the atom occupies a position where there is usually no atom, then it is called interstitial oxygen. The

interstitial defects can originate from oxygen (O_i) or zinc (Zn_i) atoms. The interstitial oxygen (O_i) atoms are deep acceptors while zinc interstitials (Zn_i) are shallow donors. Another type of the point defects is the anti-site defects where an oxygen atom occupies a position normally taken by a zinc atom in the zinc lattice (or vice versa). Both zinc anti-sites (Zn_O) and oxygen anti-sites (O_{Zn}) have high formation energies and are created under non equilibrium condition such as ion implantation. Oxygen anti-site defects are deep acceptors; however zinc anti-site defects are shallow donors. Finally, substitution defects can be created during ZnO growth process. In such case, an impurity atom has to replace an oxygen atom or a zinc atom in the ZnO lattice. The schematic diagram showing the illustration of formation of various defects and the value of energy levels are depicted in Figure 1.10.[45]

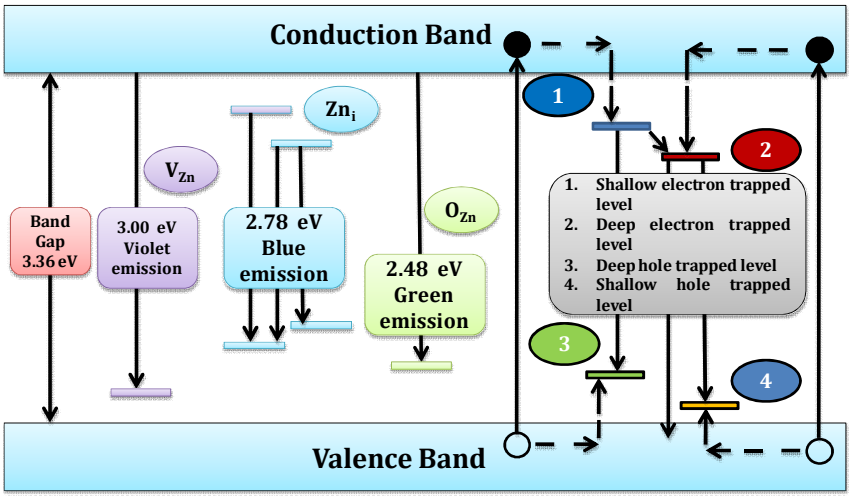

Figure 1.10. Schematic illustration of various defect energy level of ZnO

1.5.3. Hierarchical Structure

In general, nanostructures possess four different morphologies: zero-dimensional (0D), one-dimensional (1D), two-dimensional (2D) and three

dimensional (3D) nanostructures. Among them, 3D hierarchical structures (nanocrystalline aggregates) are an exciting new frontier for materials research. The advantages of hierarchical materials are good mesoporous and microporous structure that help to impart a high surface area and pore volume. It provides numerous reactive sites and a substantial interfacial area that can improve an enhanced surface-to-volume ratio and reduced transport lengths for both mass and charge transport.[46,47] Owing to their structure, hierarchical materials provide the substantial performance enhancement in numerous applications such as energy storage, energy conversion, catalysis and sensing.[48-51]

Hierarchical structure of ZnO and TiO_2 are widely used as active materials in DSSCs and photocatalytic application. In DSSCs the major restricting problem of improving the higher conversion efficiencies is a dynamic competition between the charge carrier generation and recombination of photoexcited carriers.[52,53] One dimensional nanostructures are able to provide a direct pathway for the rapid collection of photogenerated electrons and thus reduce the degree of charge recombination. However, such one dimensional nanostructures seem to have insufficient internal surface area which limits their energy conversion efficiency at a relatively low level for example 1.5% for ZnO nanowires and 4.7% for titania nanotubes.[54,55] Another way to increase the light harvesting capability of the photo electrode films is utilizing optical enhancement effects. This can be achieved by means of light scattering via introducing scattering particles into the photo electrode film.[56,57]

The following criteria's are essential for improving the power conversion efficiency of solar cell. It should allow the complete light absorption in the spectral

range of the dye, increase the light scattering of the absorbing layer for enhancing the time spent by light inside the sensitized film and improving light absorption, inhibition of back electron transfer between the conducting layer at the anode and the electrolyte.[58,59] Figures 1.11(a and b) shown the hierarchical structure of ZnO and the effect of light scattering and photon localization within a film consisting of submicrometer sized aggregates.

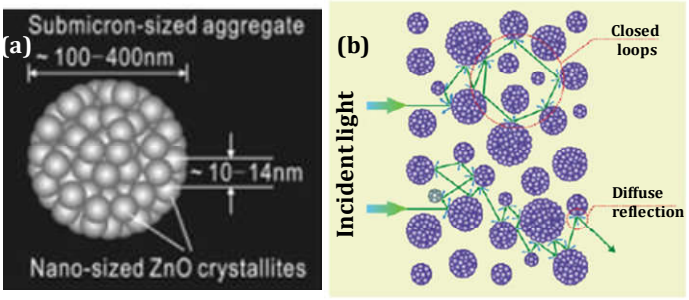

Figure 1.11. (a) Cartoon showing the hierarchical structure of ZnO and **(b)** effect of light scattering and photon localization within a film consisting of submicrometer sized aggregates [Adapted from the reference 58]

However, the major drawback is that the introduction of larger particles into nanocrystallline films will unavoidably lower the internal surface area of the photoanode film and therefore counteract the enhancement effect of light scattering on the optical absorption spectra. Also the incorporation of a layer of titania photonic crystal may lead to an undesirable increase in the electron diffusion length and consequently increase the recombination rate of photogenerated carriers.[60]

Cao et al. demonstrated the dye sensitized solar cell performance with polydisperse and monodisperse aggregates of zinc oxide hierarchical films.[61] Figure 1.12 displays the SEM images of the films consisting of polydisperse and monodisperse aggregates. Sample 1 is comprised of well-packed polydisperse ZnO

aggregates, sample 2 consists of monodisperse aggregates with slight distortion of the spherical shape, sample 3 includes monodisperse with average size of 250 nm and sample 4 is constructed with monodisperse aggregates with average size of 210 nm. It has been demonstrated that all these samples showed crystallite size of ~ 15 nm and specific surface area of ~80 m^2 g^{-1}. However, their photovoltaic behaviors exhibited significant difference in their short-circuit current density which resulted in the variation of overall power conversion efficiency. Typically, a maximum short-circuit current density of 19 mA cm^{-2} and conversion efficiency of 5.4% are observed for sample 1, while minimum values of 10 mA cm^{-2} and 2.4% respectively are observed for sample 4. Intermediate current densities and efficiencies are found for samples 2 and 3. In other words, the aggregation of ZnO nanocrystallites is favorable for achieving DSSC with high performance.

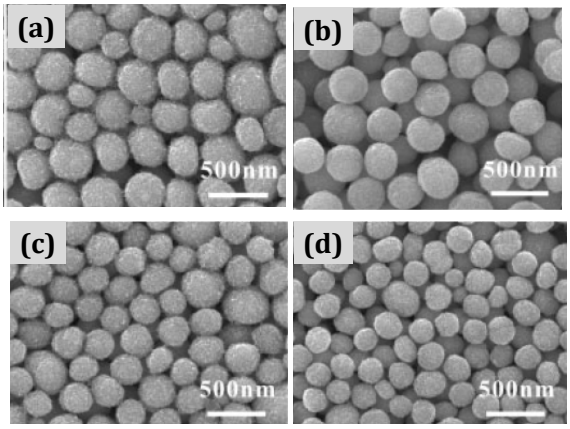

Figure 1.12. SEM images of the films consisting of polydisperse and monodisperse aggregates with average sizes of 350 nm (sample 1), 300 nm (sample 2), 250 nm (sample 3) and 210 nm (sample 4) [Adapted from the reference 61].

Hierarchical hollow sphere of TiO_2 was prepared by *Kuang et al*. through sonochemical method and utilized it as a photoanode in DSSC application.[62] Recently, Chen et al constructed three-dimensional hierarchical spheres by

spontaneous assembly of large ultrathin anatase titania nanosheets with nearly 100 % exposed (001) facets. In the solvothermal synthetic system, the presence of diethylenetriamine could effectively stabilize the high-energy (001) surfaces and induce the 2D lateral growth of such facets, and finally self assembled into diverse hierarchical architectures. Notably, the surface induction assembly strategy for 1D nanostructure greatly improves their electrochemical and photocatalytic performance. Even though 1D titania nanostructures can provide enhanced charge transfer facilitated by retarding the recombination of photogenerated electrons and holes, 3D hierarchical titania nanostructures comprised of 1D titania units such as nanorods/nanowires have been widely studied and showed enhanced photocatalytic performance.[63]

1.5.4. Strategies for the Preparation of Nanostructured Metal Oxides

In the past two decades, tremendous efforts have been made towards the development of synthetic strategies for the preparation of nanostructured materials with well controlled size, shape, and composition. In general bottom up and top down approach are used for the synthesis of metal oxide nanomaterials which are shown in Figure 1.13.

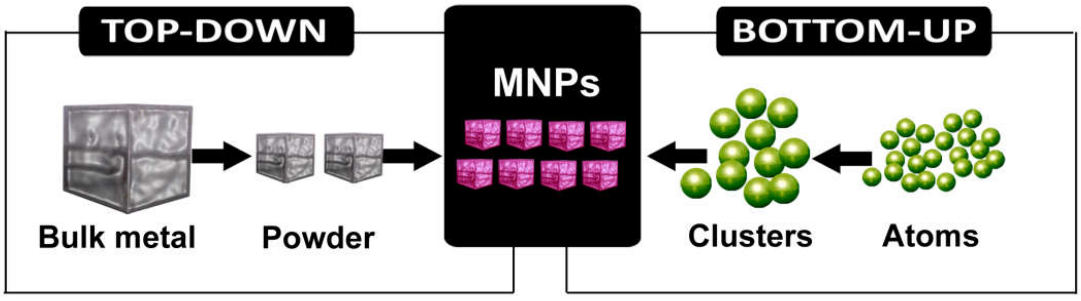

Figure 1.13. Schematic representation of Bottom–up and Top–down technique

1.5.5. Top-down approach

This approach begins with large (macroscopic) and complex structures of bulk materials is sliced or reduced to get the objects with nano-scale order. The top-down approach is essentially a miniaturization technique and leads to the bulk production of nanomaterials. This approach introduces internal stress and imperfections of surface structure and it will continue to play an important role in the synthesis of nanostructures. Lithography, attrition or milling, quenching, etching, and successive cutting are typical examples of top-down approach for the synthesis of metal oxide nanomaterials.[64]

1.5.6. Bottom-up Approach

In "bottom-up" processes, fundamental building blocks or primary units (atoms or molecules) self-associate, interact with each other in a coordinated way, and form ordered, complex and integrated 0-D, 1-D, 2-D and 3-D nanostructures with macroscopic nanoscale objects. During self-assembly or organization of basic units into ordered nanostructures, several non-covalent interactions such as hydrophobic, aromatic stacking, or electrostatic interactions, hydrogen bonds, and physical forces controlling at nanoscale are used to aggregate the building blocks into nanoscale stable structures. Fabrication of metal oxide nanostructures by this synthetic approach is much less expensive. Most of the existing strategies suffer from different drawbacks such as expensive and externally controlled equipments, prolonged reaction times, high temperatures, formation of undesirable by products, complex chemicals or complicated reaction conditions to produce metal oxides in the nanoregime. Therefore the bottom-up strategy, be able to create such nanoscale products in much cheaper than the top-down approach, is normally used for the

high yield production with size and shape controllable metal oxide nanostructures.[65]

A number of physical, chemical, hybrid and biological synthetic techniques have been adopted to control the shape, size, homogeneity, crystalline phases in these metal oxide nanostructures. Nanomaterials have been produced by physical processes such as spray pyrolysis, laser ablation, vapour depositions, arc-discharge, molecular beam epitaxy and sputtering. Several chemical methods including precipitation, hydrothermal, solvothermal, sol-gel, electrochemical and sonochemical methods are widely used for the preparation of metal oxide nanomaterials by bottom-up strategy.[66-68] To produce metal oxide nanomaterials in controlled size, large scale at economic cost, sol-gel approach is one of the most popular and well known methods. As the name suggests sol gel involves; the sol (or solution) is a colloidal suspension of solid particles or clusters in a liquid where bond formation between different molecules is induced, and the gel is a solid like state in which the colloids agglomerate to the extent to where percolation (connectivity) is accomplished. A gel consists of a three dimensional continuous network, which encloses a liquid phase. Synthesis via sol-gel process generally requires three steps: (i) hydrolysis of precursors and condensation followed by polycondensation (i.e., formation of sol), (ii) gelation (known as sol-gel transformation) and (iii) drying or calcination of various routes. For the preparation of metal oxide nanoparticles, precursors are to be chosen so that they have a tendency to form gels such as alkoxides and metal salts can be used. A series of processes involves under this technique such as gelling, drying, designing, and casting, which results with a variety of phase, structure and shape formations of

metal oxide nanostructures such as dense powders, porous structures, nanoparticles, fibers, wires, rods and thin-films especially the oxides of aluminium, copper, magnesium, titanium, and zinc. Figure 1.14 shows sol–gel process of preparation of zinc oxide thin film. [69]

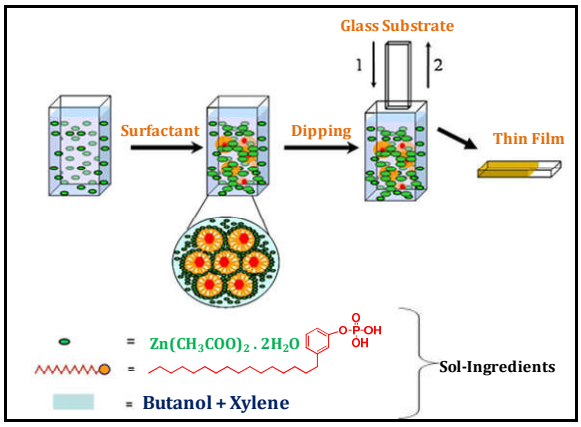

Figure 1.14. An illustration of the preparation of ZnO thin film by sol-gel process

1.6. Semiconducting Polymer-Inorganic Nanocomposites

Nanocomposites of conjugated polymers and inorganic nanoparticles (NPs) have emerged as an area of interest motivated by potential applications of these materials in electronics, optics, catalyst and biomedical area. Nanocomposites, in which materials are self assembled or organized in the nanoscale and it will help to tailor the optical as well as electronic behavior of both the NPs and conjugated materials. Additionally, these materials offer an effective route for the stabilization of inorganic nanoparticles and allow accessing of their fascinating physical and chemical properties in a simple and facile way. It has been observed that organic conducting polymers have been shown to be excellent hosts for trapping nanoparticles of metals and semiconductors because of their ability to act as stabilizers or surface capping agents.[70] The properties of nanocomposites strongly depend on the composition and nanoscale morphology, most importantly interfacial

area, contact between the components. To prepare the nanocomposites materials, several approaches have been employed such as physical mixing, sol-gel technique, in-situ chemical polymerization in aqueous solution in the presence of monomer and inorganic particles, emulsion technology, sonochemical process and ϒ-radiation technique. Based on the method of preparation nanocomposites can be classified into three main categories: (i) ex situ (sequestered) synthesis, (ii) in situ (sequential) synthesis; and (iii) one-pot synthesis.

1.6.1. Ex-situ Synthesis

In ex-situ polymerization method, conducting polymer and inorganic species are synthesized separately and then hybridization is achieved during a subsequent step by simple blending of two or more components in which interfacial interaction between the different components determines the major properties of the resulting nanocomposites. Figure 1.15 shows the preparation of hybrid nanocomposites by ex-situ polymerization method. These procedures are simple and highly suitable for solution based processing, which is a milestone for enabling mass production and processing via roll-to-roll printing. Another benefit of these methods is the well established synthetic procedures because each component is manufactured separately using a known process. As for the hybridization process, there are various valuable strategies available, ranging from very simple methods such as mechanical mixing of the two components, to more sophisticated methods such as ligand exchange or layer-by-layer fabrication procedures. Finally, physical infiltration of conducting polymers into inorganic nanostructures can also be achieved, resulting in highly ordered nanoarchitectures. However, these are not direct process because the polymeric guest materials may be prevented from

infiltrating the pores of the nanostructured host due to high interfacial tension as a result of physical limitations such as the hydrodynamic radius of the polymer, leading to incomplete pore filling.[71]

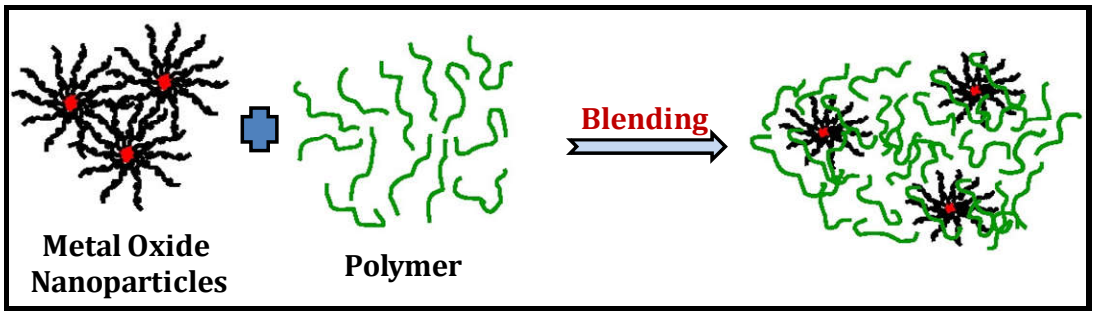

Figure 1.15. Ex-situ preparation of hybrid nanocomposites

1.6.2. In situ Synthesis

In this strategy the conducting polymer is synthesized by the in-situ polymerization of the monomer in the presence of the semiconductor nanostructures. However the opposite sequence is also possible, namely the semiconductor component is generated in situ inside the conducting polymer, either through chemical or electrochemical methods. It is apparent that nanohybrids obtained by in situ methods may have several advantages over their ex-situ prepared counterparts because the organic/inorganic interface can be better controlled at the molecular level. Under this method, two distinctly different strategies can be followed for the preparation of hybrid composites either chemical polymerization or electro-polymerization method. Specifically, in the case of the electrochemical in-situ route, heterogeneous components can be incorporated into conducting polymer that grown in the form of a film on the electrode surface. One benefit of such an approach is that the structure and properties of the hybridized material can be controlled by changing the critical variables including deposition time and current

density. Figure 1.16 shows the one step method of synthesize of MnO_2/PEDOT coaxial nanowires by coelectrodeposition in a porous alumina template.[72] For chemical in-situ synthesis the formation of the nanohybrid is rather straight forward because conducting polymer coexisting with nanoparticles and self assembled to form hybrid composites. In this method, conducting polymers are formed in the presence of the inorganic species; however, the opposite is also possible inorganic component which is synthesized in-situ within conducting polymer. The most important advantage of this method is very good control over the structure and morphology of the resultant composite material.

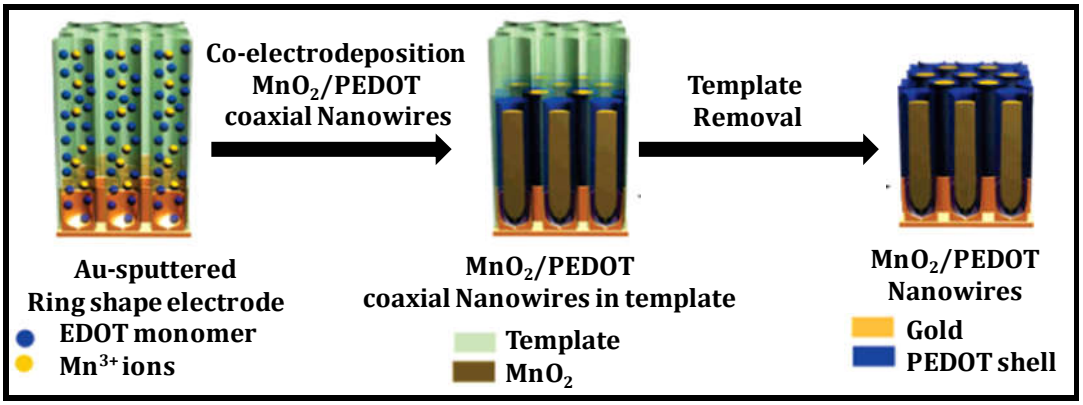

Figure 1.16. Schematic representation of electro-chemical polymerization route for the semiconducting polymer-inorganic nanocomposite [Adapted from the reference 72]

1.6.3. Synergistic Opto-Electronic Properties in Nanocomposites

Semiconducting polymer inorganic nanomaterial is expected to exhibit unassuming high performance arising from the synergistic effects of both nanoparticles and conducting polymer which can affect the optical, electrical and mechanical properties of the hybrid nanocomposites. The property of nanocomposites depends on the (i) percolation of nanoparticles on polymer matrix,

(ii) Interfacial interaction between nanoparticle and polymer (iii) effective charge-energy transfer between nanoparticles and conducting polymers.[73-75]

In the case of well dispersed nanoparticles which can provide better optical, electrical and mechanical properties than bulk nanoparticles because of intimate contact between the polymers and nanoparticles. In the second case, polymer-nanoparticle interactions can control the chain anchoring, carrier mobility, carrier concentration, morphology and interfacial area of conducing polymers and nanoparticle. Depending on the nature of interactions it may be (i) nanoparticles strongly coupled with conducting polymer (ii) nanoparticle adsorbed on the surface of polymer or vice versa, (iii) remain mobile at the interface. The strong interactions can lead to formation of a well defined network that can provide an enhancement of opto-electronic properties. The electrical properties of the material can be enhanced further by the formation of a percolating network structure that can provide a direct charge/electron transfer.[76]The electrical properties of these nanocomposites are strongly dependent on the film morphology, chemical and physical structure, which can be strongly modified via a variety of post treatments such as solvent and thermal treatment. In nanocomposites, large interface between the nanoparticles and conducing polymer facilitates charge and energy transfer between the two components which can occur through a number of potential routes depending upon the electronic energy levels of both the nanoparticle and semiconducting polymer. Figure 1.17 shows formation of conductive network in (a) insulative polymer-filler composites and (b) semiconducting polymer-inorganic composites.

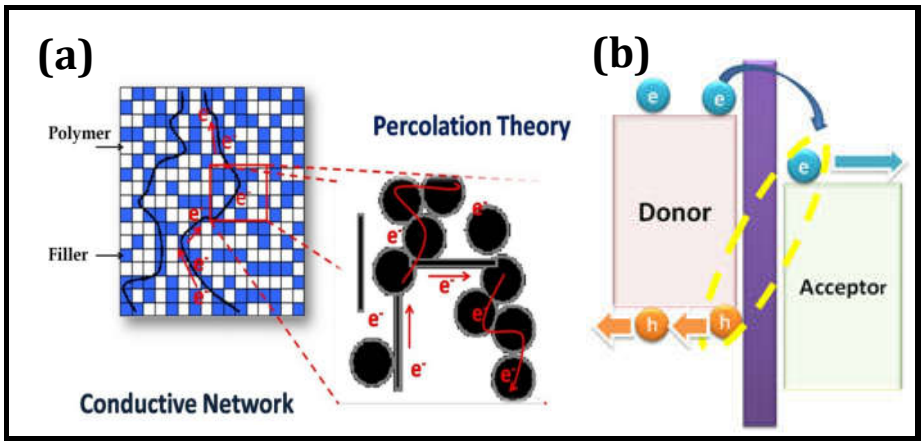

Figure 1.17. Formation of conductive network in **(a)** insulative polymer-filler composites and **(b)** semiconducting polymer-inorganic composites

1.7. Application of Semiconducting Polymer Inorganic Nanocomposites

1.7.1. Memory Devices

Memory devices are simple metal-insulator-metal structure with an active layer sandwiched between two electrodes and the resistance of the active layer is changed by applying a bias, constituting the set and reset states of the device as shown in Figure 1.18(a). Ideally, the device at the low conductivity state (OFF) is switched by a threshold voltage to a high conductivity state (ON) and the two states of bistable device differ in their conductivity by several orders in magnitude, retaining a remarkable stability. More importantly, the high and low conductivity states of the device can be precisely controlled by applying a positive voltage pulse to write or a negative voltage pulse to erase respectively.[77, 78] Based on the ability of retain information, the electrical switching characteristics of organic memory devices are categorized in two classes, volatile and non-volatile as shown in Figure 1.18(b). Volatile switching requires periodic refreshing of data as a result of the loss of stored information similar to Dynamic Random Access Memory (DRAM).

Conversely, electrically programmed organic memory devices with non-volatile switching characteristics can retain data for extended periods of time. This is similar to conventional flash memory. Non-volatile switching is often classified into three types based on current-voltage (*I-V*) curves: write once read many times (WORM), unipolar and bipolar switching memory (II, III, and IV in Figure 18b). WORM type memory devices show electrically irreversible switching characteristics and the original state is never recovered. These devices can be used as storage components for radio frequency identification tags. Both unipolar and bipolar memory systems exhibit electrically reversible switching. Unipolar memory devices use the same voltage polarity to write and erase, while bipolar memory devices require different voltage polarities.[79]

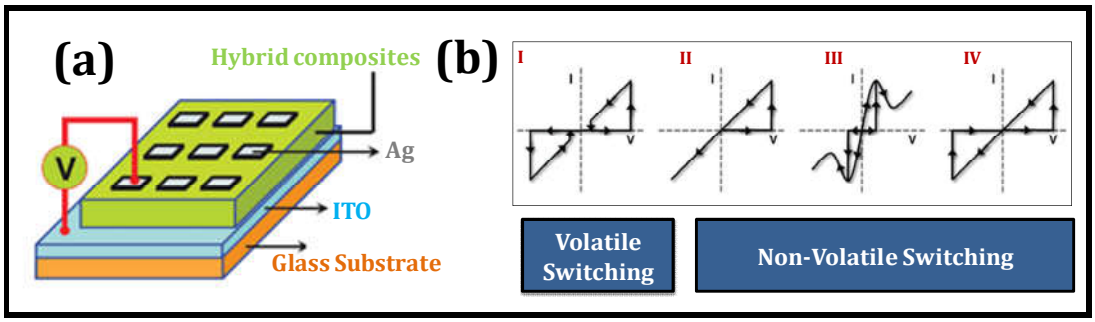

Figure 1.18. (a) Configuration of hybrid nanocomposite based memory device and **(b)** Typical I-V curve of resistive memory devices; (I) DRAM, (II) WORM, (III) unipolar and (IV) bipolar switching behaviour.

Teng et al. reported electrical bistability and negative differential resistance in diodes based on copper (I) sulphide- poly (N-vinylcarbazole) composites system. The current ratio between the high-conducting state and low-conducting state can reach more than 10^3 at room temperature. The electrical bistability of the device is attributed to the electric filed induced charge transfer between the silver

nanoparticles and the PVK.[80] The origin of this change in conductivity is still unambiguous. Each conductance state has been thoroughly described using the following well established conduction mechanisms: charge transfer, conformational change, space charge limit current and filament formation. The filament formation in conduction mechanism is due to anionic (oxygen vacancies) and cationic (electro metallization) migration of ions. *Pan et al*. reported hybrid nanocomposite of P3HT-PCBM enabling the realization of reproducible electrical switching which involves metallic filament formation in memory systems.[81] When a voltage bias is applied to the Cu electrode, mobile copper ions formed by electrochemical oxidation of the Cu top contact can migrate within the active polymer. Schematic of dynamic resistive switching processes of hybrid nanocomposites is shown in Figure 1.19.

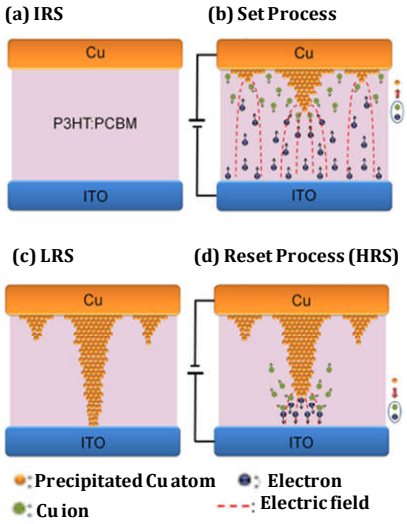

Figure 1.19. Schematics of dynamic resistive switching processes. **(a)** Virgin device structure with two clear interfaces. **(b)** Growing of Cu filament due to oxidation and reduction of Cu atoms under positive voltage. **(c)** Cu filament finally reaches BE, leading to the appearance of LRS. **(d)** The weakest part of Cu filament near organics/ITO interface ruptures under negative voltage, switching the device back to HRS. [Adapted from the reference 81]

1.7.2. Thermo Electric Devices

The direct conversion of electricity from heat source using thermoelectric (TE) materials is an emerging area of research and it offers a promising route towards the development of power generation and refrigeration without moving parts.[82,83] The energy conversion efficiency of this technology is simple, automatic and eco-friendly. TE devices is quantified by the dimensionless figure-of-merit (ZT) is shown in equation (1.2),

$$ZT = \alpha . \sigma . T / k \qquad (1.2)$$

where σ is the electrical conductivity, α is the Seebeck coefficient (also called the thermo power), k is the thermal conductivity and T is the absolute temperature. The power factor (PF) is calculated from the measured electrical conductivity and Seebeck coefficient, $PF = \alpha.\sigma^2$. Sketch of a thermoelectric module composed of p-type and n-type hybrid composites of carbon nanotubes are coated by PEDOT:PSS particles was shown in Figures 1.20(a and b).

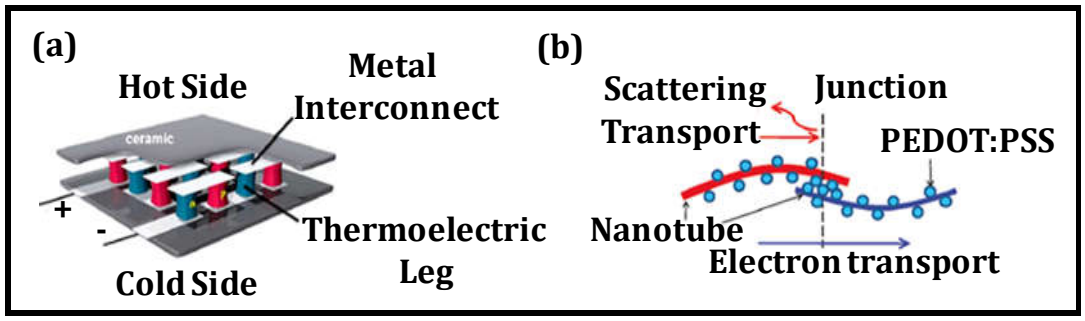

Figure 1.20. (a) Sketch of a thermoelectric module composed of p-n type legs and **(b)** hybrid nanocomposites of nanotubes are coated by PEDOT: PSS [Adapted from the reference 83]

A high-performance TE material requires a low thermal conductivity to prevent thermal shorting, a high electrical conductivity to reduce Joule heating and

a high Seebeck coefficient to promote the energy conversion of heat to electricity or electricity to cooling. Examples of polymers that have been researched for thermoelectric applications are polyacetylene, polypyrrole, polyaniline, polyethylenedioxythiophene, polythiophene, and poly(carbazole)s. It is found that the molecular weights of the polymers have a substantial effect on the electron mobility and consequently affect the electrical conductivity through electron hopping along the polymer backbone.[84] A high molecular weight polymer will promote the charge carriers to move longer distances before hopping to another chain, and can result in an increased charge carrier mobility. The electrical conductivity of device can be tuned by doping, however it's found that the higher doping causes decreasing in the Seebeck Coefficient. This is because as the Fermi energy is pushed inside the conduction band due to increase number of charge carriers and the number of electronic states above and below the Fermi energy becomes more equal. *Pipe et al.* studied the doping of conducting polymers and its effect on thermoelectric properties. They investigated the effect of treatment on PEDOT.PSS film with 5 vol% of ethylene glycol and 5 vol% dimethylsulphoxide.[85] The maximum power factor of 340 $\mu Wm^{-1}K^{-2}$ and 470 $\mu Wm^{-1}K^{-2}$ observed for EG and DMSO treated polymeric films respectively. PEDOT:PSS exhibited highest figure of merit of 0.42 observed for EG treated polymeric film. Similarly inorganic nanoparticles such as tellurium, bismuth telluride, lead telluride and $MoCl_5$ also utilized for thermo electric device applications. *Lin et al*. reported Bi_2Te_3 based alloy nanosheet (NS)/PEDOT-PSS composite films to be used for thermoelectric applications.[86] The drop cast composite film with 4.1 wt % BST nanoparticles which showed highest electrical conductivity (1295.21 S/cm) among all the composite

films with a power factor value as high as 32.26 μWm $^{1}K^{2}$. *Chen et al.* studied hybrid nanocomposites containing carbon nanotubes and ordered PANI. The ordered structures exhibited increase in the carrier mobility, electrical conductivity and Seebeck coefficient. The maximum power factor of the composites reached 2 $x10^{-5}$ Wm^{-1} K^{-1} with ZT value of 0.004 at room temperature.[87]

1.7.3. Photocatalysts

Photocatalysts are materials which utilize light energy and convert it to chemical energy through a series of electronic processes and surface reactions. Organic dyes are an important source of environmental contamination, as they are toxic and mostly non- biodegradable. The key to the success of photocatalyst is the development of high performance materials having well matched photo absorption with the solar spectrum, an efficient photoexcited charge separation to prevent electron–hole recombination and an adequate energy of charges that carry out the desired chemical reactions.[88] Semiconductor photo-catalysts such as TiO_2 and ZnO are the mostly studied photocatalysts because of their good stability, low cost, band gap and non-toxicity.[89] However, the applications of these metal oxides are limited because of weakly absorb visible light and can only collect UV light owing to a large band gap (3.20eV). Additionally, high recombination efficiency of the photogenerated electron–hole pairs also results in poor photocatalytic property. Therefore, many approaches have been developed to improve the photocatalytic performance of TiO_2 and ZnO under visible light, including non-metal doping, noble metal deposition, semiconductor coupling and conducting polymer sensitized nanoparticles.[90] Among them, conducting polymer sensitized metal nanoparticles are drawn great interest in recent years because of metal nanoparticles will

immobilize on a polymeric support. An ideal photocatalyst should have a narrow bandgap for absorbing solar light, a perfect conjugated structure for fast transfer of charge carriers, good adhesion with the photocatalyst, high adsorption capability toward the reaction species, high chemical inertness, good mechanical stability and a large specific surface area for adsorbing target pollutants. In the past decade, several kinds of conducting polymers, including PANI, P3HT, PPy, PEDOT and others have been used in the preparation of photo-catalysts based on polymer/semiconductor nanocrystal nanocomposites. Upon excitation with light conducting polymer catalyst absorbs light to induce $\pi \rightarrow \pi^*$ electron transition. The excited electrons in the π^*-orbital of CP (lowest unoccupied molecular orbitals, LUMO) activate the adsorbed oxygen molecules to superoxide radicals ($O_2^{\bullet}$) for oxidizing pollutants. The holes in the highest occupied molecular orbitals (HOMO) of CP can also directly oxidize the pollutants through the formation of hydroxyl radical by interacting water in the environment. Photocatalytic performance of hybrid material is arising from the effective solar sensitization and suppression of electron-hole recombination.[91,92]

Recently we reported photocatalytic properties of rutile titania nanocubes in the visible region which was prepared by a bio-capping strategy and demonstrated its applicability in photocatalytic degradation of dyes.[93] The excellent photocatalytic efficiency exhibited by titania is due to the synergistic effect of both photocatalytic and photosensitized oxidation mechanism which is attributed to the low band gap, higher surface area and small crystallite size. *Gan et al*. prepared hybrid composites of micro scale hierarchical three-dimensional flowerlike TiO_2/PANI composite by in-situ polymerization method and demonstrated its application as a photocatalyst

for the degradation dye molecules under both UV and UV-visible light as shown in Figures 1.21 (a and b).[94]

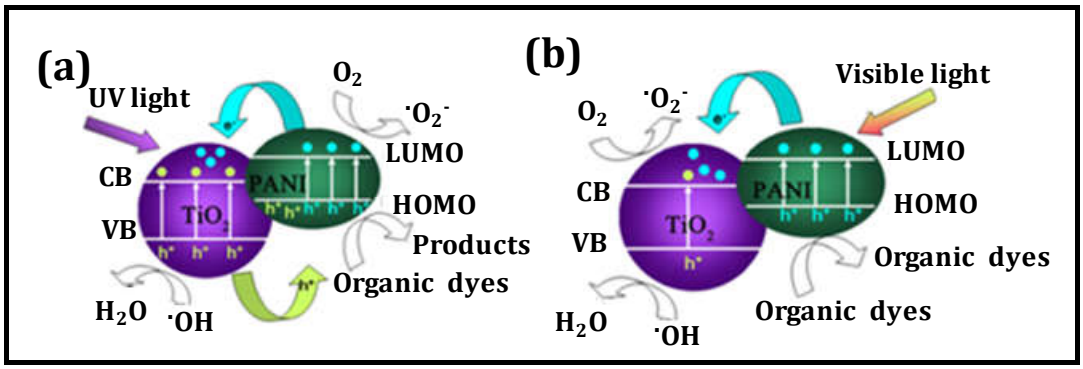

Figure 1.21. Mechanism of electron hole migration under **(a)** UV light and **(b)** sunlight (e , electron; h^+, hole) [Adapted from the reference 92]

1.7.4. Organic Field Effect Transistor (OFET)

Organic thin film transistors are the basic building blocks for flexible integrated circuits and displays. A schematic structure of OFET and representative gate/source current-voltage graph are shown in Figures 1.22(a and b). It find potential applications in organic integrated circuits such as radio frequency identification (RFID) tags, smart cards, and organic active matrix displays.[95] The field effect mobility of OFETs is now comparable to that of devices based on amorphous silicon. Recent attention has been devoted for improving device performance and stability to reduce the power consumption, flexible and lightweight devices for developing simple fabrication techniques compared to typical inorganic semiconducting materials.[96] During the operation of the transistor, a gate electrode is used to control the current flow between the drain and source electrodes. Typically, a higher applied gate voltage leads to the higher current flow between the drain and the source electrodes. The current flow between the drain

and the source electrode is low when no voltage is applied between the gate and the drain electrodes. This state at which the gate voltage is zero is called the "off' state of a transistor. When a voltage is applied to the gate, charges can be induced into the semiconducting layer at the interface between the semiconductor and dielectric layer. As a result, the drain-source current increases due to increased number of charge carriers, and this is called the "on" state of a transistor. Therefore to construct a FET, the materials ranging from insulating (dielectric material), semiconducting to conducting are required. From the point of a device, its performance is dominated by the properties of its components as well as the properties of the interfaces. In fact, it is well accepted that interface modification is an excellent way to achieve high performance OFETs, since it is an effective approach for improving mobility, device stability, reducing the operating voltage, etc.[97, 98]

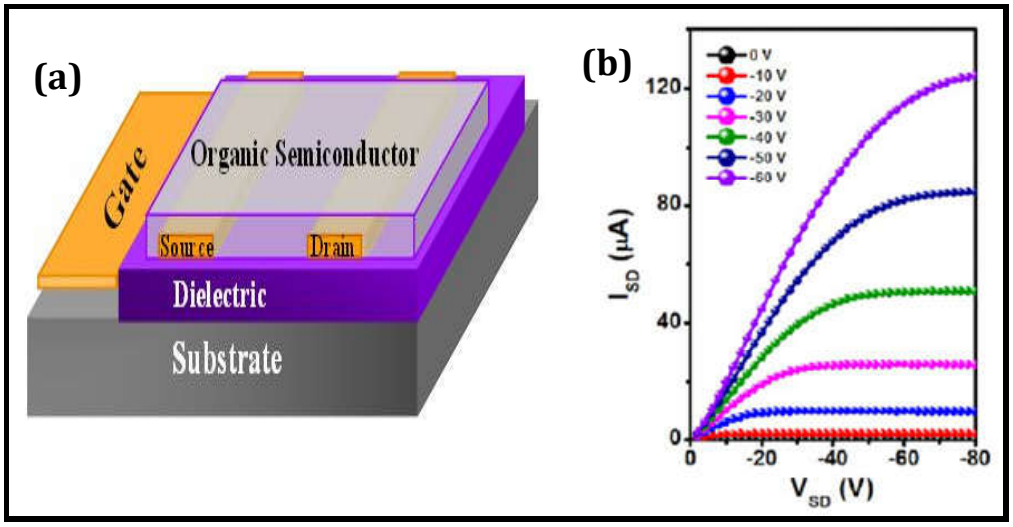

Figure 1.22. (a) Schematic displays of thin film field effect transistor and **(b)** representative gate/source current-voltage graph

Khondaker et al. fabricated OFETs by directly growing of P3HT crystalline nanowires on solution processed aligned array single walled carbon nanotubes.[99] The device exhibits high mobility and high current on-off ratio with a maximum of 0.13 cm^2/Vs and $3.1x10^5$ respectively. The reason for improvement of device performance can be attributed to improve the contact via π-π* interaction between SWNT with the crystalline P3HT nanowires. Thus, interface engineering has become a general way to fabricate OFETs with excellent device characteristics.

1.7.5. Solar cell

Solar cell is the device which converts the light into electricity. At present, the active materials used for the fabrication of solar cells are mainly inorganic materials, such as silicon, gallium-arsenide, cadmium-telluride, and cadmium-indium-selenide.[100] The large production costs for these inorganic materials based solar cells is one of the major obstacles. Polymer solar cells have attracted considerable attention in the past few years owing to their potential for providing environmentally safe flexible, light weight, inexpensive, efficient solar cells.[101-103]Especially bulk heterojunction solar cells consisting of a mixture of conjugated polymer with a methanofullerne acceptor are considered as a promising approach. In the last five years there has been an enormous increase in the understanding and performance of polymer-fullerene bulk heterojunction solar cells.[104] Comprehensive insights have been obtained in crucial material parameters in terms of morphology, energy levels, charge transport, and electrode materials. To date, the power conversion efficiencies close to 5% are routinely obtained and some laboratories have reported power conversion efficiencies of ~5–7 % and now aiming at the efficiency increased to 10%. By combining synthesis, processing,

materials science with device physics and fabrication we can improve the performance of the solar cell. In general, for a successful solar cell four important processes have to be optimized to obtain a high conversion efficiency of solar energy into electrical energy. Absorption of light, charge transfer, separation of the opposite charges, charge transport and charge collection.[105] Schematic diagram showing the bulk heterojunction solar cell and working principle are given in Figures 1.23(a and b) respectively.

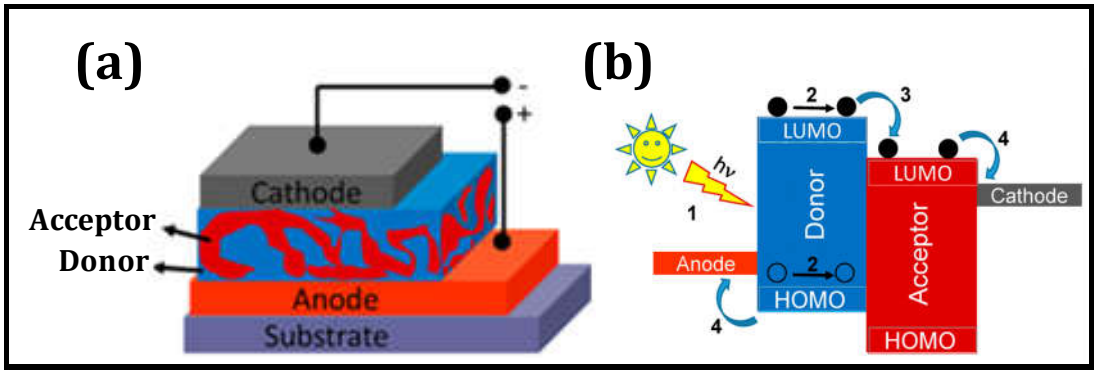

Figure 1.23. (a) Schematic diagram of bulk heterojunction solar cell and **(b)** working principle of solar cell

For an efficient collection of photons, the absorption spectrum of the photoactive organic layer should match the solar emission spectrum and the layer should be sufficiently thick to absorb all incidents light. New combinations of materials that are being developed in various laboratories focus on improving the three parameters which determine the energy conversion efficiency of a solar cell, i.e. the open-circuit voltage (V_{oc}), the short-circuit current (J_{sc}), and the fill factor that represents the curvature of the current density-voltage characteristic.[106] For ohmic contacts the open-circuit voltage of bulk-heterojunction polymer solar cells is governed by the energy levels of the HOMO and the LUMO of donor and acceptor,

respectively. Novel molecular chemistry and materials offer hope for revolutionary, rather than evolutionary, breakthroughs in future device efficiencies.

1.7.6. Organic Light Emitting Diodes (OLED)

OLED is a light-emitting diode in which the emissive electroluminescent layer is a film of organic compound which emits the light in response to an electric current.[107] This layer of organic semiconducor is sandwich between two electrodes. The first observation of electroluminescence in organic materials was reported in the early 1950s by André Bernanose at the Nancy Université, France in acridine orange. The first diode device was reported at Eastman Kodak by Ching W. Tang in 1987. This device used a novel two layer structure with separate hole transporting and electron transporting layers such that recombination and the light emission occurred in the middle of the organic layer. This resulted in a reduction in operating voltage and improvements in efficiency and led to the current era of OLED research and device production. Figures 1.24 (a and b) shown the schematic diagram of OLED and its working principle.

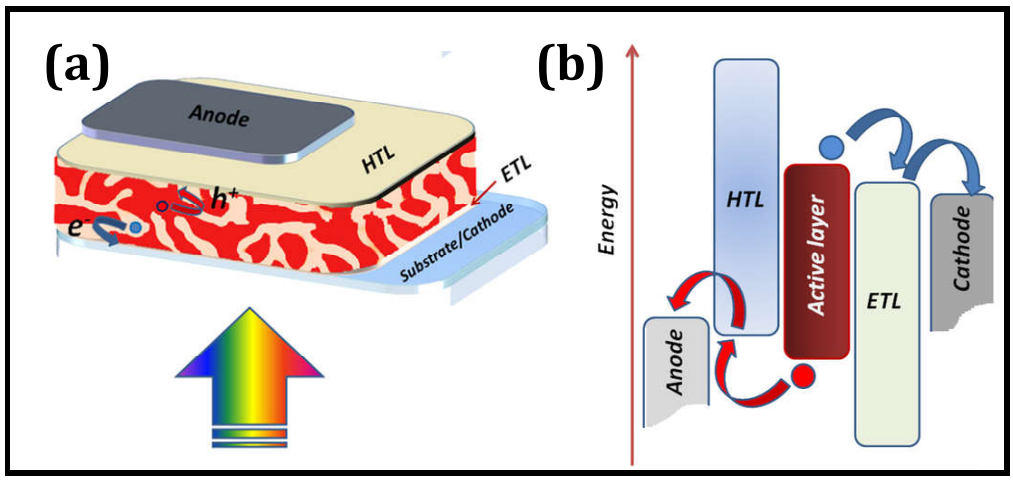

Figure 1.24. (a) Schematic diagram of OLED and **(b)** working principle of OLED

Research into polymer electroluminescence culminated in 1990 with J. H. Burroughes et al. at the Cavendish Laboratory in Cambridge reporting a high efficiency green light-emitting polymer based device using 100 nm thick films of poly(p-phenylenevinylene).[108] OLEDs are used to create digital displays in devices such as television screens, computer monitors, portable systems such as mobile phones, hand held games con-soles and PDAs.[109,110] Electroluminescent lighting is a form of screen printed lighting that has been used for many years in auto-motive dashboard and exit signs. The first LED TV was introduced in 2009 today over 40 percent of LCD TVs feature LED backlighting technology.

1.8. Scope and Objective

Semiconducting nanocomposites based opto-electronic devices are rapidly evolving field of research with vast number of applications having high potential for commercial success. Although a great progress has been made in opto-electronic devices such as photovoltaics, memory devices, thermoelectric devices, organic light-emitting diodes, field-effect transistors etc, it's still require further optimization for the active semiconducting material to fulfil the requirements for successful commercialization. Therefore, the key ingredient needed for enhancing the performance of opto-electronic devices is gaining in-depth knowledge in the physical, chemical, interfacial and morphological aspects of nanocomposites and its properties in the various parameters enhancing for device performance.

Nanostructured conducting polymers possess unique opto-electronic properties, high surface area, high charge carrier concentration, mechanical flexibility, light weight, solution processability and printability over a large area. Among the conducting polymers, PANI, PEDOT and PVK are receiving much

importance due to their low cost, environmental stability and unique doping mechanism. Conversely, semiconducting inorganic metal oxides such as zinc oxide and titania nanomaterials are endowed with low band gap, small crystalline size and unique opto-electronic properties. Under this background, research on design and development of semiconducting polymer-inorganic metal oxide nanocomposites are receiving interest since it is expected to exhibit synergistic properties arising from the molecular level mixing of conducting polymer and inorganic counter parts. Understanding in depth knowledge on the mechanism of the performance of the device and also studies on the correlation between the properties and device performance are critical for bringing fruitful revolution in affordable electronic industry. So the first objective of this program is the preparation of an overview of semiconducting polymers-inorganic nanocomposites after conducting an exhaustive literature survey on the design, development, various properties of semiconducting nanocomposites and its function on the various device performances.

Design and development of polyaniline-clay-titania nanocomposites are receiving importance since it is endowed with low band gap, effective interfacial area, high aspect ratio. So the second objective of this program is design and development of novel semiconducting polyaniline-clay-titania nanocomposites and evaluation of various properties and photocatalytic performance for the degradation of organic dyes.

Studies show that the use of hierarchical multiscale photoanodes with high porosity and surface area can enhance photoconversion efficiency of DSSCs by enhancement in the quantity of absorbed light, high dye loading and effective

electron-hole pair separation in dye sensitized solar cells. So the third objective of this program is preparation of hierarchical mesoscale porous ZnO using a biocapping methodology under controlled calcination temperature. Further study on the role of morphology and defect states of ZnO in the photoconversion efficiency of DSSC application.

Emerging applications of flexible electronic devices such as electronic paper, smart labels, and RFID tags require non-volatile memory devices capable of retaining information when power is turned off. Such memories are typically made from bistable materials exhibiting hysteresis in one of their properties. Among bistable materials, semiconducting polymer-inorganic metal oxide nanocomposites are receiving importance since they exhibit excellent processability, flexibility, printability, large scale production and can be switched by the application of an electric field. So the fourth objective of this research program is preparation of nanocomposites of poly(N-vinylcarbazole)-zinc oxide and demonstration and evaluation of its performance in non volatile memory device.

Thermoelectric materials (TE) are receiving a tremendous potential application in both power generation and solid-state cooling or heating. The conversion efficiency of a TE is the functions of the Seebeck coefficient, electrical conductivity, temperature and thermal conductivity. So the fifth objective of this program involves the preparation of hybrid nanocomposite based on PEDOT-ZnO/TiO_2 and demonstration of its performance as a thermoelectric material.

Finally, summarize the salient findings from this program.

1.9. References

1. C. A. Hewitt, A. B. Kaiser, S. Roth, M. Craps, R. Czerw and D. L. Carroll, *Nano Lett*, **2012**, *12*, 1307.

2. K.C. See, J. P. Feser, C. E. Chen, A. Majumdar, J. J. Urban and R. A. Segalman, *Nano Lett*, **2010**,*10*,4664.

3. N. E. Coates, S. K. Yee, B. McCulloch, K. C. See, A. Majumdar, R. A. Segalman and J. J. Urban, *Adv. Mater.* **2013**, *25*, 1629.

4. M. He, J. Ge, Z. Lin, X. Feng, X. Wang, H. Lu, Y. Yang and F. Qiu, *Energy Environ. Sci*. **2012**, *5*, 8351.

5. C. Janáky, N. R. D. Tacconi, W. Chanmanee and K. Rajeshwar, *J. Phys.Chem. C.* **2012**, *116*, 19145.

6. C. K. Chiang, C. R. Fincher, Y. W. Park, A. J. Heeger, H. Shirakawa, E. J. Louis, S. C. Gau and A. G. MacDiarmid, *Phys. Rev. Lett.* **1977**, *39*, 1098.

7. S. Virji, R. B. Kaner and B. H. Weiller, *J. Phys. Chem. B.* **2006**, *110*, 22266.

8. E. Song and J. W. Choi, *Nanomaterials,* **2013**, *3*, 498.

9. J. T. Hu, T. W. Odom, C. M. Lieber, *Acc. Chem. Res*. **1999**, *32*, 435.

10. S. Bhadraa, D. Khastgir, N. K. Singha and J. H. Lee, *Prog. Polym. Sci.* **2009**, *34*, 783.

11. S. Chen, Y. Lia and Y. Li, *Polym. Chem*. **2013**, *4*, 5162.

12. C. R. Martin, *Acc. Chem. Res.* **1995**, *28*, 61.

13. J. I. Lee, S. H. Cho, S. M. Park, J. K. Kim, J. K. Kim, J. W. Yu, Y. C. Kim and T. P. Russell, *Nano Lett.* **2008**, *8*, 2315.

14. C. J. Brinker, Y. Lu, A. Sellinger and H. Fan, *Adv. Mater.***1999**, *11*, 579.

15. M. Ramanathan, L. K. Shrestha, T. Mori, Q. Ji, J. P. Hill and K. Ariga, *Phys.Chem. Chem. Phys.* **2013**, *15, 10580*.

16. Y. Liao, X. G. Li and R. B. Kaner, *ACS Nano* **2010,** *4*, 5193.

17. S. J. Devaki, N. K. Sadanandhan, R. Sasi, H. J. P. Adler and A. Pich, *J. Mater. Chem. C*. **2014**, *2*, 6991.

18. M. Wan, *Adv. Mater.* **2008**, *20*, 2926.

19. F. S. Kim, G. Ren and S. A. Jenekhe, *Chem. Mater.* **2011**, *23*, 682.

20. J. Huang and R. B. Kaner, *J. Am. Chem. Soc*. **2004**, *126*, 851.

21. W. S. Huang, B. D. Humphery and A. G. MacDiarmid, *J. Chem. Soc. Faraday Trans*, **1986**, *82*, 2385.

22. H. Kaneko, T. Ishiguro, A. Takahashi and J. Tsukamoto, *Synth.Met*. **1993**, *57*, 4900.

23. P. Camurlu, *RSC Adv.* **2014**, *4*, 55832.

24. G. A. Ozin, A. C. Arsenault and L. Cademartiri, Nanochemistry: A Chemical Approach to Nanomaterials, RSC, Cambridge, **2008**.

25. C. Burda, X. B. Chen, R. Narayanan and M. A. E. Sayed, *Chem. Rev*. **2005**, *105*, 1025.

26. A. P. Alivisatos, *J. Phys. Chem*. **1996**, *100*, 13226.

27. S. Colodrero, A. Mihi, L. Haggman, M. Ocana, G. Boschloo, A. Hagfeldt and H. Miguez, *Adv. Mater.* **2009**, *21*, 766.

28. P. D. Ye, B. Yang, K. K. Ng, J. Bude, G. D. Wilk, S. Halder and J. C. M. Hwang, *Appl. Phys.Lett*. **2005**, *86*, 063501.

29. V. Wood, M. J. Panzer, J. E. Halpert, J. M. Caruge, M. G. Bawendi and V.Bulovic´, *Nano Lett*. **2009**, *3*, 3581.

30. P. Poizot, S. Laruelle, S. Grugeon, L. Dupont and J. M. Tarascon, *Nature* **2000**, *407*, 496.

31. N. K. Allam and C. A. Grimes, *J. Phys. Chem. C.* ***2007****, 111*, 13028.

32. H. Chen, R. C. McDonald, S. Li, N. L. Krett, S. T. Rosen and T. V. O'Halloran, *J. Am. Chem. Soc*. **2006**, *128*, 13348.

33. S. I. Stoeva, J. S. Lee, J. E. Smith and C. A. Mirkin, *J. Am. Chem. Soc.* **2006**,*128*, 8378.

34. S. Bae, S. W. Lee and Y. Takemura, *Appl. Phys. Lett*, **2006**, *89*, 252503.

35. M. T. F. Aernandez, A. Yakovlev, R. A. Sperling, C. Luccardini, S. Gaillard, A. S. Medel, J. M. Mallet, J. C. Brochon, A. Feltz, M. Oheim, and W. J. Parak, *Nano. Lett*. **2007**, *7*, 2613.

36. N. Suzuki, H. Tanaka and T. Kawai, *Adv. Mater.* **2008**, *20*, 909.

37. C. R. Patra and A. Gedanken, *New J. Chem*. **2004**, *28*, 1060.

38. J. Xia, H. Li, Z. Luo, H. Shi, K. Wang, H. Shu and Y. Yan, *J. Phys. Chem. Solids.* **2009**,*70*, 1461.

39. P. Yu, X. Zhang, Y. Chen, Y. Ma and Z. Qi, *Mater. Chem. Phys.* **2009**, *118*, 303.

40. X. L. Hu, Y. J. Zhu and S. W. Wang, *Mater. Chem. Phys*. **2004**, *88*, 421.

41. Z. R. R. Tian, J. A. Voigt, J. Liu, B. Mckenzie, M. J. Mcdermott, M. A. Rodriguez, H. Konishi and H. F. Xu, Nat. Mater. **2003**, *2*, 821.

42. T. Bak, M. K. Nowotny, L. R. Sheppard, and J. Nowotny, *J. Phys. Chem. C.* **2008**, *112,* 13248.

43. A. B. Djurisic and Y. H. Leung, *Small*, **2006**, *2*, 944.

44. X. Pan, M. Q. Yang, X. Fu, N. Zhang and Y. J. Xu, *Nanoscale*, **2013**, *5*, 3601.

45. A. Janotti and C. G. Van de Walle, *Rep. Prog. Phys*. **2009**, *72*, 126501.

46. X. Lai, J. E. Halpert and D. Wang, *Energy Environ. Sci*, **2012**, *5*, 5604.

47. N. D. Petkovich and A. Stein, *Chem. Soc. Rev.* **2013**, *42*, 3721.

48. Y. Huang, X. F. Duan, Q. Q. Wei and C. M. Lieber, *Science* **2001**, *291*, 630.

49. D. Wang, F. Qian, C. Yang, Z. H. Zhong and C. M. Lieber, *Nano Lett.* **2004**, *4*, 871.

50. Y. L. Hong, X. S. Chen, X. B. Jing, H. S. Fan, B. Guo, Z. W. Gu and X. D. Zhang, *Adv. Mater.* **2010**, *22*, 754.

51. L. Jing, W. Zhou, G. Tian and H. Fu, *Chem. Soc. Rev.* **2013**, *42*, 9509.

52. J. B. Baxter and E. S. Aydil, *Appl. Phys. Lett,* **2005**, *86*, 053114.

53. H. Wang, C. T. Yip, K. Y. Cheung, A. B. Djurisic, M. H. Xie, Y. H. Leung and W. K. Chan, *Appl. Phys. Lett*. **2006**, 89, 023508.

54. M. Law, L. E. Greene, J. C. Johnson, R. Saykally and P. D. Yang, *Nat. Mater*. **2005**, *4*, 455.

55. M. Paulose, K. Shankar, O. K. Varghese, G. K. Mor and C. A. Grimes, *J. Phys. D: Appl. Phys.* **2006**, *39*, 2498.

56. S. Nishimura, N. Abrams, B. A. Lewis, L. I. Halaoui, T. E. Mallouk, K. D. Benkstein, J. V. D. Lagemaat and A. J. Frank, *J. Am. Chem. Soc*. **2003**, *125*, 6306.

57. L. I. Halaoui, N. M. Abrams and T.E. Mallouk, *J. Phys. Chem. B.* **2005**, *109*, 6334.

58. Q. Zhang, C. S. Dandeneau, X. Zhou and G. Cao, *Adv. Mater*. **2009**, *21*, 4087.

59. T. P. Chou, Q. Zhang, G. E. Fryxell, and G. Cao, *Adv. Mater*. **2007**, *19*, 2588.

60. E. Guillen, E. Azaceta, A. V. Poot, J. Idígoras, J. Echeberría, J. A. Anta, and R. Tena-Zaera, *J. Phys. Chem. C.* **2013**, *117*, 13365.

61. Q. Zhang, T. P. Chou, B. Russo, S. A. Jenekhe, and G. Cao, *Adv. Funct. Mater*. **2008**, *18*, 1654.

62. C. X. He, B. X. Lei, Y. F. Wang, C. Y. Su, Y. P. Fang and D. B. Kuang, *Chem. Eur. J*. **2010**, *16*, 8757.

63. J. S. Chen, Y. L. Tan, C. M. Li, Y. L. Cheah, D. Luan, S. Madhavi, F. Y. C. Boey, L. A. Archer and X. W. Lou, *J. Am. Chem. Soc*, **2010**, *132*, 6124.

64. Z. L. Lu, E. Lindner and H. A. Mayer, *Chem. Rev.* **2002**, *102*,3543.

65. J. Yang, S. Mei and J. M. F. Ferreira, *J. Am. Ceram. Soc*. **2000**, *83*, 1361.

66. X. L. Li, Q. Peng, J. X. Yi, X. Wang and Y. D. Li, *Chem. Eur. J.* **2006**, *12*, 2383.

67. J. M. Wu, H. C. Shih and W. T. Wu, *Chem. Phys. Lett*. **2005**, *413*, 490.

68. V. Jokanovic, A. M. Spasic and D. Uskokovic, *J. Colloid. Interface Sci.* **2004**, *278*, 342.

69. J. Locklin, D. Patton, S. Deng, A. Baba, M. Millan and R. C. Advincula, *Chem. Mater.* **2004**, *16*, 5187.

70. V. Barlier, V. B. Legare, G. Boiteux., J. Davenas, A. Slazak, A. Rybak and J. Jung, *Synth. Metals.* **2009**, *159*, 508.

71. R. Liu and S. B. Lee, *J. Am. Chem. Soc*, **2008**, *130*, 2942.

72. Y. F. Zhou, M. Eck and M. Kruger, *Energy Environ. Sci.* **2010**, *3*, 1851.

73. Y. Shen, Y. Lin, M. Li, and C. W. Nan*, Adv. Mater.* **2007**, *19*, 1418.

74. G. Kaur, R. Adhikari, P. Cass, M. Bown and P. Gunatillake, *RSC Adv.* **2015**, *5*, 37553.

75. M. He, F. Qiu and Z. Lin, *J. Phys. Chem. Lett.* **2013**, *4*, 1788.

76. P. Reiss, E. Couderc, J. D. Girolamo and A. Pron, *Nanoscale*, **2011**, *3*, 446.

77. P. Heremans, G. H. Gelinck, R. Muller, K. J. Baeg, D. Y. Kim and Y. Y. Noh, *Chem. Mater*. **2011**, *23*, 341.

78. Q. Zhang, J. Pan, X. Yi, L. Li and S. Shang, *Org. Electron*. **2012**, *13*, 1289.

79. B. Cho, T. W. Kim, M. Choe, G. Wang, S. Song and T. Lee, *Org. Electron.* **2009**, *10*, 473.

80. A. Tang, F. Teng, L. Qian, Y. Hou, and Y. Wang, *Appl. Phys. Let.* **2009**, *95*,143115.

81. S. Gao, C. Song, C. Chen F. Zeng and F. Pan, *J. Phys. Chem C.* **2012**, *116*, 17955.

82. T. M. Tritt, H. Boettner and L. Chen, *MRS Bull*. **2008**, *33*, 366.

83. C. Yu, K. Choi, L. Yin and J. C. Grunlan, *ACS Nano,* **2011**, *5*, 7885.

84. R. J. Kline, M. D. McGehee, E. N. Kadnikova, J. Liu, and J. M. J. Frechet, *Adv. Mater*. **2003**, *15*, 1519.

85. G. H. Kim, L. Shao, K. Zhang, and K. P. Pipe, *Nat. Mater*. **2014**, *12*, 719.

86. Y. Du, K. F. Cai, S. Chen, P. Cizek, and T. Lin, *ACS Appl. Mater. Interfaces.* **2014**,*6*, 5735.

87. Q. Yao, L. Chen, W. Zhang, S. Liufu and X. Chen, *ACS Nano* **2010**, *4*, 2445.

88. N. Serpone, A. V. Emeline, *J. Phys. Chem. Lett.* **2012**, *3*, 673.

89. H. Zhang, G. R. Li, L. P. An, T. Y. Yan, X. P. Gao and H. Y. Zhu, *J. Phys. Chem. C.* **2007**, *111*, 6143.

90. S. Ghosh, N. A. Kouame, S. Remita, L. Ramos, F. Goubard, P. H. Aubert, A. Dazzi, A. D. Besseau and H. Remita, *Sci. Rep.* **2015**, *5*, 18002.

91. Q. Zhou and G. Shi, *J. Am. Chem. Soc.* **2016**, *138*, 2868.

92. Y. W. Su, W. H. Lin, Y. J. Hsu and K. H. Wei, S*mall* **2014**, *10*, 4427.

93. A. Aashish, R. Ramakrishnan, J. D. Sudha, M. Sankaran and G. K. Priya, *Mater. Chem. Phys.* **2015**, *157*, 31.

94. N. Guo, Y. Liang, S. Lan, L. Liu, J. Zhang, G. Ji and S. Gan, *J. Phys. Chem. C.* **2014**, *118*, 18343.

95. C. A. Di, Y. Liu, G. Yu, and D. Zhu, *Acc. Chem. Res*. **2009**, *42*, 1573.

96. N. Guo, Y. Liang, S. Lan, L. Liu, J. Zhang, G. Ji and S. Gan, *J. Phys. Chem. C.* **2014**, *118*, 18343.

97. H. Sirringhaus, *Adv. Mater.* **2014**, *26*, 1319.

98. B. Fu, J. Baltazar, Z. Hu, A. T. Chien, S. Kumar, C. L. Henderson, D. M. Collard and E. Reichmanis, *Chem. Mater*. **2012**, *24*, 4123.

99. B. K. Sarker, J. Liu, L. Zhai and S. I. Khondaker, *ACS Appl. Mater. Interfaces.* **2011**, *3*, 1180.

100. P. V. Kamat, K. Tvrdy, D. R. Baker, and J. G. Radich, *Chem. Rev.* **2010,** *110,* 6664.

101. M. Jørgensen, K. Norrman, S. A. Gevorgyan, T. Tromholt, B. Andreasen, and F. C. Krebs, *Adv. Mater*. **2012**, *24*, 580.

102. W. J. E. Beek, M. M. Wienk, and R. A. J. Janssen, *Adv. Funct. Mater*. **2006**, *16*, 1112.

103. T. W. Zeng, C. C. Ho, Y. C. Tu, G. Y. Tu, L. Y. Wang and W. F. Su, *Langmuir*, **2011**, *27*, 15255.

104. S. H. Chan, C. S. Lai, H. L. Chen, C. Ting and C. P. Chen, *Macromolecules*, **2011**, *44*, 8886.

105. J. L. Bredas, J. E. Norton, J. Cornil and V. Coropceanu, *Acc. Chem. Res.* **2009**, *42*, 1691.

106. W. Jaegermann, A. Klein and T. Mayer, *Adv. Mater*. **2009**, *21*, 4196.

107. P. K. H. Ho, J. S. Kim, J. H. Burroughes, H. Becker, S. F. Y. Li, T. M. Brown, F. Cacialli and R. H. Friend, *Nature* **2000**, *404*, 481.

108. R. H. Friend and J. H. Burroughes, *Faraday Discuss. Chem. Soc*. **1989**, *88*, 213.

109. L. Li, Z. Yu, C. Chang, W. Hu, X. Niu, Q. Chen and Q. Pei, *Phys. Chem. Chem. Phys*. **2012**, *14*, 14249.

110. Q. Zhang, J. Li, K. Shizu, S. Huang, S. Hirata, H. Miyazaki and C. Adachi, *J. Am. Chem. Soc*. **2012**, *134*, 14706.

Chapter 2

Nanostructured Polyaniline-Titanate-Clay Composite for Photocatalytic Application

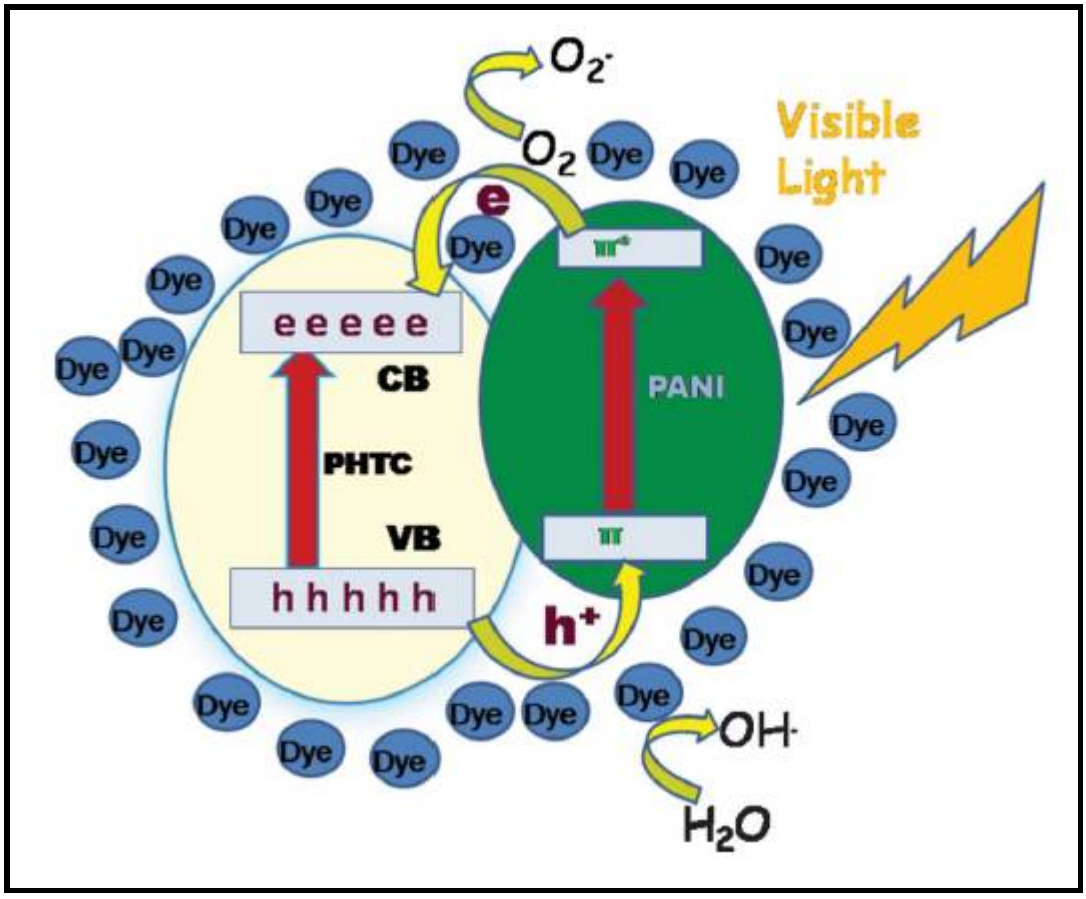

2.1. Abstract

Nanostructured polyaniline-titania-clay composite (PPTC) was prepared by the polymerization of anilinium hydrochloride in a dispersion of titania functionalized clay at room temperature. Modified clay- titania adsorbs anilinium ions by ion-dipole interactions and will act as a template. During polymerization, polyaniline forms linkages between these disorganized titania modified clay layers and may co-structure with the self-assembled polyaniline layers. Further rolled up to form three dimensionally ordered nanotubes by self-assembly process which was confirmed by morphological and structural analyses and XRD. The photocatalytic efficiency of PPTC was demonstrated by performing the photodegradation of methyl orange and methylene blue at room temperature under sunlight. Studies revealed that this novel PPTC nanocomposite can be utilised as a prospective candidate for the disposal of pollutants present in the environment.

2.2. Introduction

Designing nanocomposites by co-assembly of organic and inorganic precursors at the molecular level by controlling the interfaces, structure and morphology is a challenging task. Such hybrid materials are receiving attention because of its synergism between the components often gives rise to properties that are superior to those of the individual components. Harnessing the advantages of both the components requires fine tuning of the spatial assembly of individual domains and their interfaces. Nanocrystalline titanium dioxide has unique physico-chemical properties and can be used in advanced coatings, cosmetics, sensors, solar cells and photocatalyst applications.[1–8] Clays are layered materials having large surface area, high cation exchange capacity and can adsorb organic substances

either on their external surfaces or within their interlaminar spaces by interaction or substitution. Titania intercalated clays are receiving attention since they have a mesoporous structure, high adsorption ability, stable photocatalytic activity and large specific surface area.[9, 10] Recently, TiO_2 pillared clays have been studied for their photocatalytic activity in the degradation of some organic pollutants in water.[11] They can enhance the electron transfer between host and guest and can also impart high thermo-mechanical stability to the formed composites. Several methods have been developed to prepare TiO_2–clay composites. Which are usually prepared by the exchange of Ca^{2+}, Na^{+}, K^{+} present in the clay gallery by OH–Ti cation species.[12,13] *Zhao et al*. and *Xiang et al*. deposited nanocrystallites of anatase on the clay particles by sol–gel method.[14] *Tao Guo* et al. studied the photocatalytic properties of a polyaniline-intercalated layered protonic titanate nanocomposite.[15] *Yoda et al*. prepared TiO_2–MMT nanocomposites in supercritical CO_2.[15a] In general, titanate complexes are reported to be prepared by the hydrolysis of $TiCl_4$[16] or $TiOSO_4$.[17] Researchers have reported that such polytitanate cations exhibit well defined HOMO–LUMO gaps (semiconductor ‘‘band gaps’’).[18–20] *Einaga et al*. observed the existence of polytitanate cation species $[(TiO)_8(OH)_{12}]^{4+}$ in solutions prepared under certain conditions.[21]

The formation of semiconductor polytitanate by self-assembly offers distinct advantages such as low cost, uniformity and large surface area over other techniques. Ideally, photocatalysts should be able to harvest the visible source of sunlight. The most important challenge in the design of photocatalytic materials is to possess a band gap in the range of 1.8–3.1 eV. TiO_2 with a wide band gap of 3.2 eV can be activated only by UV light with wavelength 400 nm or shorter and is

considered as an n-type semiconductor. To induce visible light activity in TiO_2, the band gap must be shifted to lower values. Several attempts have been made to increase the photocatalytic efficiency of TiO_2 such as dye photosensitization, [22] ion doping [23] and preparing its precursors such as protonated polytitanate.[24] It has been shown that titanium dioxide on hybridising with a conducting polymer can increase the photocatalytic activity towards the decomposition of organic molecules when irradiated with visible light.[25]

Conjugated polymers with extended π-electron systems such as PANI, PT, PPy and their derivatives have shown great promise due to their high absorption coefficients in the visible part of the spectrum, high mobility of charge carriers, and good stability.[26] PANI is one of the most important conducting polymers because of its unique opto-electrical properties, ease of preparation, excellent environmental stability and tunable conductivity via special proton doping mechanism.[27,28] Therefore, conjugated polymers with wide band gap inorganic semiconductors are receiving attention for optical, electronic, photocatalytic and photoelectric conversion applications.[29–32] Conducting PANI behaves as a p-type semiconductor with a band gap absorption edge that can extend in the whole visible light, which also possess good environmental stability and has been used in a variety of applications. Thus p-n junctions can be realized by intercalating a p-type conducting polymer into the n-type polytitanate functionalised nanoclay layers. This will address the drawbacks of the latter, such as its poor response to visible light, high rate of electron-hole recombination, leaching and thermal decomposition. In addition to the photocatalytic properties, a successful candidate for a global scale catalyst material needs to be non-toxic, inexpensive, stable and widely available.

Thus, the preparation of a polyaniline-polytitanate-clay composite is receiving attention since it can exhibit unique properties arising from the synergetic effects of electrically conductive PANI, semiconducting and photocatalytic effect of polytitanate, absorbability and high aspect ratio of nanoclays.

Nanostructured photocatalytic polyaniline-polytitanate-clay composite was prepared by the polymerization of anilinium hydrochloride in presence of polytitanate functionalised clay using ammonium persulphate as radical initiator at room temperature. Here, the polytitanate functionalised nanoclay acts as a template and will control the molecular configuration of the PANI guest molecules within the confined environment. The resulting PPTC nanocomposites are hybridized at the molecular level and behave as a p-n heterojunction structure. They were characterized by SEM, HR-TEM, X-ray diffraction, Fourier transform infrared spectroscopy and UV-visible spectroscopy. The photocatalytic efficiency of these nanocomposites was investigated by performing the photo degradation studies of methyl orange (MO) and methylene blue (MB) at room temperature under natural light irradiation, and by performing UV-visible absorption studies.

2.3. Results and Discussion

2.3.1. Preparation of Nanocomposite

Nanocomposites were prepared by a three step process. Initially polytitanate (PHT) was prepared by hydrolysis of titanium tetrachloride using hydrochloric acid and polytitanate-intercalated clay (PHTC) was obtained by intercalation of polytitanate inside the clay layers by the cation exchange process as shown in Scheme 2.1. PHT is either intercalated inside the nanoclay layers or adsorbed on the outer surface of the exfoliated silicate layers and is stabilized by the hydrogen bond

and van der Waals force of interaction between the clay layers and PHT. PHTC was prepared with different mmol/meq of PHT/clay ratio. The maximum surface area was 230m^2/g obtained for (90 mmol/meq) polytitanate/clay ratio and the details are shown in Table 2.1. Particle size and zeta potential of the PHT and PHTC was measured using dynamic light scattering method and was found to be ~25 nm, ~40 nm, -41.3 mV and -49.7 mV, respectively.

Table 2.1. Surface area of PHTC with different molar ratio of PHT:clay

PHT-clay ratio (mmol/meq)	Surface area of PHTC (m^2/g)
10	**81**
50	**98**
70	**210**
90	**232**
110	**218**

Nanostructured PPTC was prepared by in-situ intercalative emulsion polymerization of anilinium hydrocholoride in aqueous dispersion of PHTC using ammonium persulphate (APS) as initiator at room temperature. During the addition of aniline hydrochloride, anilinium ions get adsorbed on the surface of PHTC and act as a template during the polymerization of aniline to form three dimensional network structures as observed during morphological analysis. The emeraldine green coloured nanocomposite was isolated by repeated centrifugation and washing with water and finally dried by freeze drying. Experiments were also performed with varying the composition of aniline hydrochloride content in the

nanocomposites under same condition and were designated as PPTC-2, PPTC-3 and PPTC-4.

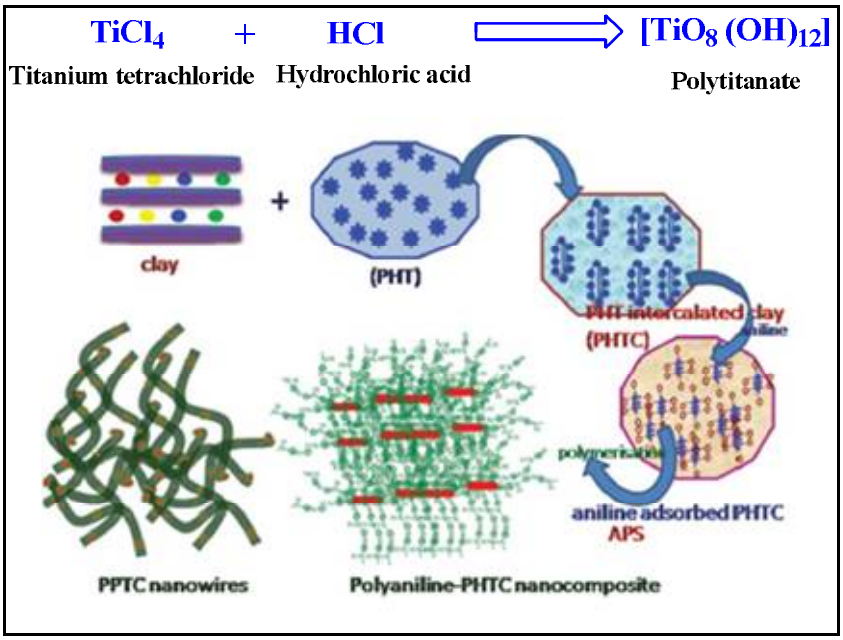

Scheme 2.1. Preparation of PPTC nanocomposites through self assembly.

2.3.2. Opto-Electronic Properties

Opto-electronic structures of PHT and PHTC were studied by diffused reflectance spectra (DRS). The DRS of PHT and PHTC are shown in Figure 2.1 (a–b).

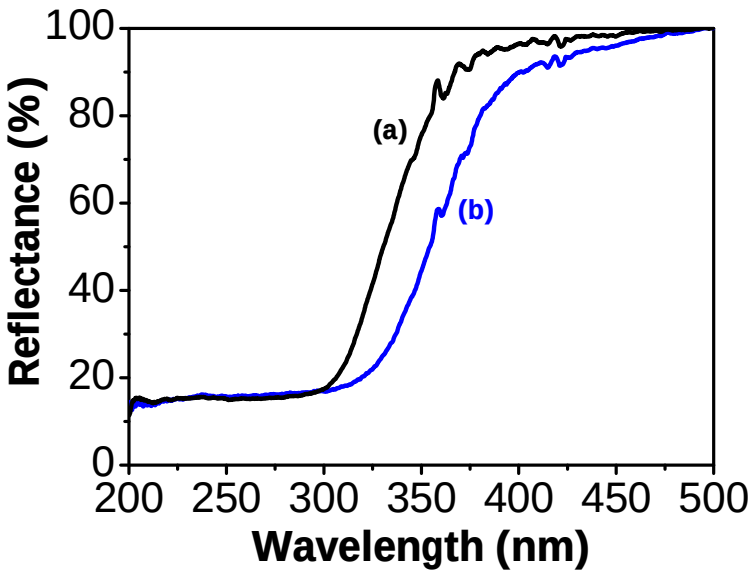

Figure 2.1. Diffused reflectance spectra of (a) PHT and (b) PHTC

DRS spectra of PHT and PHTC exhibited reflectance maxima at 382 nm and 402 nm. The band gap of the same was calculated using the following equation, Band gap = 1240/ reflectance wave length.

The band gap measured to be 3.24 eV and 3.08 eV for PHT and PHTC.

The protonated state and the interaction among different moieties in the nanocomposites were studied by UV-visible absorption spectroscopy using samples in aqueous dispersion. UV-visible spectra of PANI, PPTC-1, PPTC-2, PPTC-3 and PPTC-4 are shown in Figure 2.2(a to d), respectively. The UV-visible spectra of PANI exhibited three peaks at 340 nm, 430 nm and 750 nm characteristic of the π–π*, π-polaron and polaron-π* transitions respectively.[33,34] In all PPTCs, the first two bands (340 nm and 430 nm) merged to form a single broad band and appeared at 430, 436, 440, 448 nm, respectively. The red shift observed in PPTC compared to PANI is due to the interaction between titanate ions and PANI chains present in PPTC. In pure PANI, the strong interaction of chains caused π-conjugated defects and always leads to a ‘‘compact coil’’ conformation. The third peak in the nanocomposites is red shifted to 809 nm and 812 nm, respectively which is attributed to the presence of delocalized polarons arising from the confined environment of nanoclay layers.[35] Here, the nanoclay layers not only eliminate the interaction of different PANI chains, but also limit the contraction of the chains. Thus in PPTC, PANI is in a more expanded conformation[36] and thus there is strong interaction between PANI chains and PHT nanoparticles.[37] The PPTC nanocomposites can be activated by absorbing both the UV and visible light (λ = 200–900 nm). All these results suggest that this PPTC composite can be considered

as a promising candidate for the photoelectric conversion and photocatalytic applications.

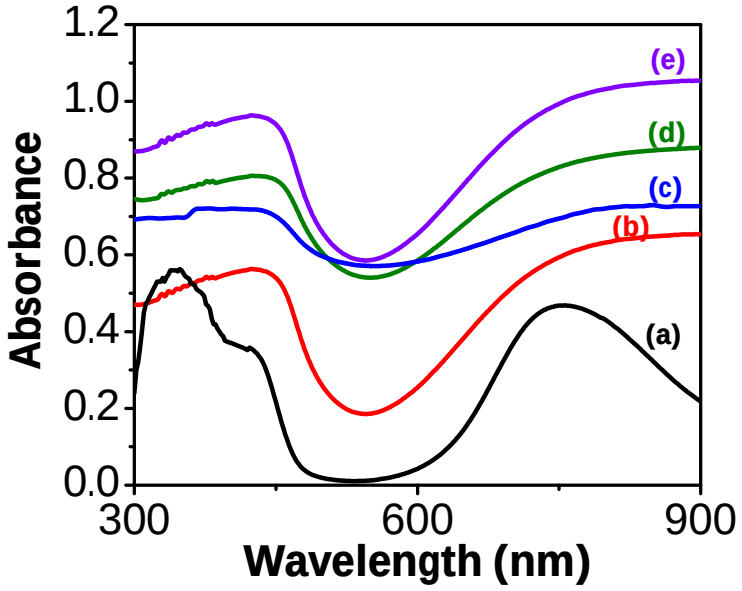

Figure 2.2. UV-visible spectra of (a) PANI (b) PPTC-1 (C) PPTC-2 (d) PPTC-3 and (e) PPTC-4

2.3.3. FT-IR Spectral Analysis

The chemical structure of these nanocomposites and the interaction among the moieties were manifested from the studies made by FT-IR spectroscopy. FT-IR spectra of PHT, PHTC, clay, PANI and PPTC-4 are shown in Figure 2.3(a to e) respectively. Generally, FT-IR spectra of PANI and PPTC exhibited bands at 1552 and 1479 cm^{-1} and were attributed due to the C=C stretching mode of the quinoid and benzenoid ring, respectively. The band at 1296 is attributed to the C–N stretching mode of the benzenoid ring. The bands at 1120 and 895 cm^{-1} were assigned to the in-plane and out-of-plane bending vibration and C–H stretching. The characteristic band of PANI at 1552 and 1237 cm^{-1} shifted to a higher wave number corresponding to the stretching mode of C=C and C–N in PPTC. The bands at 1479 and 1120 cm^{-1} shifted to a lower wave number, corresponding to the stretching

mode of C=C and C–H. These obvious changes in the wave number of PPTC, suggested that an interaction exists between PHT nanoparticles and PANI.[38] The titanium present in PHT can form a coordination bond with the nitrogen atoms present in PANI macromolecules and hence the shift in the characteristic values of PANI in PPTC.[39,40]

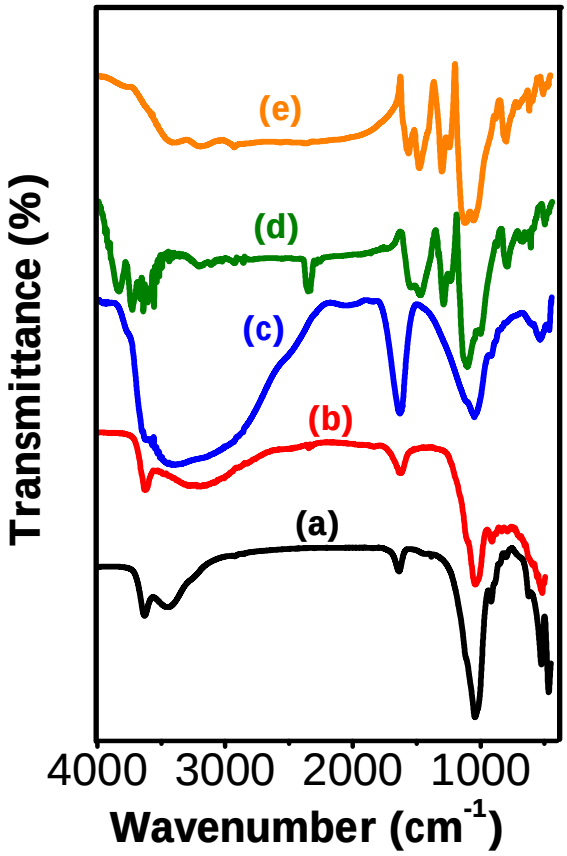

Figure 2.3. FT-IR spectra of (a) Clay (b) PHT (c) PHTC (d) PANI and (e) PPTC-4

The characteristic bands of clay were observed at 3630 cm^{-1} (stretching vibration of the OH group of Mg–Al–OH) and broad band at 3454 cm^{-1} (stretching vibration of the water and hydroxyl group). The amount of water absorbed in clays is related to the deformation of H–O–H group. The bands at 1046 and 792 cm^{-1} are attributed to Si–O vibration. The bands at 528 and 462 cm^{-1} correspond to the deformation vibration of Si–O–Al and Si–O–Si, respectively. The band at 906 cm^{-1} arises from the

stretching vibration of Al–OH. Compared with clay, PHTC showed a new band at 470 cm^{-1} which is due to the stretching vibration of Ti–O.[41]

2.3.4. X-ray Diffraction Analysis

X-Ray powder diffraction patterns of the PHT, clay, PHTC, PANI and PPTC are shown in Figure 2.4(a–e) respectively. Figure 2.4a shows XRD patterns of clay exhibited two distinct types of reflections, general and basal. The general reflections are called the hk bands, which are asymmetrical lines with characteristic ‘‘sawtooth’’ type reflections. Such reflections are caused by the structures of the smectite layers themselves and are independent of external condition. The basal reflections (hkl) on the other hand have symmetrical peaks, whose positions vary with the spacing between the layers. The diffractogram of clay showed reflection peaks at 2θ = 7.2 (d001), 19.8 (d003), 21.9 (d004), 28.6 (d006), 35.3 (d007), 54.2 (d31, d15, d24), and 61.8 ^{0}(d33, d06).[42] The basal reflection peak at 2θ = 7.2 with a d spacing of 12.1 Å corresponds to the (d001) basal spacing of the clay. The diffraction pattern of PHT exhibited peak at 2θ = 25.2 which confirms the (101) plane of the anatase phase of TiO_2. Figure 2.4b shows the diffractogram of PHT also exhibited additional reflections peak at 2θ = 37.4 (004), 47.7(200), 54.4 (105), 62.3 (204) and 67.6^0 (116) characteristics of the crystalline anatase structure of titanium dioxide (JCPD. no. 73–1764). The diffractogram of PHTC is shown in Figure 2.4c, which exhibited peaks at lower angle 2θ = 5.8 corresponding to the (d001) spacing at 21.3 Å. The increased gallery spacing in the c-axis direction of clay corresponds to the dimension of the confined PHT nanoparticles. It was also observed that the nature of the peaks corresponding to (d003) and (d006) spacing became sharp and only a small incremental shift happened to these peaks due to the high charge of the

ions present in these layers.[43,44] The diffraction pattern of PANI showed broad reflections at 2θ = 20.1 and 25.8^0 which are due to the periodicity parallel and perpendicular to the PANI chains as shown in Figure 2.4d .[45–47] The diffraction pattern of PPTC showed reflections peaks at 2θ = 19.0, 24.6, 34.5, 53.5, 61.6^0 suggesting the presence of distorted anatase phase in PPTC. Moreover, the presence of peak at 2θ = 19.0 and 24.5 suggested the presence of slightly distorted PANI chains. This is due to the increased interaction among the clay, PANI and PHT present in PPTC.[48, 49]

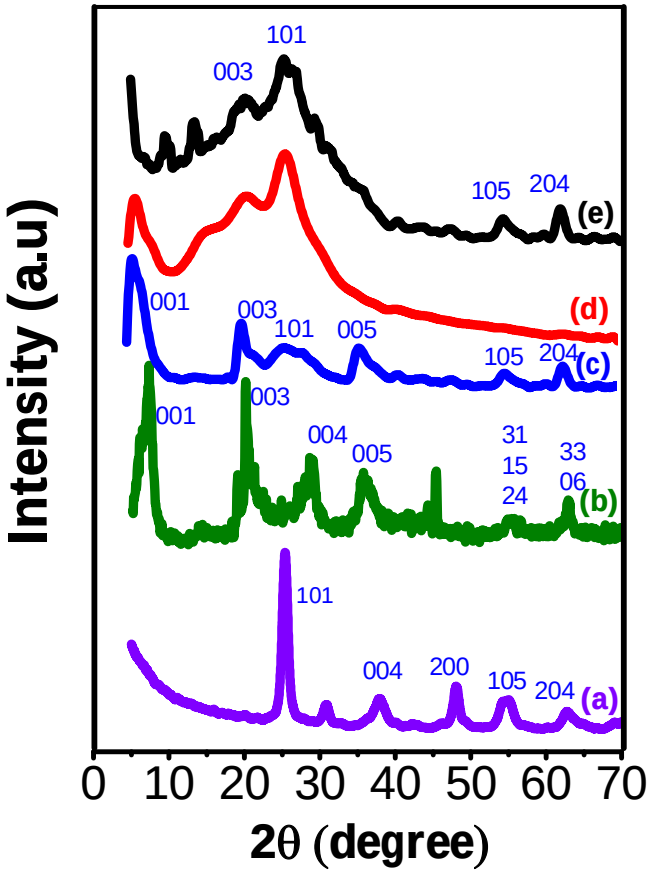

Figure 2.4. XRD pattern of (a) PHT (b) Clay (C) PHTC (d) PANI and (e) PPTC-4

2.3.5. Morphological Analysis

Morphological observations were made using SEM and TEM. SEM images of PHT, PHTC, PPTC-1and PPTC-4 are shown Figure 2. 5(a to d). SEM picture of PHT

shown in Figure 2.5a exhibited spherical particles and PHTC (Figure 2.5b) exhibited particles of PHT adsorbed on the surface of clay layers in an ordered fashion. SEM picture of PANI and PPTC-4 are shown in Figure 2.5c and 2.5d. PANI exhibited nanotubes like morphology and PPTC-4 shows PHTC embedded nanotubes of 50 nm diameter and several micrometer lengths. The dark portion indicates the presence of PHTC and the bright portion is due to PANI chains. The nanotubular structure is formed by the rolling of the self-assembled and co-structured PANI-PHTC. These are again engulfed by the self-assembled PANI layers.

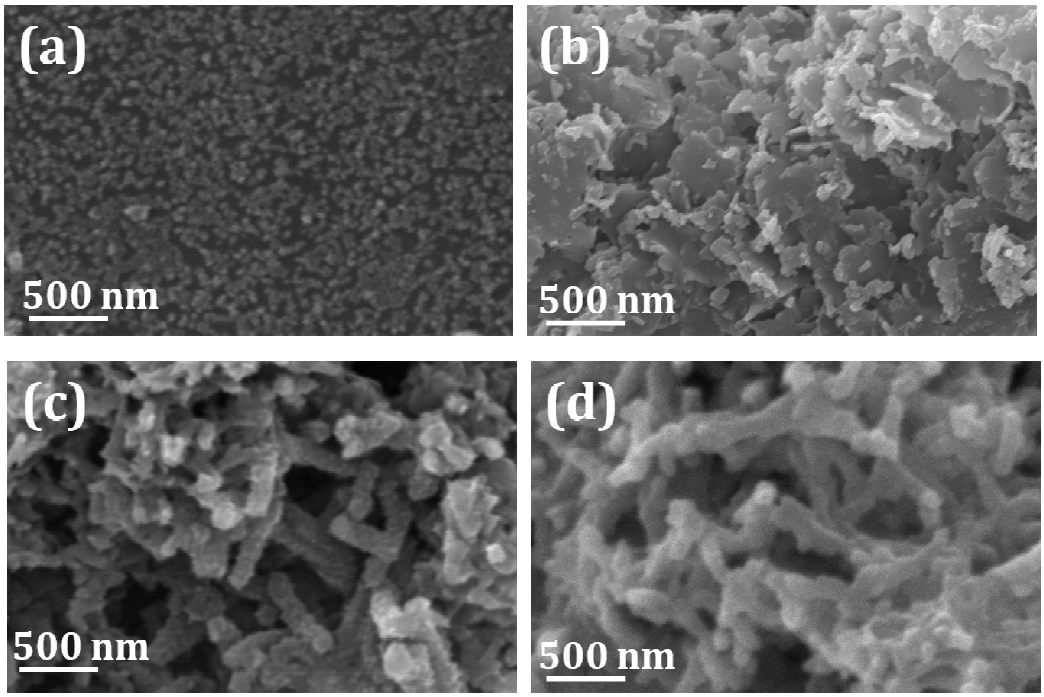

Figure 2.5. SEM images of (a) PHT (b) PHTC (C) PANI and (d) PPTC-4

HR-TEM analysis was carried out for better insight in the morphology of the prepared nanocomposites. TEM pictures of PHT, PHTC, PANI and PPTC-4 are shown in Figure 2. 6(a–d)respectively. Figure 2.6a shows the HR-TEM image of PHT exhibit spherical particle. PHTC revealed that the spherical PHT particles are confined inside the exfoliated clay layers. The TEM image of PANI exhibited as nanorods,

which also matches the observation made during SEM analysis. PPTC-4 exhibited a nanotubular structure with dark and bright areas. The dark portion indicates the presence of PHTC particles the bright portion is from the PANI layers. This contrast in the image is due to the difference in the intensity of the radiation when it is passing through the inorganic and organic moieties. The diameter of the nanotubes in PPTC-4 is observed to be 40 and 50 nm, respectively. Further composition of PHT and PPTC is confirmed by analyzing HR-TEM energy dispersive X ray spectra (EDS) and is shown in Figure 2. 6e. The exhibited peaks correspond to Ti, Si, Al, C and N which confirmed the presence of all these elements in the PPTC nanocomposite.

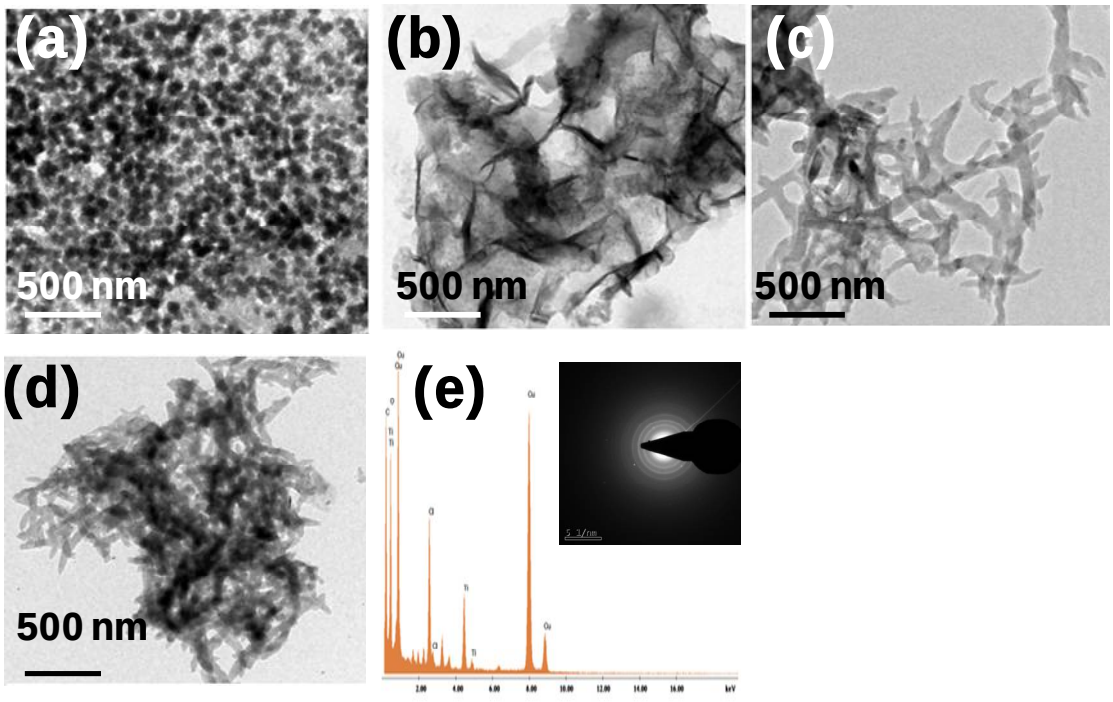

Figure 2.6. HR-TEM image of (a) PHT (b) PHTC (C) PANI (d) PPTC-4 and (e) EDS spectra of PPTC-4 (inset SAED image of PPTC-4)

2.3.6. Electrical Conductivity

The room temperature electrical conductivity of PPTC was measured using a four-probe conductivity meter. Details of the electrical conductivity measurements

of PHT, PHTC, PANI, PPTC-1, PPTC-2, PPTC-3 and PPTC-4 containing different percentage of PHTC/PANI is shown in Table 2.2. PHT exhibited electrical conductivity of 1.8 x 10^{-4} S/ cm and PHTC was measured to be (3.3x10^{-5} S/cm). The decreased conductivity may be due to the presence of insulative clay layers present in PHTC. PANI showed conductivity of 3x10^{-3} S/cm. PPTC showed increase in conductivity in the range of 1.26x10^{-3} S/cm to 6.2x10^{-2}S/cm with increasing PANI content in the system. Enhanced conductivity in PPTC with the increased amount of PANI might be due to the formation of a more efficient network for charge transport in the PPTC nanocomposites.[50, 51]

2.3.7. Photocatalytic Activities

Photocatalytic activity of PHT, PANI, PHTC and PPTCs were studied by photocatalytic decolorization of methyl orange and methylene blue. Photocatalytic decolorization efficiency of the catalyst was monitored by performing UV-visible spectral studies at different intervals of time. The absorption spectra of PHT, PANI, PHTC and PPTC-4 in presence of methyl orange (MO) are given in Figure 2.7a–d, respectively. In generally, all the samples exhibited two bands at 270 nm and 464 nm. The initial band at 270 nm corresponds to the aromatic ring and the peaks at 464 nm related to the azo group present in the MO. It has been observed that band at 270 nm in PHT and PHTC remains intact. However, in the presence of PANI, the band at 270 nm is distorted, and it is absent in the presence of PPTC-4. Furthermore, the band observed at 464 nm in MO showed a red shift to 497 nm in (PHT), 469 nm in (PHTC), 508 nm in (PANI) and 510 nm in (PPTC-4). The high extent of red shift observed in PPTCs compared with other samples is due to greater interaction of the azo group with the electrons present in PPTCs. The photographs

showing the decrease in colour intensity with time is shown in Figure 2.7(a-d) (inset snap shot). The photocatalytic degradation efficiency was observed in the order PHT (64.5%), PANI (67.6%), PHTC (80.4%) and PPTC-4 (99.6%).

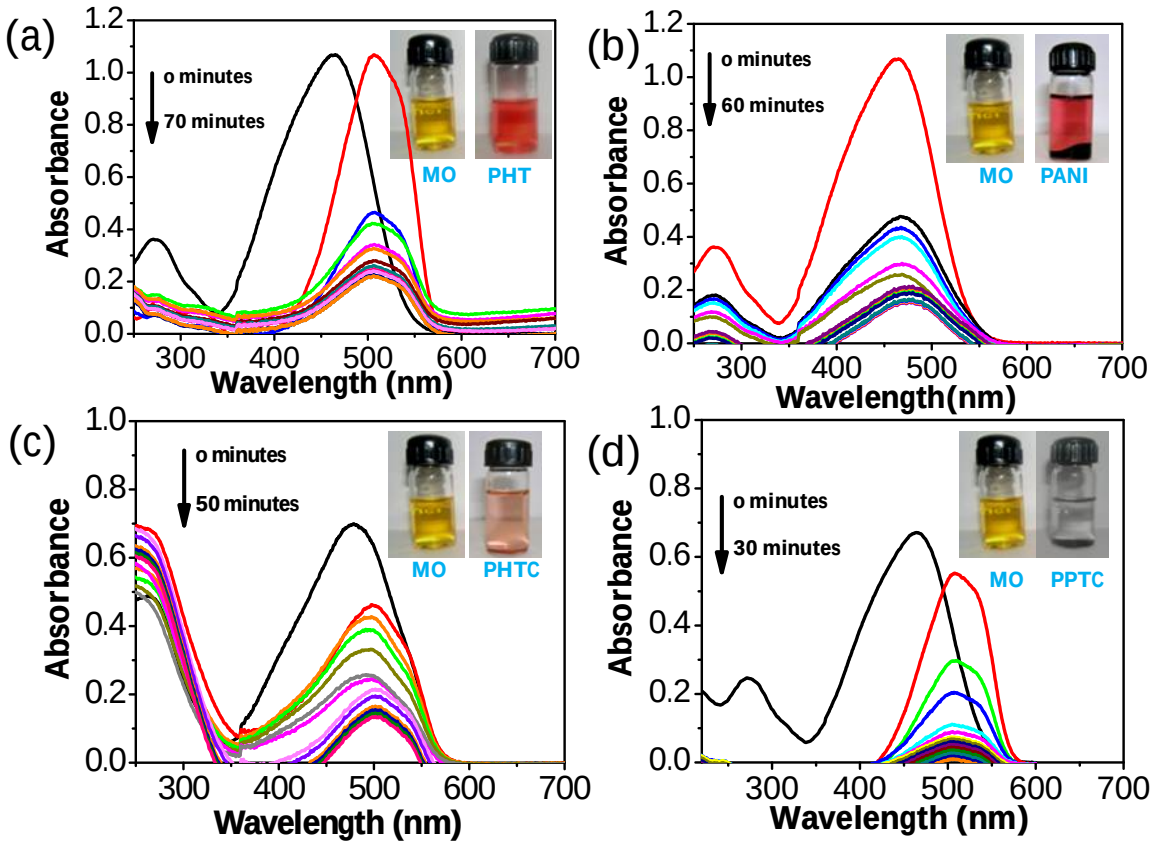

Figure 2.7. UV-visible spectra of methyl orange in presence of (a) PHT (b) PANI (c) PHTC and (d) PPTC-4 at different time intervals

The absorption spectrum of PHT, PANI, PHTC and PPTC-4 in presence of methylene blue (MB) is given in Figure 2.8(a–d), respectively. UV-Visible spectra of MB exhibited three peaks at 240 nm 296 nm and 665 nm. Generally, the absorption intensity of all the peaks showed a decrease in intensity with time. The photographs showing the decrease in colour intensity with time is shown in Figure 2.8(a-d) (inset snap shot). The photocatalytic degradation efficiency was observed in the order PHT (34.3%), PANI (43.1%), PHTC (51.2%) and PPTC-4 (94.3%). The

photocatalytic efficiency of PHT, PANI, PHTC, PPTC-1, PPTC-2, PPTC-3 and PPTC-4 are shown in Table 2. 2.

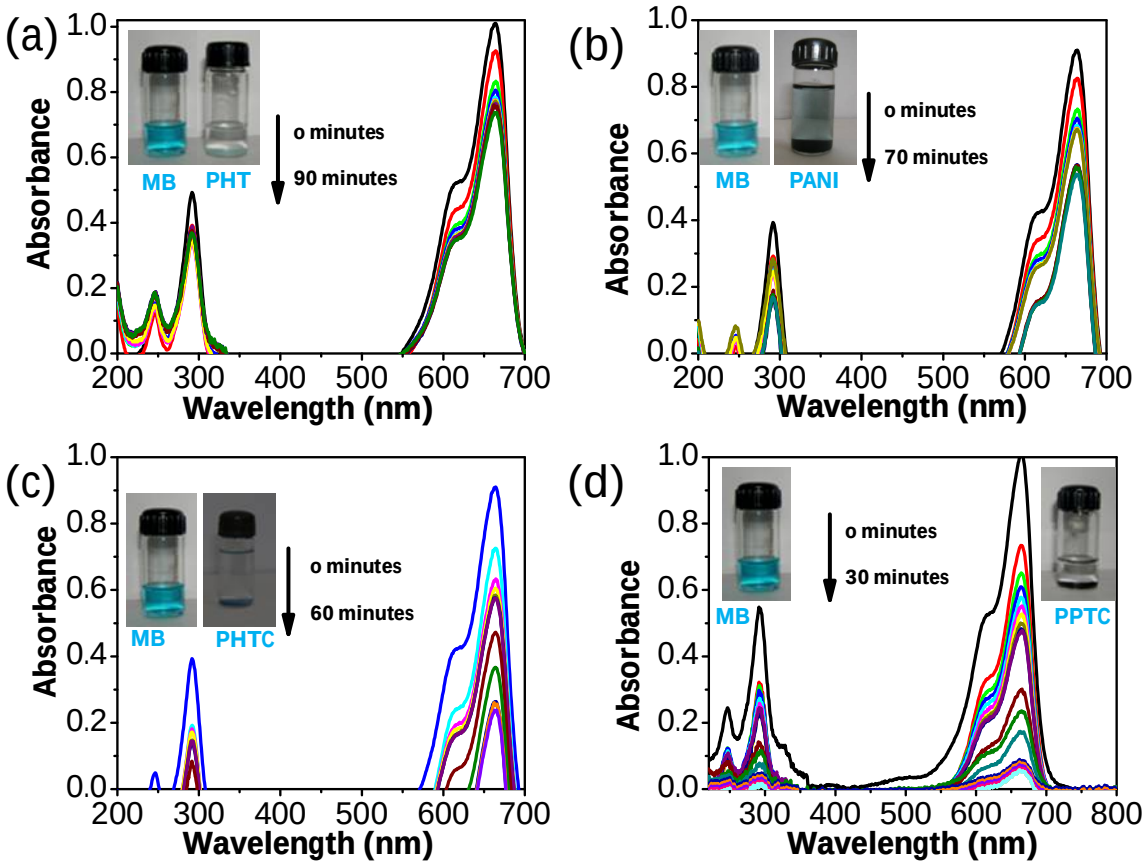

Figure 2.8. UV-visible spectra of methylene blue in the presence of (a) PHT (b) PANI (c) PHTC and (d) PPTC-4 at different time intervals

Figure 2.9(A and B) showing the plot of $\ln(C/C_0)$ vs. time for MO and MB. The reaction rate constant was calculated by taking the slope of $\ln(C/C_0)$ vs. time graph. The rate constant was found to be [PPTC-4 (0.04467 min^{-1}), PHTC (0.0315 min^{-1}), PANI (0.0212 min^{-1}) and PHT (0.0037 min^{-1})] for MO and [PPTC-4 (0.0152 min^{-1}), PHTC (0.00930 min^{-1}), PANI (0.00634 min^{-1}) and PHT (0.0007 min^{-1})] for MB. The photocatalytic degradation reaction followed pseudo first order reaction for both MO and MB.

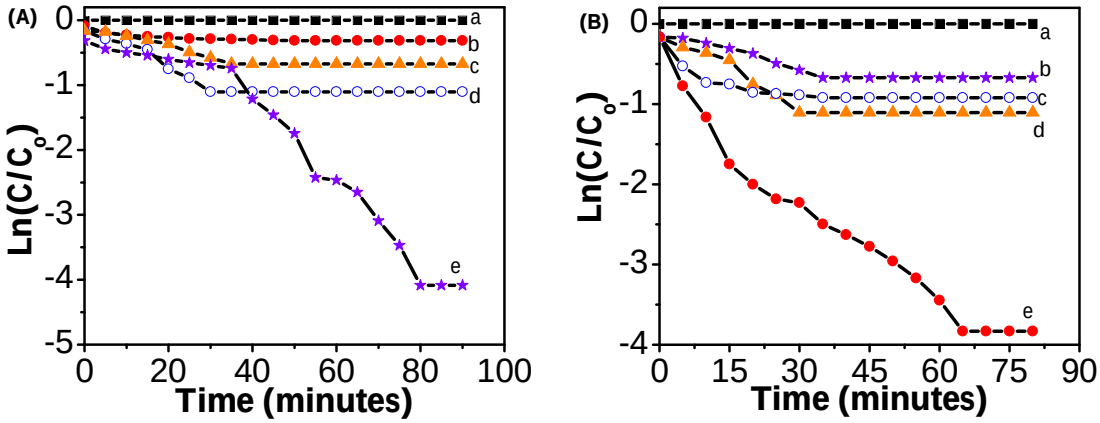

Figure 2.9. (A) Photocatalytic degradation of methyl orange (a) blank (b) PHT (c) PANI (d) PHTC and (e) PPTC-4; **(B)** Photocatalytic degradation of methylene blue (a) blank (b) PHT (c) PANI (d) PHTC and (e) PPTC-4.

Table 2.2. Experimental details, electrical conductivity and photocatalytic efficiency of nanocomposites

Samples	PHTC: PANI (%)	Conductivity (S/cm)	*P.C.E M.B	*P.C.E M.O
PHT	-	1.8×10^{-4}	34.3	64.5
PANI	0:100	3×10^{-3}	43.1	67.6
PHTC	100:0	3.3×10^{-5}	51.2	80.4
PPTC-1	15:85	1.26×10^{-3}	90.4	97.2
PPTC-2	10:90	8.2×10^{-3}	91.6	98.1
PPTC-3	5:95	2.1×10^{-2}	92.1	98.9
PPTC-4	1:99	6.2×10^{-2}	94.3	99.6

***P.C.E.M.B=Photocatalytic efficiency of methylene blue; *P.C.E.M.O = Photocatalytic efficiency of methyl orange.**

The mechanism for the photo degradation of MB and MO in presence of PPTC can be explained as per the schematic representation given in Scheme 2. 2. When PPTC is illuminated under natural light, both PHTC and PANI absorb photons and then charge separation occurs at the interface. The conduction band of PHTC and the lowest unoccupied molecular orbital (LUMO) level of PANI are well matched for the efficient charge transfer. The generated electrons from PANI are transferred to the conduction band of PHTC, whereas holes in the valence band of PHTC are transferred into the PANI, which enhances the charge separation occurs and promoting the photocatalytic activity of photocatalyst. It is well-known that surface Ti–OH groups play an important role in enhancing the activity of PHT photocatalysts.[51] They are considered to have two effects on enhancing the photocatalytic activity. The Ti–OH group acts as an effective trapping site for the photogenerated holes, reducing their recombination with the electrons, and the surface OH groups allow the adsorption of O_2 from water. Then, the excited electrons reduce O_2 to O_2^- species, which in turn can interact with water to form further oxygenated radicals (mainly hydroxyl radicals ·OH). Consequently, the presence of Ti–OH groups may improve the photocatalytic activity of PPTC by both photo oxidation and photosensitizing mechanisms. Under the same conditions, adsorption of MB and MO on PPTC sample in the dark condition was studied. The results showed that dye is not decolourised even after 70 min, and the decolourisation efficiency of MB is only about 3% and MO is 5% which does not change with the further increase of the time. By comparison of the degradation efficiency values of MB and MO with and without natural light, it can be confirmed that the decolourisation is due to photocatalytic degradation but not adsorption.

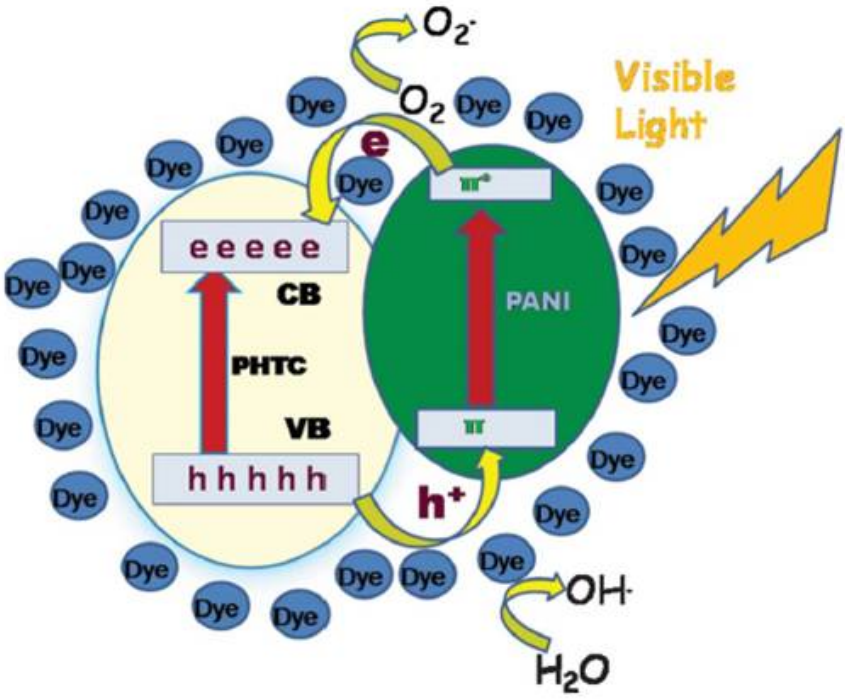

Scheme 2.2. Mechanism for the photodegradation of dye in the presence of PPTC

To evaluate the reusability of the PPTC catalyst several photocatalytic degradation runs of methyl orange and methylene blue were completed under visible light. After the first run, the catalyst was separated and used immediately for further runs without any treatment. The results show that after eight recycles for the photo degradation of methyl orange and methylene blue, the activity of PPTC catalyst did not exhibit any significant loss of activity. It indicates that the PPTC composites have high stability and reusability. Moreover, the PPTC photocatalyst had an advantage over the pure PHT. They had good sedimentation ability and could decant in a few minutes by gravity sedimentation. All the nanocomposites settled on the bottom of a cylinder within 15 min, whereas pure PHT did not settle even after 2 h. Thus the easy sedimentation and reusability of PPTC implies that it is potentially employable for practical applications under mild conditions such as natural light and ambient temperature.

2.4. Conclusions

Photocatalytic PPTC nanocomposites were prepared by the polymerization of anilinium hydrochloride in presence of titanate functionalized nanoclay at room temperature by a facile strategy. Studies showed that PPTCs forms electrically conductive nanotubes through template/self-assembly process. The photocatalytic effect of PPTCs towards methyl orange and methylene blue is due to the photo-oxidation and photosensitizing mechanisms between PANI and PHTC. A rapid charge separation and slow recombination occurs in the PPTCs nanocomposite. The interface formed between PHTC and PANI transfers the excited electrons to the conduction band of PHTC and hole transferring to the valency band of PANI which in turn increases the yield of hydroxyl, super oxide and positive carbon radicals. Studies revealed that this multifunctional PPTCs nanocomposite with higher photocatalytic efficiency will be a potential candidate for environmental purification under visible light at ambient conditions. This low cost environmentally benign PPTC composite prepared in this work may find other applications in catalysis, sensors and photovoltaic fields.

2.5. Experimental Section

2.5.1. Materials

Anilinium hydrochloride monomer (99.5% pure, Sigma Aldrich), ammonium persulphate (APS), titanium tetrachloride (s.d. fine Chem limited, Bombay, India) were used without further purification. Na^+ cloisite clay with cation exchange capacity of 92.6 meq/100 g and a mean chemical formula of $(Na,Ca)_{0.33}(Al_{1.67}Mg_{0.33})Si_4O_{10}(OH)\ 2nH_2O$ (Loba Chemie, Bombay, India). Methyl orange (MO) chemical

formula of $C_{14}H_{14}N_3NaO_3S$ and methylene blue (MB) chemical formula of $C_{16}H_{18}N_3ClS$ were purchased from Aldrich, USA.

2.5.2. Preparation of polytitanate (PHT)

PHT was prepared by the hydrolysis of titanium tetrachloride solution with 6M hydrochloric acid. A typical procedure is as follows: 7.778 g (0.082 mol) of titanium tetrachloride was mixed with 4.7 mL (6 N) HCl in 40.8 mL of water and stirred vigorously for 20 min. The product was dialysed to remove any chloride ions. The prepared PHT was aged for 3 days at room temperature to allow the growth of the polytitanate cation under nitrogen atmosphere.

2.5.3. Preparation of polytitanate intercalated clay (PHTC)

0.5 g clay in 50 mL of water (1 wt%) was added slowly to a vigorously stirred solution of 2.53 mL of PHT. The ratio of cation to clay was 90 mmol/meq for the synthesis. Upon complete addition of clay to the PHT solution, the reaction mixture was stirred for an additional 2 h. The product was washed and filtered with water. The resulting material was then dried in a vacuum oven at 75 ^oC for 12 h and made into a powder for further characterisation.

2.5.4. Preparation of polyaniline-polytitanate-clay nanocomposites (PPTC)

0.1 g clay in 10 mL of water (1 wt%) was added slowly to a vigorously stirred solution of 0.506 mL of PHT. It was stirred for 1hour and 2.0 g of anilinium hydrochloride ($1.6x10^{-2}$ mol) in 20 mL water was added. Stirring continued for further 1 hour. Then the system was cooled to 5 ^oC and 3.5 g of APS (9.16 1023 mol) in 35 mL of water was added dropwise to the system. After the addition of APS, polymerization was continued to achieve high molecular weight PANI species. The green emeraldine salt of PPTC formed was isolated by centrifugation. Washing and

centrifugation was repeated a number of times with distilled water. The product was then dried under freeze drying for 12 h and made into a powder. Experiments were also performed by varying the composition of aniline hydrochloride content in the composites and prepared samples were designated as PPTC-1, PPTC-2, PPTC-3 and PPTC-4 is shown in Table 2.2.

2.5.5. Photocatalytic Degradation Studies

Visible light photocatalytic activity was evaluated by the degradation of methyl orange (MO) and methylene blue (MB) in an aqueous solution. An aqueous suspension of (100 mL) of MO ($1x10^{-5}$ M) and 0.01g of PPTC nanoparticles was stirred in the dark for 30 minutes to establish an adsorption/desorption equilibrium before irradiation in a reaction cell made of quartz. Light from a 300 W Xe lamp passed through a UV light filter film (to remove the radiation with $\lambda < 400$ nm) and was focused onto the reaction cell. Aliquots (3 mL) were take it out at given time intervals and centrifuged to remove the particles. The residual MO concentration was detected using a UV-visible spectrophotometer. The absorbency of the original methyl orange and methylene blue solution (namely C_0) and absorbencies of methyl orange and methylene blue solution for every 5 min (namely C) was measured by UV-visible spectroscopy. The photocatalytic efficiency was calculated by using the equation (2.1),

$$d = (C_0-C)/C_0 \qquad (2.1)$$

Where, d = photocatalytic efficiency; C_0 = absorbance of original dye solution; C = absorbance of dye solution, were measured every 5 min.

The order of photocatalytic reaction was calculated by using the equation (2.2),

$$\ln(C/C_0) = k(min^{-1})t + a \qquad (2.2)$$

where k is the apparent reaction rate constant C_0 is the initial concentration of aqueous dye solution and C is concentration of aqueous dye solution at the reaction time t.

2.6. Characterization Techniques

Diffused reflectance spectra (DRS) were recorded using a Shimadzu integrating sphere assembly attached to a Shimadzu UV-visible 3101PC spectrometer. $BaSO_4$ was used as the reflectance standard. FT-IR measurements were made with a fully computerized Nicolet impact 400D FT-IR spectrophotometer. Polymers were mixed thoroughly with potassium bromide and compressed into pellets before recording. All spectra were corrected for the presence of moisture and carbon dioxide in the optical path. Powder X-ray diffraction studies were performed with an X-ray diffractometer (Philip's X'pert Pro) with Cu-Ka radiation (I = 0.154 nm) employing an X'celarator detector and a monochromator at the diffraction beam side. Powder samples were used by employing a standard sample holder. The d-spacing of the nanocomposite was calculated from the angular position 2θ of the observed d001 reflection peaks based on the Bragg's formula $n\lambda = 2d\sin\theta$, where λ is the wavelength of the X-ray beam and θ is the diffraction angle. Electrical conductivity measurements were performed with a standard four-probe conductivity meter using a keithely 6221 programmable current source and a 2128A nanovoltmeter at room temperature. The samples were pressed into a 11 mm diameter disk for the measurement. The BET surface area measurements of the samples were measured using Micrometritics tristar 3000 model surface area analyser. 0.5 gm of the sample was heated to 200 ^oC for 3 h under nitrogen atmosphere for degassing. Then it was subjected to absorption of

nitrogen using sorptometer at liquid nitrogen temperature. Particle size and zeta potential measurement of the samples were carried out in a Nano ZS Malvern instrument employing a 4 mW He–Ne laser (l = 632.8 nm) and equipped with a thermostated sample chamber. DLS is a non-invasive, well-established technique for measuring the size of molecules and particles typically in submicron region, and with the latest technology lower than 1 nm. SEM measurements of samples were performed by subjecting the samples for thin gold coating using a JEOL JFC-1200 fine coater. The probing side was inserted into JEOL JSM-5600 LV scanning electron microscope for imaging. Transmission electron microscopy was performed in an FEI (TECNAI G^2 30 S-TWIN) microscope with an accelerating voltage of 100 KV. For TEM measurements, the sample solutions were prepared by dispersion under an ultrasonic vibrator. They were then deposited on a formvar coated copper grid and dried in a vacuum at room temperature before observation. Photocatalytic activities of the materials of PPTC, PHT, PHTC and PANI were evaluated by monitoring photodegradation studies of methyl orange and methylene blue solution using UV-visible spectrophotometer (Shimadzu model 2100) in the range of 200–900 nm.

2.7. References

1. J. Tang, Y. Wu, E. W. McFarland and G. D. Stucky, *Chem. Commun*. **2004**, *14*, 1670.

2. Y. Cho, W. Choi, C. H. Lee, T. Hyeon and H. I. Lee, *Environ. Sci. Technol*. **2001**, *35*, 2988.

3. K. Iuchi, Y. Ohko, T. Tatsuma and A. Fujishima, *Chem. Mater*. **2004**, *16*, 1165.

4. B. O'Regan and M. Gratzel, *Nature* **1991**, *353*, 737.

5. H. X. Li, J. X. Li and Y. N. Huo, *J. Phys. Chem. B.* **2006**, *110*, 1559.

6. J. G. Yu, M. H. Zhou, B. Cheng and X. J. Zhao, *J. Mol. Catal. A: Chem*. **2006**, *246*, 176.

7. M. S. Wong, H. P. Chou and T. S. Yang, *Thin Solid Films*, **2006**, *494*, 244.

8. M. R. Hoffmann, S. T. Martin, W. Choi and D. Bahnemann, *Chem. Rev*. **1995**, *95*, 69.

9. S. M. Sun, Y. S. Jiang, L. X. Yu, F. F. Li, Z. W. Yang, T. Y. Hou, D. Q. Hu and M. S. Xia, *Mater. Chem. Phys.* **2006**, *98*, 377.

10. C. Ooka, H. Yoshida, K. Suzuki and T. Hattori, *Appl. Catal, A.* **2004**, *260*, 47.

11. C. Ooka, S. Akita, Y. Ohashi, T. Horiuchi, K. Suzuki, S. Komai, H. Yoshida and T. Hattori, *J. Mater. Chem*. **1999**, *9*, 2943.

12. G. Zhang and X. M. Ding, *Langmuir* **2008**, *24*, 1026.

13. C. Volzone, *Mater. Res.* **2009**, *12*, 191.

14. X. P. Zhao and L. Q. Xiang, *J. Mater. Chem*. **2003**, *13*, 1529.

15. (a) T. Guo and L. Wang, *J. Phys. Chem. B.* **2010**, *114*, 4765; (b) S. Yoda, Y. Sakurai, A. Endo, T. Miyata, K. Otake, H. Yanagishita and T. Tsuchiya, *Chem. Commun*. **2002**, *14*, 1526.

16. R. Q. Long and R. T. Yang, *J. Catal*. **1999**, *186*, 254.

17. N. N. Binitha and S. Sugunan, *Microporous Mesoporous Mater.* **2006**, *93*, 82.

18. J. Sterte, *Clays Clay Miner.* **1986**, *34*, 658.

19. B. I. Nabivanets and L. N. Kudritskaya, *Russ. J. Inorg. Chem*. **1967**, *12*, 616.

20. F. B. Baes and R. E. Mesmer, Wiley, New York, **1976**,147.

21. H. Einaga, *J. Chem. Soc. Dalton Trans*. **1979**, *12*, 1917.

22. V. P. S. Pereraa, P. K. D. D. P. Pitigala, M. K. I. Senevirathne and K. Tennakone, *Sol. Energy Mater. Sol. Cells.* **2005**, *85*, 91.

23. M. Iwasaki, M. Hara, H. Kawada, H. Tada and S. Ito, J. Colloid Interface Sci. **2000**, *224*, 202.

24. C. Ooka, H. Yoshida, K. Suzuki and T. Hattori, *Microporous Mesoporous Mater*. **2004**, *67*, 143.

25. H. Zhang, R. Zong, J. Zhao and Y. Zhu, *Environ. Sci. Technol*. **2008**, *42*, 3803.

26. A. Pron and P. Rannou, *Prog. Polym. Sci.* **2002**, *27*, 135.

27. G. Gustafsson, Y. Cao, G. M. Treacy, F. Klavetter, N. Colaneri and A. J. Heeger, *Nature* **1992**, *357*, 477.

28. M. J. Sailor, E. J. Ginsburg, C. B. Gorman, A. Kumar, H. Grubbs and N. S. Lewis, *Science* **1990**, *249*, 1146.

29. S. H. Jang, M. G. Han and S. S. Im, *Synth. Met*. **2000**, *110*, 17.

30. S. S. Ran and M. Biswas, *Synth. Met*. **2000**, *108*, 231.

31. Y. J. He, *Mater. Chem. Phys*. **2005**, *92*, 134.

32. R. V. Kumar, Y. Diamant and A. Gedanken, *Chem. Mater*. **2000**, *12*, 2301.

33. J. Li, L. Zhu, Y. Wu, Y. Harima, A. Zhang and H. Tang, *Polymer***2006**, *47*, 7361.

34. S. Min, F. Wang and Y. Han, J. Mater. Sci. **2007**, *42*, 9966.

35. J. Ruokolainen, H. Eerikainen, M. Torkkeli, R. Serimaa, M. Jussila and O. IKkala, *Macromolecules* **2000**, *33*, 9272.

36. R. Lv, S. Zhang, Q. Shi and J. Kan, *Synth. Met*. **2005**, *150*, 115.

37. V. L. Reena, J. D. Sudha and C. Pavithran, *J. Appl. Polym. Sci*. **2009**, *113*, 4066.

38. Q. Wu, Z. Xue, Z. Qi and F. Wang, *Polymer* **2000**, *41*, 2029.

39. H. Xia and Q. Wang, *Chem. Mater*. **2002**, *14*, 2158.

40. L. J. Zhang and M. X. Wan, *J. Phys. Chem. B*. **2003**, *107*, 6748.

41. X. W. Li, G. C. Wang, X. X. Li and D. M. Lu, *Appl. Surf. Sci*. **2004**, *229*, 395.

42. P. R. Somani, R. Marimuthu, U. P. Mulik, S. R. Sainkar and D. P. Amalnerkar, *Synth. Met*. **1999**, *106*, 45.

43. J. Liu, X. Li, S. Zuo and Y. Yu, *Appl. Clay Sci*. **2007**, *37*, 275.

44. B. E. Warren, *Phys. Rev*. **1941**, *59*, 693.

45. O. Elvira Alonso and C. Brime, *Clays and Clay Miner* **1990**, *38*, 257.

46. P. Yuan, X. L. Yin, H. P. He, D. Yang, L. J. Wang and J. X. Zhu, *Microporous Mesoporous Mater*. **2006**, *93*, 240.

47. W. Feng, E. Sun, A. Fujii, H. C. Wu, K. Niihara and K. Yoshino, *Bull. Chem. Soc. Jpn*. **2000**, *73*, 2627.

48. L. J. Zhang and M. X. Wan, *Adv. Funct. Mater*. **2003**, *13*, 815.

49. F. G. Cheng, W. Tang, C. S. Li, J. Chen, H. K. Liu and P. W. Shen, *Chem.Eur. J*. **2006**, *12*, 3082.

50. D. C. Schnitzler, M. S. Meruvia, I. A. Hummelgen and A. J. G. Zaberin, *Chem. Mater*. **2003**, *15*, 4658.

51. W. Jia, E. Segal, D. Kornemandel, Y. Lamhot, M. Narkis and A. Siegmann, *Synth. Met*. **2002**, *128*, 115.

52. S. J. Su and N. Kuramoto, *Synth. Met*. **2000**, *114*, 147.

53. F. Y. Chuang and S. M. Yang, *Synth. Met*. **2005**, *152*, 361.

Chapter 3

Hierarchical Multiple Structured ZnO Crystals: Preparation and Its Application as a Photoanode in Dye Sensitized Solar Cells

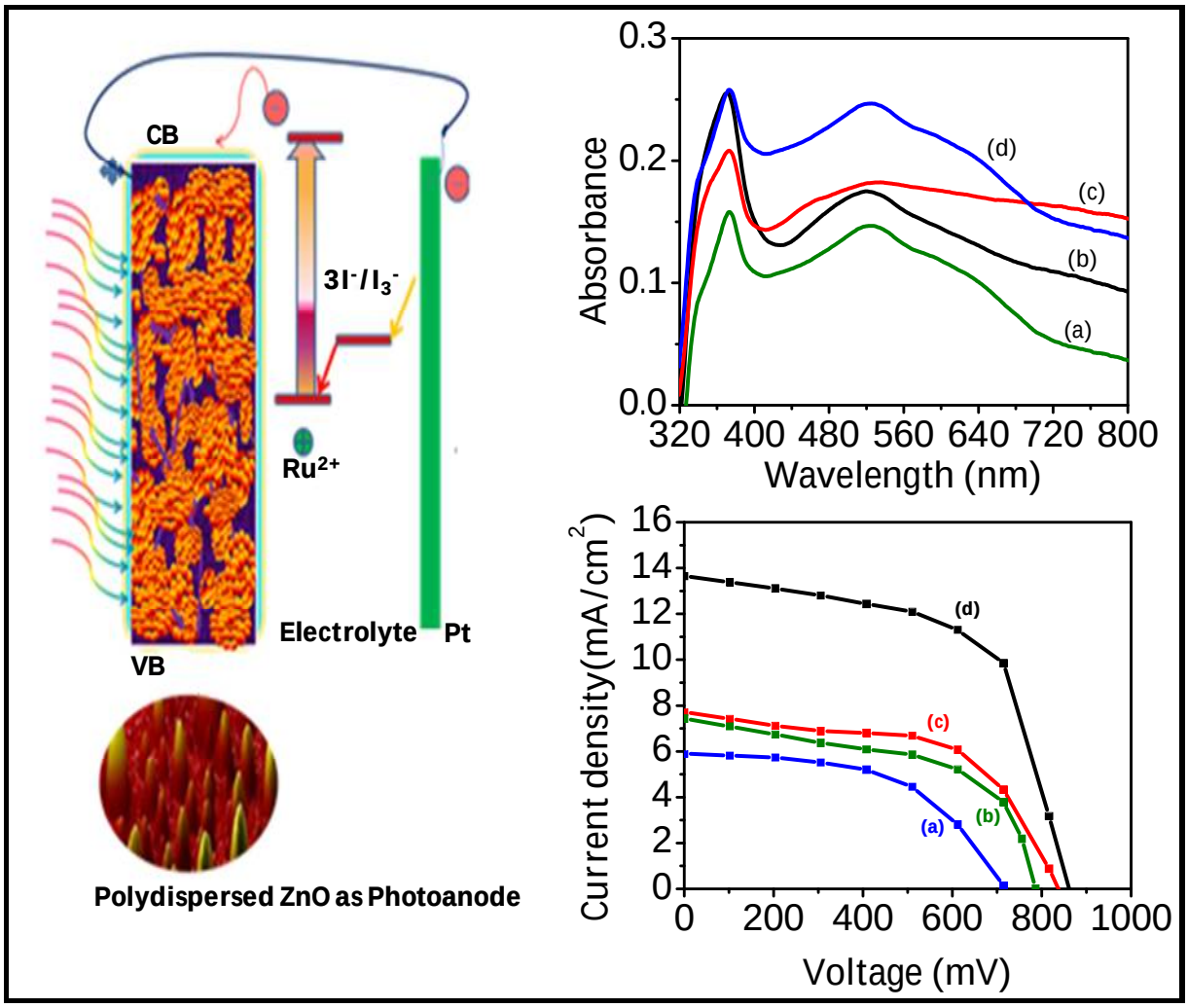

3.1. Abstract

In this chapter we demonstrate a facile bioanchoring strategy for controlling the crystal growth process of ZnO crystals during calcination to form hierarchical multiple structures. Crystalline phase and morphology of ZnO was investigated using X-ray diffraction, scanning electron microscopy, transmission electron microscopy, and atomic force microscopy. Results revealed the evolution of ZnO nanocrystallites from nanosize to hierarchical self-assembly of polydispersed microstructures of bars/sheets/spheres/hollow spheres in wurzite hexagonal phase. ZnO exhibited photoluminescence attributed to the presence of various defects which was further supported by Raman spectroscopy and energy dispersive X-ray spectroscopy analysis. On the basis of the various experimental results, a plausible growth mechanism for the formation of multiple structures of ZnO crystals is proposed. Further demonstrated is the application of the ZnO crystals as photoanode in dye sensitized solar cells with power conversion efficiency (~5.3%) which is due to high dye loading and enhanced light absorption edge via inherent light reflection mechanism.

3.2. Introduction

The increasing demand for energy has impelled researchers in the development of cost-effective and environmentally friendly energy resources. Due to the surge in the production cost of silicon solar cells, researchers have been focused on the development of organic solar cells especially dye sensitized solar cells (DSSCs).[1] Recently, DSSCs have emerged as one of the promising solutions to the global energy and environmental problems because of its advantages like clean, low cost, high efficiency and ease of fabrication. However, enhancing the efficiency of DSSC is still a major concern among the research community. Many wide band

gap semiconducting metal oxides such as titania (TiO_2),[2] stannous oxide (SnO_2),[3] zinc oxide (ZnO),[4] and niobium oxide (Nb_2O_5)[5] have been used as photoanode in DSSCs. Compared with TiO_2, ZnO finds advantages such as ease of preparation, high charge carrier mobility, and controlled morphology. ZnO nanostructures such as nanowires, nanorods, nanobelts, and nanodisks can provide a direct pathway for the rapid collection of photogenerated electrons and reduce the degree of charge recombination in the devices.[6–9]Furthermore, they possess many inherent properties such as wide band gap of 3.39 eV, large exciton binding energy, and various types of crystal defects such as zinc vacancies, oxygen vacancies, zinc interstitials, oxygen interstitials, O_{Zn} antisites, Zn_O antisites,[10] shallow level and deep levels defects.[11] In DSSCs, the power conversion efficiencies (PCE) depend not only on the electron transport mobility of the photoanode but also on other significant features such as dye loading, absorption of light, open circuit voltage (V_{oc}), short circuit current density (J_{sc}), and fill factor (FF).[12–23] The recent literature survey on ZnO based DSSCs have shown a significant progress over the years in enhancing the PCE from 0.4% in 1994 to a maximum of 7.5% to till date.[24–30] Recently, tremendous efforts have been made toward the preparation of ZnO crystals by various strategies such as sol–gel,[31] hydrothermal,[32] thermal evaporation,[33] laser induced deposition,[34] microwave,[35] solvothermal,[36] and chemical vapor deposition.[37] Among the various synthetic strategies, the sol–gel method is one of the low cost and facile techniques for controlling the size and shape of nanostructured materials. ZnO nanocrystals with controllable aspect ratio were reported to be prepared by introducing a capping agent based on surfactant such as cetyltrimethylammonium bromide, sodium dodecyl sulfate, and ionic liquid during the crystal growth process.[38–40] To achieve high performance solar cell, tremendous

research effort has been focused on the design and fabrication of photoanodes. The photoanode affects the optical path, selection of light wavelength, efficiency of dye absorption, and photoelectron transport. To enhance the light absorption by the dyes, the management of incident light becomes an important issue. For instance, the light absorption can be enhanced by increasing the light scattering particles or trapping in the photoanode. *Zuowan et al*. prepared ZnO nanocrystals with different morphologies including microrods, hierarchical microspheres, and hollow microspheres via the citrate-assisted hydrothermal method and measured the PCE in DSSC as 0.79%.[41] *Zhang et al*. developed polydispersed aggregates of ZnO with broad size distribution by the sol–gel method for improving the PCE up to 4.4%.[42] In polydispersed ZnO nanoaggregate systems, the incident photon is scattered inside the closed loops, which result in a higher absorption in the visible region and improve the conversion efficiencies compared with the monodispersed aggregates.[43]

In this context, the exploration of a simple and low cost methodology to prepare well-defined hierarchical three-dimensional ZnO nanostructures is receiving tremendous interest among researchers. Because of the high cost of petroleum based chemicals, researchers are presently focused on low cost abundantly available renewable resource based materials. In the present work, we have used 3-pentadecylphenylphosphoricacid (PDPPA) as a bioanchoring agent which is derived from cardanol by phosphorylation. Cardanol is a long alkyl chain substituted phenol obtained by the distillation of cashew nut shell liquid which is obtained as a by product from the cashew industry. The dual role of PDPPA as a dopant cum structure directing agent during the formation of nanostructured polyaniline was previously reported from our group.[44] Herein, we present a low

cost facile environmentally friendly bioanchoring strategy for the synthesis of hierarchical polydispersed ZnO multiple structures. The role of PDPPA as an anchoring agent and the effect of calcination temperature on the growth of hierarchical ZnO crystals to form multiple structures were studied using various techniques. Finally, we have demonstrated the role of polydispersed ZnO crystal as photoanode for improving the power conversion efficiency of DSSC through enhancing absorption of light edge via inherent light reflection and high dye loading.

3.3. Results and Discussion

3.3.1. Preparation of Hierarchical ZnO Multiple Structures

Hierarchical ZnO particles were synthesized via acid-catalyzed esterification using PDPPA as a bioanchoring agent by the sol gel method. ZnO was prepared with PDPPA was designated as ZBS. Further the prepared ZBS was calcined under various temperatures such as 500, 600, 700 and 800 °C. They are designated as ZB-500, ZB-600, ZB-700, and ZB-800, respectively. FT-IR spectra of the ZBS and ZB-800 are shown in Figure 3.1A (a, b). ZBS exhibited a broad peak at 3393 cm^{-1}, which is assigned to hydroxyl groups and water molecules. The bands observed around 1563, 1450, and 1340 cm^{-1} were attributed to the asymmetric and symmetric C=O stretching.[45] The band appearing at 2922, 2853, and 1045 cm^{-1} corresponds CH_2 vibrations.[46] The characteristic band of P=O group is observed at 1252 cm^{-1} and the aromatic vibration peak is observed at 695 cm^{-1}. The band observed at 1740 cm^{-1} corresponds to the stretching vibration of C=O groups. All these results suggested the intermediate formation of phosphate anchored zincite. FT-IR spectra of ZB-800 calcined at 800 °C showed silence signals corresponding to the above peaks suggesting the complete removal of the organic matter, and the band observed at

470 cm^{-1} confirmed the formation of zinc oxide. The above observation was further confirmed by studies on the thermal stability of ZBS and ZB-800 by TGA, and the profile of the same is shown in Figure 3.1B (a, b). ZBS showed a two-step weight loss of zinc oxide. In the initial step, 7% weight loss was observed at ~175 °C due to the removal of moisture and volatile matter. In the second step, 11% weight loss was observed at 220–470 °C due to the loss of small molecules from phosphate anchored hydrozincite. TG profile of ZB-800 shown in Figure 3.1B(b) which exhibited a stable profile revealing the absence of any organic moiety in ZnO and supported the results obtained from FT-IR.

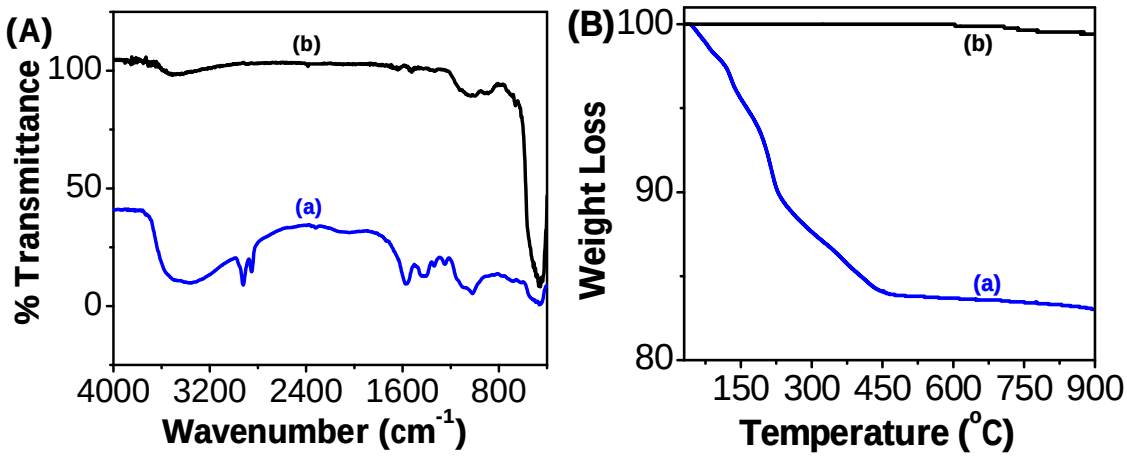

Figure 3.1.(A) FT-IR spectra of (a) ZBS and (b) ZB-800; **(B)** TG curve of (a) ZBS and (b) ZB-800

3.3.2. Optical and Photoluminescence Spectral Analysis

Optical properties of the prepared hierarchical ZnO nanoparticles were studied by UV–visible absorption in combination with photoluminescence spectroscopy. UV–visible absorption spectra of ZBS, ZB-500, ZB-600, ZB-700, and ZB-800 are shown in Figure 3.2A (a-e). Absorption spectra of ZBS, ZB-500, ZB-600, ZB-700, and ZB-800 showed maxima at 351 nm, 354 nm, 358 nm, 365 and 368 nm respectively with variation in the band maxima and intensity. It was observed that

during calcination both ZB-700 and ZB 800 exhibited a red shift in the absorption and reflection edge due to internal reflection of light arising from the polydispersed microspherical particles. The optical band gap was calculated from the Tauc plot and shown in figure 3.2B (a-e).

$$\alpha = 1/t\ ln(1/T)$$

Where α is absorption coefficient, h is the plank's constant, ν is the wavenumber, t is optical path length of zinc oxide, and T is percentage transmittance, respectively.

The band gap values for ZnO were observed to be 3.45, 3.27, 3.25, 3.22, and 3.16 eV for ZBS, ZB-500, ZB-600, ZB-700, and ZB-800. The decrease in observed band gap for ZB-800 is attributed to the high density of defect levels originated in between the conduction and valence band. This may facilitate the effective charge separation and high V_{oc} which will be discussing in detail below.

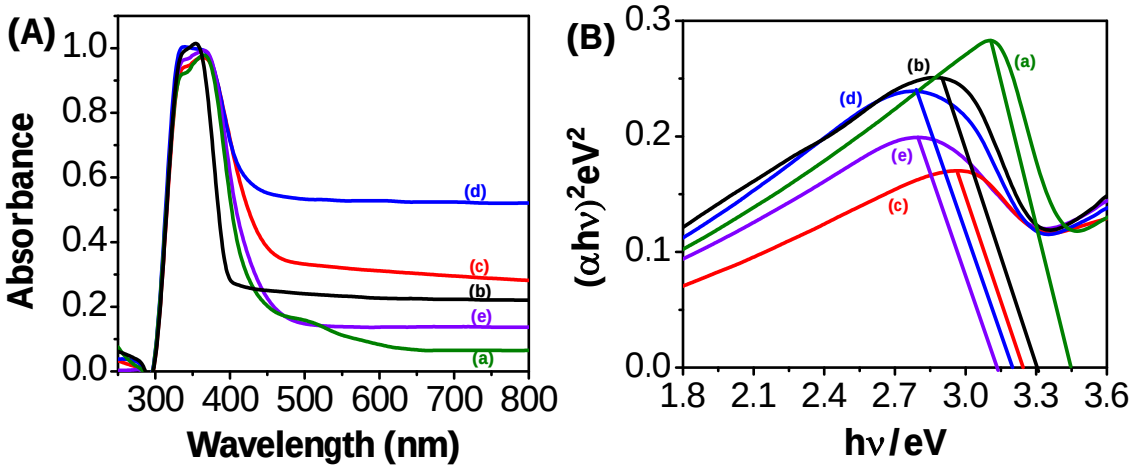

Figure 3.2.(A) UV-Visible spectra of (a) ZBS (b) ZB-500 (c) ZB-600 (d) ZB-700 and (e) ZB-800; **(B)** Tauc plot of (a) ZBS, (b) ZB-500 (c) ZB-600 (d) ZB-700 and (e) ZB-800

The photoluminescence spectra of ZBS, ZB-500, ZB-600, ZB-700, and ZB-800 were recorded by exciting the samples at a wavelength corresponding to the absorbance maxima and are shown in Figure 3.3 (a–e). ZBS, ZB-500, ZB-600, ZB-700, and ZB-800 exhibited emission maxima at 432, 457, 512, and 682 nm, respectively.[52–54] The

maxima observed can be correlated with various defects originated in ZnO crystals during the growth process, and the details regarding the emission maxima, intensity, and the nature of defects are illustrated in Table 3.1. The observed emission maxima at ~432 nm (3.0 eV) is attributed to the radiative recombination of free excitons such as deep level defects.[55,56] Weak bluish green emission observed at ~457 nm (2.7 eV) and strong emission at ~512 nm (2.48 eV) probably originate from defect state luminescence due to the interaction of single ionized oxygen vacancy. The broad yellow emission peak observed at 682 nm attributed to the presence of a large amount of oxygen and zinc interstitial. With an increase in calcination temperature, the intensity of emission also enhanced due to an improved crystallinity and also the presence of large density of generated defects.[47]

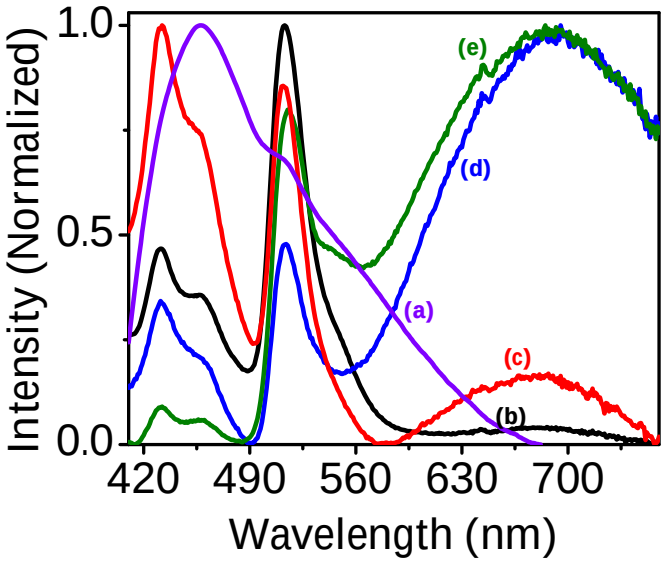

Figure 3.3. Photoluminescence spectra of (a) ZBS (b) ZB-500, (c) ZB-600, (d) ZB-700 and (e) ZB-800

3.3.3. Raman spectral Analysis

Figure 3.4A (a to d) shows the Raman spectra of the ZB-500, ZB-600, ZB-700, and ZB-800. All these samples exhibited hexagonal wurtzite structure, which belongs to the space group C_{6V}.[49] As per literature report, Raman active phonon

modes for wurtzite ZnO arising from the combined symmetry of $A_1 + 2E_2 + E_1$. A_1 and E_1 symmetry are due to polar phonons, and they split into transverse-optical (TO) and longitudinal-optical (LO) phonons. The E_2 modes are nonpolar and have two frequencies: E_2 (high) correlated with oxygen atoms and E_2 (low) associated with Zn sublattice. According to the phonon dispersion curve of ZnO, Raman spectra usually give the following phonon modes: E_2(high) at 437 cm^{-1}, E_2(low) at 101 cm^{-1}, A_1(LO) at 574 cm^{-1}, A_1(TO) at 381 cm^{-1}, E_1(LO) at 583 cm^{-1}, E_1(TO) at 408 cm^{-1}.[50] It can be seen from Figure 3.4A during the growth process, the bands showed a slight difference in the position of maxima and intensity arising from variation in the defects occurring in the crystal phase. All these ZnO samples exhibited vibration bands at 332 cm^{-1}, 391 cm^{-1}, 438 cm^{-1}, 583 cm^{-1}, and 660 cm^{-1}. The highest band observed at 438 cm^{-1} is characteristic E_2 (high) of ZnO wurtzite structure. The band maxima at 208, 332, and 660 cm^{-1} is attributed to the second-order multiphonon scattering, and the band observed at 391 cm^{-1} is due to the first-order phonons of A_1(TO). The E_1 (LO) at observed at 583 cm^{-1} corresponds to the defects arising from the oxygen vacancies or oxygen interstitial. The band at 583 cm^{-1} in the ZB-500 sample exhibited minimum defect intensity as compared to ZB-600, ZB-700, and ZB-800 revealing less density of defect due to oxygen vacancy. As the calcination temperature increased from 500 to 800 °C, the defect intensity also increased revealing the formation of high oxygen defect density.[51] These observations were further supported by the studies made from photoluminescence spectra, and the details are depicted in Table 3. 1. Figure 3.4B shows the graphical representation of the defect states and variation in the intensity exhibited by multiple structured ZnO.

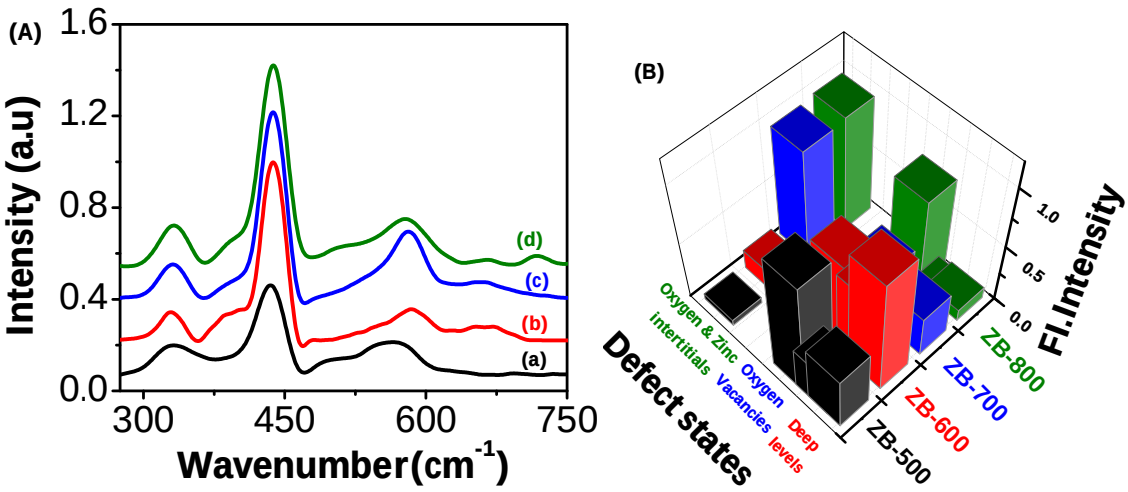

Figure 3.4.(A) Raman spectra of (a) ZB-500, (b) ZB-600, (c) ZB-700, and (d) ZB-800; **(B)** Defect states and variation in the intensity exhibited by ZnO nanostructures

Table 3. 1. Details of the defect state present during the growth process elucidated from the Raman and photoluminescence spectra.

Sample Code	Wavenumber (cm^{-1})	Emission wavelength (nm) /Defect state	Fl. Intensity/Defect state
ZB-500	202, 329,391,435, 567 (oxygen vacancy)	431(deep level defect), 459 nm and 512 (oxygen vacancy), 682 (oxygen and zinc interstitial)	0.47 (deep level defect), 0.36 and 1,0 (oxygen vacancy), 0.5 (oxygen and zinc interstitial)
ZB-600	329,401,435, 584 (oxygen vacancy) and 666	432 (deep level defect), 458 and 512 nm (oxygen vacancy), 682 (oxygen and zinc interstitial)	1 (deep level defect), 0.74 and 0.85 (oxygen vacancy), 0.17 (oxygen and zinc interstitial)
ZB-700	329,401,437, 582 (oxygen vacancy) and 657	431 (deep level defect), 459 and 512 (oxygen vacancy), 694 (oxygen and zinc interstitial)	0.35 (deep level defect), 0.20 and 0.48 (oxygen vacancy)0.94 (oxygen and zinc interstitial)
ZB-800	332,401,438, 579 (oxygen vacancy) and 664	431 (deep level defect), 459 and 516 (oxygen vacancy), 694 (oxygen and zinc interstitial)	0.1 (deep level defect), 0.06 and 0.8 (oxygen vacancy),0.96 (oxygen and zinc interstitial)

3.3.4. Morphological Analysis

Morphology of the prepared zinc oxide nanoparticles was characterized by SEM, HR-TEM, and AFM. SEM image of ZnO nanoparticle prepared without (ZB) and with anchoring agent (ZBS) are shown in Figure 3. 5, panels a and b respectively. SEM image of ZBS was observed as bar like morphology, whereas ZB was observed as aggregates of nanospheres.

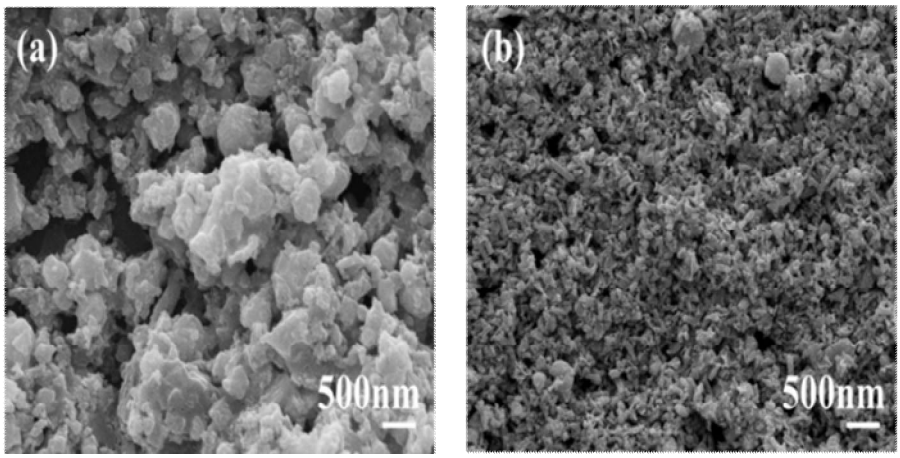

Figure 3.5. SEM images of (a) ZB and (b) ZBS

SEM image of ZB-500 (Figure 3.6a) was observed as nano bars with an average width of ~250 nm, length ~500 nm and ~2–3 nm in thickness. TEM and AFM images of the same showing the formation of nanobars are given in Figure 3.6, panels b and c, respectively. The 3D AFM image showing a height profile of 180 nm is depicted in Figure 3.6d. The SAED and HR-TEM is shown in Figure 3.6, panels e and f, respectively. This result is further strengthened by the measurement made during XRD analysis. The inter lattice spacing was measured as ~0.26 nm which matches the (0001) plane of wurtzite hexagonal phase in ZB-500.[41] As the calcination temperature increased to 600°C, ZB-600 exhibited hierarchical microspheres with a diameter of 0.8 μm confined by thin nanosheet having thickness of ~30 nm, and the corresponding SEM and AFM images are shown in

Figure 3.7, panels a–c respectively. The 3D AFM image and height profile of 60 nm the same is shown in Figure 3.7d. SAED and HR-TEM is shown in Figure 3.7, panels e and f, respectively. The lattice spacing between adjacent fringes is measured as 0.28 nm corresponding to the (002) plane of wurzite hexagonal ZnO.[41]

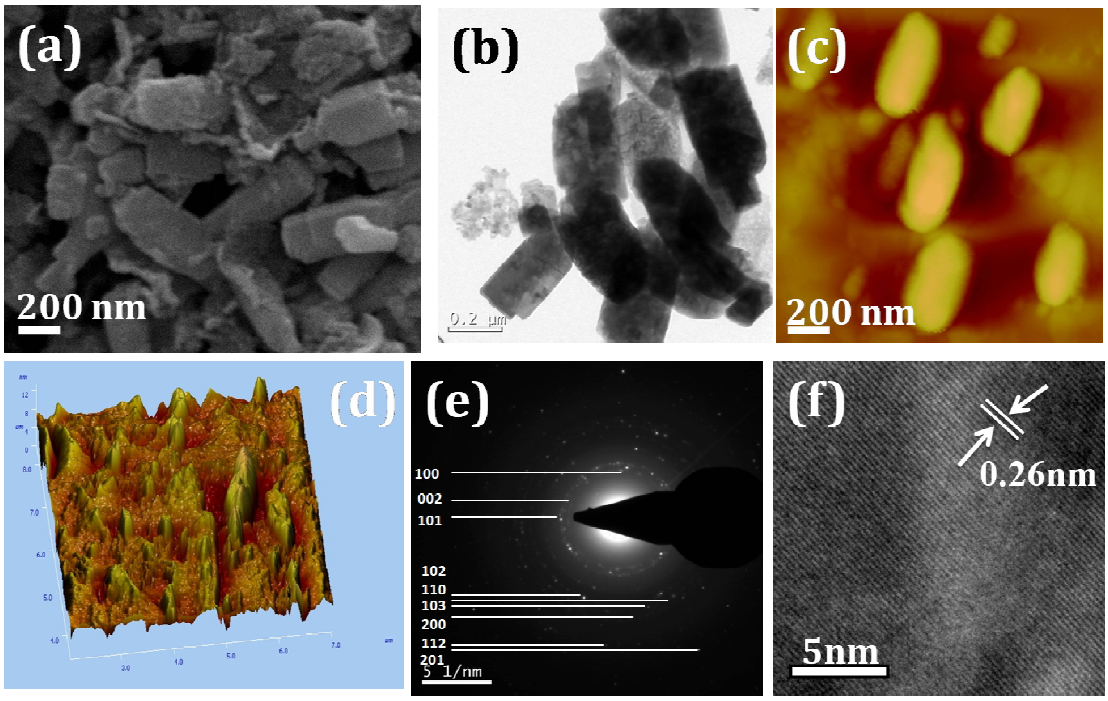

Figure 3.6. ZB-500 showing the formation bar like morphology at 500 °C (a) SEM, (b) TEM, (c) AFM, (d) AFM-3D image, (e) SAED, and (f) HR-TEM image

Further increasing the calcination temperature from 600 to 700 °C observed the formation of hierarchical aggregates of nanospheres to form polydispersed uniform microspherical particles with a diameter of 0.6 μm. The magnified SEM image showed that these microspheres possess coarse surfaces. SEM, TEM, and AFM picture of ZB-700 are shown in Figure 3.8a–c. The 3D AFM image and height profile (100 nm) of the same is shown in Figure 3.8d. The SAED and HR-TEM are shown in Figure 3.8, panels e and f, respectively.

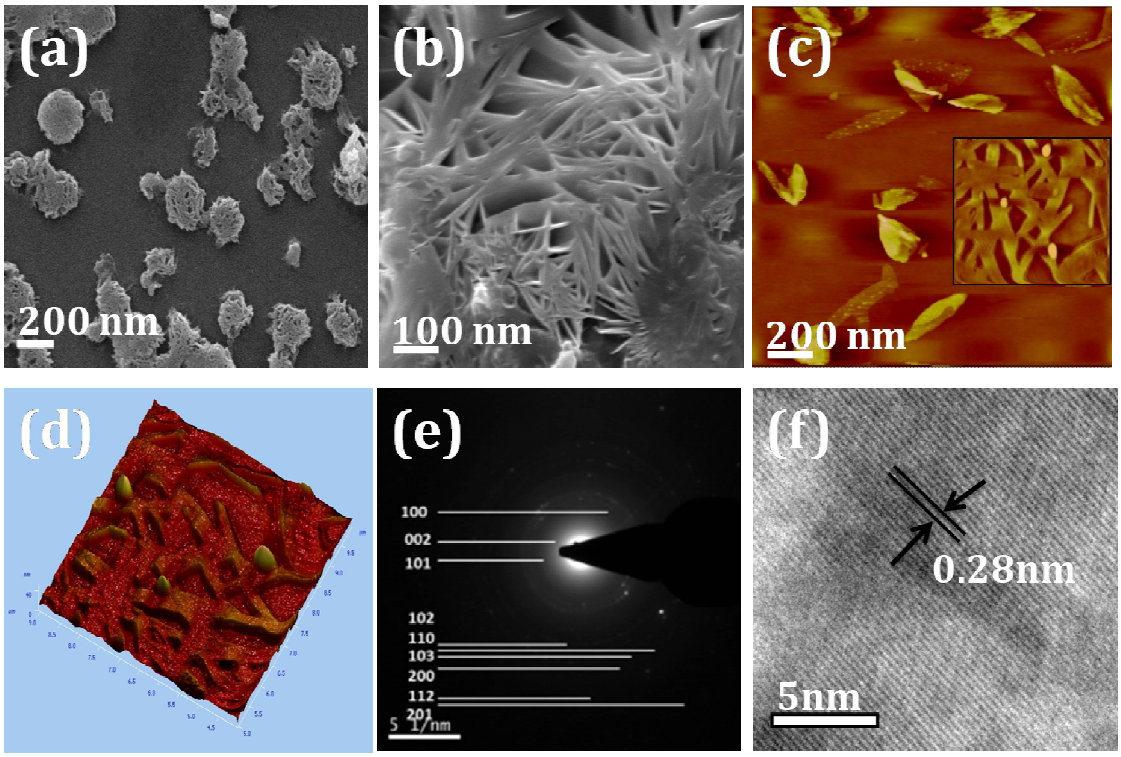

Figure 3.7. ZB-600 showing the formation sheet like morphology at 600 °C (a) SEM, (b) higher magnification image of SEM, (c) AFM, (d) AFM-3D image, (e) SAED, and (f) HR-TEM image

When the temperature is further increased to 800 °C, morphology of the ZnO particles changed into hierarchical hollow microspheres having a 1 μm diameter and the walls of the hollow microsphere formed by the aggregation of 50 nm spherical nanoparticles with wall thickness of 60 nm. SEM, TEM, and AFM images showing formation of hierarchical hollow spheres are shown in Figure 3. 9a–c. The AFM picture of ZB-800 showing the 3D AFM image of well-defined hollow microspherical particles is given in Figure 3.9d. SAED and HRTEM of the same are shown in Figure 3.9, panels e and f, respectively. The d-spacing from FFT pattern measured as 0.28 nm which correspond to the (101) lattice plane of hexagonal ZnO. These observations were supported by the measurement made during the XRD analysis.

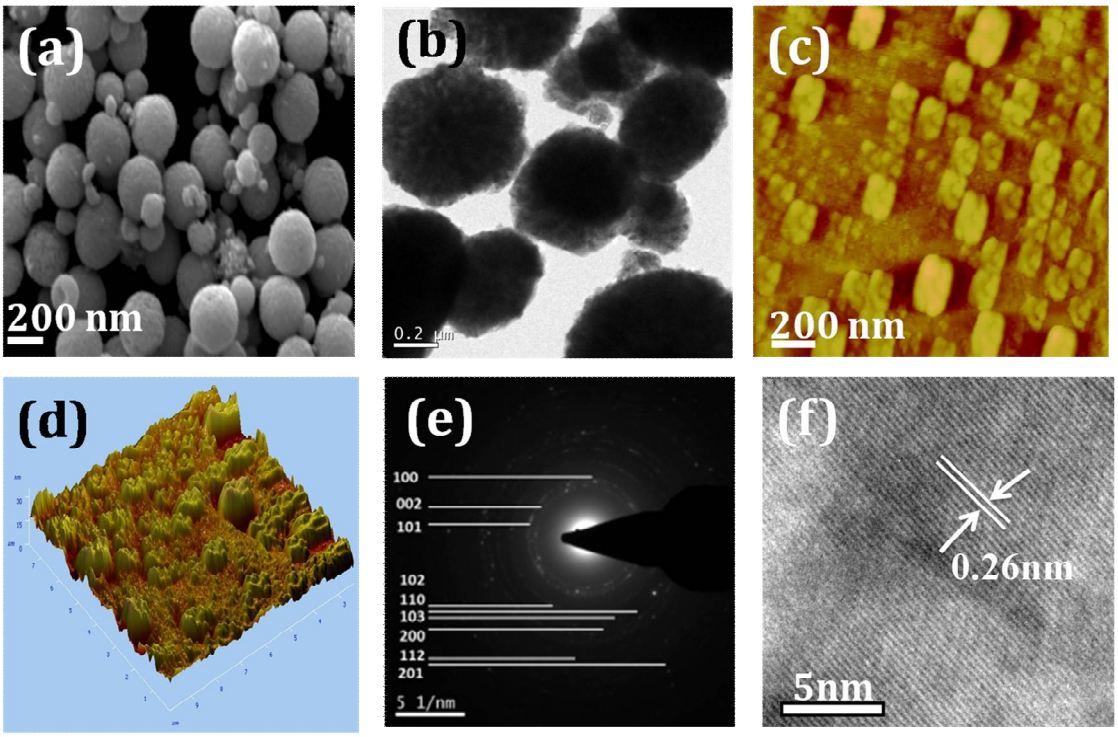

Figure 3.8. Microscopic images of ZB-700 at 700 °C (a) SEM, (b) TEM, (c) AFM, (d) AFM-3D image, (e) SAED, and (f) HRTEM image

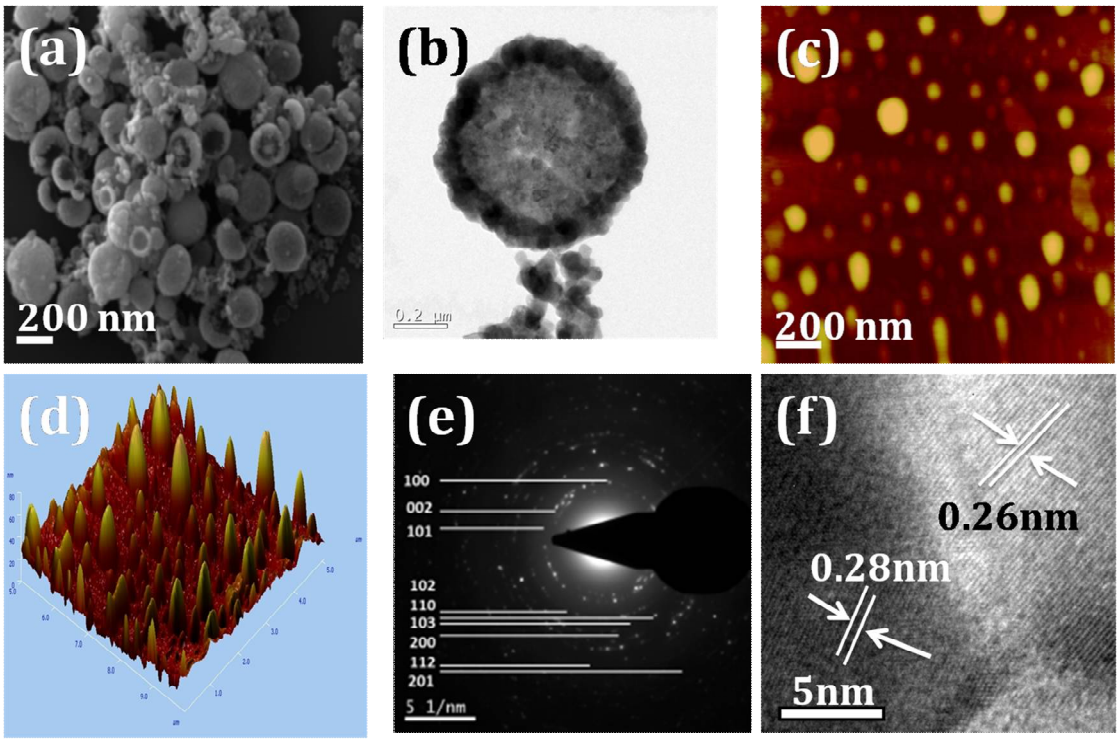

Figure 3.9. Microscopic images of ZB-800 at 800 °C (a) SEM, (b) TEM, (c) AFM, (d) AFM-3D image, (e) SAED and (f) HRTEM image

The energy dispersive x-ray spectra (EDS) of ZB-500, ZB-600, ZB-700, and ZB-800 are shown in Figure 3.10 (a–d), which confirmed the presence of various defects in the hierarachically formed ZnO multiple structures. The summary of atomic ratio of Zn/O is shown in the Table 3. 2. Presence of phosphorus was observed for samples ZB-500, ZB-600, ZB-700 and complete absence of phosphorus shown by sample ZB-800. It has been observed that as the calcination temperature increased, the stoichiometric ratio of zinc and oxygen showed variation revealing the formation of various defects in the formed hierarchical ZnO crystals. These observations were further strengthened during the Raman and optical property measurements.

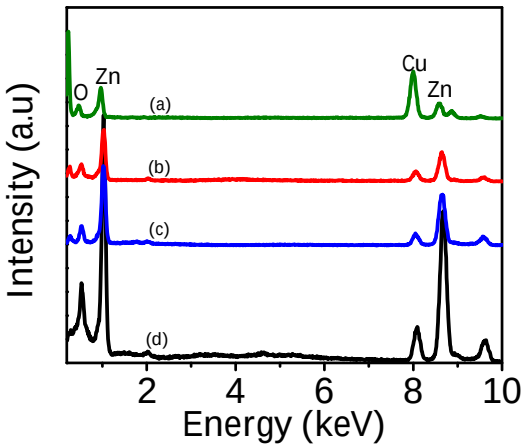

Calcination Temperature (°C)	Zn	O	P	Total
ZB-500	49.5	48.0	2.5	100.00
ZB-600	51.3	47.5	1.2	100.00
ZB-700	54.8	44.3	0.9	100.00
ZB-800	58.3	41.7	-	100.0

Figure 3.10. EDS spectra of ZBS with different calcination temperature (a) ZB-500,(b) ZB 600 (c) ZB-700 and (d) ZB-800. **Table 3.2.** Atomic ratio of zinc, oxygen and phosphorous

3.3.5. Particle Size and Zeta Potential Properties

Particle size distribution profiles of ZBS calcined at various temperatures are shown in Figure 3.11(a–e). ZBS showed a narrow particle size distribution with a z-average of 395 nm. While the calcination temperature was increased from 500 to 800 °C, the particle size of ZnO crystal exhibited broad distribution profile, and also

it showed fluctuation due to formation of multiple hierarchical structures. The particle size of the ZnO is observed to vary from 525, 650, 532, and 712 nm when calcination temperature increased as of 500, 600, 700, and 800°C, respectively. Zeta potential of ZnO nanoparticles were measured as +20, +18.0, +4.6, +3, and −9.5 mV for ZBS, ZB-500, ZB-600, ZB-700, and ZB-800, respectively. Except for ZB-800, all the samples have shown a positive zeta potential value due to anchoring of PO_4^{2-} on the surface of ZnO crystals. However, ZB-800 showed a negative zeta potential attributed to the complete removal of phosphate anchored hydrozincite from the surface of zinc oxide and also a small extent scission might have occurred in the Zn−O bond leading to a negative zeta potential value.[47] ZnO nanocrystals with low surface potential tends to aggregate via self-assembling into metastable structures. Formation of these hierarchical nano and micro self-assembled structures may favour photoinduced light reflection and hence improved broad absorption of solar spectrum. This will be discussed more in the ZnO crystal growth mechanism.

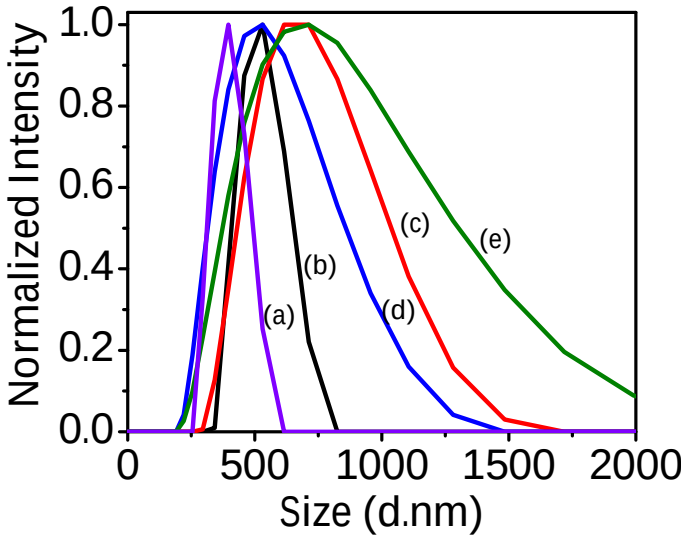

Figure 3.11. Dynamic light scattering (DLS) showing the effect of calcination temperature on the particle size distribution of (a) ZBS, (b) ZB-500, (c) ZB-600, (d) ZB-700, and (e) ZB-800

3.3.6. X-ray Diffraction Analysis

The crystalline phase and crystallite size of the hierarchically structured ZnO were analyzed using XRD. Figure 3.12(a–f) showed the XRD peaks of ZBS, ZB, ZB-500, ZB-600, ZB-700 and ZB-800. The ZBS showed peak at 2θ = 12.2°, 19.4°, 24.7°, 28.9°, 31.5°, 33.9°, 36.07°, 39.3°, and 40.1°, which can be indexed as the monoclinic phase of zinc oxide (JCPDS 19-1458).[48] ZB prepared in the absence of an anchoring agent showed the wurtzite form of the hexagonal phase (Figure 3.12b). It showed characteristic sharp signals at 2θ = 31.77°, 34.42°, 36.25°, 47.54°, 56.58°, 62.9°, 66.4°, 67.96°, and 69.1°. They were indexed by Miller indices as (100), (002), (101), (102), (110), (103), (200), (112), and (201) planes with d-spacing characteristic of a hexagonal wurtzite structure (JCPDS no. 36-1451). Effect of calcination temperature on the crystalline phase of ZBS studied by XRD, and the corresponding diffractograms of ZB-500, ZB-600, ZB-700, and ZB-800 are shown in Figure 3.12(c–f). All the samples exhibited a characteristic peak of zinc oxide with wurtzite hexagonal phase with variation in the intensity. The variations in the intensity are attributed to the change in the size and shape of ZnO nanoparticles. During the calcination process changes in the morphology occurred due to crystal growth through formation and reformation of various metastable structures and were confirmed by various microscopic observations. The crystalline sizes of the nanoparticles were calculated by the Debye–Scherrer formula.

$$d = 0.89\lambda / \beta \cos \theta$$

where λ is the wavelength of X-rays (λ = 1.5406 Å), β is the full width in radians at half-maximum (fwhm) of diffraction peaks, and θ is the Bragg angle of the X-ray pattern.

The average crystal sizes of the ZnO nanoparticles were calculated and it has been observed that as the calcination temperature increased, crystalline size of ZnO increased from 43 nm (500°C) to 62 nm (600°C). Further increasing the calcination temperature to 700°C, crystalline size decreased to 28 and 19 nm (800°C) revealing the organization and reorganization of the crystalline pattern. It also suggested that as the calcination temperature increased beyond 700°C, crystallite size decreases to form hierarchical structures which will favour for the formation of more porosity inside the structure. This enhancement in the porosity may favour induced light reflection and also high dye loading. This may favour increasing the photocurrent density in DSSC.

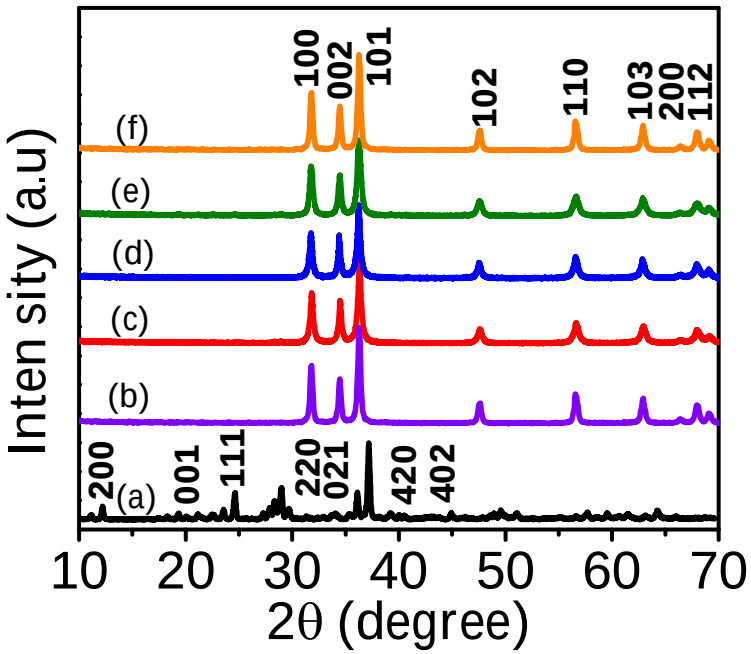

Figure 3.12. XRD pattern of (a) ZBS, (b) ZB, (c) ZB-500, (d) ZB-600, (e) ZB-700, and (f) ZB-800

3.3.7. Growth Mechanism

From Raman and photoluminescence spectroscopic results, it could be suggested that during the growth process, various types of defects are generated at the surface and interfaces of self-assembled hierarchical ZnO nanostructures to

form defect energy bands. These defect bands can facilitate the separation of charge carriers and enhance the open circuit voltage (V_{oc}) as well as improve the power conversion efficiency. The defect intensity and type of the defect change with the growth process. A deep level defect is prominent for ZB-500 and ZB-600, but the density of the deep level defects is low in ZB-700 and ZB- 800. In ZB-700 and ZB-800 oxygen and zinc interstitial is more dominant than that of ZB-500 and ZB-600. It is reported that the presence of high surface oxygen deficiencies in ZnO nanoparticles can become the electron capture center, which will reduce the recombination rate of electrons and holes and is expected to enhance the open circuit voltage (V_{oc}).[57] The mechanism for the formation of hierarchical aggregates of ZnO with multiple shapes during calcination could be established from the results obtained from XRD, SEM, and FFT patterns of HR-TEM as shown in Scheme 3.1.

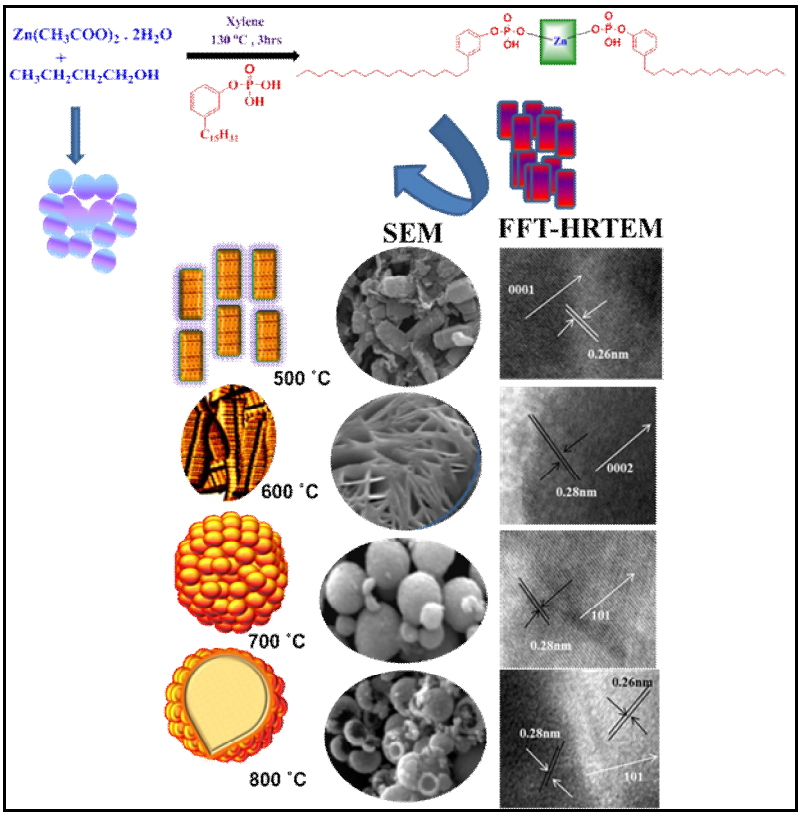

Scheme 3.1. Growth process showing the formation of hierarchical multiple structures of ZnO

It has been observed that ZnO crystals prepared in the presence of an anchoring agent showed nanobar-like morphology due to the growth process taking place through the [0001] plane which has a higher surface energy. In the presence of PDPPA, phosphate ions anchored on the positively charged Zn^{2+} ions by Coulombic force attraction, which further slowed down the crystal growth along the [0001] direction for ZB-500. Further self-assembly process through bilayer formation of the long alkyl chains also favours the formation of bar like morphology. ZBS particles calcined at 600 °C observed as sheet like morphology under various microscopic techniques (Figure 3.7). The FFT pattern of the HR-TEM image (Figure 3.7f) measured interlateral fringe spacing of 0.28 nm characteristic of the [002] plane. The XRD signal exhibited a hike in the intensity of the [002] plane, while the intensity of [001] remained intact suggesting that the growth process propagated through the [002] direction. This might be the fact that the phosphate ions anchored ZnO nanobars undergoing the growth process through oriented attachment sideways and self-assembled to form sub-microsheets aggregated inside a spherical envelope as shown in Figure 3.7. When the calcination temperature is increased to 700 °C, polydispersed microspherical particles were observed under various microscopic techniques (Figure 3.8). At 700 °C, the phosphate group may decompose, and the [101] plane may become more active and crystal growth may take place through the [101] plane to form polydispersed spherical particles. The XRD signal showed a hike in the signals corresponding to the [101] plane with a concomitant decrease in the [002] plane suggesting change in the direction of the crystal growth process. Results suggests that the formed nanosheeets were further self-assembled at a higher level due to lateral interactions to form hierarchical polydispersed microspheres for the minimization of total

energy of the system through the well-known growth mechanism of "oriented assembly".[41] Electrostatic interaction between the hydrophilic group of phosphate ions and the positive polar plane of ZnO surface randomly generates on the surface of the ZnO crystal. It will minimize their surface energy, which leads to modulation of the morphology of the formed ZnO during calcination and the formation of coarse on the surface. The FFT pattern under HRTEM showed interlateral fringe growing in the direction of the [101] plane. The observed variation in the particle size and zeta potential values also strengthened the above growth mechanism. The changes in the zeta potential can be ascribed to the variation in the surface energy of the crystal planes due to anchoring of the phosphate ions and removal of the same followed by the change in the direction of the growth process during calcination at high temperature. Further increase in the temperature to 800°C showed the formation of hollow microspheres with walls made up of hierarchically arranged edge to edge etched nanospheres. This can be due to the complete removal of the phosphate group at 800°C and the hollow interior structure was formed by dissolution of the nanoparticles in the interior metastable spheres through an Ostwald ripening process on prolonged heating.

3.3.8. Photoanode in DSSC

The role of hierarchical multiple structures of ZnO as photoanode in DSSCs were studied using N719 dye as photosensitizer. Figure 3.13A(a-d) shows the typical current density versus voltage curves of DSSCs with the prepared hierarchical ZnO nanostructures of ZB-500, ZB-600, ZB-700, and ZB-800, which were illuminated under AM 1.5G sunlight with a power density of 100 mW cm^{-2}. Five cells were fabricated for each sample, and an average standard deviation value was mentioned. The detailed parameters such as the short-circuit current density

(J_{sc}), the open circuit voltage (V_{oc}), the fill factor (FF), power conversion efficiencies (PCE), and thickness of the cells are summarized in Table 3.3. It has been observed that open circuit voltage increased in the order 715 mV, 784 mV, 835 mV and 861 mV for ZB-500, ZB-600, ZB-700, and ZB-800, respectively. Short circuit current density varied as 5.86 mA/cm^2, 7.39 mA/cm^2, 7.84 mA/cm^2, and 13.7 mA/cm^2 for ZB-500, ZB-600, ZB-700, and ZB-800, respectively. PCE calculated as 2.7 ± 0.3%, 3.6 ± 0.6%, 4.5 ± 0.3%, and 5.3 ± 0.5% for ZB-500, ZB-600, ZB-700, and ZB-800. The variation in the open circuit voltage is due to the defect state density variations in the hierarchical structures of ZnO since it is determined by the energy difference between the quasi Fermi level of the semiconductor and the redox potential of the electrolyte.[58] The short circuit current density and PCE are observed to be in the order ZB-500 < ZB-600 < ZB-700 < ZB-800. The reason for the improved PCE for ZB-800 might be arising from the excellent optical absorption and improved molar extinction coefficient. ZB-800 consists of nano and submicron sized spherical particles that are aggregated to form hierarchical polydisperse hollow structures with a crystal size of 19 nm. These polydispersed hollow structures induce the multiple reflection of incident photon inside the closed loops and lead to the absorption of light at the higher wavelength as well as improve the electron diffusion length. But in the case of ZB-700 polydispersed spheres were observed with a crystal size of 28 nm, which will provide effective light scattering of incident photon but less PCE than ZB-800.

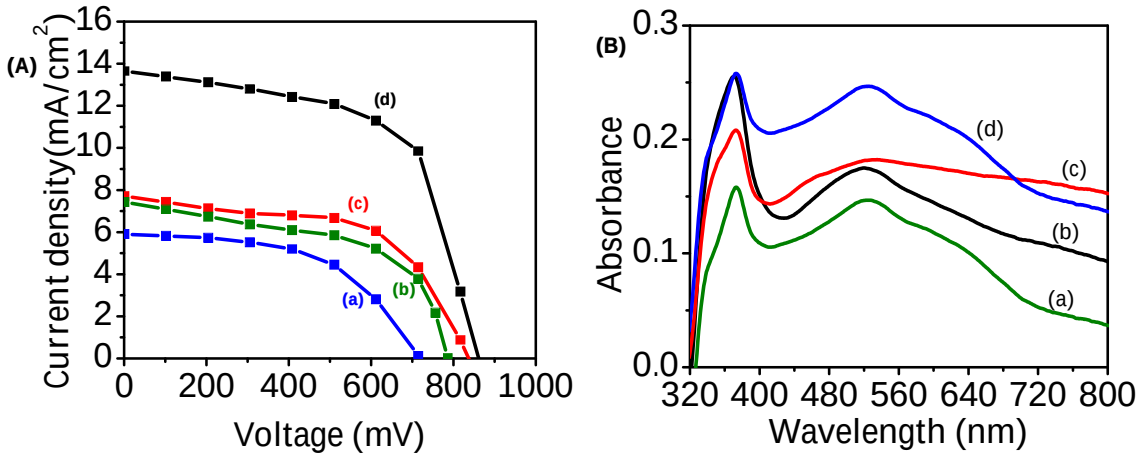

Figure 3.13. (A) I–V curves of the DSSC measured under one sun illumination (AM 1.5G, 100 mW cm^{-2}) (a) ZB-500, (b) ZB-600, (c) ZB-700, and (d) ZB-800; **(B)** film state UV–visible absorption spectra of dye desorbed films of (a) ZB-500, (b) ZB-600, (c) ZB-700, and (d) ZB-800

Figure 3.13(B) shows UV–visible absorption spectra of dye desorbed films ZB-500, ZB-600, ZB-700, and ZB-800. The amount of adsorbed dye was determined from the optical spectra. Molar extinction coefficient was calculated to be 8.04 × 10^4 dm^3 mol^{-1} cm^{-1}, 9.88 × 10^4 dm^3 mol^{-1} cm^{-1}, 10.4 × 10^4 dm^3 mol^{-1} cm^{-1}, and 10.8 × 10^4 dm^3 mol^{-1} cm^{-1} for ZB-500, ZB-600, ZB-700, and ZB-800, respectively. The amount of dye loading can be greatly influenced by the porosity of the crystals and also the size of crystallites. It is observed that polydispersed hollow structures (ZB-800) are endowed with small crystallite size and porosity could contribute to adsorption of a higher amount of dye. The high density of defect band present in the ZB- 800 also facilitates efficient electron hole pair separation. Thus, the reason for the improved PCE for ZB-800 arises from the excellent optical absorption of light and as well as generation of more excitons. Moreover, the polydispersed multiple structures may enhance the amount of light absorption by light induced multiple reflection mechanism as reported by other researchers.[27]

Table 3.3. Performance characteristics of DSSC

Sample Code	V_{oc} (mV)	J_{sc} (mA/cm²)	Fill Factor (%)	Efficiency (%) (average ± standard deviation)	Film thickness (μm)
ZB-500	715	5.86	54.86	2.72±0.03	10
ZB-600	784	7.39	69.53	3.64±0.06	10
ZB-700	835	7.84	72.91	4.51±0.03	10
ZB-800	861	13.7	76.32	5.34±0.05	10

3.4. Conclusion

In summary, hierarchical multiple structures of zinc oxide were prepared successfully using a bioanchoring sol–gel process with controlled shapes of bars, sheets, polydispersed spheres, and hollow spheres with nano-submicro aggregates by calcination at different temperatures. Growth mechanism for the formation of various structures was proposed from the results obtained by microscopic and XRD analyses. Various defect state such as oxygen vacancies and zinc interstitials in the prepared ZnO manifested from the results observed from Raman, photoluminescence spectroscopy, and EDS analysis. DSSCs were fabricated using the prepared ZnO as photoanodes. Polydispersed ZnO hollow spheres exhibited a higher PCE of 5.3% with a J_{sc} of 13.7 mA cm^{-2}, V_{oc} of 861 mV, and FF of 76.3%. The hierarchical aggregates with small crystallite size and high porosity could increase the optical absorption edges and also high dye loading, which favour improved PCE.

3.5. Experimental Section

3.5.1. Materials

Zinc acetate dihydrate $Zn(AcO)_2 \cdot 2H_2O$, phosphorus pentoxide, and butanol were purchased from Sigma-Aldrich, India. Xylene and all solvents were of analytical grade purchased from s.d. Fine Chem Limited, Mumbai, India. Cardanol (3-pentadecyl phenol) was obtained by the double distillation of cashew nut shell liquid (Cashew Export Promotion Council, India). Cis-bis(isothiocyanat)bis(2,2′-bipyridyl-4,4′-dicarboxylate)ruthenium(II) bis tetra butyl ammonium (N719) and Platisol T were purchased from Solaronix SA, Switzerland. Electrolyte EL-HPE was purchased from Dyesol, Australia.

3.5.2. Preparation of 3-Pentadecylphenylphosphoricacid (PDPPA)

A total of 60 mL of 3-pentadecyl phenol (0.3 mol) and 600 mL of dry hexane were taken in a round bottomed flask and kept for stirring. 18 grams of phosphorous pentoxide (0.0634 mol) was added slowly to the stirred solution. The reaction was continued for 6h at 80–85°C. The pyrophosphate formed was hydrolyzed with dil. HCl, and then it was filtered and dried under a vacuum at 80 °C for 6 h. Detailed characterization of PDPPA was reported earlier from our group.[44]

3.5.3. Preparation of zinc oxide

Zinc oxide was prepared by the acid catalyzed esterification of zinc acetate dihydrate ($Zn(AcO)_2 \cdot 2H_2O$) in butanol followed by calcination at different temperatures. In a typical procedure, 0.173 g (0.45 mmol) of PDPPA was dissolved in a mixture of m-xylene (25 mL) and butanol (50 mL). A total of 3.29 g (14.9 mmol) of zinc acetate was added to the above solution, and the mixture was refluxed for 1 h. The solution turned into a milky suspension, and the white precipitate formed was separated by centrifugation at 2500 rpm for 10 min. Then it was rinsed with

distilled water and ethanol. The solvent was evaporated under reduced pressure at 40 °C to obtain zinc oxide nanoparticles (ZBS). ZnO also prepared in the absence of PDPPA was designated as ZB. Further, the prepared ZBS was calcined under various temperatures such as 500, 600, 700, and 800 °C. They are designated as ZB-500, ZB-600, ZB-700, and ZB-800, respectively. Experimental details of preparation of hierarchical ZnO nanostructures are given in Table 3.4.

Table. 3.4. Experimental details of the preparation of hierarchical ZnO nanostructures

Sample Code	Zinc acetate dihydrate (mmol)	PDPPA (mmol)	Calcination temperature (^oC)
ZBS	14.9	0.45	-
ZB-500	14.9	0.45	500
ZB-600	14.9	0.45	600
ZB-700	14.9	0.45	700
ZB-800	14.9	0.45	800

3.5.4. Fabrication of Devices

A conductive FTO plate was washed with soap solution, ethanol, and acetone. It was finally rinsed with isopropyl alcohol and air-dried for 15 min. Parallel edges of each substrate were covered with scotch tape to control the thickness of the film. We made a viscous paste of ZnO in ethanol and cast it into film using a doctor blade and kept it for slow evaporation of the solvent at room temperature for 1 h. Then it was kept in the oven at 60 °C for 30 min for the complete removal of the solvent to form a smooth thin film. Later, this film was immersed in a 0.5 mM cis-bis-(isothiocyanato)bis(2,2′-bipyridyl−4,4′-dicarboxylate)-ruthenium(II) bis tetra butyl

ammonium (N719) solution in ethanol and kept for 6h at room temperature. Desorption of the dye was performed by dipping the dye absorbed film in a aqueous solution containing 0.1 M NaOH and later the solvent was evaporated off and the respective spectra were recorded. Pt counter electrode was prepared on the FTO glass using a platisol T solution, followed by heating at 400 °C for 15 min in air. The active area of dye-coated ZnO film was measured as 0.25 cm^2. Dried film and counter electrolyte attached together through which electrolyte was injected into the cell from the edges by capillarity action. The current–voltage characteristics were measured by using a Keithley 2440 source meter under simulated AM 1.5 G one sun 100 mW cm^{-2} illumination provided by a solar simulator Newport 69911.

3.6. Characterization Techniques

Description of FT-IR, XRD, DLS, zeta potential and HR-TEM are given in Section 2.6 of Chapter 2. Details of UV-visible absorption spectra of the ZnO were studied by dispersing the sample in distilled water and recorded spectra using UV-visible spectrophotometer (Shimadzu model 2100) in the range of 200–900 nm. The photoluminescence spectra were recorded on a SPEX-Flourolog F112X spectro fluorimeter using a front face sample holder. Raman confocal microscope analyses of ZnO sample were done using WITec alpha 300R. Raman confocal microscope equipped with a 100× oil immersion objective and 300/600 grooves/nm grating. A CCD detector operating at room temperature was used as detector. A 785/532 nm laser source was used for excitation.SEM measurements of samples were performed by subjecting the samples to thin gold coating using a Zesis EVO 18 cryo SEM special Edn with variable pressure working at 20–30 kV. Atomic force microscopic images were recorded under ambient conditions using a NTEGRA (NT-MDT) operating with a use tapping mode regime. Micro fabricated TiN cantilever tips (NSG10) with

a resonance frequency of 299 kHz and a spring constant of 20–80 N m^{-1} were used. Samples for the imaging were prepared by drop casting the ZnO solution on cover slip. Thermal stability measurements were performed at a heating rate of 10 °C/min in nitrogen atmosphere using Schimadzu, DTG-60 equipment.

3.7. References

1. B. Oregan and M. Gratzel, *Nature* **1991**, *353*, 737.

2. M. J. Gratzel, *Sol Gel Sci. Technol*. **2001**, *22*, 7.

3. B. V. Bergeron, A. Marton, G. Oskam and G. J. Meyer, *J. Phys. Chem. B.* **2005**, *109*, 937.

4. M. Saito and S. Fujihara, *Energy Environ. Sci*. **2008**, *1*, 280.

5. K. Sayama, H. Sugihara and H. Arakawa, *Chem. Mater*. **1998**, *10*, 3825.

6. J. J. Wu and C. S. Liu, *Adv. Mater*. **2002**, *14*, 215.

7. X. Zhou, S. Chen, D. Zhang, X. Guo, W. Ding and Y. Chen, *Langmuir* **2006**, *22*, 1383.

8. Y. Yan, P. Liu, J. G. Wen, B. To and M. M. Al Jassim, *J. Phys.Chem. B.* **2003**, *107*, 9701.

9. J. X. Wang, C. M. L. Wu, W. S. Cheung, L. B. Luo, Z. B. He, G. D. Yuan, W. J. Zhang, C. S. Lee and S. T. Lee, *J. Phys. Chem.* **2010**, *114*, 13157.

10. L. H. Zhao and S. Q. Sun, *CrystEngComm*. **2011**, *13*, 1864.

11. A. F. Kohan, G. Ceder, D. Morgan, G. Van and D. Walle, *Phys. Rev. B.* **2000**, *61*, 15019.

12. J. Ferber and J. Luther, *Sol. Energy Mater. Sol. Cells.* **1998**, *54*, 265.

13. A. Usami, *Sol. Energy Mater. Sol. Cells.* **2000**, *64*, 73.

14. G. Rothenberger, P. Comte and M. Gratzel, *Sol. Energy Mater. Sol. Cells.* **1999**, *58*, 321.

15. S. Zhu, X. Chen, F. Zuo, M. Jiang, Z. Zhou and D. Hui, *J. Solid State Chem.* **2013**, *197*, 69.

16. S. H. Ko, D. Lee, H. W. Kang, K. H. Nam, J. Y. Yeo, S. J. Hong, C. P. Grigoropoulos and J. H. Sung, *Nano Lett*. **2011**, *11*, 666.

17. W. T. Jiang, C. T. Wu, Y. H. Sung and J. J. Wu, *ACS Appl. Mater. Interfaces.* **2013**, *5*, 911.

18. X. H. Lu, Y. Z. Zheng, S. Q. Bi, Y. Wang, X. Tao, L. Dai and J. F. Chen, *Adv. Energy Mater*. **2014**, *4*, 1301802.

19. J. A. Anta, E. Guillen and R. T. Zaera, *J. Phys. Chem. C.* **2012**, *116*, 11413.

20. E. Guillen, L. M. Peter and J. A. Anta, *J. Phys. Chem. C.* **2011**, *115*, 22622.

21. A. Ajayaghosh, *Chem. Soc. Rev*. **2003,** *32*, 181.

22. J. Eldo and A. Ajayaghosh, *Chem. Mater*. **2002**, *14*, 410.

23. K. Graf, M. A. Rahim, S. Das and M. Thelakkat, *Dyes Pigm*. **2013**, *99*, 1101.

24. F. Xu, M. Dai, Y. Lu and L. Sun, *J. Phys. Chem. C.* **2010**, *114*, 2776.

25. E. Guillen, E. Azaceta, A. V. Poot, J. Idigoras, J. Echeberria, J. A. Anta and R. T. Zaera, *J. Phys. Chem. C.* **2013**, *117*, 13365.

26. Y. Shi, K. Wang, Y. Du, H. Zhang, J. Gu, C. Zhu, L. Wang, W. Guo, A. Hagfeldt, N. Wang and T. Ma, *Adv. Mater*. **2013**, *25*, 4413.

27. C. X. He, B. X. Lei, Y. F. Wang, C. Y. Su, Y. P. Fang and D. B. Kuang, *Chem. Eur. J.* **2010**, *16*, 8757.

28. N. Memarian, I. Concina, A. Braga, S. M. Rozati, A. Vomiero and G. Sberveglieri, *Angew. Chem. Int. Ed*. **2011**, *50*, 12321.

29. M. Saito and S. Fujihara, *Energy Environ. Sci*. **2008**, *1*, 280.

30. F. Xu, and L. Sun, *Energy Environ. Sci*. **2011**, *4*, 818.

31. M. Vafaee and M. S. Ghamsari, *Mater. Lett*. **2007**, *61*, 3265.

32. C. Yan and D. Xue, *J. Phys. Chem. B*. **2006**, *110*, 11076.

33. C. Fauteux, R. Longtin, J. Pegna and D. Therriault, *Inorg. Chem*. **2007**, *46*, 11036.

34. X. Y. Kong and Z. L. Wang, *Nano Lett*. **2004**, *3*, 1625.

35. C. J. Lee, T. J. Lee, S. C. Lyu, Y. Zhang, H. Ruh and H. Lee, *J. Appl. Phys. Lett*. **2003**, *81*, 3648.

36. T. Ghoshal, S. Kar and S. Chaudhuri, *Cryst. Growth Des*. **2007**, *7*, 136.

37. J. Y. Park, I. O. Jung, J. H. Moon, B. T. Lee and S. S. Kim, *J. Cryst. Growth*. **2005**, *282*, 353.

38. H. Tang, J. C. Chang, Y. Shan and S. T. Lee, *J. Phys. Chem. B*. **2008**, *112*, 4016.

39. Z. Li, A. Shkilnyy and A. Taubert, *Cryst. Growth.Des*. **2008**, *8*, 4526.

40. E. Azaceta, J. Idigoras, J. Echeberria, A. Zukal, L. Kavan, O. Miguel, H. J. Grande, J. A. Anta and R. T. Zaera, *J. Mater. Chem. A*. **2013**, *1*, 10173.

41. S. Zhu, X. Tian, J. Chen, L. Shan, X. Xu and Z. Zhou, *J. Phys. Chem. C*. **2014**, *118*, 16401.

42. R. Gao, Y. Cui, X. Liu, L. Wang and G. Cao, *J. Mater. Chem. A*. **2014**, *2*, 4765.

43. A. Usami, *Chem. Phys. Lett*. **1997**, *277*, 105.

44. J. D. Sudha and T. S. Sasikala, *Polymer* **2007**, *48*, 338.

45. Z. Xingfu, H. Zhaolin, F. Yiqun, C. Su, D. Weiping and X. Nanping, *J. Phys. Chem. C.* **2008**, *112*, 11722.

46. X. Liu, J. Zhang, L. Wang, T. Yang, X. Guo, S. Wu and S. Wang, *J. Mater. Chem*. **2011**, *21*, 349.

47. H. Usui, *J. Phys. Chem. C*. **2007**, *111*, 9060.

48. H. Zhang, R. Wu, Z. Chen, G. Liu, Z. Zhang and Z. Jiao, *CrystEngComm*. **2012**, *14*, 1775.

49. T. C. Damen, S. P. Porto and B. Tell, *Phys. Rev.* **1966**, *142*, 570.

50. H. M. Cheng, K. F. Lin, H. C. Hsu, C. J. Lin, L. J. Lin and W. F. Hsieh, *J. Phys. Chem. B.* **2005**, *109*, 18385.

51. X. L. Xu, S. P. Lau, J. S. Chen, G. Y. Che and B. K. Tay, *J. Cryst. Growth.* **2001**, *223*, 201.

52. H. Zeng, G. Duan, Y. Li, S. Yang, X. Xu and W. Cai, *Adv.Funct Mater*. **2010**, *20*, 561.

53. A. B. Djurisic and Y. H. Leung, *Small* **2006**, *2*, 944.

54. S. Gao, H. Zhang, X. Wang, R. Deng, D. Sun and G. Zheng, *J. Phys. Chem. B.* **2006**, *110*, 15847.

55. M. M. Demir, R. M. Espi, I. Lieberwirth and G. Wegner, *J. Mater. Chem.* **2006**, *16*, 2940.

56. P. P. Das, S. A. Agarkar, S. Mukhopadhyay, U. Manju, S. B. Ogale and P. S. Devi, *Inorg. Chem*. **2014**, *53*, 3961.

57. J. L. Yang, S. J. An, W. I. Park, G. C. Yi and W. Y. Choi, *Adv. Mater*. **2004**, *16*, 1661.

58. X. Feng, K. Shankar, M. Paulose and C. A. Grimes, *Angew. Chem*. Int. Ed. **2009**, *48*, 8095.

Chapter 4

Non-volatile Bistable Memory Devices Based on Semiconducting Polyvinylcarbazole Zinc oxide Nanocomposites

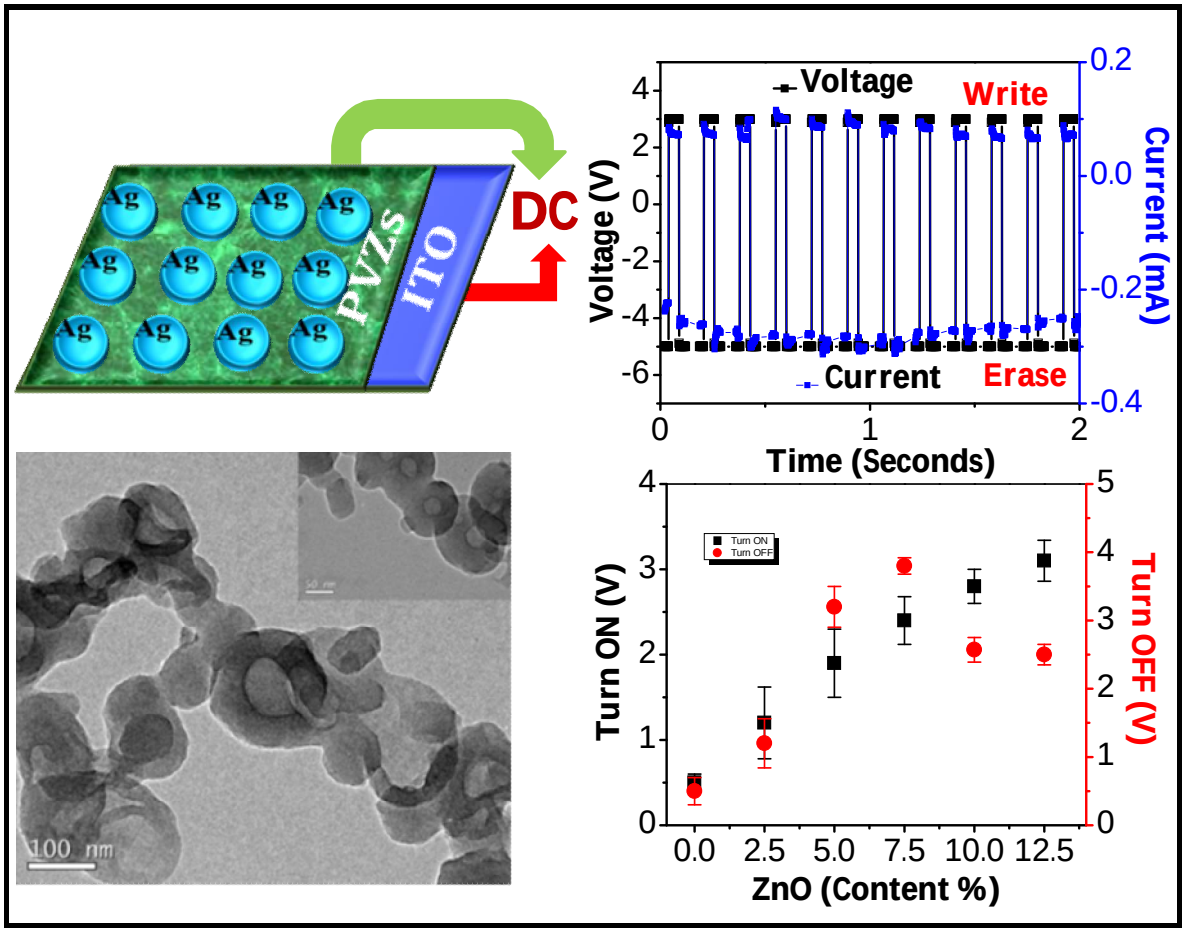

4.1. Abstract

This chapter describes the development of semiconducting polyvinylcarbazole-zinc oxide nanocomposites (PVZs) comprising electron donor carbazole moiety (p-type) and electron acceptor zinc oxide (n-type) through a facile strategy and demonstrated its application as an active layer in the fabrication of non-volatile memory device. Effect of zinc oxide on the various properties were evaluated by UV-visible absorption, photoluminescence, Raman, FT-IR, XRD, SEM, HR-TEM, and AFM. PVZs exhibited good solubility in dichlorobenzene and memory devices were fabricated by sandwiching PVZs nanocomposites between indium tin oxide and silver electrode (ITO/PVZ/Ag). By fitting the data to various charge transport models, the conduction mechanisms of the device were proposed as Ohmic, Poole–Frenkel emission, and trap filled space charge limited conduction that depends on the applied voltage. Endurance performances of the devices were stable for more than 100 cycles with ON/OFF current ratio of 5.2×10^3 and retention time of 10^5 seconds.

4.2. Introduction

Recently, there is growing interest in the investigation of resistive switching memory for the demand of next-generation information and communication technology with high speed, low operation voltage, and high integration density.[1–4] Electrical resistive memory devices based on nanocomposites are gaining much attention since they exhibit significant advantages over inorganic semiconductor based memory devices.[5–7] This includes low fabrication cost, printability, good scalability, mechanical flexibility, simple device structures, and high ON/OFF ratio. The electrical resistive switching device is a simple metal–insulator–metal structure

with an active layer sandwiched between two electrodes and the resistance of the active layer is changed by applying a bias, constituting the set and reset states of the device. Ideally, the device at the low conductivity state (OFF) is switched by a threshold voltage to a high conductivity state (ON) and the two states of bistable device differ in their conductivity by several orders in magnitude, retaining a remarkable stability. More importantly, the high and low conductivity states of the device can be precisely controlled by applying a positive voltage pulse to write or a negative voltage pulse to erase, respectively. Polymeric materials that exhibit resistive switching characteristics include functional polyimides,[8,9] conjugated polymers,[10,11] and polymer nanocomposites comprising conductive particles such as metal nanoparticles,[12,13] fullerene,[14] and graphene oxide[15] and so forth. In comparison to inorganic memory technologies, devices based on the blend of polymeric materials with inorganic nanoparticles show the potential tuning of overall physico-chemical properties. [16]

Conducting polymers such as polyaniline,[17] polythiophene,[18] and polyvinylcarbazole[19] are gaining much attention because of their ease of preparation, processing, good optoelectronic properties, and they find applications in organic field effect transistor,[20] light-emitting diode,[21] and memory devices.[22,23] Among the conducting polymers, PVK is one of the most widely utilized materials for memory device application since it exhibits interesting properties such as good environmental stability, operation stability, easy processability and unique electro-optical properties.

Several semiconducting metal oxide nanoparticles are used in resistive switching application such as ZnO, NiO, HfO_2 and MnO_2.[24-27] ZnO has been

particularly attractive due to its novel physical properties, large exciton binding energies, excellent chemical stabilities, nontoxicity, low cost, and various crystal defects.[28] However, hierarchical ZnO nanostructures are promising material for resistive random access memory because of non-volatility, fast programming, small bit cell size and low power consumption. [29] The crystal defects in the metal oxide also play a significant role in memory switching. When an electric field is applied to these devices, the defects align along with the electric field to form tiny conducting filaments in the low conductivity state. These tiny conducting filaments are combined together to form stronger and more conducting filaments which leads to the transition from low current state to the high conductive state.[30] To generate the filaments in the forming process, the diffusion of the ions or the electro-migration of the defects are essential. It is known that extended defects, such as grain boundaries and dislocations, provide easy diffusion paths for oxygen or metal ions in metallic oxides.[31] Point defects, such as oxygen vacancies or metallic ions, are easy to form and gather around the grain boundaries. Recently *Pan et al*. reviewed a comprehensive summary of the development of memory materials, important switching mechanisms, and performance of restive switching memory devices.[32]

In nanocomposite-based memory devices, the electrical bistability originates from a combination of intriguing conduction mechanisms shown by inorganic semiconducting materials with conducting polymers such as formation of conducting filaments, formation of charge transfer complexes, [33] charge-trapping and so forth.[34–38] Thus, in this context development of memory devices with an active material composed of p–n junction that creates depletion regions at the interfaces receives attention in recent years. *Onlaor et al*. reported

polyvinylpyrrolidone-zinc oxide hybrid composite with a device configuration of (Al/PVP-ZnO/ITO) exhibited ON/OFF current of 10^{3}.[12] *Wu et al*. reported ZnO-based memory device with a configuration Pt/ZnO/Pt having ON/OFF current ratio of 10^{3}.[30] Literature revealed that ON/OFF ratio can be improved by enhancing the number of charge carriers present in the active layer. In the present work, we have adopted low cost facile strategy for preparation of non-volatile bistable memory device by polyvinylcarbazole-ZnO composite system as the active layer. The porous self-assembled hierarchical ZnO nanostructures having various defects were prepared using bio-anchoring strategy as reported in the previous Chapter 3. These hierarchical ZnO structures (n-type) will be expected to play a significant role in improving the ON/OFF current ratio of device due to large surface area which acts as a major role in memory switching. Apart from this, the presence of PVK in the nanocomposites expected to prevent the aggregation of ZnO particles, reduce the charge loss, current leakage, and also solution processable. Also the formation of p–n junction will be expected to improve the switching and ON/OFF resistance state with narrow sweeping voltage.

Hence, this chapter describes the preparation and characterization of PVZs nanocomposite by oxidative emulsion polymerization of vinyl carbazole in the presence of ZnO at room temperature. The bistability behavior of memory device was performed by varying the ZnO content in the nanocomposites. By fitting the data to the various charge transport models, the conduction mechanisms of the device were proposed. The retention time and the endurance of the memory devices (ITO/PVZ/Ag) also have been studied in this chapter.

4.3. Results and Discussion

4.3.1. Preparation of Nanocomposite

PVZs nanocomposites were prepared by oxidative emulsion polymerization of vinylcarbazole and zinc oxide using ferric chloride anhydrous as oxidative initiator at room temperature as shown in Scheme 4.1. Nanocomposites with the various composition of ZnO were prepared under same condition and designated as PVZ1, PVZ2, PVZ3, PVZ4 and PVZ5. Products were isolated and purified as explained in the experimental section.

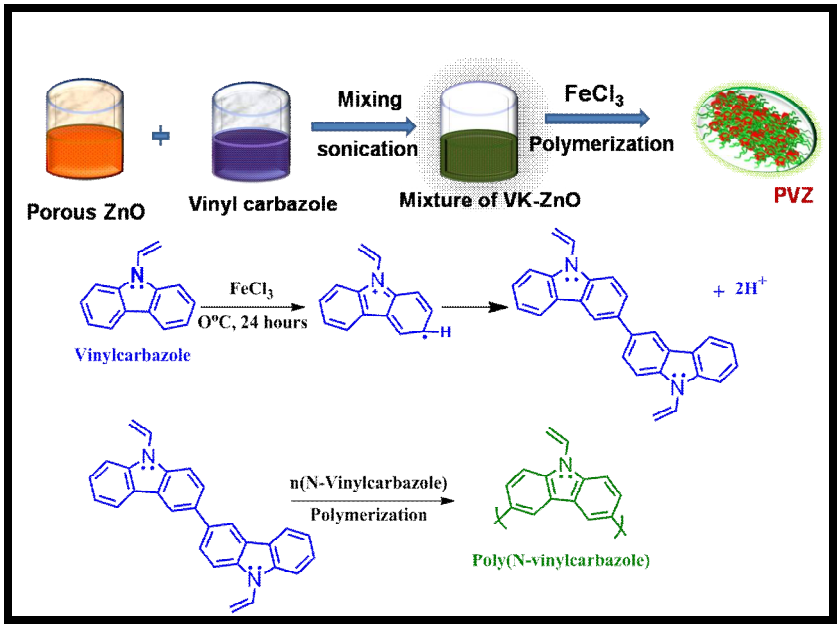

Scheme 4.1. Preparation of PVZs nanocomposites

4.3.2. Optical and Photoluminescence Spectral analysis

The UV-visible spectrum of the PVK, PVZ1, PVZ2, and PVZ3 nanocomposites in chloroform are shown in Figure 4.1(a–d), respectively. Figure 4.1a exhibited distinct bands at 294, 330, and 342 nm assigned to the π–π* and n–π* band of the carbazole moieties.[39] Figure 4.1b showed bands at 294, 330, and 342 nm which are similar to that of PVK with an enhancement in the band intensity. On further

increasing the ZnO content in nanocomposites, the characteristic bands of PVK showed a red shift in their wavelength. PVZ2 exhibited band maxima at 294 and 345 nm and PVZ3 exhibited the major bands at 306 and 347 nm as shown in Figure 4.1 (c and d). Similarly PVZ4 showed band maxima at 308 and 349 nm and PVZ5 exhibited band maxima at 312 and 354 nm, respectively. The red shift observed in the band maxima for PVZ2, PVZ3, PVZ4 and PVZ5 may be attributed to the interaction between the PVK and ZnO[40] and is further supported by the studies made by FT-IR, Raman and XRD analysis.

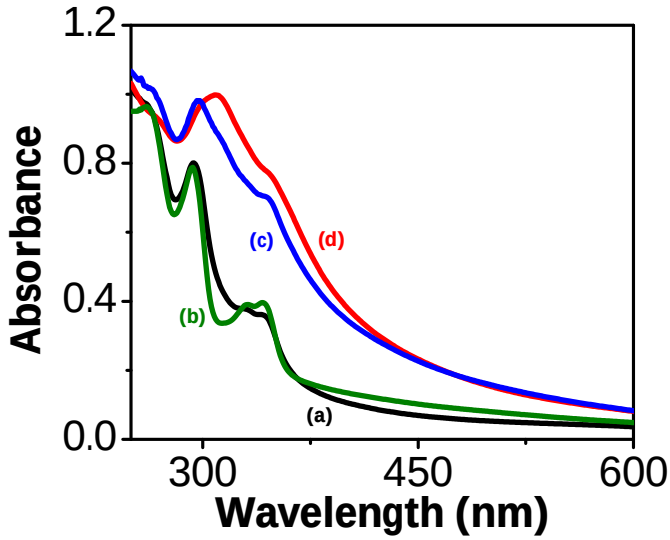

Figure 4.1. UV-visible spectrum of (a) PVK (b) PVZ1 (c) PVZ2 and (d) PVZ3

Photoluminescence (PL) spectra of the PVK, PVZ1, PVZ2, and PVZ3 nanocomposites are shown in Figure 4.2(a–d). Figure 4.2a shows PL spectra of PVK taken an excitation wavelength of 294 nm, which showed broad emission band in the range of 370–500 nm. [41] The maximum of the PL were observed at 470 and 430 nm with a shoulder peak at 377 nm. The emission bands at 377 and 430 nm correspond to the totally eclipsed conformation of the carbazole groups in which carbazole groups are aligned face to face in adjacent position along the polymer

backbone. The band at 470 nm corresponds to the partially overlapped excimer. PL spectra of PVZ1, PVZ2, and PVZ3 are shown in Figure 4.2(b–d) which is excited at the wavelength of 294 nm. Emission maximum of PVZ1 appeared a broad emission at 432–465 nm with shoulder emission at 377 nm. PVZ2 exhibited emission maxima at 376, 428, and 472 nm similar to that of PVZ1 with drastic quenching of fluorescence intensity. In the case of PVZ3, PVZ4 and PVZ5 the weak emission at 375 nm and broad emission maxima at 420–482 nm were observed. The shift in the higher wavelength (10 nm) in emission spectra of PVZ3 due to effective electron transfer between the PVK (electron donor) and ZnO (electron acceptor) to form p–n junction interface and also broadening of emission band due to the increasing interaction among the carbazole groups.[40]

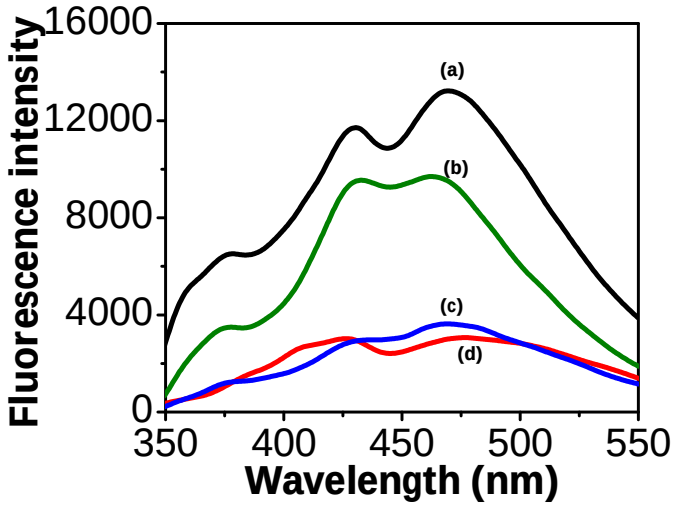

Figure 4.2. Photoluminescence spectra of (a) PVK (b) PVZ1 (c) PVZ2 and (d) PVZ3

The broading and shift in the wavelength of PVZs in emission spectra was further confirmed by measuring the electrochemical band gap. HOMO–LUMO values for PVK and PVZs were calculated by cyclic voltammetry. The HOMO values are as follows for PVK (-5.8 eV), PVZ1 (-5.84 eV), PVZ2 (-5.76 eV), PVZ3 (-5.72 eV), and LUMO values for PVK (-2.2 eV), PVZ1 (-2.3 eV), PVZ2 (-2.24 eV), PVZ3 (-2.16 eV),

respectively. The band gap calculated from electrochemical studies showed that it is gradually reduced with increasing ZnO contents in the nanocomposites which has found to be 3.6, 2.3, 2.24, 2.16, 2.04 and 1.96 eV for PVK, PVZ1, PVZ2, PVZ3,PVZ4 and PVZ5 respectively. This effective reduction of band gap favours for fast transfer of electron from PVK to ZnO .[39]

4.3.3. Raman Spectral Analysis

Raman spectra were measured using 633 nm Ar^+ laser line at room temperature. Figure 4.3 (a–d) shows the Raman spectra of the ZnO, PVZ1, PVZ2, and PVZ3. Figure 4.3a showed the Raman spectrum of ZnO has been already discussed in Section 3. 3. 3 of Chapter 3.

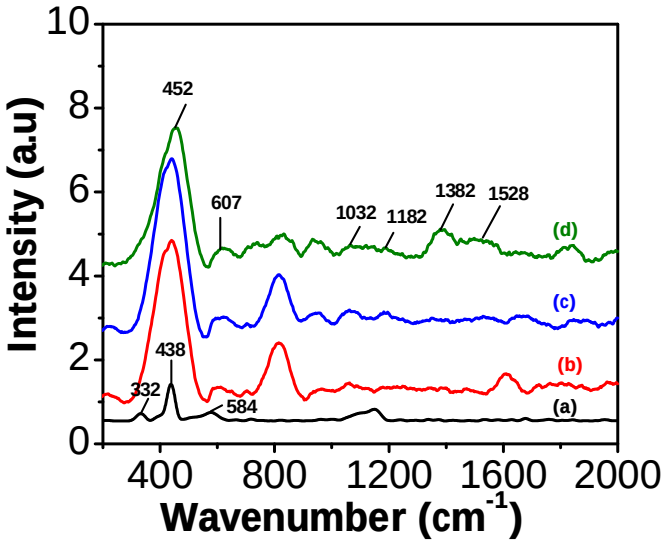

Figure 4.3. Raman spectra of (a) ZnO (b) PVZ1 (c) PVZ2 and (d) PVZ3

In PVZ1 (Figure 4.3b), the observed intense band at 438 cm^{-1} corresponds to the characteristic band of ZnO in hexagonal wurtzite phase. The broad and weak bands at 590 cm^{-1} were assigned to the formation of defects such as oxygen vacancy in the zinc oxide. Further, we have observed peaks at 1053, 1183, 1246, 1394, 1470, 1554, and 1610 cm^{-1} due to vibration modes of PVK such as C–H deformation in benzene

rings, rocking of methylene in polyvinyl, ring vibration, quinoid C–C stretching, C–N stretch, symmetric CH_2 stretch, asymmetric CH_2 stretch, and CH–CH_2 stretching,[42] respectively. Similar observations were made in PVZ2, PVZ3, PVZ4 and PVZ5. Details of shift in the wavenumber of ZnO, PVZ1, PVZ2, and PVZ3 are given in Table 4.1. It has been observed that PVZs exhibited slight shifts in the vibration modes compared to ZnO substantiating the interaction between ZnO and PVK in nanocomposites.[43]

Table 4.1. Details of shift in the wavenumber of ZnO, PVK, PVZ1, PVZ2 and PVZ3

Sample	Wavenumber (cm^{-1})
ZnO	332,438,583
PVK	1183, 1246, 1394, 1470 and 1554
PVZ1	438,590,1057, 1175, 1346, 1463,1531and 1615
PVZ2	440,593,1064, 1178, 1348, 1469 and 1608
PVZ3	452,607,1032, 1182, 1382, 1470,1582 and 1662

4.3.4. FT-IR Spectral Analysis

The chemical structure and interaction among the moieties of PVK and PVZs were studied by the FT-IR spectroscopy. FT-IR spectra of PVK, PVZ1, PVZ2, and PVZ3 are shown in Figure 4.4(a–d) respectively. Figure 4.4a shows the FT-IR spectra of PVK with bands at 724 and 748 cm^{-1} which are attributed to the ring deformation of substituted aromatic ring (doublet) for the carbazole group and CH_2 rocking vibration.[39] The bands at 1158, 1224, and 1327 cm^{-1} correspond to the out of plane deformation of vinylidene group, C–N stretching of vinylcarbazole and CH_2 deformation of vinylidene group, respectively. The bands at 1452, 1483, and 1627

cm^{-1} are due to the ring vibration of vinylcarbazole moiety and also C-C stretching vibration of vinylidene group. Also, the bands at 2925 and 3050 cm^{-1} are due to aliphatic C–H vibration and C–H stretching vibration of aromatic ring. The observed band at 800–880 cm^{-1} is mainly due to substituted benzene ring, which confirms that polymerization is taking place through vinylcarbazole groups.[44] In figure 4.4(b–d) the FT-IR spectra of PVZ1, PVZ2, and PVZ3 showed band at 721 and 745 cm^{-1} were attributed to ring deformation of substituted aromatic ring and CH_2 rocking vibration. While the bands at 1158 and 1224 cm^{-1} correspond to the out of plane deformation of vinylidene group and C–N stretching of vinylcarbazole but band at 1327 cm^{-1} shifted to the higher wavenumber 1331 cm^{-1} which corresponds to CH_2 deformation of vinylidene group. The shift in the band maxima at higher wave number observed at 1452, 1483, and 1627 cm^{-1} to 1454, 1485, and 1629 cm^{-1} is due to ring vibration of VK moiety and also C=C stretching vibration of vinylidene group. Similar characteristic bands were observed for PVZ4 and PVZ5.The changes in the wavenumber of PVZs compared to PVK substantiate the interaction between the PVK and ZnO in the nanocomposites. [39, 45]

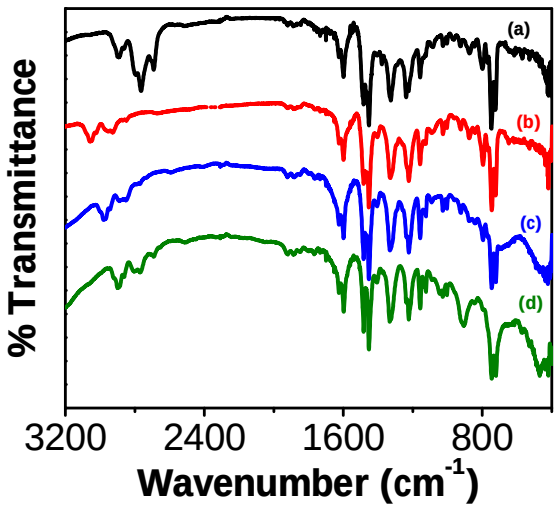

Figure 4.4. FT-IR spectrum of (a) PVK (b) PVZ1 (c) PVZ2 and (d) PVZ3

4.3.5. X-ray Diffraction Analysis

X-ray powder diffraction patterns of the ZnO, PVK, PVZ1, PVZ2, and PVZ3 are shown in Figure 4.5(a–e), respectively. Figure 4.5a shows the XRD patterns of ZnO, which exhibited sharp peaks at 2θ=32, 34.4, 36.3, 47.5, 56.5, 62.9, 66.3, and 67.88 °. These peaks are assigned to the ZnO crystal structure with miller indices (100), (002), (101), (102), (110), (103), (200) (112), and (201) confirms the formation of ZnO in wurzite hexagonal phase. In figure 4.5b the XRD pattern of PVK exhibited two peaks at 2θ=8 and 20.8° with d-spacing of 10.8 and 4.2 Å revealed face-to-face ordered structure of PVK.[46]

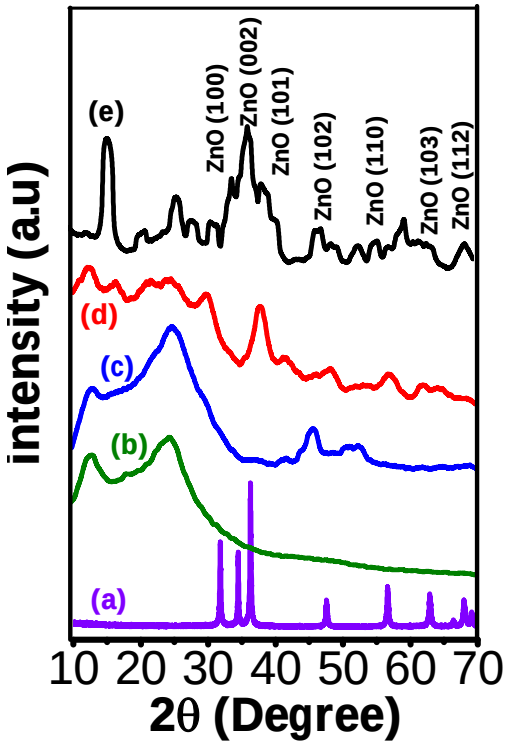

Figure 4.5. XRD spectra of (a) ZnO (b) PVK (c) PVZ1 (d) PVZ2 and (e) PVZ3

Figure 4.5c shows the XRD profile of PVZ1 which observed broad peaks at 2θ= 8.2, 21.2, 34.3, 39.4, 44.1, 49.6, 51.1, 61.2, 64.5, and 68.6° corresponds to the characteristic peaks of ZnO and PVK. Two peaks at 2θ = 8.2 and 21.2° become stronger with lower (VK)/(ZnO) ratios, accompanied with decreasing intensity of

the ZnO peaks. This observation was further confirmed by morphology analysis. Figure 4.5d shows peaks at 2θ=8.4, 20.8, 31.8, 36.1, 39.2, 47.3, 56.2, 61.2, 64.6, and 68.7° corresponding to PVZ2 composites, which includes the characteristic peaks of ZnO as well as PVK. Figure 4.5e shows peak at 2θ= 7.8, 11.2, 17.4, 22.1, 24.9, 28.1, 31.2, 33.9, 36.1, 45.2, 47.4, 51.2, 54.2, 58.6, and 68.7° corresponding to PVZ3 composites which also suggests the presence of crystalline phase of zinc oxide and polyvinylcarbazole. Similar observations were made for PVZ4 and PVZ5. Further, we observed sharp intense peak at 33.98 corresponds to the (002) plane of ZnO, confirming the one dimensional growth of zinc oxide within the polymer chain.

4.3.6. Morphological Analysis

Morphology of ZnO, PVK, and nanocomposites was studied by SEM, HR-TEM, and AFM. The formation and mechanism of hierarchically structured porous ZnO was discussed in Section 3. 3. 4 of Chapter 3. Figure 4.6(a–d) and Figure 4.7(a-d) show the SEM, TEM images of PVK, PVZ1, PVZ2, and PVZ3. Figure 4.6a shows the formation of well defined nanotubular structures with an average diameter of 70 nm and micrometer length. The TEM image of the same is shown in Figure 4.7a which further confirms the formation of nanotubes. SEM and TEM image of PVZ1 showed the co-structured porous ZnO with tubules of PVK to form chains and is depicted in Figure 4.6b and 4.7b, respectively. The contrast in the image (dark portion corresponds to ZnO and bright portion corresponds to PVK) is due to difference in the electron migration through the organic and inorganic particles. On further increasing the amount of ZnO, PVZ2 exhibited the formation of nanotubes with diameter 80 nm in which ZnO nanobars are embedded inside the PVK nanotubes as shown in Figure 4.6c and 4.7c. However, on further increasing the

amount of ZnO, PVZ3 showed ZnO nanorods are embedded in the nanotubes of PVK as seen in Figure 4.6d. TEM image of the same is shown in Figure 4.7d which confirmed ZnO nanorods are completely entrapped into polyvinylcarbazole chains indicating the molecular level mixing of n-type ZnO particles with the p-type conducting polymer PVK.

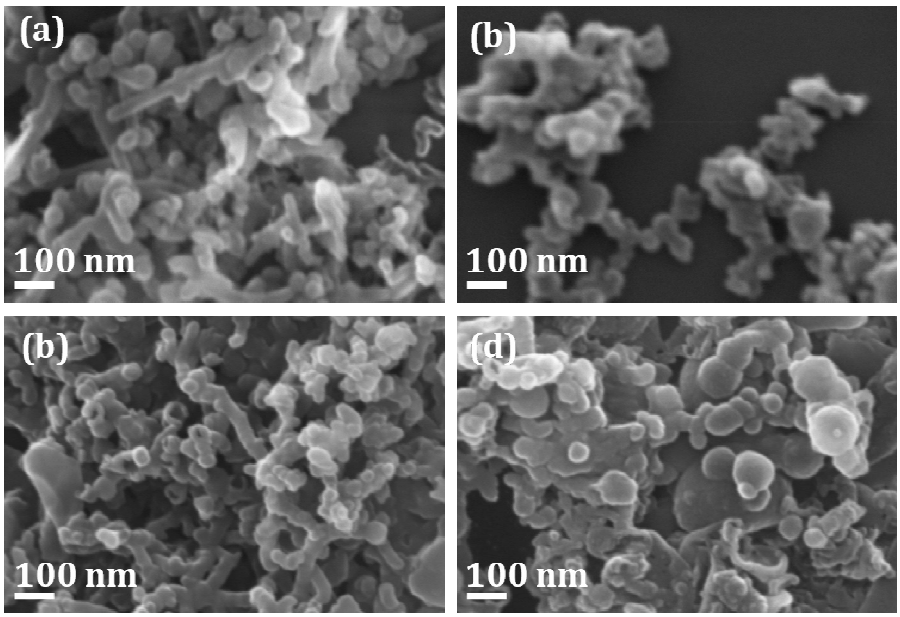

Figure 4.6. SEM images of (a) PVK, (b) PVZ1, (c) PVZ2, and (d) PVZ3.

Further morphology was confirmed by recording AFM analysis and is shown in Figure 4.8(a–d), respectively. AFM image of PVK reveals the formation of highly aggregated nanotube-like structure with the root mean square surface roughness of 12 nm. AFM image of PVZ-1, PVZ-2, and PVZ-3 are matching with the observation made by HR-TEM and SEM analysis which revealed that ZnO nanostructures well embedded into the PVK matrix. The root mean square surface roughness value of PVZ-1, PVZ-2, and PVZ-3 measured as 16, 20, and 29 nm, respectively. The surface roughness values are enhanced with increasing amount of ZnO content in the nanocomposites.

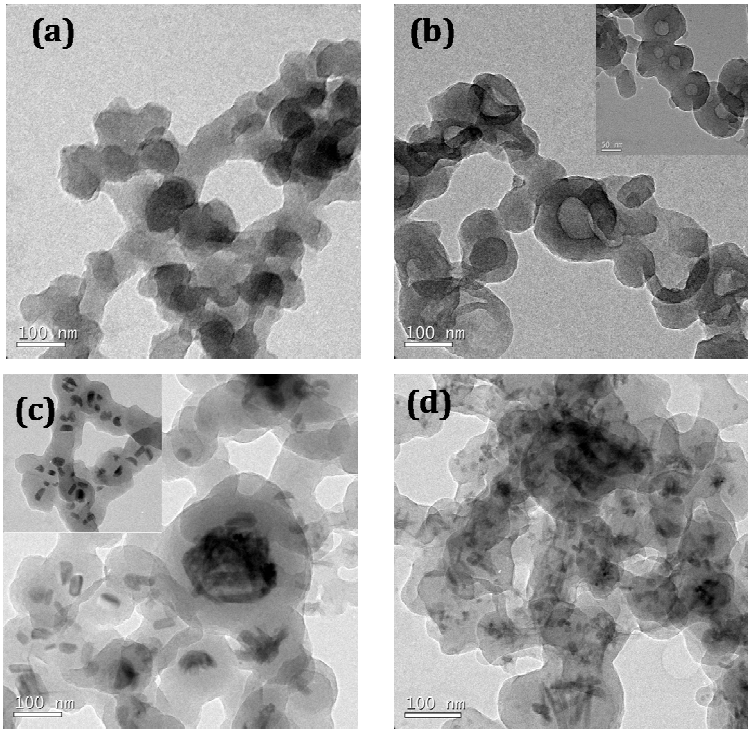

Figure 4.7. TEM images of (a) PVK, (b) PVZ1 (inset higher magnification), (c) PVZ2 (inset higher magnification), and (d) PVZ3

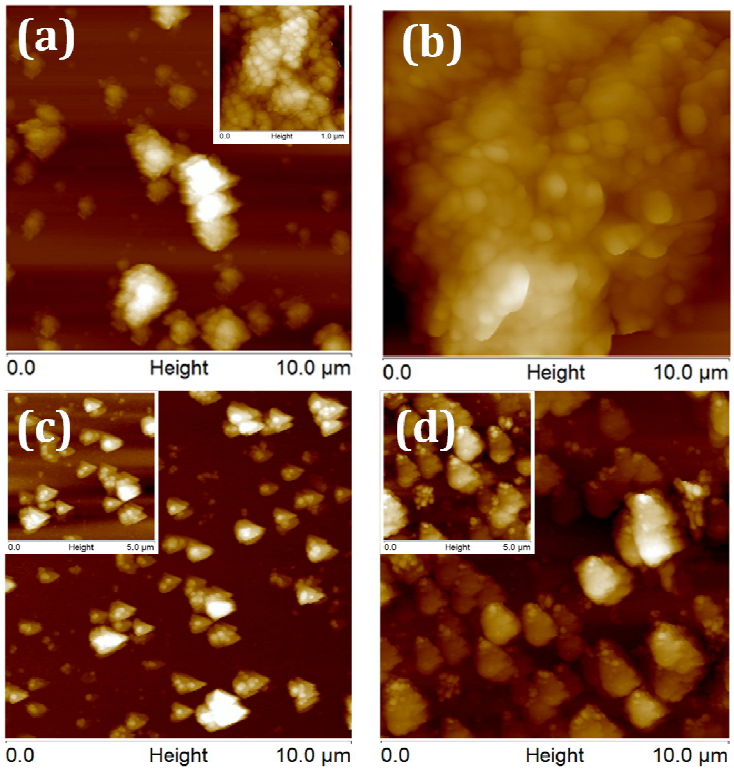

Figure 4.8. AFM images of (a) PVK (inset higher magnification), (b) PVZ1, (c) PVZ2 (inset higher magnification), and (d) PVZ3 (inset higher magnification)

4.3.7. Memory Device Performance

The electrical resistive switching performances of the PVZs were studied by fabricating the device with configuration of ITO/PVZs/Ag. The active layer comprising PVZs is sandwiched between electrochemically active silver and ITO electrodes. The electrical switching performances of the nanocomposites were studied by measuring semi lograthimic current–voltage (I–V) characteristics of the device. Figure 4.9(a–f) shows the electrical switching behavior of devices fabricated with PVK, PVZ1, PVZ2, PVZ3, PVZ4, and PVZ5 as active layers. I–V plots of all devices exhibited hysteresis with currents of a high-conductive state (ON state) and a low-conductive state (OFF state) at the same sweeping voltages. Such electrical hysteresis behavior is characteristic feature of bistable devices.[47] Figure 4.9a shows the I–V characteristics of the PVK exhibiting the resistive switching to the ON/OFF states at around -1V, with a noticeable negative differential resistance (NDR). The OFF state current resistance of the device is 0.38 mA which becomes 54.35 mA upon switching to ON state. The electrical bistability of the device was observed to be enhanced with increasing the amount of ZnO in PVZ nanocomposite. Figure 4.9b shows the I–V plot ITO/PVZ1/Ag device and the ON/OFF states are observed to be abruptly increased at a higher voltages compared to ITO/PVK/Ag device, which is typical characteristic of the ZnO-based resistive switching devices.[24] Figure 4.9c shows the I–V plot of the ITO/PVZ2/Ag device. The set voltage of the device has increased to 1.9V and the reset measured at -3.2 V. The negative differential resistance effect observed can be associated with the presence of trapped charges in the nanocomposite.[48] Figure 4.9d shows the I–V plot of the ITO/PVZ3/Ag based

device, which displayed that the set voltage has enhanced to 2.4V and the reset voltage of the device is measured at -3.8 V.

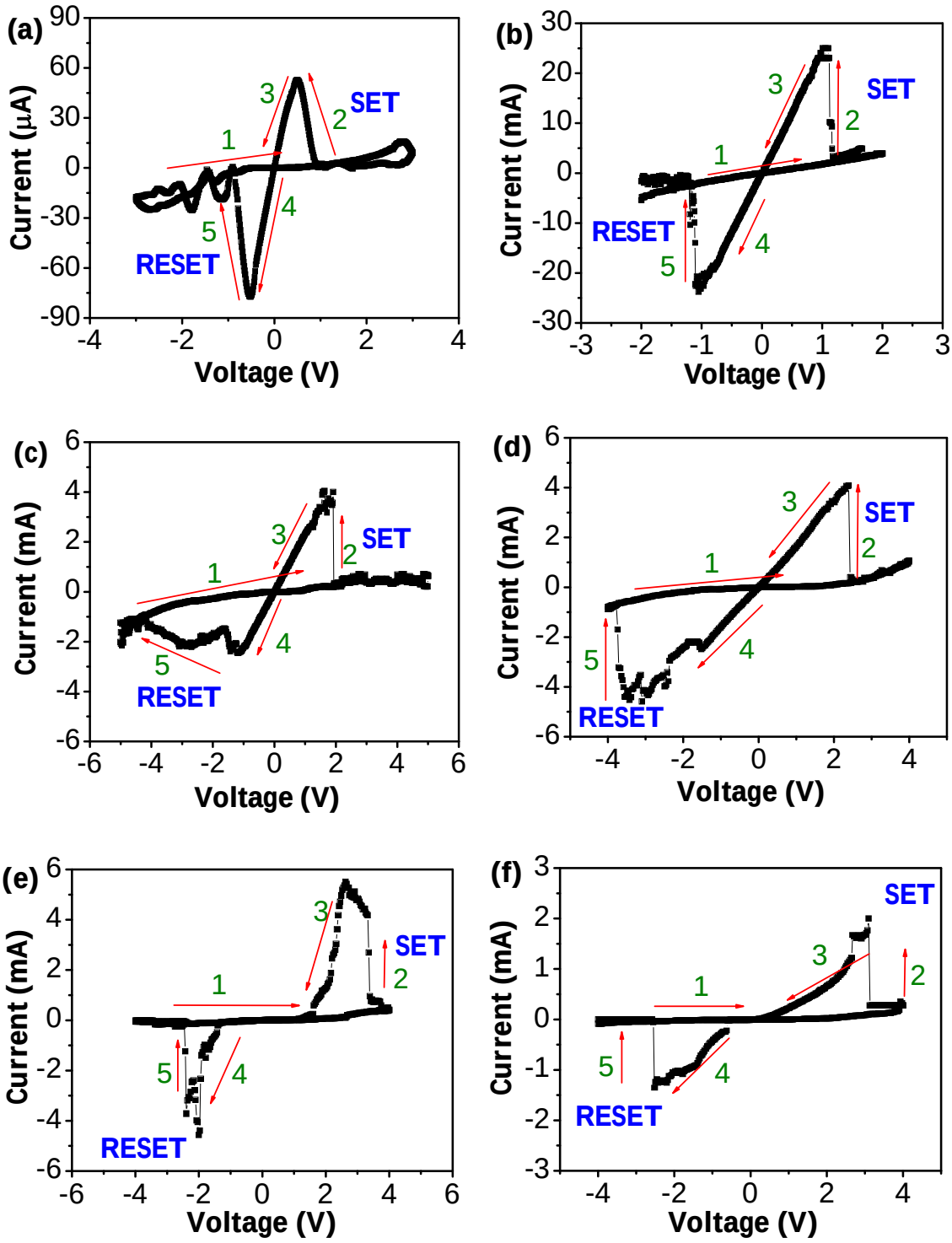

Figure 4.9. Semi lograthimic I–V curves of the ITO/active layer/Ag devices with active layers of **(a)** PVK, **(b)** PVZ1, **(c)** PVZ2, **(d)** PVZ3, **(e)** PVZ4 and **(f)** PVZ5

The I–V plot of the device fabricated with PVZ4 was measured set voltage of 2.8V and the reset voltage of -2.57 V. Figure 4.9f shows the I–V characteristics of the device fabricated with PVZ5 where the set voltage has further enhanced to 3.1V and the reset voltage of the device changed at -2.5 V.

Figure 4.10(A and B) shows the ON/OFF voltage and ON/OFF current ratio plots of PVK and PVZs-based devices (effect of ZnO in PVZ) against the applied voltage. The ON/OFF voltage and current ratios of each concentration for both positive and negative voltage region are measured for 10 random cells and the data were plotted with standard deviations. The set voltage of the bistable devices increases from 1.2 to 3.1V as ZnO content varies from 2.5 to 12.5%. Similarly, the ON/OFF current ratio increases from 10^2 to $5.2x10^3$ as ZnO content varies from 2.5 to 10%. On further increase in the ZnO content to 12.5%, the ON/OFF current ratio decreased to $3.7x10^3$ suggesting that the device parameters can be well controlled by tuning the ZnO content in the composite as well as due to the formation of aggregated ZnO nanoparticles inside the PVZs which hinders the transport of charge carriers. This result is supported by the report made by other researchers.[12, 35]

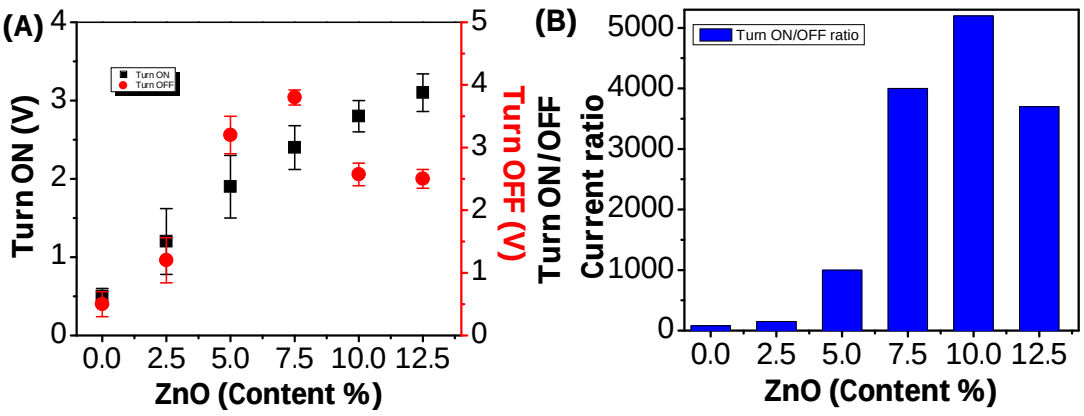

Figure 4.10. (A) Turn ON/OFF Voltage and **(B)** ON/OFF current ratio of the devices

Reliability or failure analyses of the devices were studied as reported by Pan et al.[49] Figure 4.11(a–e) shows a plot of cumulative probability (%) versus threshold voltage (V_{SET} and V_{RESET}) of devices PVZ1, PVZ2, PVZ3, PVZ4, and PVZ5. The devices were repeatedly switched between ON and OFF states. From the plot, it can be observed that V_{SET} distributes in the range of 1.08–1.64 V (PVZ1), 1.6–2.3 V (PVZ2), 2.4–2.98V (PVZ3), 2.32–2.72V (PVZ4), and 2.94–3.68V (PVZ5) while V_{RESET} distributes in the range of –1.14 to –1.6V (PVZ1), –2.92 to –3.5V (PVZ2), –3.4 to–3.92V (PVZ3), –2.71 to –3.2V (PVZ4), and –2.04 to –2.8V (PVZ5). We have observed narrow distribution in both V_{SET} and V_{RESET} for all the fabricated devices. It further confirms the reliability of the prepared devices.

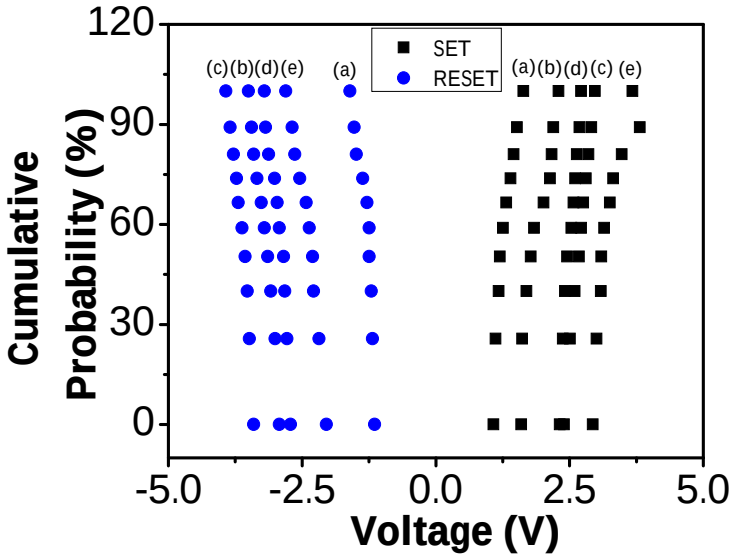

Figure 4.11. Cumulative distribution plots of devices (a) PVZ1 (b) PVZ2, (c) PVZ3 (d) PVZ4 and (e) PVZ5

To understand the electrical switching and conduction mechanism of the PVK and PVZs devices, the measured I–V data showing both ON and OFF states were drawn on double logarithmic plot. The double logarithamic I–V characteristics plot of both OFF and ON state of PVK device are shown in the Figure 4.12(a and b).

Figure 4.12a shows the OFF state of PVK device which exhibit a slope value of 1 related to the ohmic conduction behavior. Figure 4.12b shows ON state of the device exhibited two regions: First region voltage up to 0.46V fitted with slope value of 1, indicating the ohmic conduction mechanism. Further increasing the voltage above 0.46 V, device set in the ON state.

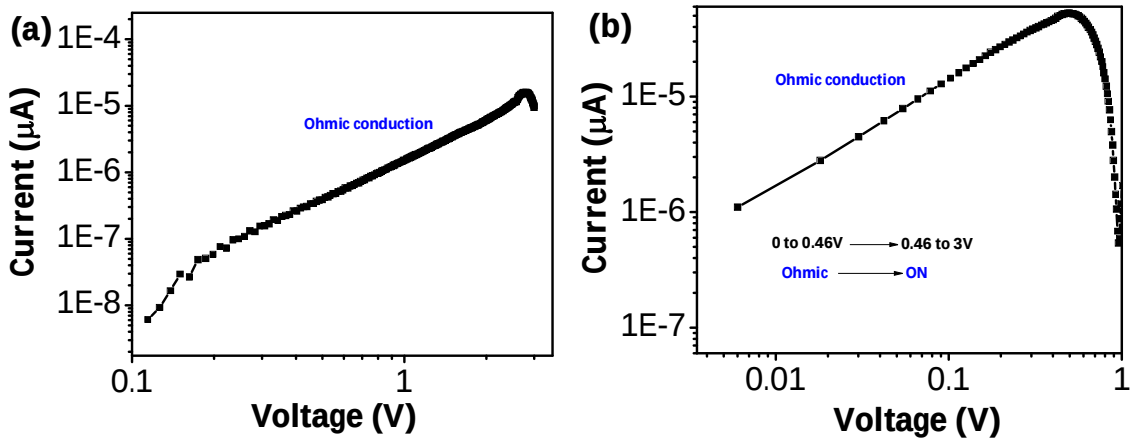

Figure 4.12. log (*I*) – log (*V*) Curve of the **(a)** OFF and **(b)** ON state of PVK

The double logarithamic I–V characteristics plot of PVZs devices both OFF and ON state is shown in Figure 4.13 (a–e). Figure 4.13a shows OFF state of the PVZ1 device which has a slope value of 1 which can be related to the Ohmic conduction behavior. However, ON state of the PVZ1 device (Figure 4.13a) exhibited three regions: at low voltage exhibited linear region with a slope of 2.0. This corresponds to the ohmic conduction mechanism. At voltage >1V, the curve showed a steep increase in current with a slope of 4.59. This slope value corresponds to the trap controlled space charge limit conduction mechanism.[12,50] This is a measure of charge carrier injection into dielectric medium. The total flow of charge carrier in dielectric is determined by the electric field and the presence of carrier concentration. In the present case as voltage increases (electric field increases), more electrons are trapped in the defects. Hence there is sudden increase in the concentration of

charge carriers.[51] This mechanism is according to the Child's law in the presence of trapping. The double logarithmic I–V plot showing both OFF and ON state of PVZ2 is shown in Figure 4.13b, respectively. In figure 4.13b OFF state of PVZ2 exhibited a two different region: straight line was observed up to 1.9V with a slope value of 1 associated with the Ohmic conduction. Above 1.9 V, showed a straight line (inset figure 4.13b) with a linear fitting of ln(I/V) versus $V^{1/2}$ and a slope value of 1 shows characteristic mechanism of Poole–Frenkel emission model.[29] According to this model, current density expressed by equation (4.1),

$$I = C_o V_e (-q/KT) [\phi-(qv/\pi\varepsilon l)^{1/2}] \qquad (4.1)$$

where *I* is the current, *V* the voltage bias, Φ the energy barrier height, *q* the electronic charge, K the Boltzmann constant, C_0 is a constant, and ε the dynamic permittivity.

Figure 4.13b shows the double logarithmic I–V plot in the ON state of PVZ2 device. We observed a similar mechanism of ohmic conduction as discussed in PVZ1. Further increasing the voltage up to 5V, it followed space charge limit current (SCLC) mechanism. The measured large voltage window during the SCLC can be associated with the formation of various conductive species from the conductive polymer and also several defect states originating from wurzite ZnO. Apart from these defects, formation of the conductive filaments (silver ions) generated from the silver top electrode during the passage of voltage also plays crucial role for the conducting mechanism.[29] The double logarithmic I–V plot of both OFF and ON state of the PVZ3 device is shown in Figure 4.13c, respectively. The OFF state of the PVZ3 device exhibited similar kind of mechanism as shown in Figure 4.13b (OFF state of PVZ2 device).

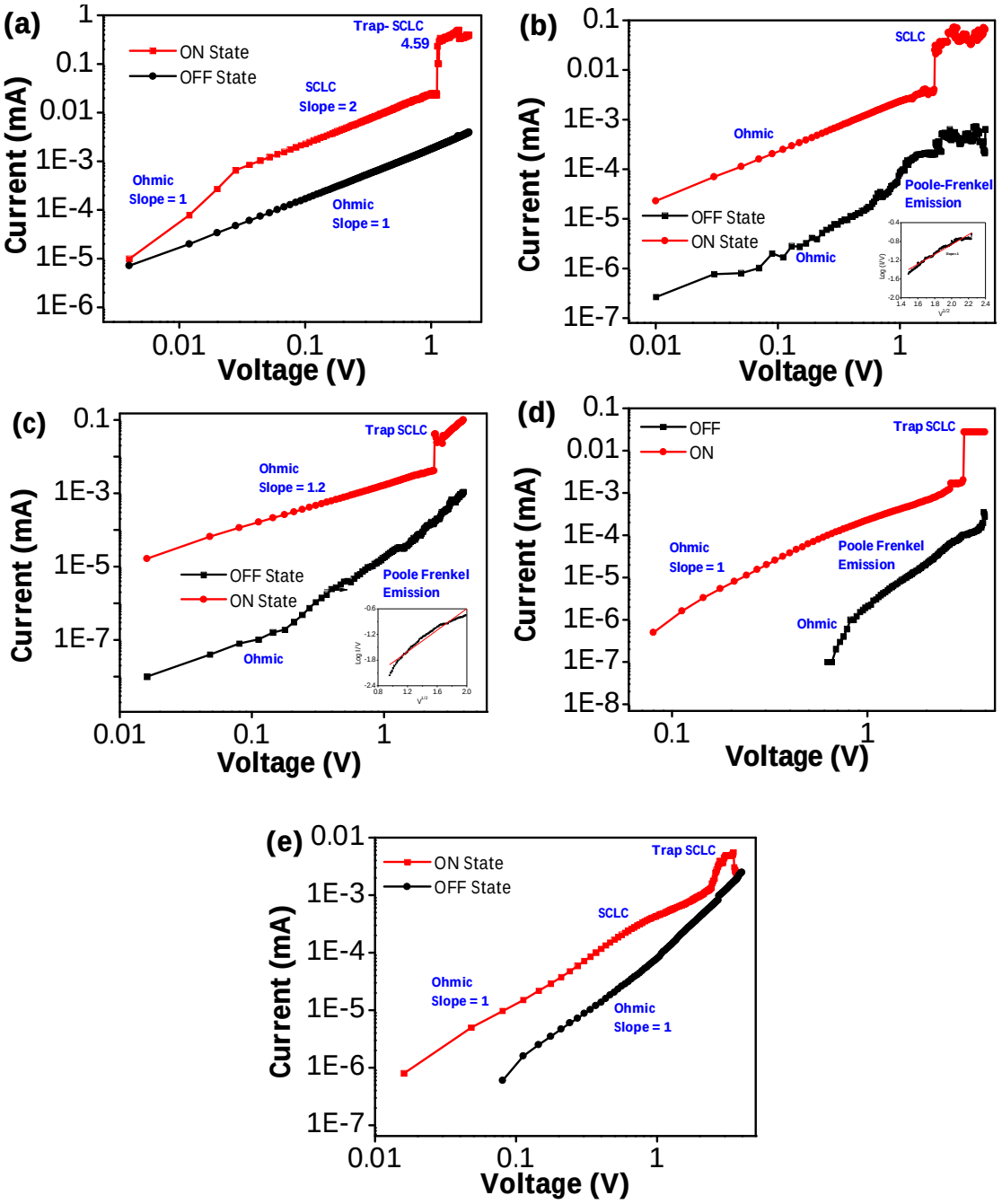

Figure 4.13. Log (I)–log (V) curve of the **(a)** OFF and ON state of PVZ1, **(b)** OFF and ON state of PVZ2; The inset presents a log (I/V) versus $V^{1/2}$ plot of the OFF state of PVZ2 device, **(c)** OFF and ON state of PVZ3.The inset presents a log (I/V) versus $V^{1/2}$ plot of the OFF state of PVZ3 device, **(d)** OFF and ON state of PVZ4 and **(e)** OFF and ON state of PVZ5

The ON state of PVZ3 device exhibited two regions: straight line was observed at the initial voltage up to 2.2V with a slope value of 1.2 which shows characteristic

mechanism of ohmic conduction model. On further increasing the voltage above 2.2 V, current linearly increased with trap controlled space charge limit conduction mechanism.[14] According to this model, current is expressed by equation (4.2),

$$I = 9\pi\varepsilon\varepsilon_0\mu V^2/8d^3 \qquad (4.2)$$

Where *I* is the current density, ε is the dielectric constant of the material, ε_0 is the permittivity of free space, *d* is the thickness of the film, and μ the carrier mobility.

The double logarithmic I–V plot of PVZ4 and PVZ5 are shown in Figure 4.13 (d to e). Figure 4.13(d) shows OFF and ON state of the PVZ4 device which reveals same conduction mechanism of PVZ2 and PVZ3. Figure 4.13(e) shows OFF and ON state of the PVZ5 device which exhibited similar conduction mechanism of PVZ3. The slope value of double logarithmic I–V plot revealed that Ohmic, space charge limited current (SCLC), and Poole–Frenkel emission model mechanism is responsible for the conductive mechanism in PVZs. According to the literature, cation migration mechanism also plays a vital role for the physical origin of the resistive switching, since the silver metal was used as the top electrode.[29, 52] When external bias voltage is applied to the top silver electrode, both silver cations (Ag^{n+}) and electrons generated from the electrode can be represented by the reaction, $nAg \rightarrow Ag^{n+} + ne^-$. These silver cations diffuse through the PVZs hybrid composites leading to the formation of conductive filament toward the ITO bottom electrode. The transportation of the Ag cations is affected by the various types of charges present in the active layer of PVZ nanocomposites (p–n type semiconductor).Recently, several researchers pointed out that generation of conductive ions depends completely on the cation mobility in the midst of the dielectric material.[53] In

general, growth dynamics of the conductive filament is controlled by three main factors: (i) anodic dissolution of the electrochemically active metal component; (ii) the transport of cations through the dielectric layers; (iii) the reduction of cations and the crystallization of conductive clusters. With longer voltage stress, more conductive silver ions emerge from the silver electrode (top electrode) and it extends to form the chains of cluster ions toward to the bottom electrodes. When these clusters are strong enough to short circuit the electrodes, it results in switching from HRS to LRS. The observed bipolar switching behavior can be attributed to the formation and dissolution of conductive ions during positive and negative voltage sweeps, respectively. Thus under external voltages, the device can be reversibly modulated between a high resistance state and low resistance state by generation and dissolution of silver ions. [54–56]

4.3.8. Retention Time and Endurance Performance of the Memory Device

The retention time ability and endurances performance of the devices were evaluated under ambient conditions. Figure 4.14 (a–e) shows the time versus current plots in the ON and OFF states of the PVZ1, PVZ2, PVZ3, PVZ4, and PVZ5 devices at a constant applied voltage of +1V for ON and -1V for OFF state. From the plot, ON/OFF current ratio was observed as 10^1, 10^2, 10^3, $4x10^3$, $5.2x10^3$, and $3.7x10^3$ for PVK, PVZ1, PVZ2, PVZ3, PVZ4, and PVZ5, respectively. The maximum ON/OFF current ratio of $>5.2x10^3$ has been achieved for the memory device based on PVZ4. The ability of PVZs to retain these two states was tested further under a constant stress voltage. No significant degradation was observed for the device performance in both ON and OFF states even after 10^5 seconds of the continuous stress test revealing the stability of the device.

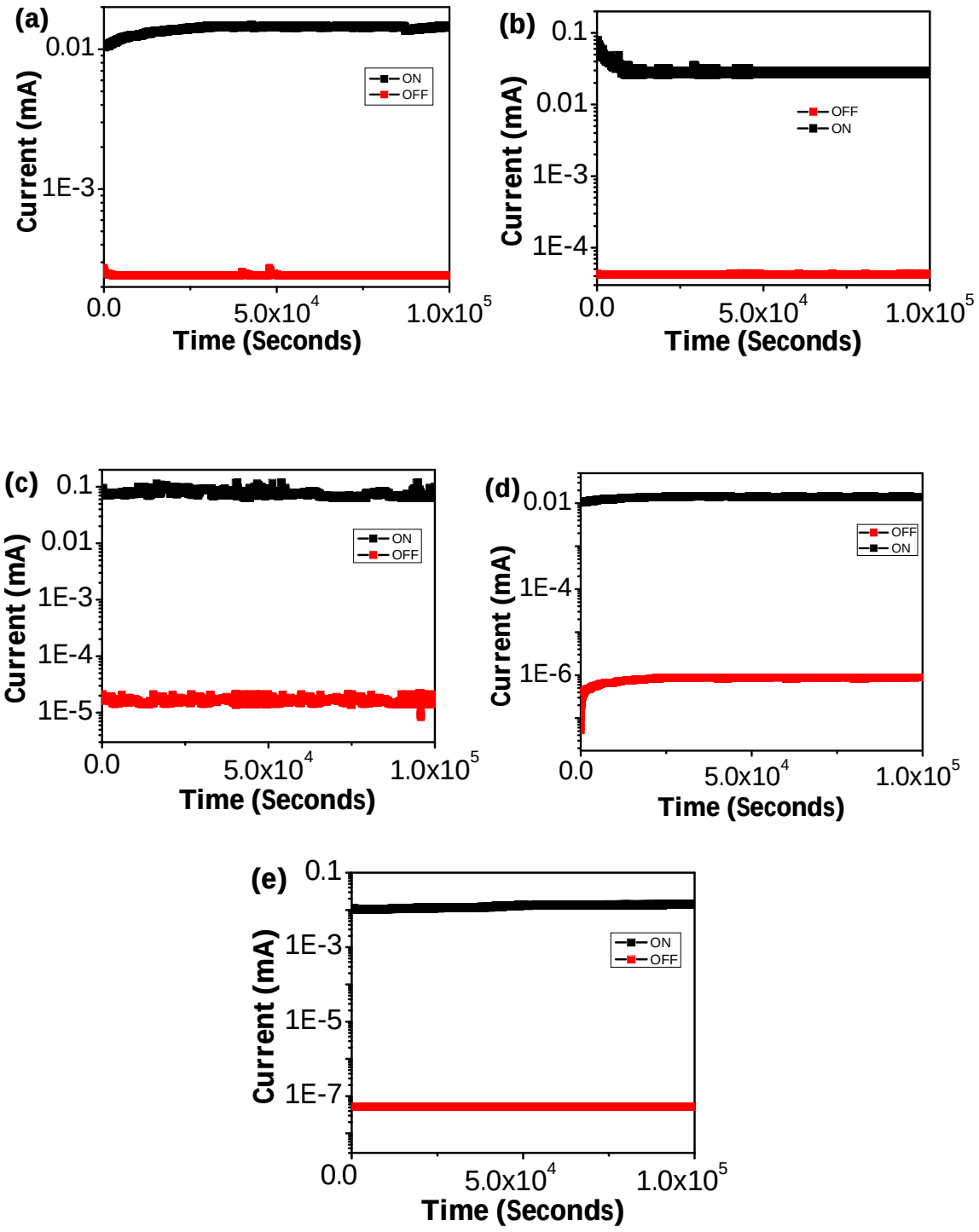

Figure 4. 14. Retention time on the ON and OFF states of devices **(a)** PVZ1, **(b)** PVZ2, **(c)** PVZ3, **(d)** PVZ4 and **(e)** PVZ5 under a constant voltage

Endurance performance was studied by plotting time versus current/voltage of the PVZs devices. Figure 4.15(a) shows effect of 100 cycles on the ON (write)/OFF (erase) current and voltage state of device PVZ1. When a write pulse is

applied to the device, switching from OFF state to ON state was triggered with large current and a low resistance was recorded. In contrast to erase pulse, the device switches back to OFF state. It is evident from the graph that the switching process is reproducible from cycle to cycle, which confirms the feasibility of the devices.

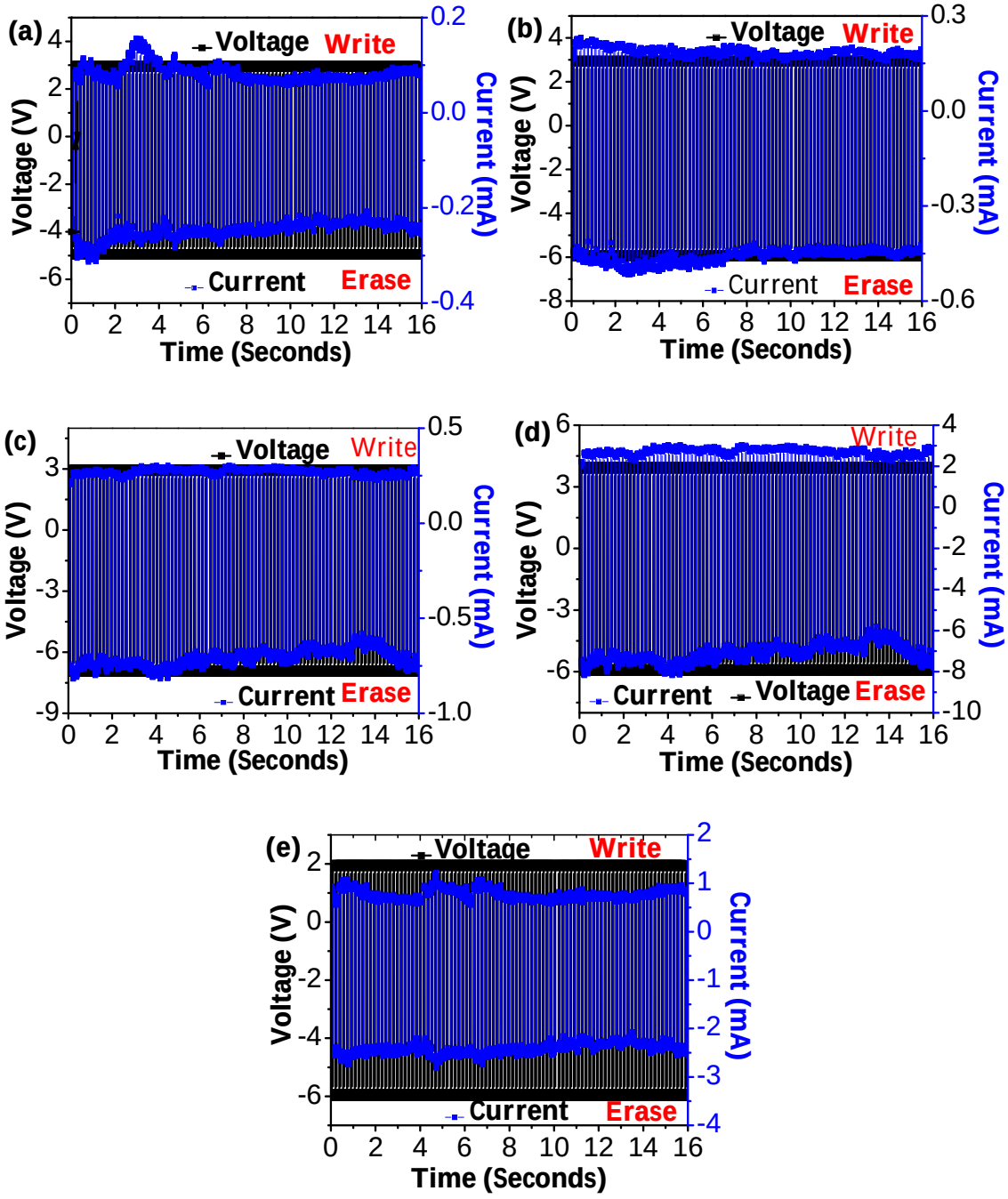

Figure 4.15. Endurances performance of memory devices **(a)** PVZ1, **(b)** PVZ2, **(c)** PVZ3, **(d)** PVZ4 and **(e)** PVZ5 showing ON & OFF current for 100 cycles

Effect of 100 cycles on the ON/OFF voltage and current state of devices PVZ2, PVZ3, PVZ4 and PVZ5 is shown in Figure 4.15 (b to e) and the results indicated its reliability and endurance stability.

4.4. Conclusions

In summary, non-volatile bistable memory devices having the configuration of Ag/PVZs/ITO with excellent ON/OFF ratio along with high endurance stability and reliability were successively fabricated using PVZs nanocomposite as an active material. Various experimental results revealed that ZnO preserves its crystalline wurtzite phase and hierarchical porous morphology in the PVZ nanocomposite. Studies showed that electrical bistability and conduction mechanism of the devices depends upon the amount of ZnO nanoparticles present in the nanocomposite. PVZ4 device exhibited ON/OFF current ratio of 5.2×10^3. Conduction mechanism is due to the conductive filament formation arising from the cation migration along with Ohmic, Poole–Frenkel emission, SCLC, and trap-filled SCLC processes. Our result suggests that this system can be an excellent prospectable candidate for the fabrication of non-volatile memory devices.

4.5. Experimental Section

4.5.1. Materials

N-Vinylcarbazole (VK) monomer and butanol were purchased from Sigma–Aldrich, Bangalore, India. Ferric chloride anhydrous ($FeCl_3$) was purchased from Merk chemicals, India. Zinc acetate dihydrate and all solvents of analytical grade were purchased from s.d. fine Chem Ltd., Bombay, India. Detailed preparation, characterization of ZnO was described in Section 3.5.3 of Chapter 3.

4.5.2. Preparation of Nanocomposites

0.028 g of zinc oxide was dispersed in 10 ml of chloroform solution to that 0.5 g of VK (2.5 mmol) was dissolved in 20mL chloroform solution was added and stirred for 20 min. Anhydrous ferric chloride (3.69 mmol) in 20 ml chloroform was added dropwise to the vigorously stirred solution kept in an ice bath and the reaction was continued for 24 h. After completion of the reaction, the solution was poured into methanol to precipitate the nanocomposites. The nanocomposite was separated by centrifugation at 5000 rpm for 10 min, and then washed several times with methanol and distilled water to remove the unreacted monomer and ferric chloride. Finally the product was dried at 50 ^{o}C in vacuum oven and designated as PVZ1. Similarly PVZ were prepared with different weight percentage of ZnO in the VK under same condition and designated as PVZ2, PVZ3, PVZ4, and PVZ5. For comparison, PVK was also prepared under the same condition without ZnO. Experimental details are given in Table 4. 2.

Table 4. 2. Experimental details of the preparation of nanocomposites

Sl. No	Sample	Monomer (mmol)	ZnO (g)	$FeCl_3$ anhydrous (mmol)
1	PVK	2.5	-	3.69
2	PVZ1	2.5	0.028	3.69
3	PVZ2	2.5	0.058	3.69
4	PVZ3	2.5	0.091	3.69
5	PVZ4	2.5	0.116	3.69
6	PVZ5	2.5	0.158	3.69

4.5.3. Fabrication of the Memory Devices

Memory device with the configuration of ITO/PVZ/Ag was used for demonstration. The procedure for fabrication of memory device was given below. Memory devices were fabricated on ITO anode substrate with sheet resistance $20\Omega sq^{-1}$. The ITO substrates were cleaned with deionized water, acetone, and isopropanol sequentially. Then PVZs in dichlorobenzene solution was spin-coated onto the top of ITO substrate with a speed of 1000 rpm for 60 seconds, resulting in a film of thickness of 55nm. The active layer was then annealed at $80^{o}C$ for 30 min. Finally Ag was thermally evaporated onto the film surface at 10^{-7} Torr through a shadow mask to form the top electrode with thickness of about 150 nm, using a Fillunger high vacuum thermal evaporation system. The electrical characteristics of the fabricated devices were analyzed at atmospheric pressure under ambient temperature using a semiconductor parameter analyzer (Agilent B2912A) for applying voltage and measuring current. In a typical test configuration, the sample was placed in a probe station and bias voltages were applied to one of the Ag electrodes while the other electrode was grounded. The keysight B2900A quick I–V measurement software was used for analysis.

4.6. Characterization Techniques

Description of FT-IR and XRD are given in Section 2.6 of Chapter 2. Details of opto-electronic spectra, photoluminescence, Raman spectra, SEM and HR-TEM analysis are given in Section 3.6 of Chapter3. The cyclic voltammetry studies carried out using CHI6211B Electrochemical Analyzer, in a three-electrode one-compartment electrochemical cell in which glassy carbon electrode (GCE) used as working electrode and a platinum wire used as a counter electrode. All the

potentials were recorded using Ag/AgCl as the reference electrode. The experiments were conducted in 0.1 mol/L tetrabutylammonium hexafluorophosphate (Bu_4NPF_6) acetonitrile solution. Atomic force microscopic images were carried under ambient conditions using a (Bruker Multimode AFM-3COCF, Germany) operating in tapping mode. Samples for the analysis were prepared by drop casting the nanocomposite solution on mica sheet.

4. 7. References

1. J. Ouyang, C. W. Chu, C. R. Szmanda, L. Ma, and Y. Yang, *Nat. Mater*. **2004**, *3*, 918.

2. Y. Yang, J. Ouyang, L. Ma, R. J. H. Tseng, and C. W. Chu, *Adv. Funct. Mater*. **2006**, *16*, 1001.

3. Q. D. Ling, D. J. Liaw, C. Zhu, D. S. H. Chan, E. T. Kang, and K. G. Neoh, *Prog. Polym. Sci*. **2008**, *33*, 917.

4. Y. Li, H. Lv, Q. Liu, S. Long, M. Wang, H. Xie, K. Zhang, Z. Huo, and M. Liu, *Nanoscale* **2013**, *5*, 4785.

5. J. C. Scott and L. D. Bozano, *Adv. Mater*. **2007**, *19*, 1452.

6. Q. Ling, Y. Song, S. J. Ding, C. Zhu, D. S. H. Chan, D. L. Kwong, E. T. Kang, and K. G. Neoh, *Adv. Mater*. **2005**, *17*, 455.

7. J. C. Ribierre, T. Aoyama, T. Muto, and P. Andre, *Org. Electron*. **2011**, *12*, 1800.

8. T. Kurosawa, T. Higashihara, and M. Ueda, *Polym. Chem*. **2013**, *4*, 16.

9. C. L. Liu, T. Kurosawa, A. D. Yu, T. Higashihara, M. Ueda, and W. C. Chen, *J. Phys. Chem. C.* **2011**, *115*, 5930.

10. R. Sim, M. Y. Chan, A. S. W. Wong, and P. S. Lee, *Org. Electron*. **2011**, *12*, 185.

11. N. Fan, H. Liu, Q. Zhou, H. Zhuang, Y. Li, H. Li, Q. F. Xu, N. Li, and J. Lu, *J. Mater. Chem*. **2012**, *22*, 19957.

12. K. Onlaor, T. Thiwawong, and B. Tunhoo, *Org. Electron*. **2014**, *15*, 1254.

13. P. Y. Lai and J. S. Chen, *Org. Electron*. **2009**, *10*, 1590.

14. D. Yue, R. Cui, X. Ruan, H. Huang, X. Guo, Z. Wang, X. Gao, S. Yang, J. Dong, F. Yi, and B. Sun, *Org. Electron*. **2014**, *15*, 3482.

15. Q. Zhang, J. Pan, X. Yi, L. Li, and S. Shang, *Org. Electron*. **2013**, *13*, 1289.

16. V. Armel, O. W. Jensen, R. Kerr, D. R. MacFarlane, and B. W. Jensen, *J. Mater. Chem*. **2012**, *22*, 19767.

17. R. Ramakrishnan, J. D. Sudha, and V. L. Reena, *RSC Adv*. **2012**, *2*, 6228.

18. J. Lin and D. Ma, *Appl. Phys. Lett*. **2008**, *93*, 093505.

19. B. Pradhan, S. K. Batabyal, and A. J. Pal, *J. Phys.Chem. B.* **2006**, *110*, 8274.

20. D. Jurchescu, S. Subramanian, R. J. Kline, S. D. Hudson, J. E. Anthony, T. N. Jackson, and D. J. Gundlach, *Chem. Mater*. **2008**, *20*, 6733.

21. G. Qian, Z. Zhong, M. Luo, D. Yu, Z. Zhang, Z. Y. Wang, and D. Ma, *Adv. Mater*. **2009**, *21*, 111.

22. F. Verbakel, S. C. J. Meskers, and R. A. J. Janssen, *Appl. Phys. Lett*. **2006**, *89*, 102103.

23. L. H. Xie, Q. D. Ling, X. Y. Hou, and W. Huang, *J. Am. Chem. Soc*. **2008**, *130*, 2120.

24. S. Peng, F. Zhuge, X. Chen, X. Zhu, B. Hu, L. Pan, B. Chen, and R. W. Li, *Appl. Phys. Lett*.**2012**, *100*, 072101.

25. J. Y. Son, Y. H. Shin, H. Kim, and H. M. Jang, *ACS Nano* **2014**, *4*, 2655.

26. J. Y. Son, O. Y. Kim, H. Kim, W. J. Maeng, Y. S. Shin, and Y. H. Shin, *Electro. Chem. Solid State Lett*. **2011**, *14*, H311.

27. M. K. Yang, J. W. Park, T. K. Ko, and J. K. Lee, *Appl. Phys. Lett*. **2009**, *95*, 042105.

28. A. F. Kohan, G. Ceder, D. Morgan, G. Van, and D. Walle, *Phys. Rev. B.* **2000**, *61*, 15019.

29. S. Lee, H. Kim, D. J. Yun, S. W. Rhee, and K. Yong, *Appl. Phys. Lett*. **2009**, *95*, 262113.

30. W. Y. Chang, Y. C. Lai, T. B. Wu, S. F. Wang, F. Chen, and M. J. Tsai, *Appl. Phys. Lett*. **2008**, *92*, 022110.

31. W. Lu and Y. Yang, *NanoScale* **2013**, *5*, 10076.

32. F. Pan, S. Gao, C. Chen, C. Song, and F. Zeng, *Mater. Sci. Eng. R.* **2014**, *83*, 1.

33 C. L. Liu and W. C. Chen, *Polym. Chem*. **2011**, *2*, 2169.

34. G. Nenna, S. Masala, V. Bizzarro, M. Re, E. Pesce, C. Minarini, and T. D. Luccio, *J. Appl. Phys.* **2012**, *112*, 044508.

35. G. Liu, Q. D. Ling, E. Y. H. Teo, C. X. Zhu, D. S. H. Chan, K. G. Neoh, and E. T. Kang, *ACS Nano **2009**, 3*, 1929.

36. J. Y. Hong, S. O. Jeon, J. Jang, K. Song, and S. H. Kim, Org. Electron.**2013**, *14*, 979.

37. M. Y. Chuang, Y. C. Chen, Y. K. Su, C. H. Hsiao, C. S. Huang, J. J. Tsai, and H. C. Yu, *ACS Appl. Mater. Interf*. **2014**, *6*, 5432.

38. R. J. Tseng, J. Ouyang, C. W. Chu, J. Huang and Y. Yang, *Appl. Phys.Lett*. **2006**, *88*, 123506.

39. Q. D. Ling, S. L. Lim, Y. Song, C. X. Zhu, D. S. H. Chan, E. T. Kang, and K. G. Neoh, *Langmuir* **2007**, *23*, 312.

40. S. L. Lian, C. L. Liu, and W. C. Chen, *ACS Appl. Mater. Interf*. **2011**, *3*, 4504.

41. T. Ye, J. Chen, and D. Ma, *Phys. Chem. Chem. Phys*. **2010**, *12*, 15410.

42. R. Anandhai and S. Umapathy, *J. Raman. Spectrosc*. **1998**, *29*, 901.

43. R. D. Fonseca, D. S. Correa, E. C. Paris, V. Tribuzi, A. Dev, T. Voss, P. H. B. Aoki, C. J. L. Constantino, and C. R. Mendonca, *J. Polym. Sci. B.* **2014**, *52*, 33.

44. M. Wainwright, J. J. Griffths, T. Guthrie, A. P. Gates, and D. E. Murry, *J. Appl. Polym. Sci*. **1992**, *44*, 1179.

45. K. M. Cui, M. C. Tria, R. Pernites, C. A. Binag, and R. C. Advincula, *ACS Appl. Mater. Interf*. **2011**, *3*, 2300.

46. Y. Liu, N. Li, X. Xia, Q. Xu, J. Ge, and J. Lu, *Mater. Chem. Phys*. **2010**, *123*, 685.

47. Y. Sun, L. Li, D. Wen, X. Bai, and G. Li, *Phys. Chem. Chem. Phys*. **2015**, *17*, 17150.

48. A. Tang, F. Teng, Y. Hou, Y. Wang, and F. Tan, *Appl. Phys. Lett*. **2010**, *96*, 163112.

49. Y. C. Yang, F. Pan, Q. Liu, M. Liu, and F. Zeng, *Nano Lett*. **2009**, *9*, 1636.

50. Z. Wang, F. Zeng, J. Yang, C. Chen, and F. Pan, *ACS Appl. Mater. Interf*. **2012**, *4*, 447.

51. A. Kim, K. Song, Y. Kim, and J. Moon, *ACS Appl. Mater. Interf*. **2011**,*3*, 4525.

52. H. Zhuang, X. Xu, Y. Liu, Q. Zhou, X. Xu, H. Li, Q. Xu, N. Li, J. Lu, and L. Wang, *J. Phys. Chem. C.* **2012**, *116*, 25546.

53. S. Peng, F. Zhuge, X. Chen, X. Zhu, B. Hu, L. Pan, B. Chen, and R. W. Lia, *Appl. Phys. Lett*.**2012**, *100*, 072101.

54. S. Gao, F. Zeng, C. Chen, G. Tang, Y. Lin, Z. Zheng, C. Song, and F. Pan, *Nanotechnology* **2013**, *24*, 335201.

55. S. Gao, C. Song, C. Chen, F. Zeng, and F. Pan, *App. Phys. Lett*. **2013**, *102*, 141606.

56. S. Menzel, U. Böttger, M. Wimmer, and M. Salinga, *Adv. Funct. Mater*.**2015**, *25*, 6306.

Chapter 5

Nanostructured Semiconducting PEDOT-TiO_2/ ZnO Composites for Thermoelectric Application

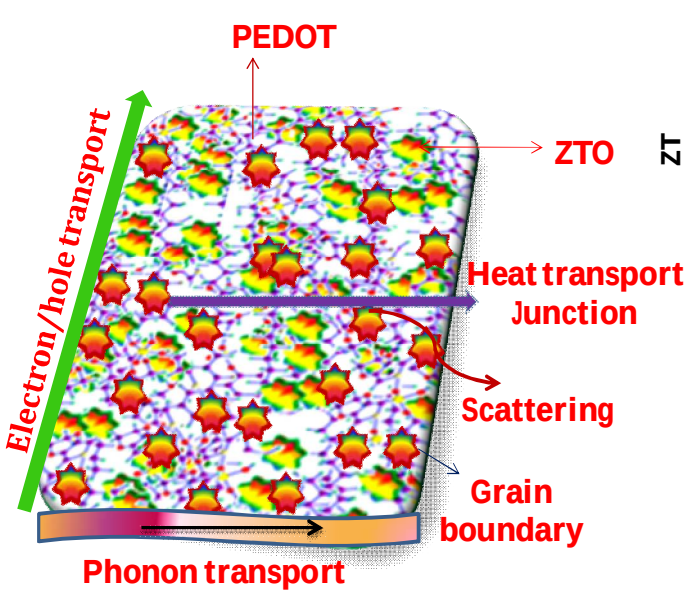

The p-n interfaces enhance the thermoelectric efficiency by deterring heat transport as opposed to favourable pathways for electrons

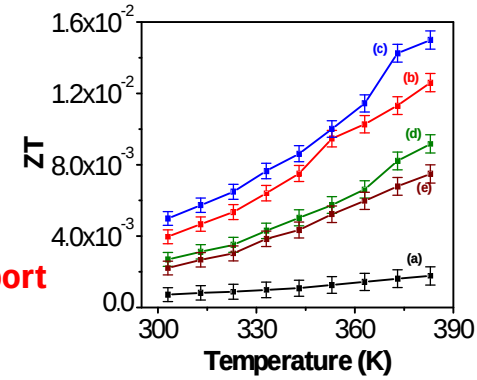

5.1. Abstract

This chapter illustrates the development of semiconducting nanocomposites of poly (3,4-ethylenedioxythiophene)–TiO_2/ZnO(PZT) and demonstrated its application in a thermoelectric device. Hierarchical hetero structured TiO_2/ZnO (ZTO) was prepared by a facile sol–gel process in the presence of a biocapping agent. PZT was prepared by in situ polymerization of EDOT in the presence of ZTO. It was characterized by UV–visible, FT-IR, XRD, Raman, SEM, TEM, and AFM analyses. Results revealed homogeneous distribution of ZTO with a heterocrystalline phase of wurtzite ZnO/anatase TiO_2 having high density of various defects in the nanocomposite. Studies showed that ZTO is excellently interfaced with highly ordered self-assembled extended π-layers of PEDOT chains, which could enhance the charge carrier concentration (3.92×10^{20} cm^{-3}) and charge carrier mobility (0.83 $cm^2V^{-1}s^{-1}$). Furthermore, we have demonstrated its application as a thermoelectric material by fabricating the device (Cu/PZT/Cu), which showed low thermal conductivity of 0.0495 $Wm^{-1}K^{-1}$, Seebeck coefficient of 19.05 μV K^{-1}, power factor of 1.28 μ$Wm^{-1}K^{-2}$ and figure of merit of 4.8×10^{-3} at ambient temperature. All these excellent material properties of PZT suggest its application as an active material for the fabrication of printable nanoelectronic devices in large area.

5.2. Introduction

Recent developments and studies on the nanostructured semiconducting polymer–inorganic nanocomposites are receiving tremendous interest among researchers from academia and industry because they find applications in various high-tech areas. This is due to the synergistic properties arising from the molecular level mixing of semiconducting polymer and inorganic counterparts combined with

their flexibility, processability and light weight along with appreciable electrical conductivity and low thermal conductivity.[1–4] In semiconducting nanocomposites, conducting polymers possess unique features such as high mechanical flexibility, light weight, low-cost synthesis, solution processability, and printability over a large area, which may favour their application in light-emitting diodes,[5] transistors,[6] memory devices,[7] thermoelectric devices,[8] and photovoltaic cells.[9] Physical and chemical properties of conducting polymers can be controlled by tuning their chemical design and synthesis. Conducting polymers such as polyaniline, polythiophene, PEDOT–PSS, polyacetylene, polypyrrole, and their derivatives have a great potential for use in electronic and energy device applications.[10–13] Among the various conducting polymers, PEDOT has advantages such as optical transparency, ease of preparation, flexibility, thermal stability, and also tunable electrical conductivity by doping.[14]

Hierarchical nanostructured metal oxides have attracted considerable interest because of their potential applications in optoelectronic devices. Among the metal oxides, TiO_2 and ZnO have advantages such as ease of preparation, high charge carrier concentration, and mobility as well as controlled morphology.[15–17] Furthermore, they possess many inherent properties such as band gap of 3–3.39 eV and large exciton binding energy due to their electronic, chemical, and optical properties.[18–20] The development of hierarchical hetero-nanostructured metal oxides is receiving importance because of their improved optoelectronic properties and also the formation of various crystal defects (such as oxygen vacancies, zinc interstitials, and titanium interstitials), which plays an important role in improving the electronic structure, charge carrier, and surface properties of metal oxide.[21–24]

They can be prepared by several methods such as doping, metal deposition, surface sensitization, and coupling of semiconductors.[25–27] Recently we reported the development of hierarchical self-assembled porous microspheres of ZnO with a wurtzite crystal phase endowed with a large number defect states prepared by biocapping agent through the sol–gel process.[28] The resulting ZnO with a large number of oxygen and interstitials defects could enhance the scattering of the photon with relatively short wavelength and help to improve the performance of dye sensitized solar cell. Therefore, the preparation of hetero nanostructure materials with defect is expected to create a large density of interfaces in which phonon scattering can occur without compromising their charge carrier concentration and carrier mobility. Thus, they reduce the electron phonon mean free path, and the resulting hetero-nanostrucutres may reduce thermal conductivity, which is a parameter gaining interest in the development of electronic and energy devices.[29, 30]

Thermoelectric materials (TE) have tremendous potential applications in both power generation and solid-state cooling or heating. They are employed as novel energy harvesting systems in waste heat recovery. The conversion efficiency of a TE can be calculated by using the dimensionless figure of merit (ZT) given in equation (5.1)[31–35.]

$$ZT = \alpha^2 \sigma T / \kappa \qquad (5.1)$$

where α, σ, T, and κ are the Seebeck coefficient, electrical conductivity, temperature, and thermal conductivity, respectively.

Therefore, simultaneous increases of the electrical conductivity and Seebeck coefficient along with the reduction of thermal conductivity are favorable for the

enhancement of ZT. Recently significant improvements in ZT have been achieved in nanostructured materials such as superlattices, nanoinclusions, and nanocomposites by phonon scattering to reduce the thermal conductivity and without loss of Seebeck coefficient and electrical conductivity.[36, 37] In this context, we demonstrate the preparation of nanocomposites based on ZTO–PEDOT through a facile strategy by in situ polymerization of EDOT in the presence of ZTO. Hetero-nanostructured ZTO having a mixed crystalline phase of wurtzite ZnO and anatase TiO_2 was prepared by the sol–gel process in the presence of a biocapping agent. The interaction between the PEDOT and ZTO was studied by FT-IR, XRD, Raman spectral analysis, and morphological observation using microscopic techniques such as SEM, TEM, and AFM. Furthermore, we have studied the effect of ZTO on the electrical conductivity, carrier concentration and carrier mobility. Finally we demonstrated its application as a thermoelectric device having configuration Cu/PZTs/Cu and measured Seebeck coefficient, power factor and figure of merit of PZTs.

5.3. Results and Discussion

5.3.1. Preparation of Nanocomposite

PZTs nanocomposite containing semiconducting PEDOT and ZTO was prepared through a facile two step strategy as shown in Scheme 5.1. Initially ZTO was prepared by a sol-gel process using titanium isopropoxide and zinc acetate as precursors in presence of 3-pentadecylphenylphosphoricacid (PDPPA) as the biocapping agent. The formed ZTO was isolated by centrifugation and then rinsed with distilled water and ethanol, the obtained white powder was calcined at 600 °C. Further, ZTO was characterized for its particle size (50 nm), zeta potential (23 mV),

and surface area (45.3 m^2/g). The crystalline phase and size of ZTO crystallites were studied by XRD, the defect phase of hetero nanostrucutres (ZTO) was confirmed by Raman spectral analysis, and the morphology of prepared ZTO was studied by various microscopic techniques, which will be discussed in the later part of this chapter. Semiconducting nanocomposites (PZTs) were prepared by emulsion polymerization of EDOT in the presence of ZTO using ferric chloride anhydrous as oxidative initiator at room temperature. Nanocomposites with various compositions of ZTO were prepared under same condition and designated as PZT-2, PZT-3 and PZT-4. Isolation and purification was conducted as explained in the experimental part. Formation of nanocomposite and the interaction between the PEDOT and ZTO was confirmed by UV–visible, FT-IR, and Raman spectroscopy.

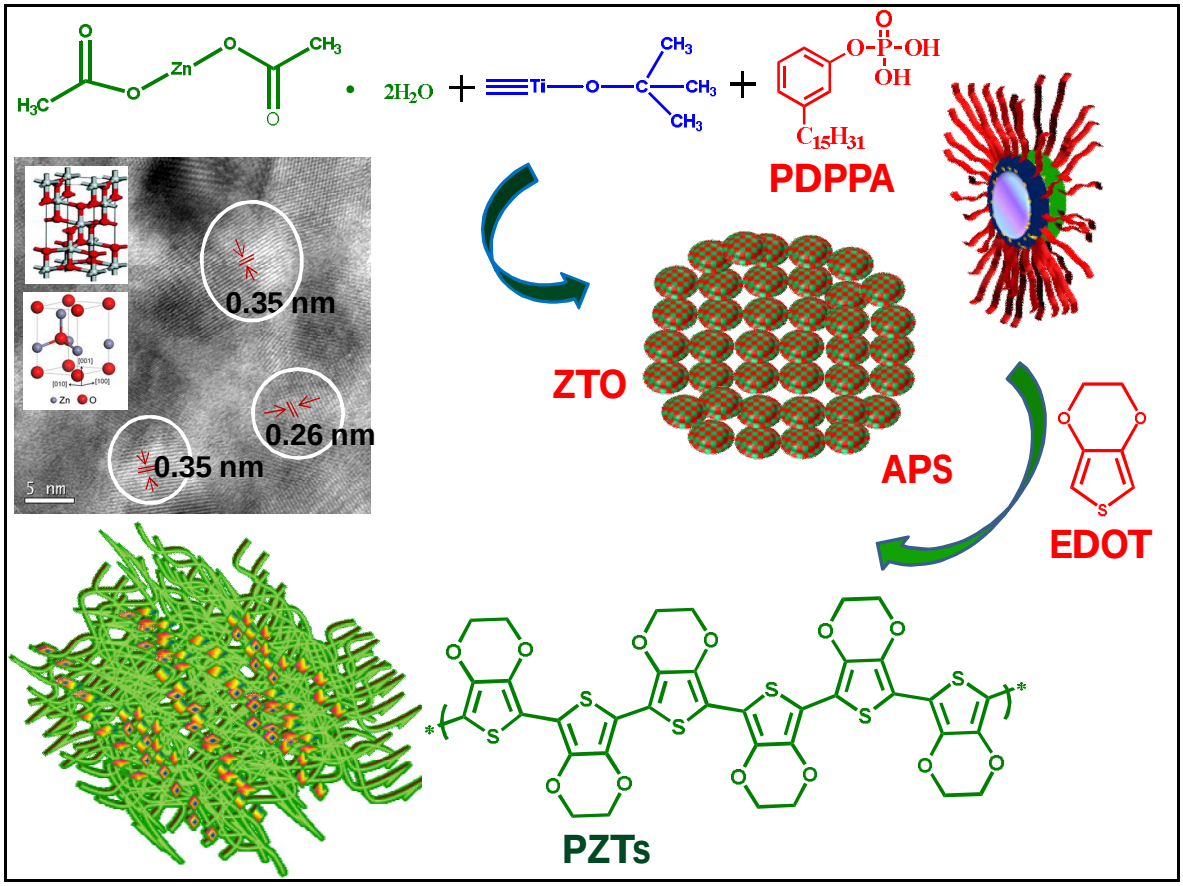

Scheme 5. 1. Preparation of PZTs nanocomposites

5.3.2. Optical Absorption Properties

The optical properties of the ZTO, PEDOT and PZTs nanocomposites were studied by UV–visible absorption spectroscopy. Figure 5.1(a) shows UV–visible spectra of the ZTO which exhibited an absorption maximum at 356 nm. In figure 5.1(b), PEDOT exhibited bands at 378 nm and a broad strong absorption band at 800–900 nm due to π–π * and polaron–π * transition. This indicates that PEDOT is in a bipolaronic state as well as the formation of a sufficient number of charge carriers.

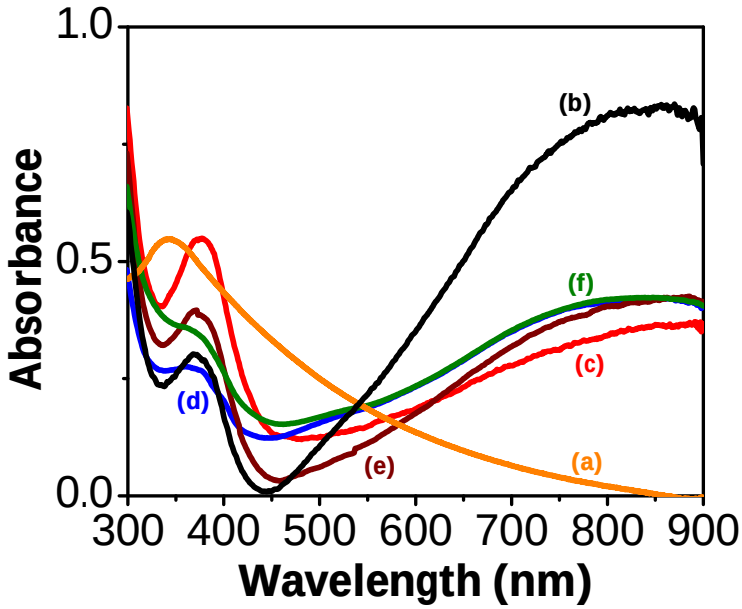

Figure 5.1. UV-visible spectra of (a) ZTO, (b) PEDOT, (c) PZT-1, (d) PZT-2, (e) PZT-3, and (f) PZT-4

The UV–visible spectra of nanocomposites PZT-1, PZT-2, PZT-3, and PZT-4 showed bands at 378, 376, 374, and 373 nm. The onset of the free carrier tail is shifted to higher wavelengths at 826, 829, 832, 838, and 842 nm, revealing the presence of the metallic state.[38] It was also observed that the UV–visible spectra of PZTs exhibited a free carrier tail with a shift in the polaron band revealing the presence of a high

density of charge carriers due to PEDOT and ZTO interactions. This is further supported by the electrical conductivity measurement.

5.3.3. FT-IR Spectral Analysis

The chemical structure and interaction among the moieties of ZTO and PZTs were studied by FT-IR spectroscopy. Figure 5.2(a-d) shows the FT-IR spectra of ZTO, PEDOT, PZT-1 and PZT-4, respectively. In figure 5.2(a), ZTO exhibited a band at 664 cm^{-1} due to the stretching of Ti–O–Ti. The sharp band at 1412 cm^{-1} can be attributed to the lattice vibrations of TiO_2. The absorption peak at 1627 cm^{-1} was caused by the bending vibration of coordinated H_2O as well as Ti–OH. Silent peaks observed at 3400, 1627, and 1246 cm^{-1} corresponding to the complete removal of the organic matter and the broad band observed at 573 cm^{-1} confirmed the formation of ZTO hetero-nanostructures.[16,17] Figure 5.2(b) shows the FT-IR spectrum of PEDOT. The bands observed at 688, 845, 926, and 983 cm^{-1} are attributed to the deformation modes of C–S–C in the thiophene ring. The bands at 1095, 1146, and 1212 cm^{-1} are associated with the C–O–C bending vibration of the ethylenedioxy moiety. The band at 1353 cm^{-1} is assigned to C–C stretching of the quinoidal structure. The bands at 1473 and 1517 cm^{-1} are due to the C=C stretching of the quinoid structure of the thiophene ring.[39, 40] The band at 1629 cm^{-1} can be attributed to the polarons present in PEDOT. Figure 5.2(c) shows the FT-IR spectrum of PZT-1 with a band at 1361 cm^{-1} corresponding to C–C stretching of the quinoidal structure. The observed bands at 1481 and 1524 cm^{-1} are due to the C=C stretching of the quinoid structure of the thiophene ring. Similar observation was also made for PZT-4. Generally all the prepared PZTs showed red shift with the increase in the amount of ZTO compared to the pure PEDOT, which is due to an

interaction of ZTO particles with PEDOT chains. Further, the interaction among the moieties was confirmed from Raman spectroscopic analysis.[38]

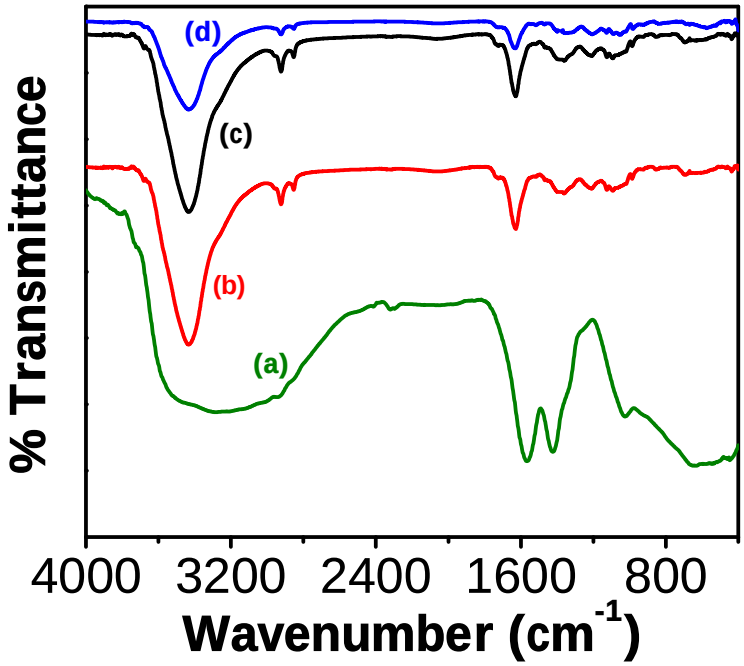

Figure 5.2. FT-IR spectra of (a) ZTO, (b) PEDOT, (c) PZT-1 and (d) PZT-4

5.3.4. Raman Spectral Analysis

The interactions and the presence of density variation in the defect states are further confirmed by Raman spectroscopy, which was measured using a 633 nm Ar^+ laser line at room temperature. Figure 5.3(a-f) shows Raman spectra of ZTO, PEDOT, PZT-1, PZT-2, PZT-3 and PZT-4, respectively. The Raman spectrum of ZTO exhibited bands at 144, 197, 400, 522, and 640 cm^{-1} (E_{g1}, E_{g2}, B_{g1}, A_{1g}, B_{1g}, and E_{g3}) which can be correlated to the anatase phase of titania. The bands observed at 144, 197 and 400 cm^{-1} can be assigned to the formation of oxygen vacancy in ZTO hetero-nanostructures.[41,42] Figure 5.3(b) shows the Raman spectrum of PEDOT, with a band at 1007 cm^{-1} corresponding to the deformation of the oxyethylene ring. The C–C inter-ring symmetric stretching band was observed at 1282 cm^{-1}, the band at 1348 cm^{-1} can be related to the C–C symmetric stretching and 1544 cm^{-1} can be

attributed to the out of plane bending of the ethylene dioxy ring of PEDOT chains. The strongest symmetric stretching band at 1449 cm^{-1} can be ascribed as due to C=C symmetric stretching of PEDOT chains. Furthermore, we observed bands at 446, 566, 724, and 850 cm^{-1} for PEDOT.[38, 43, 44] Figure 5.3(c) shows Raman spectrum of PZT-1 which showed major shifts in the band position in the conjugated C=C structure of PEDOT. The red shifts in the band positions at 1449 and 1544 cm^{-1} are due to the oxidized structure of PZT-1 segments compared with PEDOT. The band positions at 1282 and 1348 cm^{-1} are also slightly shifted in the C–C structure of PEDOT. The bands at 446, 566, 724, and 850 cm^{-1} also showed broadening of wavenumber. Details of shifts in the wavenumber of ZTO, PEDOT, PZT-1, PZT-2, PZT-3, and PZT-4 are given in Table 5.1. All these observed shifts in the bands of PZTs confirm the interaction between PEDOT and ZTO hetero nanostructures in the nanocomposites.[38] The interaction increased the conjugation length of the PEDOT chain and also improved the electrical conductivity of nanocomposites.[44]

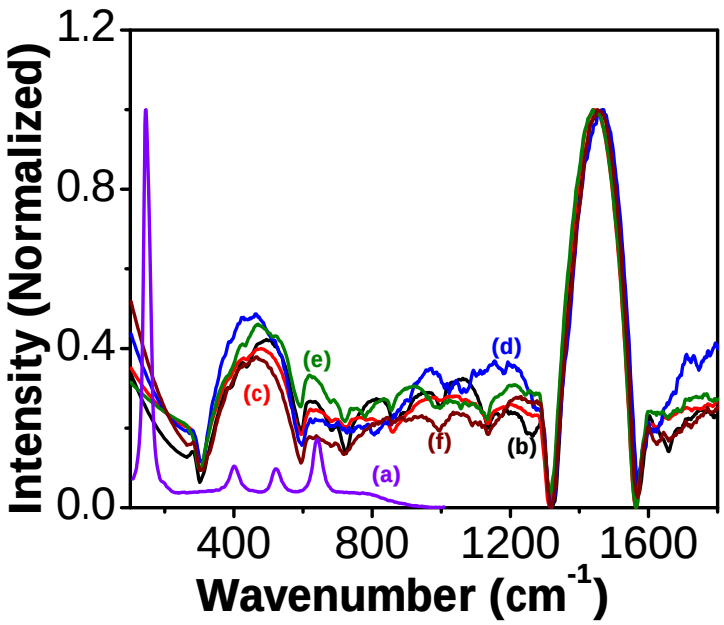

Figure 5.3. Raman spectra of (a) ZTO (b) PEDOT, (c) PZT-1, (d) PZT-2, (e) PZT-3, and (f) PZT-4

Similar observations were made for PZT-2, PZT-3, and PZT-4 as shown in Figure 5.3, spectra d–f, respectively. The intensities of these symmetric stretching peaks vary with the nanocomposites, which confirms the electrons are more delocalized on the conjugated backbone of PEDOT and agrees with the result observed in UV–visible spectra.[38]

Table 5.1. Details shift in the wavenumber of ZTO, PEDOT and PZTs

Sl. No	Sample code	Intensity (cm^{-1})
1	PEDOT	446,566,724,850,1007,1143,1282,1348,1449,1544
2	PZT-1	443,560,717,852,998,1143,1267,1341,1436,1534
3	PZT-2	344,450,560,739,970,1156,1272,1345,1452,1534
4	PZT-3	445,582,733,847,982,1130,1263,1345,1445,1550
5	PZT-4	443,569,862,1014,1130,1260,1348,1445,1534
6	ZTO	144,197,400,522,640

5.3.5. X-ray Diffraction Analysis

Crystalline phase of the prepared ZTO and PZTs were studied by XRD technique, and the XRD patterns of the ZTO, PEDOT, PZT-1, PZT-2, PZT-3, and PZT-4 are shown in Figure 5.4 A(a–f). XRD patterns of ZTO nanostrucutres, Figure 5.4A(a) showed characteristic sharp peaks at 2θ = 25.2°, 30.3°, 32.3°, 34.9°, 37.8°, 47.6°, 53.6°, 54.5°, 56.7°, and 69.1°. These peaks are indexed by Miller indices as (101), (100), (002), (004), (200), (105), (211), and (103) planes with the d-spacing characteristic of heterocrystalline anatase and wurtzite phase of titania and ZnO.[16,17] Figure 5.4A(b) shows the XRD profile of PEDOT, which showed peaks at 2θ = 6.2°, 12.2°, and 18.2° and a broad peak at 25.5° (d = 3.5 Å) attributed to the crystalline nature of PEDOT with highly ordered π–π interaction of conjugated units

of the PEDOT chains.[45] Figure 5.4A(c) shows the XRD pattern of PZT-1 nanocomposites, which exhibited peaks at 2θ = 6.2°, 12.3°, 18.7°, 25.3°, 30.5°, 34.9°, 37.8°,47.7°, 54.2°, and 62.3° corresponding to the characteristic peaks of PEDOT and ZTO. However, as the amount of ZTO increased in PZTs, it exhibited only a small deviation in the assigned peaks of ZTO as shown in Figure 5.4A(d–f). Wide angle X-ray scattering (WAXS) of PEDOT and PZTs is shown in Figure 5.4B (a-d).The observed results suggest that the molecular arrangement or interchain stacking of PEDOT chains in the nanocomposites becomes more ordered, and also it reduced the interchain hopping distance. This can be attributed to the measured hike in the electrical conductivity of nanocomposites, which will be discussed later under electrical conductivity.

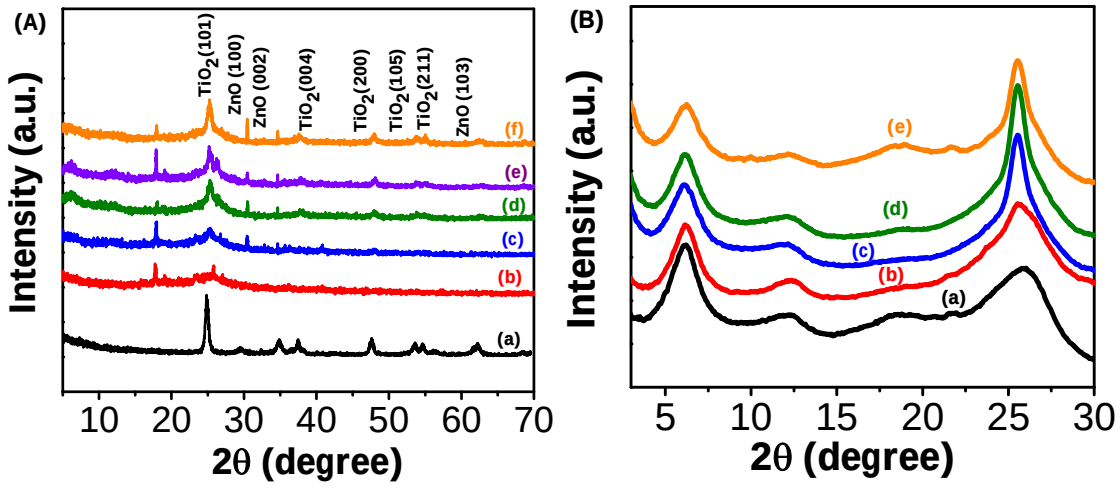

Figure 5.4. (A) XRD of (a) ZTO, (b) PEDOT, (c) PZT-1, (d) PZT-2, (e) PZT-3, and (f) PZT-4; **(B)** WAXS of (a) PEDOT, (b) PZT-1, (c) PZT-2, (c) PZT-3 and (d) PZT-4

5.3.6. Morphological Analysis

Morphology of the prepared ZTO hetero-nanostructure was characterized by HR-TEM and AFM images as shown in Figure 5.5 (a, b). The HR-TEM image of ZTO exhibited hierarchical aggregates of tetragonally oriented well defined clusters of spheres. The AFM image showed that each tetragonal column is composed of well aggregates of spheres. Figure 5.5c shows EDS of ZTO which confirms the presence of ZnO and titania in ZTO. The grain size or particle size of ZTO nanostructure were measured as 15–20 nm, and the grain boundaries between the nanoparticles are well-defined and very close together.

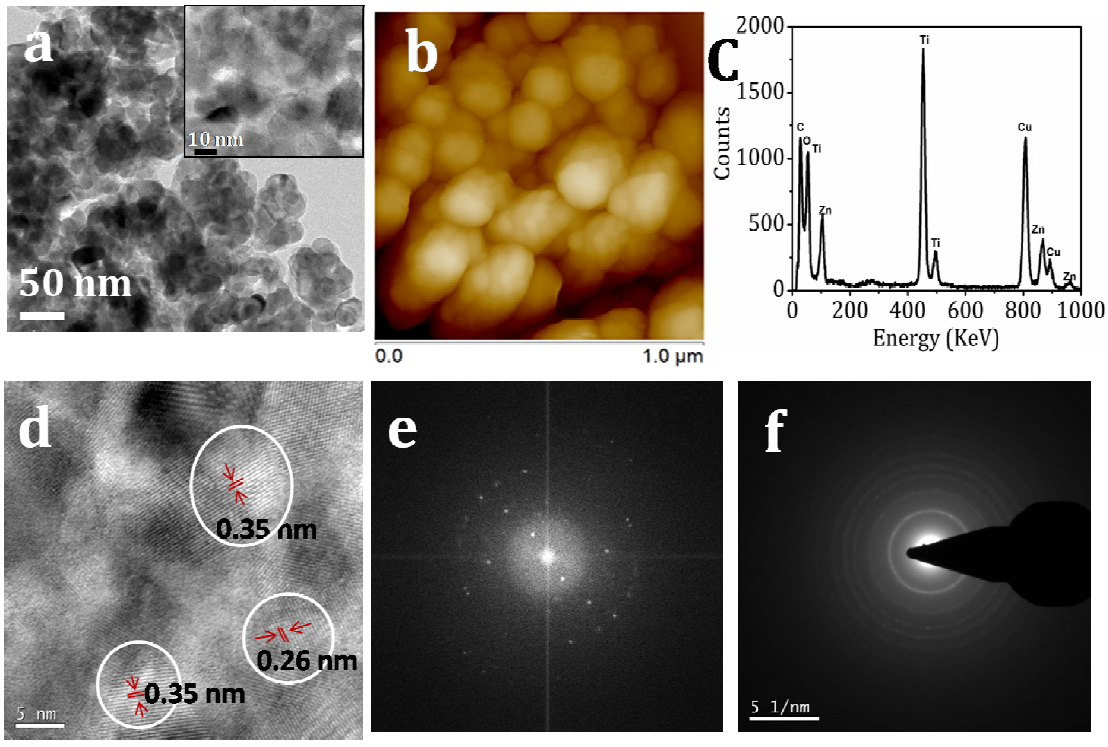

Figure 5.5. (a) HR-TEM (inset higher magnification), (b) AFM, (c) EDS, (d) HR-TEM, (e) FFT, and (f) SAED images of ZTO nanostructures

The HR-TEM image of ZTO is shown in Figure 5.5d, which showed clear and identical crystallographic orientations of the titania and ZnO with lattice fringes of 0.35 and 0.26 nm, concurring well with interplanar spacing of (101) and (002)

crystallographic planes of anatase titania and hexagonal wurzite phase of ZnO. These results strengthened the observation made during XRD analysis. Panels e and f of Figure 5.5 show the FFT and SAED images of ZTO, revealing polycrystalline type electron diffraction pattern of ZTO hetero nanostrucutres.

Further morphological analyses of PZTs were studied by using SEM, HR-TEM, and AFM. SEM and TEM pictures of PZTs nanocomposites are shown in Figures 5.6 and 5.7, respectively. Figure 5.6a shows the SEM image of PEDOT, which consists of self-assembled nanosheet like features. Further morphology of PEDOT was confirmed by HR-TEM as shown in Figure 5.7a, which shows the formation of nanosheets. SEM and HR-TEM images of PZT-1, PZT-2, PZT-3, and PZT- 4 are shown in Figure 5.6, panels b–e, and Figure 5.7, panels b–e, respectively. PZT-1 with low concentration of ZTO exhibited uniform dispersion of ZTO in PZT-1. As the amount of ZTO increases, it shows well defined self assembled PEDOT-ZTO nanostructures. The grain size of ZTO nanostructures inside the polymer matrix measured as 8–10 nm. The contrast in the image of TEM is due to difference in the electron migration through the organic and inorganic particles present in PZT-1. Dark portions correspond to the presence of ZTO, whereas light portion related to the presence of PEDOT in PZTs. As the amount of ZTO increased in the PZT nanocomposites, the size of the ZTO hetero-nanostructures inside the PZT-2 increased to 10–12 nm. Similarly, the size of ZTO hetero-nanostructure enlarged to 16 and 20 nm in PTZ-3 and PZT-4. Figure 5.6f shows the energy dispersive spectrum (EDS) of PZT-4, which showed the presence of sulfur, Zn, and Ti. Figure 5.7(f, g) shows the HR-TEM image of PTZ-4 recorded at higher magnification. This confirms the preservation of

crystalline phase of ZTO in PZT, and the FFT pattern of PZT-4 showed a bright dotted circle corresponding to the ordered phase of ZTO in PZT.

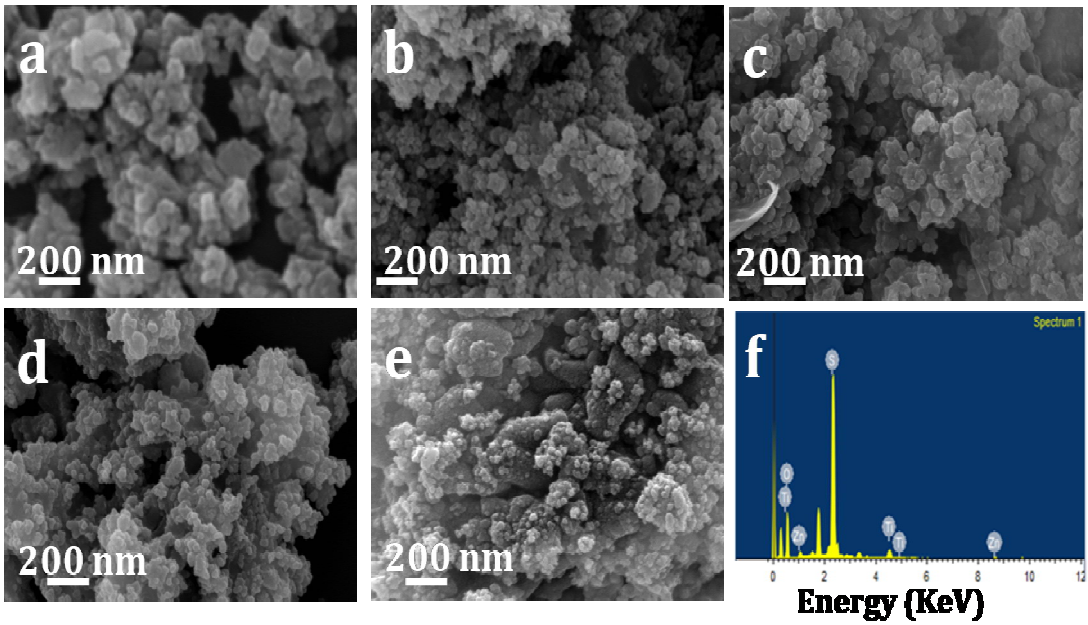

Figure 5.6. SEM images of (a) PEDOT, (b) PZT-1, (c) PZT-2, (d) PZT-3, (e) PZT-4, and (f) EDS of PZT-4.

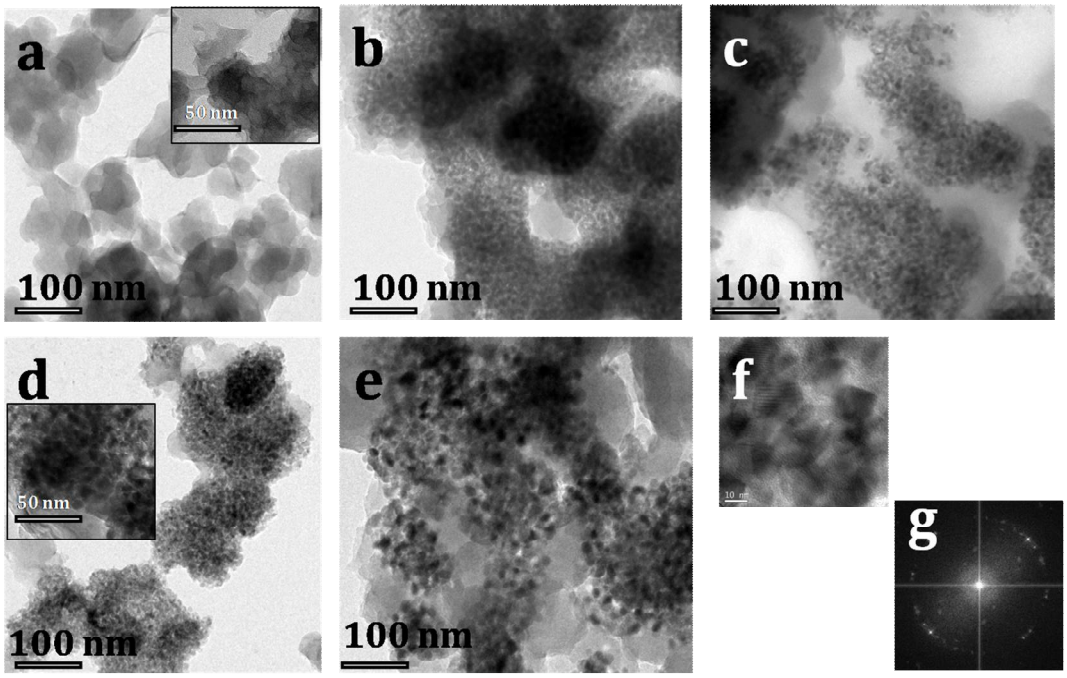

Figure 5.7. HR-TEM images of (a) PEDOT (inset higher magnification), (b) PZT-1, (c) PZT-2, (d) PZT-3 (inset higher magnification), and (e) PZT-4, (f) high-magnification image of PZT-4, and (g) FFT pattern of PZT-4

The morphology was confirmed further by recording the AFM images, and the height profile of PZTs nanocomposites are shown in the panels Figure 5.8 (a–f), respectively. The AFM image of PEDOT reveals a highly ordered nanosheet-like structure. The height profile of the PZT-1 is shown in the order of 30–40 nm with root-mean-square surface roughness of 3.8 nm.

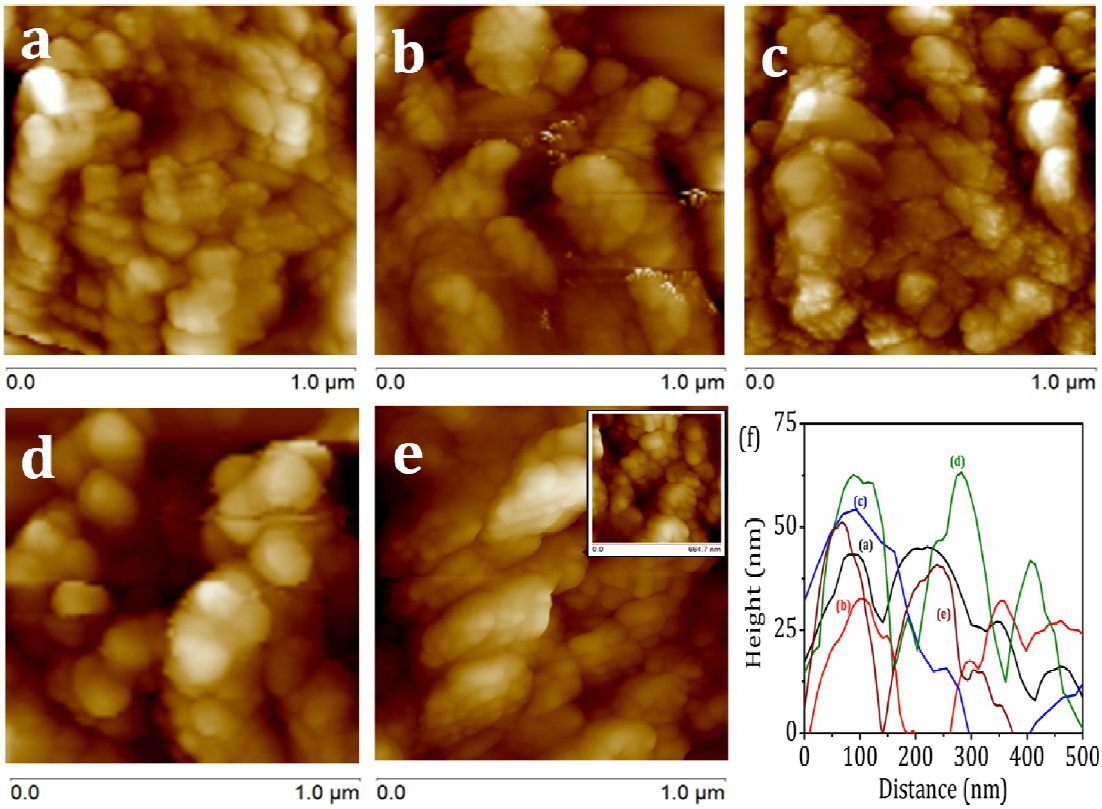

Figure 5.8. AFM images of (a) PEDOT, (b) PZT-1, (c) PZT-2, (d) PZT-3, (e) PZT-4 (inset higher magnification) and (f) height profile of PTZs

AFM images of PZT-1, PZT-2, PZT-3, and PZT-4 are matched well with the observations made by HR-TEM and SEM. The height profile of the same was measured as ~30 nm with a root-mean square surface roughness of ~5.2 nm. Similar observations were made with PZT-2, PZT-3, and PZT-4, respectively. The height profile of hybrid nanocomposites increased from 55 to 63 nm and decreased to 52 nm for PZT-2, PZT-3, and PZT-4, respectively. The root mean square surface

roughness values were measured as 6.4, 7.2, and 7.8 nm for PZT-2, PZT-3, and PZT-4. Morphology studies revealed that ZTO nanostructures embedded into the PEDOT matrix effectively reduced the grain size hopping barriers and increased the number of the grain boundary for scattering of long-wavelength phonons.[29, 46, 47] At the same time the HR-TEM picture of PZTs showed the extended sheets of PEDOT chains decorated with well-ordered ZTO hetero-nanostructures. In PZTs the PEDOT chains are in the extended aggregated or linear morphology, thereby enhancing the hopping rate in the polymer chain and improving the electrical conductivity without compromising the Seebeck coefficient as well as reducing the thermal conductivity.

5.3.7. Electrical Conductivity

Electrical conductivity of nanocomposites was measured at variable temperatures using a four-probe conductivity meter. Temperature dependent electrical conductivity was investigated in the range from 303 to 383 K. Figure 5.9A, curves a–e, shows the temperature dependent electrical conductivity of PEDOT, PZT-1, PZT-2, PZT-3, and PZT-4, respectively. Electrical conductivity of PEDOT was measured 14.47 S/cm at 303 K and 19.27 S/cm at 383 K. Electrical conductivity measurement of PZTs revealed that conductivity showed a hike in its values with increasing amount of ZTO in the nanocomposite. The electrical conductivity of PZT-1 was measured 19.32 S/cm at 303 K and 34.09 S/cm at 383 K compared to PEDOT. Electrical conductivity of PZT-2, PZT-3, and PZT-4 showed values in the range of 27.08, 40.62, and 52.03 S/cm at 303 K and 53.79, 66.34, and 71.08 S/cm at 383 K, respectively. The electrical conductivity of PZT-4 at 303 K measured as 3 orders of magnitude higher than the PEDOT. The reason for the improved electrical conductivity is mainly because of the increasing amount of ZTO in nanocomposites,

which may allow the PEDOT molecular chains to undergo a transition from compact coil to extended or linear conformation, thereby enhancing the hopping rate in the polymer chain. Another possible reason is the presence of charge carriers induced by hetero-nanostrucutres of ZTO. The interaction between the π-system of PEDOT chains with ZTO is expected to enhance the charge carrier mobility and electrical conductivity of nanocomposites.[48–50]

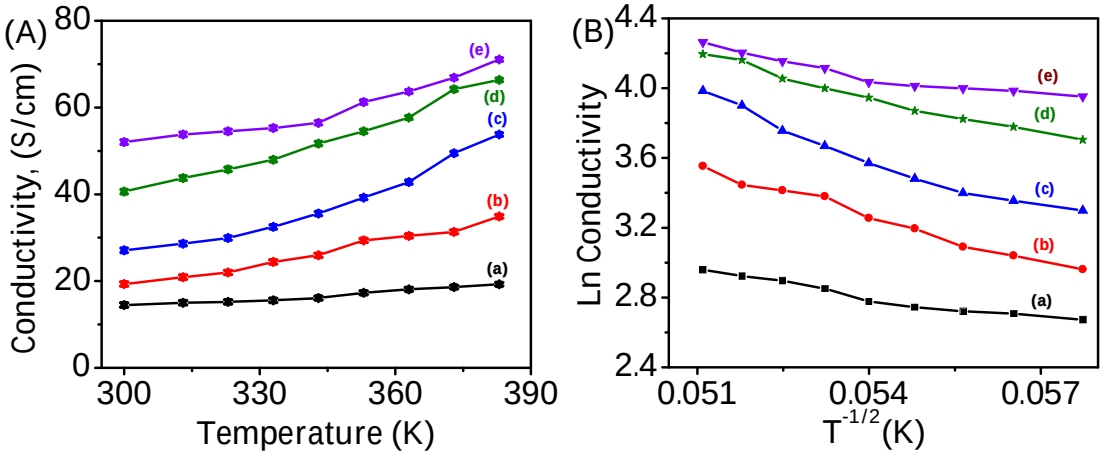

Figure 5.9. (A) Electrical conductivity versus temperature; **(B)** logarithmic plot showing the temperature-dependent electrical conductivity of (a) PEDOT, (b) PZT-1, (c) PZT-2, (d) PZT-3, and (e) PZT-4.

Figure 5.9B, curves a–e, shows the logarithmic plot of temperature-dependent electrical conductivity of PEDOT, PZT-1, PZT-2, PZT-3, and PZT-4, respectively. Temperature-dependent electrical conductivity can be described by Mott's variable range hopping (VRH) model.[12] The general form of the VRH mechanism is given in equation (5.2)

$$\sigma = \sigma_0 \exp\left[-(T/T_0)^{1/n}\right] \qquad (5.2)$$

where T_0 is the characteristic Mott temperature related to electron wave function localization degree and σ_0 is the high temperature limit of conductivity. The value of n is assigned as 2, 3, or 4 for one, two, or three-dimensional systems, respectively.

T_0 values are estimated by fitting the above equation (2). It is observed that the T_0 decreases with increasing amount of ZTO, revealing that the carrier hopping barrier decreases in PZTs, which results in increases in the electrical conductivity.

According to the VRH model, the average hopping distance (R_{hop}) and the activation energy (E_{hop}) are given in equation (5.3) and (5.4),

$$R_{hop} = (3/8) \times (T_0/T)^{1/4} L \quad (5.3)$$

$$E_{hop} = (1/4) \times KT(T_0/T)^{1/4} \quad (5.4)$$

where L is the localization length. The localization length of the EDOT monomer unit is ~2.29 Å.[51]

At room temperature, R_{hop} values for PEDOT, PZT-1, PZT-2, PZT-3, and PZT-4 are calculated from equation 3, and the average hopping distances are 0.66, 0.64, 0.60, 0.54, and 0.53 Å, respectively. At room temperature, E_{hop} values are estimated for PEDOT, PZT-1, PZT-2, PZT-3, and PZT-4 in the range of 64.60, 76.62, 79.94, 83.31, and 84.9 meV. The results suggested that a decrease in the hopping distance and an increase in activation energy are responsible for the observed enhancement in the conductivity of prepared PZT nanocomposites.[12, 51]

5.3.8. Hall Measurement Properties

The interaction between the π-system of PEDOT chains with ZTO is expected to enhance the charge carrier mobility and electrical conductivity of nanocomposites. To gain a scientific understanding for the observed enhancement, the electrical conductivity of nanocomposites was studied by measuring the Hall coefficient (R_H), carrier concentration (n), and carrier mobility (μ) using Hall measurement. A Hall Effect measurement system with a magnetic field of −9 to +9 T and an electric current of 1 mA with a good Ohmic contact was established using

silver electrodes. Hall Effect measurements were carried out on rectangular pieces of the samples. The voltage probes were connected perpendicular to the current probes and the center, keeping the applied field perpendicular to the plane of the sample. The Hall coefficient (R_H) was calculated from the slope value of resistivity versus applied magnetic field plot. The R_H values were found to be PEDOT, 4.13×10^{-2} m^3 C^{-1}; PZT-1, $5.16\times10^{-2} m^3$ C^{-1}; PZT-2, 2.37×10^{-2} m^3 C^{-1}; PZT-3, 1.8×10^{-2} m^3 C^{-1}; and PZT-4, 1.637×10^{-2} m^3 C^{-1}. The positive R_H values indicate that the majority charge carriers are holes (p-type). The positive sign value of the Seebeck coefficients in both PEDOT and PZTs was related to the holes (p-type) character of the semiconductor.

On the basis of the band model, the carrier concentration (n) can be estimated by substituting the Hall coefficient (R_H) values in the equation (5.5),

$$n = 1/(e \times R_H) \qquad (5.5)$$

where e = electronic charge and R_H = Hall coefficient.

The charge carrier concentrations were calculated for PEDOT, 1.52×10^{20} cm^{-3}; PZT-1 $1.97\times10^{20} cm^{-3}$; PZT-2, 2.63×10^{20} cm^{-3}; PZT-3, 3.48×10^{20} cm^{-3}; and PZT-4, $3.92\times10^{20} cm^{-3}$. Charge carrier mobility was calculated from the values of electrical conductivity using equation (5.6),

$$\sigma = n \times e \times \mu \qquad (5.6)$$

where σ = electrical conductivity, n = charge carrier concentration, e = electronic charge, and μ = carrier mobility.

The carrier mobilities were calculated for PEDOT, 0.58 cm^2 V^{-1} S^{-1}; PZT-1, 0.62 cm^2 V^{-1} S^{-1}; PZT-2, 0.65 cm^2 V^{-1} S^{-1}; PZT-3, 0.74 cm^2 V^{-1} S^{-1}; and PZT-4, 0.83 cm^2 V^{-1} S^{-1}. Figure 5.10 shows the room temperature Hall measurement of carrier

concentration and mobility as a function of the ZTO (wt %). The observed higher electrical conductivity was mainly because of increased charge carrier concentration and charge carrier mobility in the PZTs.[52–54] The increase of charge concentration in the PZTs reduces the energy band gap, which leads to the decreases in the Seebeck coefficient. The band gaps of PEDOT and PZTs were calculated from electrochemical studies and showed that the band gap decreased to 2.24, 2.13, 2.04, 1.896, and 1.72 eV, which confirmed the effective reduction of band gap with increasing ZTO (wt %) in nanocomposites.

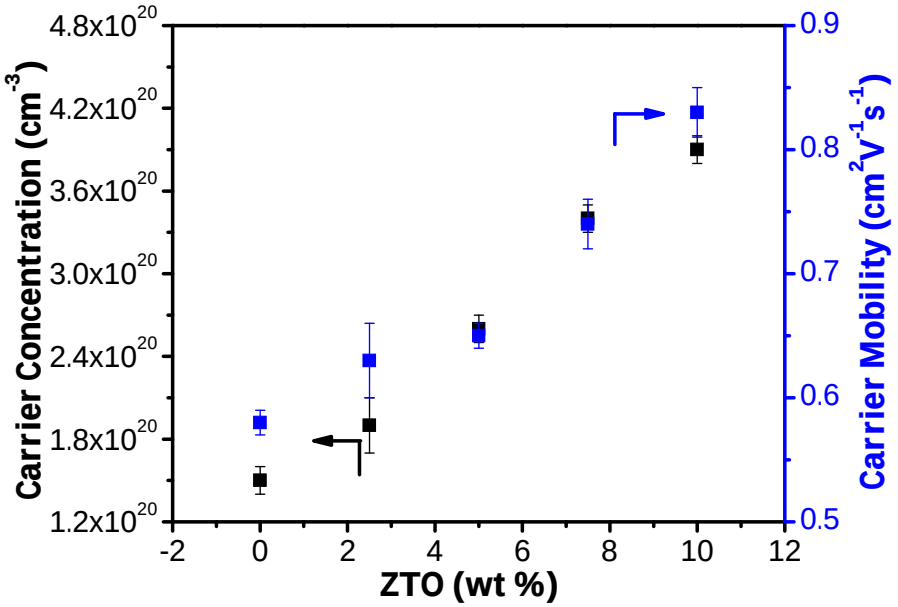

Figure 5.10. Carrier concentration and mobility as a function of the ZTO (wt %)

5.3.9. Thermoelectric Properties

Thermoelectric properties such as Seebeck coefficient, thermal conductivity, Power factor, and figure of merit of PEDOT and PZTs were evaluated from the data obtained from the temperature-dependent measurement. We have performed all these experiments with five devices for each sample, and the results were found to be reproducible. The Seebeck coefficient, thermal conductivity, power factor, and ZT

were plotted with standard deviation errors. The Seebeck coefficient is a measure of the magnitude of an induced thermoelectric voltage in response to the temperature difference across the material. This value can be positive for holes and negative for electrons as charge carriers. The temperature-dependent Seebeck coefficients of PEDOT and PZTs are shown in Figure 5.11(A). The Seebeck coefficient of PEDOT increased with temperature in the range of 303–383 K. The Seebeck coefficient of PEDOT was observed as 17.3698 μV/K at 303 K and 21.3399 μV/K at 383 K. However, nanocomposites showed enhanced values of 18.3561 and 19.0568 μV/K at 303 K and 21.8514 and 24.0723 μV/K at 383 K for PZT-1 and PZT-2, respectively. Further increasing the amount of ZTO yielded decrease in the values of Seebeck coefficients for PZT-3 (16.9258 μV/K at 303 K, 15.7356 μV/K at 383 K) and PZT-4 (15.8356 μV/K at 303 K, 19.1669 μV/K at 383 K). Due to thermal fluctuations, the thermally excited charge carriers constantly diffuse away from the hot end and produce entropy by drifting towards the cold end of the device. The observed initial increase in the values of Seebeck coefficients of PZTs may be due to the presence of ZTO with a large number of grain boundaries, which may generate higher surface roughness in the PZTs and reduce the band gap. On increasing the ZTO wt % in the PZTs, the high surface roughness leads to strong carrier scattering and also caused the charge carrier filtering effect.[55, 56] This result is substantiated by the observation made during the morphological studies.

Figure 5.11B shows the temperature-dependent thermal conductivity of PEDOT, PZT-1, PZT-2, PZT-3, and PZT-4 hybrid nanocomposites. The temperature-dependent thermal conductivity increases with hike in temperature and also showed variation with respect to the increase in the amount of ZTO. Thermal

conductivity of the PEDOT was evaluated as 0.1893 W/mK at 303 K and 0.1896 W/mK at 383 K. In the case of nanocomposites, the thermal conductivities were 0.0495, 0.0617, 0.1308, and 0.1485 W/mK at 303 K and 0.0506, 0.0796, 0.1149, and 0.1335 W/mK at 383 K for PZT-1, PZT-2, PZT-3, and PZT-4, respectively.

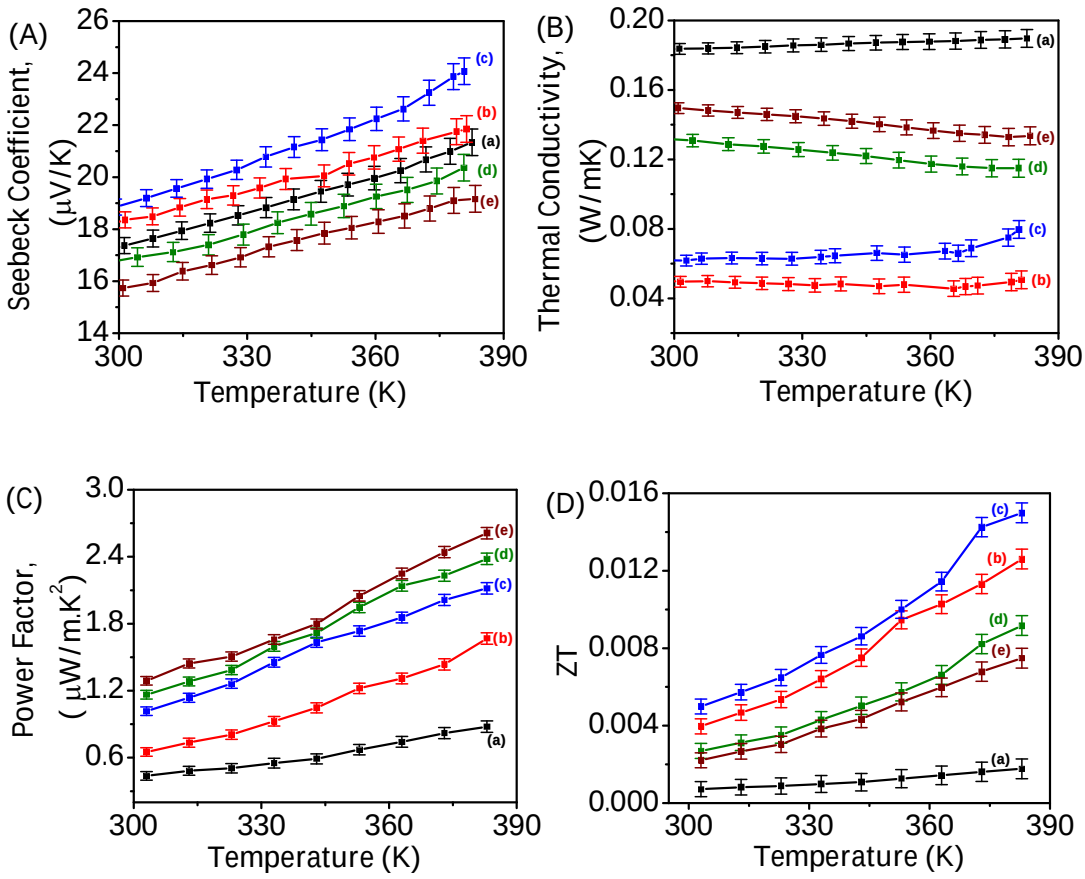

Figure 5.11. (A) Seebeck coefficient, **(B)** thermal conductivity, **(C)** power factor, and **(D)** figure of merit for (a) PEDOT, (b) PZT-1, (c) PZT-2, (d) PZT-3, and (e) PZT-4

In the present work, PZTs nanocomposites form well-defined nanointerfaces, which may act as the effective scattering centers of phonons and then decrease thermal conductivity. This observation is supported by the previous theoretical and experimental investigations made by other researchers, and they suggested that the nanostructures, including nanoinclusions and nanointerfaces in composites, can scatter phonons and reduce thermal conductivity.[57] Another possible reason for

reduced thermal conductivity behavior is due to the large number of grain boundaries created by ZTO hetero-nanostructures on PEDOT layers, which act as effective phonon scattering centers and thereby reduce thermal conductivity.[47] The intrinsically low thermal conductivity of nanocomposites provides great potential for TE applications.

The performance of the TE depends on the power factor. The power factor (PF) is calculated from the values obtained from the Seebeck coefficient and electrical conductivity. The PF is described as $PF = \alpha^2\sigma$. The temperature-dependent PF values of PEDOT and PZT nanocomposites increased with respect to temperature and are shown in Figure 5.11C. The PF of PEDOT was calculated as $0.4367\ \mu W/K^2{\cdot}m$ at 303 K and $0.8779\ \mu W/K^2{\cdot}m$ at 383 K. The PF value increased with increasing amount of ZTO hetero-nanostructure content in the PZTs. The PF values of PZT-1, PZT-2, PZT-3, and PZT-4 were found in the range of 0.6511, 1.0165, 1.1637, and $1.2885\ \mu W/K^2{\cdot}m$ at 303 K and 1.6673, 2.1173, 2.3806, and 2.6115 $\mu W/K^2{\cdot}m$ at 383 K, respectively. The highest PF was observed for PZT-4, and it is 2 times higher than that of PEDOT. These results demonstrate that the presence of ZTO has a great influence on the power factor of nanocomposites.[58, 59]

Figure 5.11D shows the effect of temperature on the figure of merit of PEDOT, PZT-1, PZT-2, PZT-3, and PZT-4 nanocomposites. ZT values of PEDOT and PZTs increased with rising temperature. The ZT values observed for PEDOT, PZT-1, PZT-2, PZT-3, and PZT-4 were 7.2×10^{-4}, 3.9×10^{-3}, 4.8×10^{-3}, 2.7×10^{-3}, and 2.21×10^{-3} at 303 K and 1.77×10^{-3}, 1.26×10^{-2}, 1.49×10^{-2}, 9.17×10^{-3}, and 7.49×10^{-3} at 383 K, respectively. In PZT the presence of conductive ZTO along with PEDOT produces more charge carriers and hence observed higher electrical conductivity.

Also, ZTO created large numbers of grain boundaries, which may generate more phonon scattering centers and reduced thermal conductivity. Furthermore, the extensive interface created by the p–n junction of p-type PEDOT chains embedded within the n-type ZTO hetero-nanostructures are responsible for the observed enhancement in the electrical conductivity and also reducing the thermal conductivity by phonon scattering. Our observations are supported by the work done by other researchers.[60–62]

5.4. Conclusions

In summary, we have successfully prepared semiconducting PZTs nanocomposites having highly extended PEDOT chains interfacing with ZTO hetero-nanostructures through a facile strategy. The synergistic effect of nanocomposite exhibited it as an efficient active material for nanoelectronic devices with excellent charge carrier concentration (3.92×10^{20} cm^{-3}), charge carrier mobility (0.83 cm^2 V^{-1} S^{-1}), electrical conductivity of (52 Scm^{-1}), low thermal conductivity (0.0495 W/mK), Seebeck coefficient (19.05 μVK^{-1}), and power factor (1.28 μW K^{-2} m^{-1}). The power factor of PZT-4 was evaluated as 2 orders higher magnitude than that of the pure PEDOT. The nanocomposites showed maximum ZT values of 4.8×10^{-3} at 303 K and 1.49×10^{-2} at 383 K in a thermoelectric device fabricated with the configuration Cu/ PZT/Cu.

5.5. Experimental Section

5.5.1. Materials

Zinc acetate dihydrate and xylene were purchased from Sd.fine Chem. Ltd., Mumbai, India. Titanium isopropoxide, ferric chloride anhydrous ($FeCl_3$), and 3,4-ethylenedioxythiophene (EDOT) were purchased from Sigma-Aldrich Chemicals,

Bangalore, India. Butanol and all solvents of analytical grade were purchased from Merck India Ltd., Mumbai, India.

5.5.2. Synthesis of Hetero Nanostructured ZnO–TiO_2 (ZTO)

ZTO nanostructured materials were prepared as follows; initially 0.88 mL (2.97 mmol) of titanium isopropoxide in a solution of 10 mL ethanol and 10 mL water was refluxed at 70 °C for 2 h. Then titania solution was added dropwise to the solution of zinc acetate dihydrate 0.432 g (1.97 mmol) and PDPPA 0.053 g (0.14 mmol) in a mixture of m-xylene (10 mL) and butanol (10 mL) under vigorous stirring and the reaction was continued for 20 hours. The solution turned into a cloudy white precipitate and the formed white precipitate was separated by centrifugation at 2500 rpm for 20 min. Then it was rinsed with distilled water and ethanol. Finally prepared ZTO was calcined at 600 °C.

5.5.3. Preparation of PEDOT–ZTO Nanocomposites (PZT)

PZTs were prepared by oxidative emulsion polymerization of EDOT in the presence of ZTO using ferric chloride anhydrous as initiator at room temperature. An amount of 0.033 g of ZTO nanostructure was ultrasonically dispersed in 25 mL of double-distilled water. EDOT (0.67 mL, 6.2 mmol) was added to the dispersion, and stirring was continued for 10 min. $FeCl_3$ anhydrous (2.30 g, 8.5 mmol in 10 mL of water) was added dropwise to the solution under vigorous stirring in an ice bath, and the reaction was continued for 24 h. After completion of the reaction, the resulting precipitate was separated by centrifugation at 5000 rpm for 20 min and washed several times with distilled water to remove the unreacted monomer. Finally, the hybrid composite was dried at 60 °C under vacuum and designated as PZT-1. Similarly, PZTs were prepared with different weight percentages of ZTO in

the EDOT under the same conditions and designated as PZT-2, PZT-3, and PZT-4. For comparison, PEDOT was also prepared under the same conditions without ZTO. Experimental details are given in Table 5.2.

Table 5. 2. Experimental details of the preparation of nanocomposites

Sl. No	Sample	EDOT (mmol)	ZTO (g)	$FeCl_3$ anhydrous (mmol)
1	PEDOT	6.2	-	8.5
2	PZT-1	6.2	0.033	8.5
3	PZT-2	6.2	0.066	8.5
4	PZT-3	6.2	0.099	8.5
5	PZT-4	6.2	0.133	8.5

5.5.4. Characterization Techniques

Description of FT-IR and XRD analysis are given in Section 2.6 of Chapter 2. Details of opto-electronic spectra, Raman spectra, SEM, TEM and AFM analysis are given in Section 3.6 of Chapter 3. WAXS measurements were performed with an XEUSS SAXS/WAXS system using a Genix microsource from Xenocs operated at 50 kV and 0.6 mA. The Cu Kα radiation (λ = 1.54 Å) was collimated with FOX2D mirror and two pairs of scatter less slits from Xenocs. The sample to detector distance which was calibrated with silver behenate standard was 214.5 mm for WAXS analysis. Electrical conductivity measurements were performed with a standard four-probe conductivity meter using a Keithely 6221 programmable current source and a 2128A nanovoltmeter. The samples were pressed into an 11 mm diameter disk for the measurement. Thermal conductivity and Seebeck coefficient measurements were performed using a thermal transport puck attached to a

physical property measurement system (Quantum Design, Dynacool). For measurements, the samples were pressed in the form of pellets of approximately 6.5 mm diameter. The pellet was then sandwiched between gold-coated copper disks from which heater, thermometer, sample current, and voltage connections were drawn. For thermal conductivity and Seebeck coefficient measurements, heat is applied to one end of the sample by running current through the heater. The temperatures T_{hot} and T_{cold} are measured at the thermometer shoes. Seebeck voltage is also monitored ($\Delta V = V^{+} - V^{-}$) during the heat pulse. The heat of the sample flows to the cold foot. The measurements were performed in the temperature range from 300 to 385 K. The room temperature Hall measurement was carried out using the Physical Property Measurement System (Quantum Design). The Hall Effect measurement system had a magnetic field of −9 to +9 T and an electric current of 1 mA with a good Ohmic contact established using silver electrodes. Hall Effect measurements were carried out on rectangular pieces of the samples. The voltage leads were connected perpendicular to the current leads and the center, keeping the applied field perpendicular to the plane of the sample.

5.6. References

1. V. M. Agranovich, Y. N. Gartstein and M. Litinskaya, *Chem. Rev*. **2011**, *111*, 5179.

2. B. T. McGrail, A. Sehirlioglu and E. Pentzer, *Angew. Chem. Int. Ed.* **2015**, *54*, 1710.

3. C. Janáky and K. Rajeshwar, *Prog. Polym. Sci*. **2015**, *43*, 96.

4. Y. Du, S. Z. Shen, K. Cai and P. S. Casey, *Prog. Polym. Sci*. **2012**, *37*, 820.

5. G. Qian, Z. Zhong, M. Luo, D. Yu, Z. Zhang, Z. Y. Wang and D. Ma, *Adv. Mater*. **2009**, *21*, 111.

6. H. R. Tseng, H. Phan, C. Luo, M. Wang, L. A. Perez, S. N. Patel, L. Ying, E. J. Kramer, T. Q. Nguyen and G. C. Bazan, et al. *Adv. Mater*. **2014**, *26*, 2993.

7. L. H. Xie, Q. D. Ling, X. Y. Hou and W. J. Huang, *J. Am. Chem. Soc.* **2008**, *130*, 2120.

8. M. He, F. Qiu and Z. Lin, *Energy Environ. Sci*. **2013**, *6*, 1352.

9. M. Jorgensen, K. Norrman, S. A. Gevorgyan, T. Tromholt, B. Andreasen and F. C. Krebs, *Adv. Mater*. **2012**, *24*, 580.

10. J. Wu, Y. Sun, W. B. Pei, L. Huang, W. Xu and Q. Zhang, *Synth. Met*. **2014**,*196*, 173.

11. C. T. Hong, W. Lee, Y. H. Kang, Y. Yoo, J. Ryu, S.Y. Cho and K. S. Jang, *J. Mater. Chem. A.* **2015**, *3*, 12314.

12. Q. Yao, L. Chen, W. Zhang, S. Liufu and X. Chen, *ACS Nano* **2010**, *4*, 2445.

13. D. Kim, Y. Kim, K. Choi, J. D. Grunlan and C. Yu, *ACS Nano* **2010**, *4*, 513.

14. S. J. Devaki, N. K. Sadanandhan, R. Sasi, H. A. P. Adler and A. J. Pich, *J. Mater. Chem. C.* **2014**, *2*, 6991.

15. C. Liu, L. Miao, J. Zhou, R. Huang, C. A. J. Fisher and S. Tanemura, *J. Phys. Chem. C*. **2013**, *117*, 11487.

16. S. Yuan, J. Mu, R. Mao, Y. Li, Q. Zhang and H. Wang, *ACS Appl. Mater. Interfaces*. **2014**, *6*, 5719.

17. L. Teruel, Y. Bouizi, P. Atienzar, V. Fornes and H. Garcia, *Energy Environ. Sci*. **2010**, *3*, 154.

18. H. Sun, Y. Yu, J. Luo, M. Ahmad and J. Zhu, *CrystEngComm*. **2012**, *14*, 8626.

19. J. Tian, L. Lv, X. Wang, C. Fei, X. Liu, Z. Zhao, Y. Wang and G. J. Cao, *J. Phys. Chem. C.* **2014**, *118*, 16611.

20. B. Liu, Z. Wang, Y. Dong, Y. Zhu, Y. Gong, S. Ran, Z. Liu, J. Xu, Z. Xie, and D. Chen, et al. *J. Mater. Chem*. **2012**, *22*, 9379.

21. K. P. Ong, D. J. Singh, and P. Wu, *Phys. Rev. B: Condens. Matter Mater. Phys.* **2011**, *83*, 115110.

22. X. Liang, *ACS Appl. Mater. Interfaces.* **2015**, *7*, 7927.

23. K. Park, J. K. Seong, Y. Kwon, S. Nahm and W. S. Cho, *Mater. Res. Bull.* **2008**, *43*, 54.

24. H. Ohta, W. S. Seo, and K. Koumoto, *J. Am. Ceram. Soc.* **1996**, *79*, 2193.

25. P. Jood, R. J. Mehta, Y. Zhang, G. Peleckis, X. Wang, R. W. Siegel, T. B. Tasciuc, S. X. Dou and G. Ramanath, *Nano Lett.* **2011**, *11*, 4337.

26. K. H. Jung, K. H. Lee, W. S. Seo and S. M. Choi, *Appl. Phys. Lett.* **2012**, *100*, 253902.

27. Y. Yang, K.C. Pradel, Q. Jing, J. M. Wu, F. Zhang, Y. Zhou, Y. Zhang and Z. L. Wang, *ACS Nano* **2012**, *6*, 6984.

28. R. Ramakrishnan, A. Aravind, S. J. Devaki, M. R. Varma and K. Mohan, *J. Phys. Chem. C.* **2014**, *118*, 19529.

29. S. K. Bux, J. P. Fleurial and R. B. Kaner, *Chem. Commun.* **2010**, *46*, 8311.

30. Q. Zhang, Y. Sun, W. Xu and D. Zhu, *Adv. Mater.* **2014**, *26*, 6829.

31. F. J. DiSalvo, *Science* **1999**, *285*, 703.

32. L. E. Bell, *Science* **2008**, *321*, 1457.

33. G. Chen, M. S. Dresselhaus, G. Dresselhaus, J. P. Fleurial and T. Caillat, *Materials. Int. Mater. Rev.* **2003**, *48*, 45.

34. Y.Q. Cao, X. B. Zhao, T. J. Zhu, X. B. Zhang and J. P. Tu, *Appl. Phys. Lett.* **2008**, *92*, 143106.

35. Y. Gelbstein, Z. Dashevsky and M. P. Dariel, *Phys. B.* **2005**, *363*, 196.

36. L. Yan, M. Shao, H. Wang, D. Dudis, A. Urbas and B. Hu, *Adv. Mater.* **2011**, *23*, 120.

37. O. Bubnova and X. Crispin, *Energy Environ. Sci.* **2012**, *5*, 9345.

38. J. Wang, K. Cai and S. Shen, *Org. Electron.* **2014**, *15*, 3087.

39. Y. Wang, K. Cai, and X. Yao, *ACS Appl. Mater. Interfaces.* **2011**, 3, 1163.

40. D. Yoo, J. Kim, S. H. Lee, W. Cho, H. H. Choi, F. S. Kim and J. H. Kim, *J. Mater. Chem. A.* **2015**, *3*, 6526.

41. X. Pan, M. Q. Yang, X. Fu, N. Zhang and Y. J. Xu, *Nanoscale* **2013**, *5*, 3601.

42. E. S. Junior, F. A. L. Porta, M. S. Liu, J. Andrés, J. A. Varela and E. Longo, *Dalton Trans.* **2015**, *44*, 3159.

43. M. R. Reyes, I. C. Cruz and R. L. Sandoval, *J. Phys. Chem. C.* **2010**, *114*, 20220.

44. K. Xu, G. Chen and D. Qiu, *J. Mater. Chem. A.* **2013**, *1*, 12395.

45. T. Y. Kim, C. M. Park, J. E. Kim and K. S. Suh, *Synth. Met.* **2005**, *149*, 169.

46. K. C. See, J. P. Feser, C. E. Chen, A. Majumdar, J. J. Urban, and R. A. Segalman, *Nano Lett.* **2010**, *10*, 4664.

47. M. He, J. Ge, Z. Lin, X. Feng, X. Wang, H. Lu, Y. Yang and F. Qiu, *Energy Environ. Sci.* **2012**, *5*, 8351.

48. C. Yi, A. Wilhite, L. Zhang, R. Hu, S. S. C. Chang, J. Zheng and X. Gong, *ACS Appl. Mater. Interfaces*, **2015**, *7*, 8984.

49. T. Y. Chiang, M. C. Huang and C. H. Tsai, *RSC Adv.* **2014**, *4*, 21201.

50. W. H. Jhang, Y. J. Lin, C. H. Ruan and D. S. Liu, *Thin Solid Films*, **2013**, *539*, 323.

51. C. Yang, P. Liu and T. Wang, *ACS Appl. Mater. Interfaces*, **2011**, *3*, 1109.

52. D. K. Taggart, Y. Yang, S. C. Kung, T. M. McIntire and R. M. Penner, *Nano Lett.* **2011**, *11*, 125.

53. G. H. Kim and K. P. Pipe, *Phys. Rev. B*, **2012**, *86*, 085208.

54. O. Bubnova, Z. U. Khan, A. Malti, S. Braun, M. Fahlman, M. Berggren, and X. Crispin, *Nat. Mater.* **2011**, *10*, 429.

55. G. H. Kim, D. H. Hwang and S. I. Woo, *Phys. Chem. Chem. Phys.* **2012**, 14, 3530.

56. J. Ouyang, Q. Xu, C. W. Chu, Y. Yang, G. Li, J. Shinar, *Polymer* **2004**, *45*, 8443.

57. M. Zebarjadi, K. Esfarjani, M. S. Dresselhaus, Z. F. Ren and G. Chen, *Energy Environ. Sci*. **2012**, *5*, 5147.

58. N. Toshima, N. Jiravanichanun and H. Marutani, *J. Electron. Mater*. **2012**, *41*, 1735.

59. G. P. Moriarty, K. Briggs, B. Stevens, C. Yu and J. C. Grunlan, *Energy Technol*. **2013**, *1*, 265.

60. J. Luo, D. Billep, T. Waechtler, T. Otto, M. Toader, O. Gordan, E. Sheremet, J. Martin, M. Hietschold and D. R. T. Zahn, et al. *J. Mater. Chem. A.* **2013**, *1*, 7576.

61. C. J. Vineis, A. Shakouri, A. Majumdar and M. G. Kanatzidis, *Adv. Mater*. **2010**, 22, 3970.

62. A. J. Minnich, M. S. Dresselhaus, Z. F. Ren and G. Chen, *Energy Environ. Sci*. **2009**, *2*, 466.

Summary

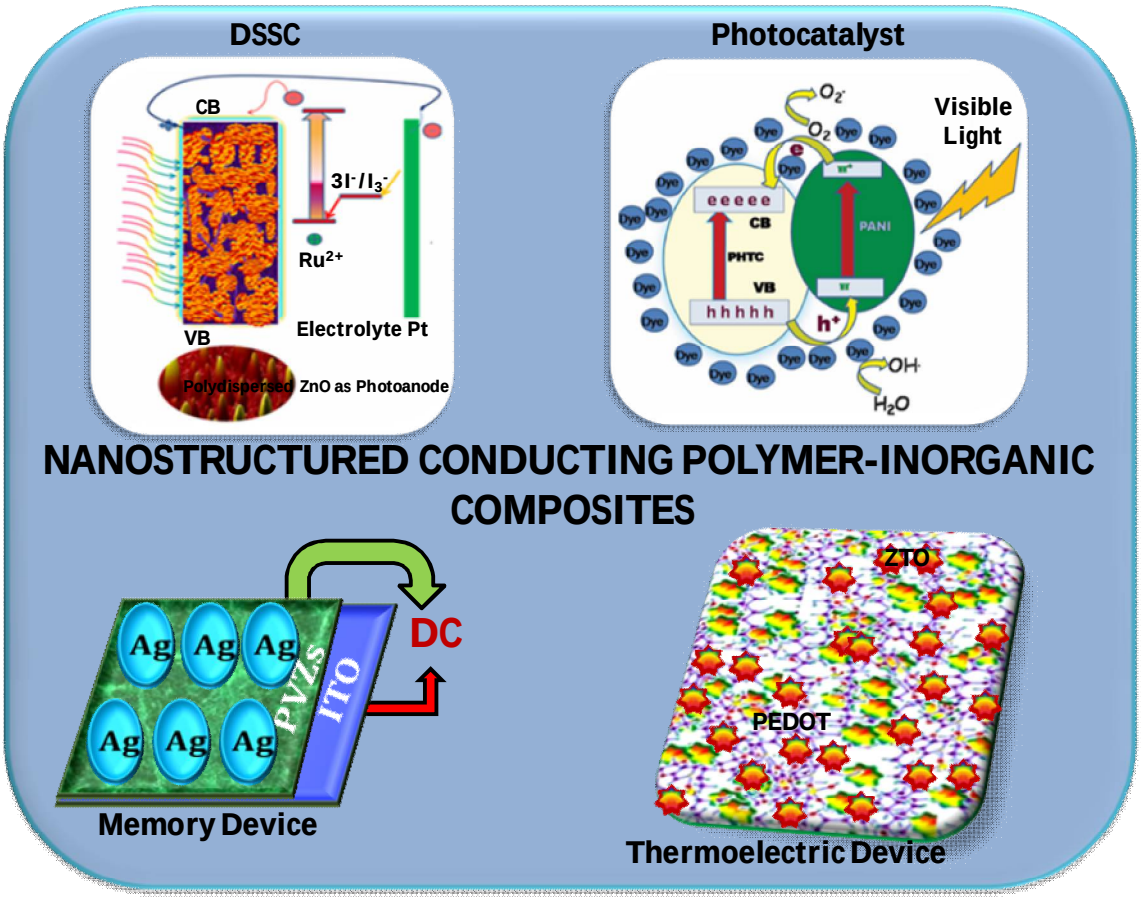

Thers has been considerable interest in the development of nanostructured semiconducting polymer-inorganic nanocomposites for wide range of applications such as in energy conversion, electronic devices, storage, sensors and biomedical devices.They exhibit facinating synergistic properties arising from the molecular level mixing of conducting polymer and inorganic counter parts. Its possess unique features such as flexibility, light weight, solution processability and printability over a large area which make them favourable for their high tech applications. The performance of all the electronic device mainly rely on the charge carrier mobility and concentration of charges apart from its fabrication.Various experimental

results of this studies revealed that development of composites comprising p- type conducting polymers having extended π-bonds intimately stacking with n-type inorganic metal oxide enhances the concentration and mobility of charge carriers by various mechanism. Performance of these materials evaluated by studying its photocatlytic activity, DSSC and also fabricating devices such as memory and thermoelectric.

The sailent results of the present research program are summarized below.

Semiconducting polyaniline-clay-titania nanocomposite was successfully prepared by the in-situ polymerization of anilinium hydrochloride in presence of titanate functionalized nanoclay at room temperature. Formation of self-assembled three dimensionally structure of PPTC was confirmed by XRD and morphological analysis. The interface formed between PHTC and PANI transfers the excited electrons to the conduction band of PHTC and hole transferring to the valency band of PANI which in turn increases the yield of hydroxyl, super oxide and positive carbon radicals. The photocatalytic mechanism of PPTC towards methyl orange and methylene blue arising from the photo-oxidation and photosensitizing mechanisms between PANI and PHTC is proposed. Studies revealed that this multifunctional PPTC nanocomposite can be employed as a potential candidate for environmental purification.

Hierarchical multiple structures of zinc oxide were prepared successfully using a bioanchoring sol–gel process. Growth mechanisms for the formation of various hierarchical structures were proposed from the results obtained by XRD and microscopic analysis. Presence of various of defect states were confirmed from Raman, photoluminescence spectroscopy. Finally demonstrated its application as

an effective photoanodes for DSSC. The maximum power conversion efficiency of 5.3 % obtained for polydispersed ZnO hollow spheres.

Semiconducting polyvinylcarbazole-ZnO composites were prepared by oxidative polymerization of VK in presence of ZnO. Studies showed that electrical bistability and conduction mechanism of the devices depends upon the amount of ZnO nanoparticles present in the nanocomposite. Memory devices were fabricated with configuration of Ag/PVZ/ITO using PVZ as active material. PVZ4 device exhibited excellent ON/OFF current ratio of $5.2x10^3$ along with high endurance stability and reliability

Semiconducting nanocomposites of PZT prepared through a facile strategy. Fabricated thermoelectric device having the configuration of Cu/PZT/Cu using PZT as an active material. The synergistic effect of conjugated polymer (PEDOT)and semiconduucting metal oxide (ZTO) nanocomposite exhibited this as an excellent active material for thermoelectric devices with excellent charge carrier concentration (3.92×10^{20} cm^{-3}), charge carrier mobility (0.83 cm^2 V^{-1} S^{-1}), electrical conductivity of (52 Scm^{-1}), low thermal conductivity (0.0495 $Wm^{-1}K^{-1}$), Seebeck coefficient (19.05 μ V K^{-1}), and power factor (1.28 μW K^{-2} m^{-1}). The hybrid composites showed maximum ZT values of 4.8×10^{-3} at 303 K and 1.49×10^{-2} at 383 K with the configuration Cu/ PZT/Cu.

The outcome of our research program suggests that proper molecular level designing and understanding on the structure-property correlation and mechanism is inevitable for tuning the electro-optical properties, charge concentration and mobility of the semiconducting polymer inorganic nanocompoite for utilizing as an efficient active material for bringing revolution in nanoelectronic device technology.

List of International Publications

1. Nanostructured Polyaniline-Polytitanate-Clay Composite for Photocatalytic Applications: Rajaraman Ramakrishna, Sudha J. Devaki and Viswan L. Reena, RSC Advance. RSC Advances, 2012, 2, 6228 – 6236.
2. Development of electromagnetic interference shielding materials Viswan L. Reena, Sudha J. Devaki and Rajaraman Ramakrishnan, Journal of Applied Polymer Science, 2013, 128,1756-1763.
3. A solution processable fluorene-fluorenone oligomer with aggregation induced emission enhancement. Soundaram Jeevarathinam Ananthakrishnan, Elumalai Varathan, Ezhakudiyan Ravindran, Narayanasastri Somanathan, Venkatesan Subramanian, Asit Baran Mandal, Sudha J. Devaki, Rajaraman Ramakrishnan, Chemical Communications, 2013, 49, 10742-10744.
4. Percolated conductive polyaniline-clay nanocomposite and self-assembly. Sudha J. Devaki, S. Sivakala, C. K. Chandrakanth, K. S. Neethu, K. N. Rohini, Rajaraman Ramakrishnan, eXPRESS Polymer Letters, 2014, 8, 107-115.
5. Effect of nano/micro-mixed ceramic fillers on the dielectric and thermal properties of epoxy polymer composites. S. S. Vaisakh, Mehrad Hassanzadeh, Renaud Metz, Rajaraman Ramakrishnan, Delphine Chappelle, Sudha J. Devaki and S. Ananthakumar, Polymers for Advanced Technologies., 2014, 25,240-248.
6. Facile Bio-anchoring Strategy for the Preparation of Hierarchical Multiple Structured ZnO Crystals and its Application as a Photoanode in DSSC. Rajaraman Ramakrishnan, Aravind Aashish, Kiran Mohan and Sudha J. Devaki, Journal of Physical Chemistry C, 2014, 118,19529-19539.

7. Offsetting the problem of charge trapping in white polymer light emitting diode Soundaram Jeevarathinam Ananthakrishnan, Elumalai Varathan, Narayanasastri Somanathan, Venkatesan Subramanian, Asit Baran Mandal, Sudha J. Devaki and Rajaraman Ramakrishnan, Journal of Material Chemistry C, 2014, 2, 9035-9044.
8. Nanocubes of rutile titania for enhanced visible light photocatalytic application, Aravind Aashish, Rajaraman Ramakrishnan, Sudha J. Devaki, M. Sankaran, G. Krishna Priya, Materials Chemistry and Physics, 2015, 157,31-38.
9. Nanostructured Semiconducting PEDOT–TiO_2/ZnO Hybrid Composite for Nanoelectronic Application, Rajaraman Ramakrishnan, Sudha J Devaki, Aravind Aashish, Senoy Thomas, Manoj Raama Varma, Najiya K P P, Journal of Physical Chemistry C, 2016, 120, 4199-4210.
10. Facile Strategy for the Fabrication of Efficient Nonvolatile Bistable Memory Device Based on Polyvinylcarbazole-Zinc Oxide, Rajaraman Ramakrishnan, K B Jinesh, Manoj Raama Varma, Sudha J. Devaki, Physica of solid statue a: Application and Material Science, 2016, 1-11.
11. Self-assembled Hybrid Polyvinylcarbazole-Titania Nanotubes as an Efficient Photoanode for Solar Energy Harvesting, Aravind Aashish, Rajaraman Ramakrishnan, Sudha J. Devaki, M. Sankaran, G. Krishna Priya, Solar Energy and Solar Materials, 2016, 151, 169-178.
12. Organic – Inorganic Hybrid Nanocomposites for Opto-Electronic Application, Rajaraman Ramakrishnan, Aravind Aashish, Sudha J. Devaki (to be communicated)

Presentations in international Conferences

1. Nanostructured polyaniline-polytitanate-clay composite for photocatalytic applications: Ramakrishnan Ramakrishnan and Sudha J. Devaki, Poster presented in International conference MACRO held at IIT Delhi during December 15-17, 2010.
2. Tuning the Size and Shape of Titania particles using bio-based template approach, Rajaraman Ramakrishnan, Aravind Aashish and Sudha J Devaki, Poster presented in International Conference Nano India 2013 held at CSIR-NIIST Thiruvananthapuram during February 19-20, 2013.
3. Biotemplate Strategy for Tweaking the Shape of Hierarchical Polydisperse ZnO Nanostructures and its Application in DSSC, Rajaraman Ramakrishnan, Aravind Aashish and Sudha J. Devaki, Poster presented in International Conference on Nanoscience & Technology" (ICONSAT-2015) held at Institute of Nano Science and Technology, Mohali and Panjab University, Chandigarh during March 2-5, 2014.
4. Nanostructured Conductive Polymer Inorganic Hybrid Nanocomposite for Electronic Applications, invited talk in Polymer Conference for Young Researchers (PCYR 2015) held at CSIR-NIIST on December 18, 2015.